TECHNISCHE UNIVERSITÄT
MÜNCHEN

Lehrstuhl für Numerische Mechanik

Computational Modeling of Multi-Field and Multi-Scale Phenomena in Respiratory Mechanics

Lena Wiechert

Vollständiger Abdruck der von der Fakultät für Maschinenwesen der Technischen Universität München zur Erlangung des akademischen Grades eines

Doktor-Ingenieurs (Dr.-Ing.)

genehmigten Dissertation.

Vorsitzender:	Univ.-Prof. Dr. mont. habil. Dr. h. c. Ewald Werner
Prüfer der Dissertation:	
1.	Univ.-Prof. Dr.-Ing. Wolfgang A. Wall
2.	Univ.-Prof. Dr. techn. Gerhard A. Holzapfel Technische Universität Graz / Österreich

Die Dissertation wurde am 17.01.2011 bei der Technischen Universität München eingereicht und durch die Fakultät für Maschinenwesen am 16.05.2011 angenommen.

Abstract

Mechanical ventilation is a vital supportive therapy for many intensive care patients. Preexisting heterogeneous lung damages, however, predispose patients towards ventilator-associated lung injuries (VALI). Biologically, these severe complications manifest themselves at the alveolar level in terms of inflammatory responses resulting from mechanical overstraining. Since the exact mechanisms that mediate lung injury are still unclear, the definition of ventilation strategies aimed at reducing the incidence of VALI is hampered.

The present work is concerned with the development of computational approaches enabling the detailed investigation of respiratory mechanics in general and VALI in particular. Conceptually, the lung is divided into two main subsystems, namely the conducting airways and the respiratory zone also known as lung parenchyma. The complexity inherent to both components inhibits a direct numerical simulation considering all relevant structures. Hence, only small portions of each subsystem can be resolved in detail. With regard to computational modeling, therefore, the major challenges are to adequately consider the unresolved parts and merge the individual components into one overall virtual lung model. Within this work, corresponding approaches are derived and their functionality is demonstrated by simple examples.

As a first step, a detailed computational model of alveoli, the parenchymal micro-structure, is established. Due to the limited availability of imaging-based geometries, a method for generating artificial ventilatory units is developed. For the mathematical description of alveolar soft tissue behavior, a hyperelastic constitutive model based upon general morphological information is suggested. The influence of the fluid film covering alveolar walls is also considered. For this purpose, a novel surface coupling of tissue and interfacial mechanics is proposed. To model the complex behavior of the surface active agents in the liquid lining, an elaborate constitutive law relating the local concentration of these substances to the surface stresses is employed.

On the global level, lung parenchyma is modeled as a homogenized continuum. At certain “hot spots”, however, the complex alveolar micro-structure is resolved to enable the quantification of local stresses and strains. To bridge the gap between global parenchymal and local alveolar level, a novel multi-scale method is proposed. The benefit of this strategy is twofold; firstly, improved overall parenchyma properties are derived based on a detailed modeling of the underlying micro-structure. Secondly, the global model serves as an “embedding” of locally resolved ventilatory units, thereby providing physiologically reasonable boundary conditions for alveolar simulations.

Finally, a novel approach to combining parenchyma and airway models into one overall lung model is established. Since only parts of both the airway tree and the alveolar structures can be resolved, the transport of air down to the respiratory zone cannot be simulated explicitly but has to be modeled. To consider the interplay of airflow in the resolved domain and tissue deformation, a coupling of air and parenchyma volumes is proposed. A combination of the developed multi-scale and volume coupling approaches enables the sensible investigation of local alveolar behavior during (mechanical) ventilation for the first time.

Zusammenfassung

Für viele Intensivpatienten ist die künstliche Beatmung lebensnotwendig. Bei Vorerkrankungen des Atemapparats besteht jedoch die Gefahr von beatmungsinduzierten Lungenschäden. Typische Symptome sind Entzündungsreaktionen im Alveolarbereich, die durch eine mechanische Überbeanspruchung hervorgerufen werden. Die genauen Ursachen für diese schwere Komplikation sind derzeit noch unklar. Daher ist es sehr schwierig, Beatmungsstrategien, die auf eine Verringerung der beatmungsinduzierten Lungenschäden abzielen, zu entwickeln.

Die vorliegende Arbeit beschreibt die Entwicklung numerischer Methoden, die die Modellierung der Lungenmechanik im Allgemeinen und beatmungsinduzierter Lungenschäden im Speziellen ermöglichen. Die Lunge wird gedanklich in die Atemwege und das als Parenchym bezeichnete Lungengewebe unterteilt. Beide Teilsysteme sind für sich genommen so komplex, dass sie sich einer ausführlichen Modellierung entziehen. Dementsprechend können stets nur kleine Bereiche detailliert aufgelöst werden. Die besondere Herausforderung bei der Modellbildung besteht daher darin, die nicht aufgelösten Bereiche sinnvoll abzubilden und die Einzelteile zu einem umfassenden virtuellen Lungenmodell zu verbinden. Nach der Vorstellung der hierzu entwickelten Methoden wird deren Funktionalität anhand einfacher numerischer Beispiele demonstriert.

In einem ersten Schritt wird ein detailliertes Modell für die alveoläre Mikrostruktur des Parenchyms entwickelt. Wegen der begrenzten Möglichkeiten bildgebender Verfahren wird zunächst eine Methode zur Generierung künstlicher Alveolargeometrien entwickelt. Das Verhalten des weichen Gewebes wird mit Hilfe eines hyperelastischen Materialgesetzes modelliert, das auf allgemeinen morphologischen Informationen basiert. Der Einfluss des Flüssigkeitsfilms, der die Alveolarwände bedeckt, wird ebenfalls berücksichtigt. Zu diesem Zweck wird eine neue Oberflächenkopplung von Gewebs- und Grenzflächenmechanik entwickelt. Das komplexe Verhalten der grenzflächenaktiven Moleküle im Flüssigkeitsfilm wird mit einem Modell beschrieben, das die lokale Konzentration dieser Substanzen mit den zugehörigen Oberflächenspannungen korreliert.

Auf globaler Ebene wird Lungenparenchym als ein homogenisiertes Kontinuum modelliert. An ausgewählten "Hotspots" wird jedoch die alveoläre Mikrostruktur aufgelöst, um eine Bestimmung der lokalen Spannungen und Dehnungen zu ermöglichen. Zur Überbrückung des vorhandenen Skalenunterschieds wird eine neuartige Mehrskalenformulierung vorgeschlagen. Dieser Ansatz ermöglicht einerseits die Bestimmung verbesserter globaler Parenchymeigenschaften durch die genaue Modellierung der zugrunde liegenden Mikrostruktur. Andererseits werden physiologisch sinnvolle Randbedingungen für die Alveolarsimulationen definiert, indem die lokal aufgelöste Mikrostruktur in das globale Modell eingebettet wird.

In einem letzten Schritt wird ein neuer Ansatz für die Verbindung von Parenchym- und Atemwegsmodellen zu einem Gesamtlungenmodell etabliert. Da nur Teile des Atemwegsbaums und der parenchymalen Mikrostruktur aufgelöst werden können, kann der Gastransport in die Alveolen nicht direkt simuliert werden. Um das Zusammenspiel von Luftströmung und Gewebedeformation dennoch zu berücksichtigen, wird eine Kopplung von Luftund Parenchymvolumina vorgeschlagen. Eine Kombination der in dieser Arbeit entwickelten Mehrskalen- und Volumenkopplungsansätze ermöglicht erstmalig eine sinnvolle Analyse des lokalen alveolären Verhaltens während der (Be-)Atmung.

Danksagung

An dieser Stelle möchte ich allen meinen Dank aussprechen, die mich in meiner Promotionszeit begleitet und zum Gelingen der vorliegenden Arbeit beigetragen haben.

Bei meinem Doktorvater Prof. Dr. Wolfgang Wall bedanke ich mich herzlich für die Anregung zu dieser Arbeit, sein Vertrauen und seine uneingeschränkte Unterstützung. Sein motivierender Führungsstil und das von ihm geschaffene Umfeld sind die optimalen Voraussetzungen für eigenständiges wissenschaftliches Arbeiten. Er hat meine Begeisterung für die Forschung geweckt und meine persönliche Entwicklung maßgeblich geprägt. Sowohl fachlich als auch menschlich ist er mir ein großes Vorbild.

Weiterhin bedanke ich mich bei Prof. Dr. Gerhard Holzapfel vom Institut für Biomechanik an der Technischen Universität Graz für die Übernahme des Mitberichts. Sein Interesse an meiner Arbeit ist mir eine große Ehre.

Für die Übernahme des Vorsitzes meiner Prüfungskommission danke ich Prof. Dr. Dr. Ewald Werner vom Lehrstuhl für Werkstoffkunde und Werkstoffmechanik der TUM.

Bei meinen derzeitigen und ehemaligen Kollegen möchte ich mich herzlich für die angenehme Arbeitsatmosphäre bedanken. Besonders die Zusammenarbeit mit Sophie Rausch und Dr. Andrew Comerford im "Team Lung" war für mich sehr wertvoll. Außerdem möchte ich mich bei Dr. Volker Gravemeier, Dr. Ulrich Küttler, Dr. Axel Gerstenberger, Dr. Peter Gamnitzer und Thomas Klöppel für ihre umfassende Unterstützung bedanken.

Für die Förderung durch die Deutsche Forschungsgemeinschaft (DFG) im Rahmen des Forschungsschwerpunktes "Protektive Beatmung" bin ich sehr dankbar. Die Zusammenarbeit mit renommierten Wissenschaftlern aus verschiedenen Disziplinen habe ich als großes Privileg empfunden. Vor allem danke ich Prof. Dr. Stefan Uhlig, Prof. Dr. Josef Guttmann, Prof. Dr. Knut Möller, Prof. Dr. Edmund Koch und Dr. Constanze Dassow. Die vielen hilfreichen Erklärungen und ergiebigen Diskussionen haben meine Arbeit sehr vorangebracht.

Besonderer Dank gebührt auch meiner Familie und meinem Verlobten Tomo für ihre Geduld, Anteilnahme und Unterstützung in allen Phasen meiner Promotion.

Lena Wiechert

Contents

Nomenclature

Representation of scalars, tensors and discretized quantities

q,Q	Scalar value
$\boldsymbol{q}$	Vector
$\boldsymbol{Q}$	Second-order tensor
$\boldsymbol{\mathscr{Q}}$	Higher-order tensor
$\boldsymbol{\mathcal{Q}}$	Voigt's notation of higher-order tensor
$\boldsymbol{\mathsf{q}}$	Discrete vector
$\boldsymbol{\mathsf{Q}}$	Discrete matrix, Voigt's notation of second-order tensor

Operators and symbols

$(\cdot)^{\mathsf{T}}$	Transpose of a tensor
$(\cdot)^{-1}$	Inverse of a tensor or mapping
$(\cdot)^{-\mathsf{T}}$	Transpose of the inverse of a tensor
$(\hat{\cdot})$	Prescribed quantity
$(\dot{\cdot})$	Time derivative at fixed reference position
$(\mathring{\cdot})$	Time derivative at fixed ALE reference position
det	Determinant
tr	Trace operator
Lin	Linearization operator
∇_0	Material gradient operator
∇	Spatial gradient operator

$\nabla_0 \cdot$	Material divergence operator
$\nabla \cdot$	Spatial divergence operator
$\otimes$	Dyadic product
$\odot$	Specific tensor product
$\mathscr{E}$	Levi-Civita symbol
$\boldsymbol{I},\mathsf{\mathbf{I}}$	Identity tensor and matrix
$\mathbf{0}$	Zero tensor or matrix
exp	Exponential function
HOT	Higher order terms
$\mathscr{S}$	Stabilization terms

Subscripts and superscripts

$(\cdot)^h$	Discretized in space with FE
$(\cdot)^{(e)}$	Element
$(\cdot)^{\mathsf{S}}$	Solid field
$(\cdot)^{\mathsf{F}}$	Fluid field
$(\cdot)^{\mathsf{A}}$	ALE field
$(\cdot)^{\mathsf{C}}$	Constraint
$(\cdot)^{\mathsf{FSI}}$	Fluid-structure interaction (FSI)
$(\cdot)^{\mathsf{BE}}$	Balance equation
$(\cdot)^{\mathsf{TBC}}$	Traction boundary condition
$(\cdot)^{\mathsf{int}}$	Internal
$(\cdot)^{\mathsf{ext}}$	External
$(\cdot)^{\mathsf{kin}}$	Kinetic
$(\cdot)^{\mathsf{effdyn}}$	Effective dynamic
$(\cdot)^{\mathsf{m}}$	Linear momentum
$(\cdot)^{\mathsf{c}}$	Continuity

$(\cdot)^{\mathsf{LM}}$	Lagrange multiplier method
$(\cdot)^{\mathsf{P}}$	Penalty method
$(\cdot)^{\mathsf{surf}}$	Surface stress
$(\cdot)^{\mathsf{mix}}$	Mixture model
$(\cdot)^{\mathsf{cond}}$	Condensed mixture model
$(\cdot)^{\mathsf{CFSI}}$	Constrained FSI
$(\cdot)^{\mathsf{lin}}$	Linear solver
$(\cdot)_{\mathsf{gp}}$	Gauss point
$(\cdot)_{\mathsf{M}}$	Macro-scale
$(\cdot)_{\mathsf{m}}$	Micro-scale
$(\cdot)_{\mathsf{stab}}$	Stabilized
$(\cdot)_{\mathsf{prec}}$	Preconditioned

Mappings

ϕ	Mapping between reference and spatial configuration
ζ	Mapping between reference configuration and parameter space
φ	Mapping between ALE reference and spatial configuration
$\bar{\boldsymbol{J}}$	Jacobian of the mapping $\phi \circ \zeta$

Domains and boundaries

Ω_0	Reference domain
Ω	Spatial domain
$\partial\Omega_0$	Boundary in reference configuration
$\partial\Omega$	Boundary in spatial configuration
$\partial\Omega_{0;\mathsf{D}}$	Dirichlet partition of boundary in reference configuration
$\partial\Omega^{\mathsf{F}}_{\mathsf{D}}$	Dirichlet partition of boundary in spatial configuration

$\partial\Omega_{0;\mathsf{N}}$	Neumann partition of boundary in reference configuration
$\partial\Omega^{\mathsf{F}}_{\mathsf{N}}$	Neumann partition of boundary in spatial configuration
I	Identifier for interior DOFs
B	Identifier for RVE or FSI boundary DOFs
$\hat{\mathsf{B}}$	Identifier for outflow boundary DOFs
$\bar{\mathsf{B}}$	Identifier for DOFs associated with both outflow and FSI boundaries
$\tilde{\mathsf{B}}$	Identifier for remaining boundary DOFs of parenchyma block
$\check{\mathsf{B}}$	Identifier for FSI boundary DOFs in case of unresolved airway wall

Kinematics

$\boldsymbol{x}_0$	Position in reference configuration
$\boldsymbol{x}$	Position in spatial configuration
$\boldsymbol{d}$	Displacement vector
$\dot{\boldsymbol{d}}$	Solid velocity vector
$\ddot{\boldsymbol{d}}$	Solid acceleration vector
V_0,V	Reference and current volume
A_0,A	Reference and current surface area
$\boldsymbol{g}_0,\boldsymbol{g}$	Basis vector in reference and spatial configuration
$\tilde{\boldsymbol{n}}_0,\tilde{\boldsymbol{n}}$	Normal vector in reference and spatial configuration
$\boldsymbol{n}_0,\boldsymbol{n}$	Unit normal vector in reference and spatial configuration
$\boldsymbol{F}$	Deformation gradient
J	Determinant of $\boldsymbol{F}$
$\bar{\boldsymbol{F}}$	Isochoric part of $\boldsymbol{F}$
$\tilde{\boldsymbol{R}}$	Rotation tensor
$\tilde{\boldsymbol{U}}$	Stretch tensor
$\boldsymbol{C}$	Right Cauchy-Green deformation tensor
$\bar{\boldsymbol{C}}$	Isochoric right Cauchy-Green deformation tensor

I_1,I_2,I_3	First, second and third invariant of $\boldsymbol{C}$
$\bar{I}_1$,$\bar{I}_2$,$\bar{I}_3$	First, second and third invariant of $\bar{\boldsymbol{C}}$
Λ_1,Λ_2,Λ_3	First, second and third principal stretch
$\boldsymbol{E}$	Green-Lagrange strain tensor
$\boldsymbol{A}$	Euler-Almansi strain tensor
χ	Position in ALE reference configuration
$\boldsymbol{d}^{\mathsf{A}}$	ALE grid displacements
$\boldsymbol{u}^{\mathsf{A}}$	ALE grid velocity
$\boldsymbol{c}$	Convective velocity
$\boldsymbol{u}$	Fluid velocity
$\mathring{\boldsymbol{u}}$	Fluid acceleration
$\boldsymbol{\epsilon}$	Strain rate tensor

Stress measures

$\boldsymbol{P}$	First Piola-Kirchhoff stress tensor
$\boldsymbol{S}$	Second Piola-Kirchhoff stress tensor
$\boldsymbol{\sigma}$	Cauchy stress tensor
$\bar{p}$	Pressure
p	Kinematic pressure

Constitutive models

μ_1^{S},μ_2^{S}	Lamé constants
E^{S}	Young’s modulus
ν^{S}	Poisson’s ratio
μ^{F}	Dynamic viscosity
ν^{F}	Kinematic viscosity

Ψ	Strain energy density function (SEF)
$\bar{\Psi}^{\mathsf{gs}}$	Isochoric ground substance SEF
c	Parameter of $\bar{\Psi}^{\mathsf{gs}}$
$\bar{\Psi}^{\mathsf{fib}}$	Isochoric collagen fiber SEF
$\boldsymbol{H}$	General structural tensor
$\boldsymbol{a}$	Fiber direction
$\hat{\rho}$	Fiber orientation density function
$\hat{\theta}$	Angle between individual fiber and preferential fiber direction
η	Fiber orientation dispersion parameter
$\bar{J}_4$	Mixed invariant of $\bar{\boldsymbol{C}}$
k_1,k_2	Parameters of $\bar{\Psi}^{\mathsf{fib}}$
U	Volumetric SEF
ϵ_1,ϵ_2	Parameters of U
δ_1,δ_3,δ_6,δ_7	Coefficients of elasticity tensor
$\mathscr{A}$,$\boldsymbol{\mathcal{A}}$	Constitutive tensor/matrix relating $\boldsymbol{P}$ and $\boldsymbol{F}$
$\mathscr{C}$,$\boldsymbol{\mathcal{C}}$	Constitutive tensor/matrix relating $\boldsymbol{S}$ and $\boldsymbol{E}$
$\boldsymbol{\Xi}$	Internal variables

Governing equations

ρ_0,ρ	Reference and current density
m	Mass
$\hat{\boldsymbol{b}}_0$,$\hat{\boldsymbol{b}}$	Body force in reference and spatial configuration
$\boldsymbol{t}$	Traction vector in spatial configuration
$\boldsymbol{t}_0$	Pseudo-traction vector in reference configuration
$\boldsymbol{r}$	Residual vector
$\boldsymbol{w}$	Weighting function vector
δ	Virtual
$\mathcal{W}$	Work
$\mathcal{P}$	Power

Spatial discretization

ξ	Position in parameter space
$\tilde{N}_I$	FE shape function of node I in reference configuration
N_I	FE shape function of node I in parameter space
$\mathbf{x}_0$,$\mathbf{x}$	Vector of nodal positions in reference and current configuration
$\mathbf{d}$,$\dot{\mathbf{d}}$,$\ddot{\mathbf{d}}$	Vector of nodal solid displacements, velocities and accelerations
$\mathbf{u}$	Vector of nodal fluid velocities (and possibly also pressures)
$\mathbf{p}$	Vector of nodal pressures
$\mathring{\mathbf{u}}$	Vector of nodal fluid accelerations
$\mathbf{d}^{\mathsf{A}}$,$\mathbf{u}^{\mathsf{A}}$	Vector of nodal ALE grid displacements and velocities
$\mathbf{c}$	Vector of nodal convective velocities
nnod	Number of element nodes
ndim	Number of spatial dimensions
ngp	Number of Gauss points per element
nele	Number of elements
w_{gp}	Gaussian weight
$\mathbf{N}^{\mathsf{F}}$	Discrete linear viscous and nonlinear convective terms
$\mathbf{G}^{\mathsf{F}}$	Discrete gradient operator
$\mathbf{M}$	Mass matrix
$\mathbf{D}$	Damping matrix
$\mathbf{f}$	Discrete force vector

Time integration

Δt	Time step size
n	Time step
$\bar{\gamma}$,$\bar{\beta}$	Parameters of Newmark's method

α_f,α_m	Parameters of generalized-α method
ρ_∞	Spectral radius of time integration scheme in the high-frequency limit
θ	Parameter of the one-step-θ method

Linearization

$\mathsf{\mathbf{r}}$	Discrete residual vector
$\mathsf{\mathbf{K}}$	Stiffness matrix
i	Nonlinear iteration

Fluid-structure interaction

τ	Factor for the transformation of interface velocity increments into displacement increments
$\overline{(\cdot)}$	Scaled with $\frac{1}{\rho^\mathsf{F}}$
$\underline{(\cdot)}$	Scaled with ρ^F
$\underset{\sim}{(\cdot)}$	Scaled with τ
$\underset{\approx}{(\cdot)}$	Scaled with $\rho^\mathsf{F}\tau$

Constrained problems

C	Constraint equation
λ	Lagrange multiplier
$\mathrm{\lambda}$	Time-discrete Lagrange multiplier
$\boldsymbol{\lambda}$	Vector of time-discrete Lagrange multipliers
ϵ	Penalty parameter

Artificial alveolar morphology

L	Edge length of tetrakaidecahedron
m,n	Number of main-level tetrakaidecahedral cells in x_1- and x_2-direction
ID	ID of individual cell
S	Starting cell
A	Active cell
N	Randomly chosen neighbor of active cell A
C	Inactive queue cell
$\boldsymbol{x}^{\mathsf{S}}$,$\boldsymbol{x}^{\mathsf{A}}$,$\boldsymbol{x}^{\mathsf{N}}$,$\boldsymbol{x}^{\mathsf{C}}$	Cell center coordinates
$\boldsymbol{a}$	$\Delta\boldsymbol{x}$ between a cell and one of its neighbors
P^{N}	Length of path to N via A
P^{A}	Length of path to A
P^{C}	Length of path to C
Δv_{max}	Absolute value of maximum component of $\Delta\boldsymbol{x}$ between C and N
Δv_{mid}	Absolute value of medium component of $\Delta\boldsymbol{x}$ between C and N
Δv_{min}	Absolute value of minimum component of $\Delta\boldsymbol{x}$ between C and N
n_{diag},n_{straight}	Number of diagonal and straight pathways
$\tilde{P}^{\mathsf{N}}$	Length of alternative path to N
$\tilde{P}^{\mathsf{N}}_{\mathsf{min}}$	Minimum length of all alternative paths to N
$\bar{\mathbf{C}}$	List of cell center coordinates
$\bar{\mathbf{N}}$	List of cell neighbors of each cell
$\bar{\mathbf{S}}$	List of connecting surfaces of each cell
$\bar{\mathbf{q}}$	Queue vector
$\bar{\mathbf{p}}$	Vector of passed cells
$\bar{\mathbf{l}}$	Vector of path lengths
$\bar{\mathbf{D}}$	List of deleted surfaces of each cell
$\mathcal{V}_{\mathsf{mid}}$,$\mathcal{V}_{\mathsf{int}}$	Vertices of mid plane and interior surfaces

$\mathcal{L}_{\mathrm{mid}}$,$\mathcal{L}_{\mathrm{int}}$	Lines connecting mid plane and interior vertices
$\mathcal{S}_{\mathrm{mid}}$,$\tilde{\mathcal{S}}_{\mathrm{mid}}$	Non-empty and empty mid plane surfaces
$\mathcal{V}^{s}_{\mathrm{mid}}$,$\mathcal{L}^{s}_{\mathrm{mid}}$	Vertices and lines associated with mid plane surface s

Interfacial phenomena

N_{mol}	Number of interfacial molecules
A_{mol}	Surface area per interfacial molecule
E_{mol}	Excess energy per interfacial molecule
ε,ε_{p},ε_{e}	Scalar overall, plastic and elastic surface strain
$\hat{\gamma}$	Surface tension
γ	Scalar surface stress
γ_{p},γ_{e}	Scalar plastic and elastic surface stress
κ	Interface curvature

Surfactant model

Γ	Interfacial surfactant concentration
Γ_{eq}	Equilibrium interfacial surfactant concentration
Γ^{*}	Maximum (dynamic) equilibrium interfacial surfactant concentration
Γ_{max}	Maximum interfacial surfactant concentration
γ_{eq}	Equilibrium surfactant surface stress
γ^{*}	Maximum (dynamic) surfactant surface stress
γ_{min}	Minimum surfactant surface stress
γ_0	Surface stress/tension of water
$\bar{C}$	Bulk concentration of surfactant
α_1,α_2	Adsorption and desorption coefficient of surfactant
ς	Small number defining the range of surfactant concentrations in which the sorption parameters diminish to zero

$\bar{\alpha}_1,\bar{\alpha}_2$	Modified adsorption and desorption coefficient for $\Gamma/\Gamma^* \in [1-\varsigma;1]$
m_1,m_2	Isotherm slopes in the first and second regime
$\mathbf{f}^{\mathsf{surf}},\mathbf{K}^{\mathsf{surf}}$	Nodal surface stress forces and corresponding stiffness matrix

Multi-scale approach

$\tilde{\boldsymbol{w}}_{\mathsf{m}}$	Non-homogeneous micro-scale displacement fluctuations
$\mathbb{D}$	Matrix containing the positions of the undeformed RVE boundary nodes
$\tilde{\boldsymbol{U}}_{\mathsf{M}}^{\mathsf{EAS}}$	Modified macroscopic stretch tensor in case of EAS formulation
$\boldsymbol{F}_{\mathsf{M}}^{\mathsf{EAS}}$	Consistent macroscopic deformation gradient in case of EAS formulation
$\boldsymbol{f}_{\mathsf{m;B}}$	Vector of RVE boundary forces

Volume-coupling approach

$\Delta V^{\mathsf{F}},\Delta V^{\mathsf{S}}$	Volume change of fluid and solid field
q	Flow rate
$\mathsf{r}^{\mathsf{C;C}}$	Discrete constraint residual
$\mathbf{f}^{\mathsf{C;S}}$	Discrete solid volume coupling force
$\mathbf{h}^{\mathsf{C;F}}$	Discrete fluid volume coupling pseudo-force
$\mathbf{f}^{\mathsf{C;F}}$	Discrete fluid volume coupling force
$\overset{\mathsf{C}}{\mathbf{K}}$	Constraint stiffness matrix

Iterative solvers for linear systems

j	Linear iteration
$\mathbf{A},\mathbf{x},\mathbf{f}$	System matrix, solution and right-hand side vector of original linear system
$\bar{\Lambda}_{\mathsf{min}},\bar{\Lambda}_{\mathsf{max}}$	Minimum and maximum eigenvalue of $\mathbf{A}$
$\mathcal{K}$	Krylov space

$\bar{\kappa}$	Condition number of $\mathbf{A}$
$\mathbf{M}_{\mathsf{R}},\mathbf{M}_{\mathsf{R}}^{-1}$	Right preconditioning matrix of the original linear system and its inverse
$\acute{\mathbf{x}}$	Intermediate solution vector of original linear system
$\mathbf{L},\mathbf{U}$	Lower and upper triangular matrix
$\mathbf{D}$	Diagonal matrix
ϵ^{lin}	Convergence criterion for linear iteration
$\mathbf{r}^{\mathsf{u}}$	Discrete constrained FSI residual vector
$\bar{\mathbf{r}}^{\mathsf{u}}$	Gauss-Seidel iteration residual
$\mathbf{r}^{\lambda}$	Discrete constraint residual vector
$\mathbf{F}$	Constrained FSI matrix
$\mathbf{B}^{\mathsf{T}},\hat{\mathbf{B}}$	Constraint coupling matrices
$\hat{\mathbf{S}}$	Approximate Schur complement
$\tilde{\mathbf{z}}$	Intermediate "solution" vector of linear system in preconditioning process
$\mathbf{z}$	"Solution" vector of linear system in preconditioning process
$\mathbf{y}$	Right-hand side vector of linear system in preconditioning process
$\mathbf{y}^{\mathsf{u}},\mathbf{y}^{\lambda}$	FSI and constraint parts of $\mathbf{y}$
$\tilde{\mathbf{z}}^{\mathsf{u};},\tilde{\mathbf{z}}^{\lambda;}$	FSI and constraint parts of $\tilde{\mathbf{z}}$
$\mathbf{z}^{\mathsf{u}},\mathbf{z}^{\lambda;}$	FSI and constraint parts of $\mathbf{z}$
α	Parameter of SIMPLE preconditioner
$\bar{\mathbf{M}}^{\mathsf{u}},\left(\bar{\mathbf{M}}^{\mathsf{u}}\right)^{-1}$	Preconditioning matrix of the FSI block and its inverse
ω	Relaxation parameter

Abbreviations

AECC	American European Consensus Conference
ALE	Arbitrary Lagrangian Eulerian
ALI	Acute lung injury
ARDS	Acute respiratory distress syndrome
ARDSNet	ARDS Clinical Trials Network
BVP	Boundary value problem
CFD	Computational fluid dynamics
CT	Computed tomography
DOF	Degree of freedom
DPPC	Dipalmitoyl phosphatidylcholine
EAS	Enhanced assumed strain
ECM	Extracellular matrix
FE	Finite element
FE^2	Nested multi-scale method based on FE discretization on both macro- and micro-scale
FEM	Finite element method
FSI	Fluid-structure interaction
GAG	Glycosaminoglycan
GMRES	Generalized minimal residual
GP	Gauss point
HMM	Heterogeneous multi-scale method
IRDS	Infant respiratory distress syndrome
LBB	Ladyzhenskaya-Babuška-Brezzi
LU	Lower and upper triangular matrix
MODS	Multiple organ dysfunction syndrome
MRT	Magnetic resonance tomography

MULF	Modified updated Lagrangian formulation
NEEP	Negative end-expiratory pressure
PBS	Pulsating bubble surfactometer
PEEP	Positive end-expiratory pressure
PL	Phospholipid
PSPG	Pressure stabilizing Petrov-Galerkin
R3M	Reduced model multi-scale method
RVE	Representative volume element
SEF	Strain energy density function
SIDS	Sudden infant death syndrome
SIMPLE	Semi-implicit method for pressure-linked equations
SIMPLEC	Modified SIMPLE
SOR	Successive overrelaxation
SP	Surfactant apoproteins
SPH	Smoothed particle hydrodynamics
SUPG	Streamline upwind Petrov-Galerkin
UMFPACK	Unsymmetric multifrontal sparse LU factorization package
VALI	Ventilator-associated lung injury
VILI	Ventilator-induced lung injury
ZEEP	Zero end-expiratory pressure

1 Introduction

> *"Being able to breathe without any apparent difficulty is something that healthy people take for granted, and most of us generally go about our daily lives without giving it a second thought."* (Bates, 2009)

If breathing becomes difficult or even impossible, however, a thorough knowledge of involved phenomena is essential for an appropriate treatment. While this seems to be an exclusively medical problem at first sight, it has to be emphasized that breathing is basically a mechanical process. In the healthy lung, i.e. in case of spontaneous breathing, a negative pressure is generated on the outside of the lungs by contraction of both the diaphragm and the intercostal muscles which cause an elevation of the rib cage. This pressure serves to overcome lung recoil forces, expand the parenchymal tissue, and prompt gas to flow in the airways in direction of the decreasing pressure. During expiration, muscle relaxation leads to a decrease of lung volume and, consequently, a backflow of air. In both stages of the respiratory cycle, the specific relationship between muscular pressures, airflow, and lung volume is governed by the mechanical properties of the respiratory system. Hence, when considering pulmonary dysfunction, mechanical models can support and amplify medical knowledge. This is particularly true since the possibilities to image structures in the lung and measure relevant quantities in vivo are still limited.

Compared to other areas in biomechanics like the circulatory or the muscosceletal system, surprisingly many open questions related to structural-functional correlations in the lung remain. Much of the uncertainty stems from the difficulties in documenting lung mechanics on the "micro-level", given the small size of corresponding interior structures and the large movement of the lung during breathing. For instance, a prominent controversial issue is the question whether specific "micro-structures" in the lung are actually expanded or rather recruited during breathing. This lack of knowledge is quite astonishing, especially when considering the impact a better understanding of respiratory mechanics can offer. A sound standing "virtual lung model" combining medical knowledge with mechanical background could be a valuable tool for various applications ranging from the better understanding of lung diseases like asthma, to progress on individual therapeutic approaches, e.g. by improving drug delivery. The main motivation for this thesis is related to understanding complications of mechanical ventilation in case of acute lung diseases. In this context, a detailed computational model can provide essential insights and open up new vistas towards improved patient-specific ventilation protocols in the long term.

Before summarizing the objective in detail and providing a short outline of this thesis, some general information about the structure of the respiratory system will be given along with an overview of acute lung diseases and related complications. Particularly, problems arising from mechanical ventilation of heterogeneously damaged lungs will be addressed.

1.1 Anatomy and physiology of the respiratory system

The development of reasonable computational models for biomechanical applications necessitates in-depth knowledge of relevant biological and medical aspects as well as a quantification of crucial mechanical properties. This section gives a brief overview of lung anatomy and physiology following Gray (1918), Weibel (1963), Weibel (1984), Drenckhahn and Zenker (1985), Guyton and Hall (1997), West (2008), and Bates (2009). It has to be noted, though, that the variability of both anatomy and mechanical behavior between different individuals (not to mention different species of mammals) is distinct. However, the general information provided in standard textbooks is sufficient if basic phenomena are of interest. For individual prognoses envisaged in the future, patient-specific data would be required.

The prime function of the mammalian lung is to continuously mediate the transport of oxygen and carbon dioxide between environment and blood. In the human being, as much as 12,000 l air and 6,000 l blood pass through the lung per day. Efficient gas exchange requires that the blood-gas barrier possesses an extremely large surface area combined with a very small thickness, such that the passage of gas molecules is impeded as slightly as possible. As stated in Weibel (1984), the barrier's surface is about the size of a tennis court and its thickness is 50 times smaller than a sheet of air-mail paper. For serving this purpose, multiple thin interior walls are formed, thereby subdividing the lung into a large number of small air chambers (also known as alveoli) which are connected with the outside air through a system of branched tubes (i.e. the airway tree). The pulmonary arteries and veins form similar trees that finally converge in dense capillary networks wrapped around the alveoli. The driving force for the gas exchange is the partial pressure difference for oxygen between the alveolar air and the capillary blood. According to Weibel et al. (2005), several physical parameters govern oxygen uptake at the alveolar level, such as alveolar membrane permeability, blood hemoglobin content, and its reaction rate with oxygen. Thus, efficient gas exchange can only be maintained if the capillaries are perfused at a high rate and alveolar air is continuously replenished with oxygen, even at the most distal points in the lung. Conversely, carbon dioxide is discharged from the blood to the alveolar gas through diffusion across the barrier and into the airways. In all these processes, lung morphology plays an essential role.

The general composition of the human respiratory system along with some relevant notations is shown schematically in Figure 1.1.1. As already indicated above, the lung can basically be subdivided into a conducting part and a distal respiratory zone where the actual gas exchange takes place.

Concerning the conducting zone, upper and lower airways have to be distinguished. The nasal cavity and the throat are part of the upper airways. The larynx (i.e. the voice box) marks the transition to the lower airways comprising the entire bronchial tree from the trachea down to the terminal bronchioles. Since the tubus of the ventilator is situated in the trachea during artificial respiration, the upper airways are of no particular interest for the models developed as part of this thesis. Hence, explanations are restricted to the lower airways and the respiratory zone from now on. The latter is often also referred to as the lung parenchyma, meaning the functional parts of the organ participating in gas exchange.

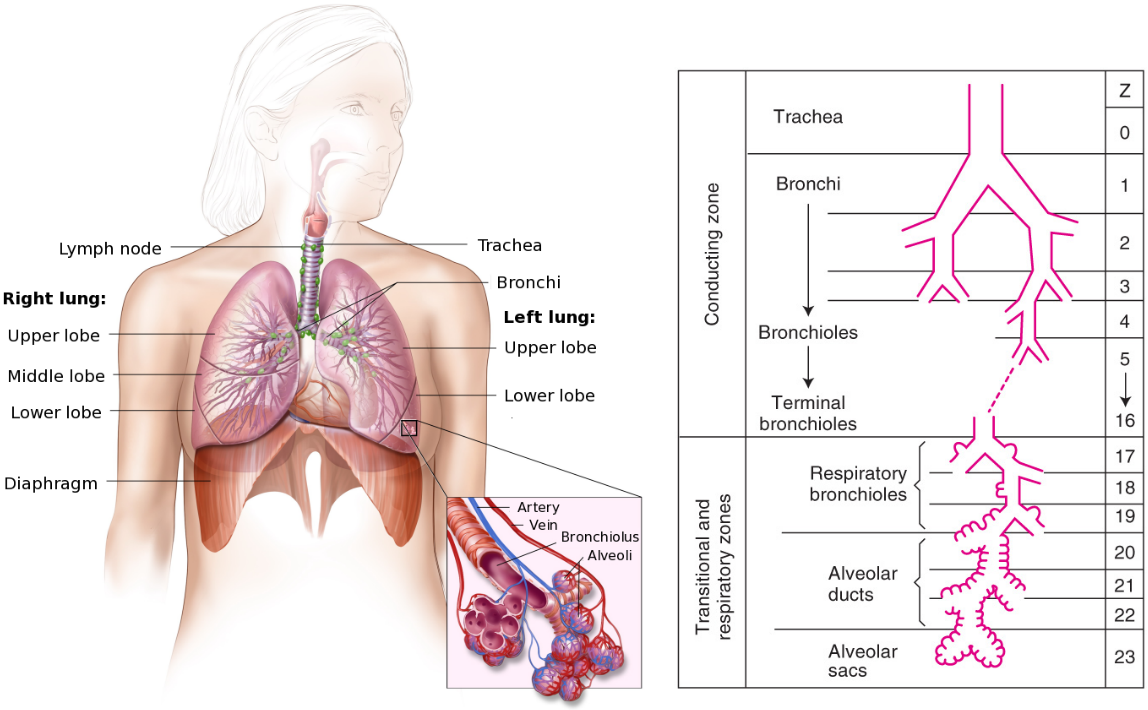

Figure 1.1.1: Overview of lung anatomy and definition of airway generations (from http://www.meb.uni-bonn.de/Cancernet/CDR0000062956.html and West (2008)).

In the following, the main focus is on the human respiratory system, although information concerning other species will also be provided in some places. This seems necessary since in many cases, experimental investigations are limited to laboratory animals. For a reasonable interpretation of corresponding data, detailed knowledge of differences in anatomy between the distinct species is essential.

1.1.1 Tracheo-bronchial tree

The trachea constitutes the trunk of the so-called tracheo-bronchial tree. With a rough length of 10 cm and a diameter of around 2 cm, the trachea is the largest among the lower airways, extending from the larynx to approximately the fifth thoracic vertebra. At this point, the trachea divides into the two main bronchi passing into each lung. The bifurcation is slightly asymmetric, with a stronger, but shorter right bronchius compared to the left one. Furthermore, the angle between right bronchius and trachea is smaller such that contaminants (and possibly also a misplaced tubus of the ventilator) enter the right bronchius rather than the left one. Both main bronchi continuously branch into subsequent so-called bronchioles penetrating deeper in the lungs, thereby progressively reducing their dimensions. In simple terms, the diameter of an airway is proportional to the volume of peripheral lung that is supplied by this branch (Weibel, 1984). Interestingly, the average length-to-diameter ratio is about the same on all levels of the airway tree. After roughly 14 generations of bronchioles, the terminal bronchioles mark the end of the conducting zone.

The total number of generations is quite variable since the airways form a space-filling tree whose endings must be homogeneously distributed and reach into every gap in the available volume of the chest cavity (Weibel et al., 2005). Thereby, some spaces are filled more rapidly such that the airways stop dividing, whereas in other regions more branches are needed. A detailed notation of the distinct airway generations in an idealized lung is provided in Figure 1.1.1.

The number of airways in the tracheo-bronchial tree multiplies throughout the conducting zone following a branching pattern known as irregular dichotomy. This simply implies that each parental airway divides into two child vessels with possibly different dimensions. Thereby, irregularity is mostly due to a variation in length rather than due to differences in diameters (Weibel, 1963). Although the mentioned pattern describes lung branching satisfactorily, the assumption of dichotomy does not strictly hold in individual human lungs. Instead, Weibel (1984) found that the branching ratio is about 1.4, meaning that on average each parental airway splits into 1.4 daughter airways. The degree of irregularity strongly varies between different species of mammals. The branching pattern is quite unsymmetric in the rat lung and large differences in diameter and branch lengths can be observed (Weibel et al., 2005). This probably comes about due to the more stocky shape of the rat lung compared to the rather "spherical" human lung.

As the name suggests, the primary function of the conducting airways is the distribution of air to the peripheral respiratory zones. Since the airways do not participate directly in gas exchange, they constitute the anatomic dead space of the lung, which approximately amounts to 150 ml in a young adult male (Guyton and Hall, 1997). Gas transport through the larger conducting passages occurs by convective flow, whereas diffusion dominates in the peripheral airways. The decrease in axial flow velocity is due to the fact that the total airway cross section increases almost exponentially with distance into the lung as a consequence of branching. Direct measurements of the pressure drop along the bronchial tree have shown that the major site of airflow resistance is the medium-sized bronchi (West, 2008).

All respiratory passages are lined by a continuous epithelial cell sheet and kept moist by a layer of mucus that coats the entire surface. This mucus is secreted by individual goblet cells in the epithelial lining and small submucosal glands. Apart from wetting the surface, the mucus also subserves a protective function for the lung. It traps small particles from the inspired air, thereby preventing them from entering the respiratory zone. Upward beating so-called cilia cause a slow mucus flow towards the pharynx (i.e. the throat) where it is either swallowed or coughed to the exterior.

Airway wall composition strongly depends on the location within the tree, i.e. the airway generation. Multiple cartilage rings enveloping the front and side walls of the trachea increase its stability and prevent collapse. In the walls of the bronchi, plate-like cartilage structures can be found. These plates become progressively less pronounced in later generations until they are completely absent. Except for cartilage, the airway walls mainly consist of smooth muscle cells which regulate local airflow resistance. In the larger bronchi, smooth muscles occur as relatively thin circular sleeves whereas they are arranged rather helically in the smaller airways. While muscle activity can cause only minor changes in the diameter of the mid-sized bronchi, the compression of small airways can be significant. Many obstructive diseases of the respiratory system result from the narrowing of smaller bronchioles due to the excessive contraction of smooth muscles, e.g. in case of asthma.

The connective tissue surrounding all airways is commonly referred to as the peribronchium. During breathing, this layer allows limited movements of the conducting passages relative to the lung parenchyma. The peribronchial tissue is connected to the surrounding parenchyma by tissue fibers that keep the airways tensioned in the unfolded lung. Thereby, sufficient stability is provided also for the smaller vessels without reinforcing cartilage structures. In case of lung diseases, though, pathological changes of local mechanical properties may lead to reduced tension forces and, consequently, to a collapse of peripheral airways, thereby cutting off successive parts of the tree from oxygen supply. The entrapped air is then absorbed within minutes to hours by the capillary blood. If the tissue is compliant enough, this leads to local parenchyma collapse. Otherwise, isolated airspaces are filled completely with fluid pulled out of the interstitium as a consequence of the tremendous negative pressures.

1.1.2 Lung parenchyma

Parenchyma refers to the portion of the lung made up of the small air chambers participating in gas exchange. These so-called alveoli are separated from each other by thin membranous structures containing the capillary network. Thus, they form the barrier separating air and blood. Alveoli are arranged in foam-like structures and fill the entire volume of the lungs surrounding the conducting passages (see Figure 1.1.2). Remarkably, the human lung consists of approximately 500,000,000 alveoli in total (Ochs et al., 2004) with an average surface area of 140 m^2 (Weibel, 1963). In this section, the complex morphology of lung parenchyma will be discussed in general, followed by a detailed characterization of the blood-gas barrier and its liquid lining.

1.1.2.1 Morphology of lung parenchyma

Lung parenchyma is separated from the chest walls by a narrow gap between parietal and visceral pleura which line the thoracic cavity and the lungs, respectively. Each of the two pleurae is a porous membrane through which small amounts of interstitial fluid continually transude into the pleural space. These fluids carry tissue proteins, giving the pleural fluid a mucoid characteristic which allows easy slippage of the moving lungs during breathing. Excess fluid is pumped away by the lymphatic vessels. The resulting negative pressure in the pleural space is required to keep lung parenchyma expanded.

The interior design of lung parenchyma is determined by the branching of the conducting airways. Right and left lung are partitioned in three and two lobes, respectively, each enclosed by the visceral pleura (cf. also Figure 1.1.1). Lung segments of conic shape are the first subdivision of the lobes. These structures are incompletely bounded by connective tissue septa such that surgical separation is often possible. In the right lung, there are usually ten segments whereas only nine can be found in the left one. Within the segments, the

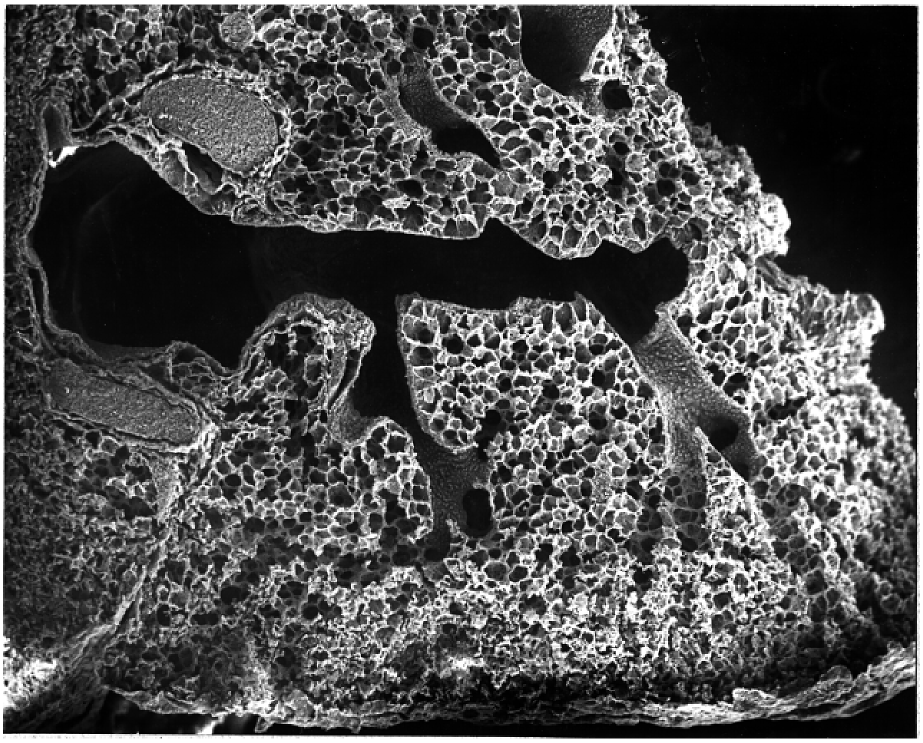

Figure 1.1.2: Organization of alveoli around conducting passages (scanning electron microscopy, from http://imglib.lbl.gov).

bronchi branch about six to twelve times. Subsequent bronchioles feed the lobules, which themselves subdivide into approximately 30,000 so-called acini. These compartments represent the largest lung units of which all airways are alveolated and, thus, participate in gas exchange.

According to Haefeli-Bleuer and Weibel (1988), an acinus starts with the first respiratory bronchiole and contains all following generations down to the terminal alveolar sacs. Thereby, the degree of alveolarization increases gradually towards the periphery. While only several alveoli are attached to the three generations of respiratory bronchioles, the circumference of subsequent so-called alveolar ducts is totally occupied by alveoli. In the dead-end alveolar sacs, even the terminal surface is covered with alveoli. In general, alveoli are collocated in clusters with a common opening towards the duct lumen. As a consequence of this specific arrangement, the surface area available for gas exchange is about five times larger than the surface of the associated duct. At the same time, the diffusion distance for oxygen molecules remains small (Weibel et al., 2005). Due to different numbers of generations and individual segment lengths, this overall diffusion path length – which is an important morphometric trait of the acinus – varies noticeably, with an estimated average of around 8 mm.

In general, data concerning the characteristic dimensions of the acinus differ considerably in literature. Therefore, only widespread morphological information will be summarized. Haefeli-Bleuer and Weibel (1988) found that the average volume of a human acinus at total lung capacity (i.e. maximum inflation) is 187 mm^3. The internal airway or duct diameter falls from 500 µm to 270 µm in the acinus, whereas the outer diameter (including the sleeve of alveoli) remains constant at 700 µm. This is attributed to the increase in alveolar size and the number of alveolar complexes towards the acinar periphery. Hansen and Ampaya (1975) determined the average "diameter" of an alveolus as 238 µm. An interesting comparison of alveolar sizes in different species can be found in Mercer et al. (1994). They observed a trend for larger lungs to be composed of both more numerous and larger alveoli. However, the proportional changes in number and size do not exhibit an apparent pattern. For instance, alveoli of the rabbit are comparable in size to those of the rat, which has a six- to sevenfold smaller lung.

Although alveoli are commonly depicted as a bunch of grapes, histological investigations clearly reveal predominantly plane walls shared among adjacent alveoli and connected in an irregular polyhedral configuration (see for instance Schreider and Raabe (1981) and Oldmixon et al. (1989)). Hence, the deformation of an alveolus is never independent from the movement of the surrounding parenchyma. Consequently, any tendency to reduce or increase the volume relative to the rest of the structure is accompanied by large opposing forces. This effect, denoted by Mead et al. (1970) as interdependence, is meanwhile universally accepted in the medical community. The exact mechanisms of alveolar deformation are, however, still controversial. The conventional approach assumes more or less uniform expansion of alveoli throughout the respiratory cycle. By contrast, some investigators believe that alveolar volume changes as a result of septal folding (comparable to the crumpling and uncrumpling of a paper bag) in the normal breathing range and that alveoli get stretched only at high lung volumes. Others state that only the alveolar ducts expand during breathing, whereas alveolar volume and surface area remain constant. Gatto and Fluck (2004) proposed that lung volume change at the alveolar level is a combination of the previously mentioned mechanisms. An overview of the different point of views can be found e.g. in Hubmayr (2002), Carney et al. (2005), and DiRocco et al. (2005).

Today's knowledge of the structure of lung parenchyma as summarized in this section predominantly stems from morphological investigations. A detailed survey of several associated methodological problems is given e.g. in Weibel (1984). First of all, the tissue has to be prepared such that it becomes accessible to microscopic observation. For this purpose, the tissue must be fixed and embedded in some suitable material. Most fixation techniques, however, come along with some more or less severe disadvantages such as removal of blood from the tissue, shrinkage, or cell damage. The second methodological problem results from the fact that morphological studies usually need to be done on thin sections of the tissue. However, the process of cutting or slicing destroys the three-dimensional nature of the structure. For instance, a slice of lung tissue rarely contains characteristic cross sections of the three-dimensional structure, thereby rendering reliable measurements difficult. When employing casting techniques (cf. e.g. Haefeli-Bleuer and Weibel (1988)), it cannot be assured that the lungs are filled homogeneously with material. Furthermore, the effective pressure (or inflation) state of the lung during the preparation is unclear. Interpretation of measured dimensions may therefore be delicate. In general, "in vitro" studies of excised human parenchyma are often limited to a small number of specimens due to the poor availability of healthy lungs. In contrast to popular laboratory animals like small rodents, however, the variability of decisive attributes in the human lung is very high due to differences in environment and preexisting conditions. Therefore, statistical inference is often problematic in these cases. Non-invasive “in vivo” imaging techniques such as magnetic resonance tomography (MRT) or computed tomography (CT) are inapplicable to lung tissue due to the small characteristic size of alveoli in combination with the high water content of the septal walls. In summary, a lot of experimental difficulties are encountered when investigating lung parenchyma anatomy. It is therefore, at least partly, understandable that many contrary statements can be found in the literature.

1.1.2.2 Composition of the air-blood barrier

The air-blood barrier is lined by two cell layers – the epithelium on the air side and the endothelium on the blood side – which can control the transit of water and solutes and repair damage to the barrier. Since these cell layers have to be very thin in order to allow efficient diffusion of oxygen, they must be supported by a scaffold of connective tissue fibers spreading within the alveolar septa. At the openings towards the alveolar ducts or sacs, these fibers form the alveolar “entrance rings” with diameters in the range from 150 µm to 290 µm (Matsuda et al., 1987). In the alveolar walls, the fibers are interlaced with the meandering single-layer capillary network containing approximately 200 ml of blood. Due to the small diameter of the capillaries (which is about 10 µm according to West (2008)), alveolar blood appears like a single layer of erythrocytes. In this way, each red blood cell is optimally exposed to the air. The transport of oxygen and carbon dioxide across the barrier occurs solely by passive diffusion. Weibel et al. (2005) put the effective barrier thickness at only 1 µm in the human lung. The overall thickness of the alveolar septal wall in general highly correlates with both alveolar surface curvature and radius (Mercer et al., 1994).

The alveolar epithelium is composed of two distinct cell types with different morphology and function. About 93% of the alveolar surface is lined by long and slender type I cells also known as squamous pneumocytes. The remaining 7% are occupied by single bulky type II cells (granular pneumocytes) that are responsible for the synthesis, storage, and secretion of specific phospholipids. These substances are needed for the formation of the alveolar liquid lining which will be addressed later in more detail. Another essential function is the renewal of alveolar type I cells which are incapable of mitosis. On top of the alveolar type I cell layer, several alveolar macrophages are situated. These scavenger cells imbibe germs and other contaminants, thereby serving vital protective functions. Furthermore, they are involved in the continuous replacement of the liquid lining. When activated, alveolar macrophages can generate a multitude of “pro-inflammatory mediators” which play a key role in the development of distinct pulmonary diseases. A schematic overview of the different cell types lining the alveolar wall is given in Figure 1.1.3. The alveolar pores introduced in this illustration connect neighboring alveoli by interrupting the continuous alveolar wall. Thereby, links between alveoli belonging to the same duct are usually established. However, connections between alveoli of sacs and those of preceding generations as well as between alveoli of neighboring acini have also been reported by Haefeli-Bleuer and Weibel (1988).

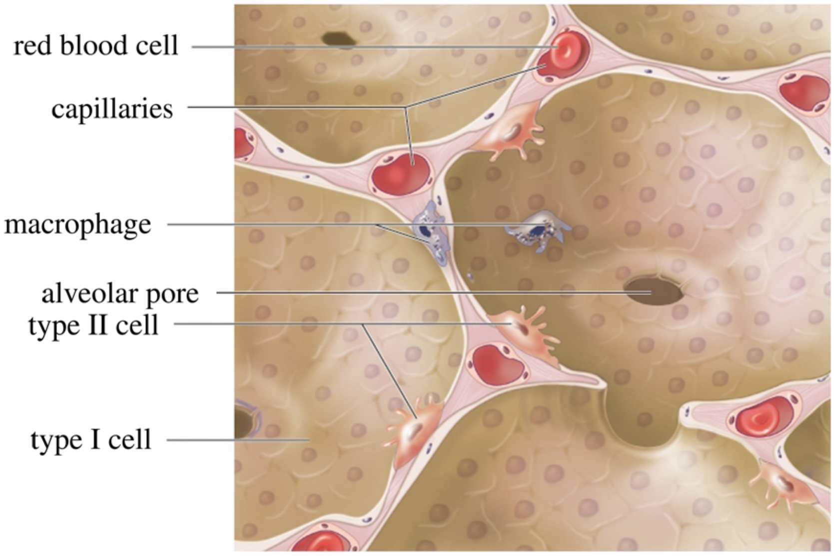

Figure 1.1.3: Illustration of different important cell types in alveolar walls (modified from http://academic.kellogg.edu/herbrandsonc/bio201_mckinley).

The space between the cell layers described above is also referred to as the interstitium or the extracellular matrix (ECM). Within an amorphous, hydrophilic ground substance composed of mainly proteoglycans, it contains some fine microfibrils and fibroblasts as well as wide-meshed bundles of elastin and collagen fibers. Like all structures of the body, these connective tissue fibers are subject to continuous turnover, breakdown, and renewal, albeit at a slow rate. Occasionally, some free cells also reside in the interstitium. Towards the lining cell layers, the ground substance condenses into a basal membrane. In regions where the capillaries are located directly beneath the epithelium, both basal membranes merge in favor of a small barrier thickness.

According to Humphrey (2003), the ECM serves many functions. Apart from endowing the tissue with strength to maintain its shape, it serves as a biologically active scaffold on which cells can migrate or adhere. Furthermore, it provides an aqueous environment for the diffusion of nutrients, ions, hormones, and metabolites between the cell and the capillary network. In a sense, therefore, the ECM regulates cell shape, orientation, movement, and overall function. However, it is the cells (i.e. fibroblasts) that fashion and maintain the ECM. A detailed review of the composition of the ECM and its interaction with the cells can also be found in Suki et al. (2005).

The three-dimensional architecture of elastin and collagen fiber networks in the interstitium was investigated by Toshima et al. (2004) (see also Figure 1.1.4). They found that collagen fiber systems extend throughout the lung and pleura. In the alveolar entrance rings, collagen fibers are condensed, whereas they subdivide into smaller fibers running in various directions in the alveolar septa, thus forming basket-like networks. Elastin fibers are arranged in band-like structures around the alveolar entrances and are only sparsely distributed in the alveolar septa. Yager et al. (1992) interpreted this condensation of fibers

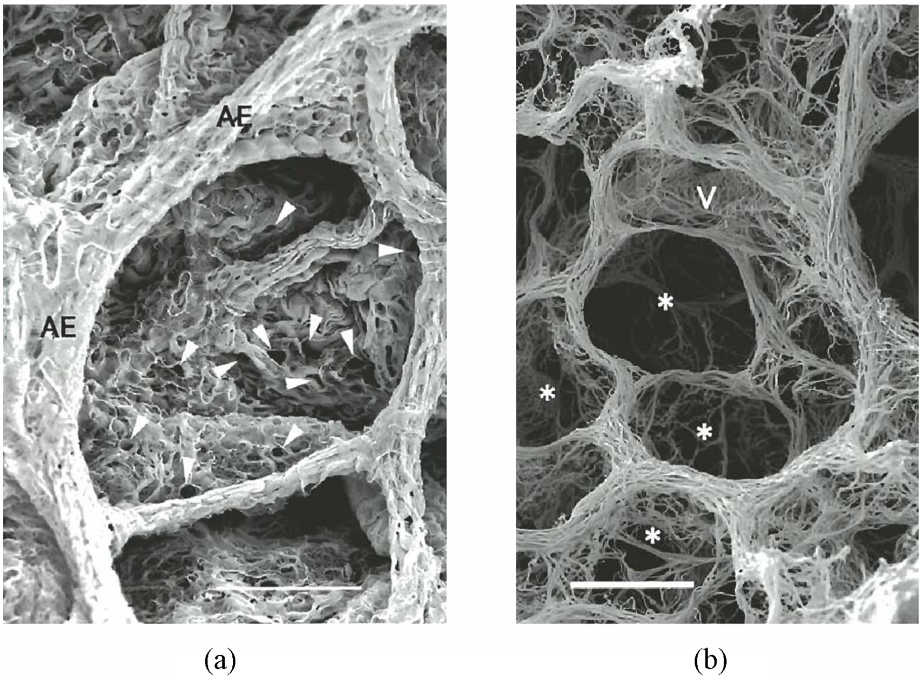

(a) (b)

Figure 1.1.4: Scanning electron micrographs of connective tissue fiber systems in the human lung (from Toshima et al. (2004)). Scale bar: 100 µm. (a) Collagen network with pronounced condensation of fibers in alveolar entrances (AE). Arrowheads indicate pores devoid of collagen fibers. (b) Elastin network with bands of fibers around alveolar entrances (*). Blood vessels (V) possess layers of dense elastin fiber systems.

around the alveolar orifices as a mechanical equivalent to missing alveolar walls. The contribution of the connective tissue fibers to the overall volume of the interstitial space was investigated by Mercer et al. (1994) for a number of distinct species. They concluded that the amount of collagen and elastin fibers was significantly increased over other interstitial components in species with thicker septal walls. Thereby, according differences were considerably greater than the corresponding changes in alveolar diameter. For instance, in the human lung with fourfold larger alveoli than the mouse, the normalized volumes of collagen and elastin in the entrance ring were both increased by a factor of approximately ten. Yager et al. (1992) assumed that the specific fiber volume fractions in human and dog parenchyma are responsible for the significant differences in microscopic deformation behavior of biaxially stretched tissue strips. Interestingly, the actual spatial concentrations of elastin and collagen fibers also varies significantly between different species (Mercer and Crapo, 1990). In rat lungs, the majority of the elastin fiber volume (77%) and half of the collagen fiber volume (44%) is located in the first 10 µm compartment adjacent to the entrance ring. By contrast, in human lungs, only 22% of the elastin and 18% of the collagen fibers are present within 20 µm of the alveolar duct wall. Thus, fibers are considerably more dispersed throughout the alveolar septal walls of human lungs. Furthermore, the collagen-to-elastin fiber ratio differs between rat (~2) and human (1.5) specimens. However, this average does not accurately reflect the spatial relationships of both fiber systems. Indeed, the ratio is approximately 1 in the entrance rings where the connective tissue fibers are most prominent. Although the average collagen and elastin content is more comparable in mouse and rat lungs, fiber composition and architecture was also found to be different (Faffe et al., 2002).

Sobin et al. (1988) investigated the orientation of the fibers in human alveolar walls. Although both fiber networks may exhibit predominant directions in individual septa, no clear trend of the orientation relative to the borders of the alveolar wall could be ascertained for a large number of alveoli considered. Therefore, they assumed that fiber directions are so random that statistically they are uniformly distributed in every direction.

Concerning the interconnection of both fiber networks, reported experimental results are ambiguous. Toshima et al. (2004), for instance, reported that both fiber systems are strongly intermingled. Mercer and Crapo (1990), however, stated that less than half of the elastin fibers are interwoven with collagen in the alveolar entrance rings. The interweavement was completely denied by Matsuda et al. (1987), although a spatial relation between the fibers was in general admitted.

Elastin is one of the most “linearly” elastic biosolid materials known (Fung, 1981). According to Ethier and Simmons (2007), the Young’s modulus of elastin fibers is around 30 kPa. They are highly flexible and can be stretched to about 200% of their original length (Larsen and Ziegenfuß, 2004). Furthermore, they can be compressed to approximately 60% while still being straight. Therefore, alveolar septa are assumed to become wrinkled not until alveolar volume goes below 20% of its maximum value. Collagen fibers exhibit a strongly nonlinear mechanical behavior. At low levels of strain (in the so-called “toe” region of the stress-strain curve), the fibrils making up single collagen fibers take a wavelike configuration and are easily extended with most of the stress being borne by adjacent elastin fibers. At higher levels of strain (in the “heel” and “linear” region), however, collagen fibrils become straight and resist further stretch by increasing the stiffness of the fiber significantly. Compared to elastin, the Young’s modulus of collagen is about 10,000 to 100,000 times larger (Ethier and Simmons, 2007). Thus, collagen is assumed to provide a mechanical framework to limit excess distension, whereas elastin seems to permit the lung to effectively recoil in the normal breathing range.

A concluding overview of the composition of the respiratory zone is given in Table 1.1. Most of lung parenchyma consists of air residing in the alveoli and the peripheral passages. About 1% is occupied by pre- and post-capillaries representing the entrance and exit points of the capillary beds. Alveolar septa containing both capillary blood and tissue composed of cells and interstitium amount to approximately 7% of lung parenchyma.

1.1.2.3 Alveolar liquid lining

It is widely known that alveolar walls are covered by a film of surface active agents, the so-called surfactant. According to Ingenito et al. (1999), this substance is a mixture of several phospholipids (PL), neutral lipids, and surfactant apoproteins (SP). The PL fraction is the major constituent of surfactant by weight (80%). Its most abundant and important

<table>
<tr><td colspan="6">Lung parenchyma</td></tr>
<tr><td colspan="4">“Tissue” septa (~7%)</td><td>pre-/post-capillaries (~1%)</td><td>alveolar/ duct air (~92%)</td></tr>
<tr><td>capillary blood (~50%)</td><td colspan="3">alveolo-capillary tissue (~50%)</td><td colspan="2" rowspan="2"></td></tr>
<tr><td></td><td>epithelium (~30%)</td><td>interstitium (~40%)</td><td>endothelium (~30%)</td></tr>
</table>

Table 1.1: Components of lung parenchyma on different levels of detail (from Weibel (1963)).

representative is dipalmitoyl phosphatidylcholine (DPPC). This molecule possesses a particular amphiphilic structure with a hydrophilic tail and a hydrophobic lipid head-group. Owing to this special dual configuration, DPPC plays an essential role in interfacial phenomena at the gas interface. The SP, which comprise only about 8% of lung surfactant, appear to be critical for the effective physiological function of surfactant, e.g. by improving adsorption and spreading behavior. More details on the biochemical composition and the morphological organization of surfactant are given in Griese (1999).

The exact appearance of the surface film has been quite controversial. The most popular notion is based on the assumption that an aqueous film of variable thickness called the hypophase underlies a monomolecular layer of surfactant molecules. This “conventional model” of the liquid lining was supported by investigations of frozen lungs reported by Bastacky et al. (1995). By analyzing the profiles of the preserved lining, they identified a thin continuous fluid film with deeper pools in the alveolar corners. From their point of view, this subphase serves to smooth the air-liquid interface and provide a substrate for surfactant movement. Similar conclusions were drawn more recently by Takayama et al. (2000). However, Hills (1999) argued that these results are purely artificial owing to the inflation of the lungs before freezing. In his opinion, the continuous liquid lining would promote excessive suction of fluid into airspace, particularly in the septal corners. Instead, he advocated a “morphological model” based on the presumption that alveolar fluid is confined to convex “pools” at the septal corners and rough spots. Surfactant adsorbs to both pools and the epithelial surface, thereby rendering the tissue less wettable. As a consequence, the formation of a continuous hypophase is prevented and a significant part of the alveolar surface is fluid-free. The control of the remaining fluid is self-regulating since surface forces tend to return any edema to the interstitium. This theory is based upon earlier studies of normal frozen lungs. Another interesting (though more exotic) theory was introduced by Scarpelli (1998). He claimed that the terminal lung units are filled with a foam of ultrathin surfactant films. This “alveolar surface network” can basically be interpreted as an agglomeration of surfactant bubbles that impart structural stability of the alveoli and modulate surfactant circulation. Due to the small thickness of about

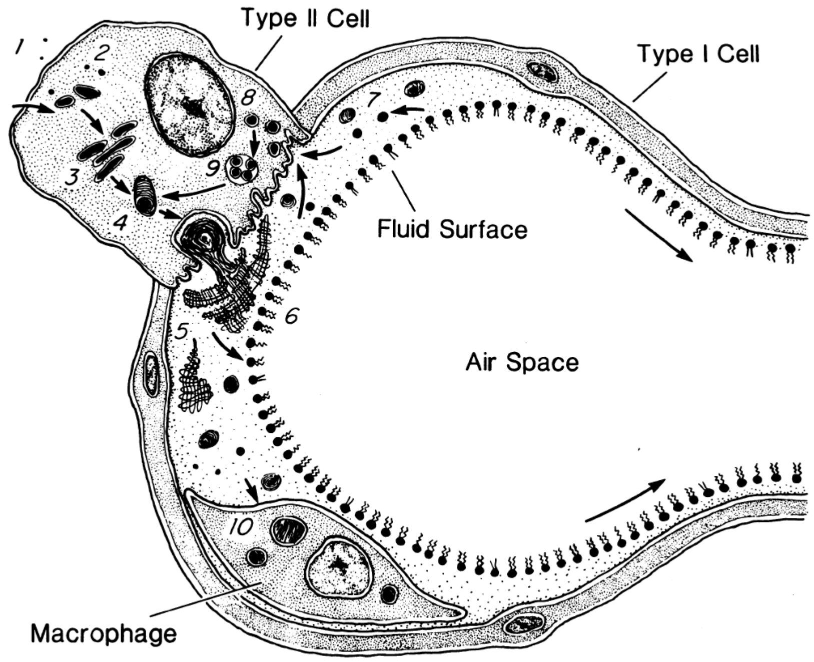

Figure 1.1.5: Schematic diagram of the surfactant system in a single alveolus (from Hawgood and Clements (1990)). 1-4 illustrates surfactant synthesis within type II cells. After secretion into the liquid lining, surfactant forms tubular myelin (5) before generating the aligned monolayer (6) at the water-air interface. Subsequently, surfactant components are taken back into type II cells by different mechanisms indicated in 7-9. Some surfactant in the liquid layer is also taken up by alveolar macrophages as shown in 10.

7 nm, the surfactant bubbles do not impair gas transport throughout the respiratory zone. It is noteworthy that the cumulative foam thickness is substantially less than the suggested mean thickness of the continuous lining proposed in the "conventional model". The alveolar surface network theory was affirmed by stereomicroscopic examination of fresh lungs. Bubble clusters could be clearly identified and even manipulated by imposing gentle microprobe pressures. However, these observations are again disputed by the proponents of the other models. An enraged debate about the validity of the "morphological model" and the "alveolar surface network" can e.g. be found in Scarpelli and Hills (2000). A clarification of the controversial liquid lining issue is beyond the scope of this thesis. All of the positions presented above were supported by experimental studies. However, the results themselves were contradictory. Due to its wide acceptance in the medical community, the "conventional model" is presumed to be valid in the following.

In Figure 1.1.5, the assumed composition of the liquid lining is shown along with some details concerning surfactant movement. Surfactant is synthesized by type II alveolar epithelial cells and released to the continuous aqueous film. After secretion, the molecules form a surfactant specific lipid lattice commonly known as tubular myelin. From these structures, lipids can rapidly adsorb to the air-water interface and form a monomolecular surfactant layer. Thereby, the hydrophilic polar group is immersed in the water and the hydrophobic part sticks out. By rendering the interface more compatible with air, surfactant substantially lowers the interfacial energy. Veldhuizen and Haagsman (2000) assumed that lipid bilayer structures are attached to the surfactant monolayer, thereby forming a lipid reservoir. During breathing, several complex dynamic processes occur in the film such as adsorption, desorption, and squeeze-out of DPPC molecules, lipid reservoir formation and modulation of monolayer packing. A single transit of the surfactant molecules through the alveolar lumen normally takes a few hours. The PLs are then taken back into the type II cell in large part. Before being degraded, the PLs can be reutilized about 10 times.

By comparing normal and liquid-filled lungs, von Neergaard (1929) demonstrated that interfacial effects account for two thirds of lung recoil forces. Hence, in case of surfactant deficiency, lung compliance is significantly reduced, the work of breathing is increased, and alveoli as well as small airways are likely to collapse or fill with fluid. According to Griese (1999), a pathophysiological role for surfactant was first discovered in premature infants. Surfactant is formed relatively late in fetal life and babies born without adequate amounts develop respiratory distress, a condition which is nowadays routinely treated with exogenous surfactant replacement. Biochemical surfactant abnormalities of varying degrees have also been described in acute lung failure and various other obstructive or infectious diseases. In particular, data obtained in several studies strongly suggest that surfactant dysfunction is also involved in the development of sudden infant death syndrome (SIDS).

Apart from being relevant for lung stability and compliance, surfactant also serves several other vital functions. For instance, the dissemination pressure of surfactant causes the aqueous hypophase to thin, thereby facilitating efficient gas exchange. Additionally, the surfactant layer keeps the alveolar epithelium moist and, therefore, prevents the cells from rupturing. By reducing the interfacial energy of the liquid lining and, thus, the stresses in the tissue surrounding the capillaries, excessive transudation of fluid into the alveolar lumen is obviated. Furthermore, it is widely assumed that inhaled particles and microorganisms entering the alveolar space are rendered innocuous by surfactant. Hence, surfactant also plays an important role in terms of lung protection.

1.2 Ventilator-associated lung injuries

> *"[...] the rationales for the various ventilatory settings are largely empirical, because the physiology and mechanics of lung inflation are poorly understood."* (Gatto and Fluck, 2004)

The complications of mechanical ventilation in case of acute lung diseases are the main motivation for this work. Therefore, some related information will be provided in the following.

1.2.1 Acute lung diseases

The nervous system normally adjusts the rate of alveolar ventilation to the demands of the body, such that arterial blood oxygen and carbon dioxide pressure are hardly altered even during moderate to strenuous exercise. In case of respiratory insufficiency, however, the lung is unable to sustain arterial blood gases in the normal range, thereby necessitating intubation and mechanical ventilation. This dysfunction may be brought about by a perturbation of ventilation, pulmonary gas exchange, or perfusion.

A prominent type of respiratory failure is the acute lung injury (ALI) which was defined by the American European consensus conference (AECC) as a syndrome of inflammation and increased permeability that is associated with a constellation of clinical, radiologic, and physiologic abnormalities (Bernard et al., 1994; Bernard, 2005). ALI can be initiated by a wide variety of direct insults to the lung such as aspiration of gastric content or pneumonia as well as lung injury from extra-pulmonary origin like multiple trauma or sepsis. Consequently, the diagnosis of ALI is difficult and not exclusive. The presence of secondary factors such as chronic lung diseases or multiple predisposing disorders substantially increases the risk of progression to ALI. Furthermore, the risk of developing ALI significantly depends on the specific initial insult. While 40% of patients with severe sepsis develop lung injury, the incidence following trauma is only 20% or less (MacCallum and Evans, 2004). A subset of ALI is the more severe acute respiratory distress syndrome (ARDS). Although not consistent with the original definition of the AECC, the term "acute" is sometimes replaced by "adult" to indicate that ARDS is an adult version of the well-known infant respiratory distress syndrome (IRDS), which is the most frequent cause of death in premature babies. The exact classification of ALI and ARDS is based on the oxygenation index, i.e. the ratio of the partial pressure of arterial oxygen to the fraction of inspired oxygen, which can be easily determined in the clinical setting. Both ALI and ARDS are acute in onset, persistent, and characterized by diffuse, heterogeneous lung injuries. As a consequence, the mechanical properties of the respiratory system are known to be adversely affected, with an increased resistance and a reduced compliance as hallmarks (Frantzeskaki et al., 2003).

According to Ware and Matthay (2000), an accurate estimation of the incidence of ALI and ARDS is difficult due to the heterogeneity of causes and clinical manifestations. Rubenfeld et al. (2005) reported that in a large-scale clinical trial in King County (US), the incidence of ALI and ARDS was found to be 86.2 and 64.0 per 100,000 person-years, respectively. From these data, they estimated that each year in the US, there are 190,600 cases of ALI which are associated with 3.6 million hospital days. Survival of affected patients strongly depends on age, chronic diseases, and non-pulmonary organ dysfunctions. In general, the primary cause of death is a multiple organ dysfunction syndrome (MODS) rather than primary respiratory failure. Therefore, the initial degree of gas exchange impairment – unless very severe – is a rather poor predictor of outcome. However, the failure of pulmonary function to improve during the first week of treatment is a negative prognostic factor (Ware and Matthay, 2000). As stated by Bernard (2005), patient mortality within the first 28 days after onset ranges between 35 and 40%. These numbers are in line with the findings of Rubenfeld et al. (2005), who specified an in-hospital mortality rate of 41.1% in case of ARDS and 38.5% for all ALI patients, corresponding to 74,500 deaths per year in the US. Interestingly, this figure is comparable to the number of adult deaths attributed to breast cancer or HIV. Since both incidence and mortality increase with age, associated numbers are assumed to nearly double within the next 25 years due to the expected de-

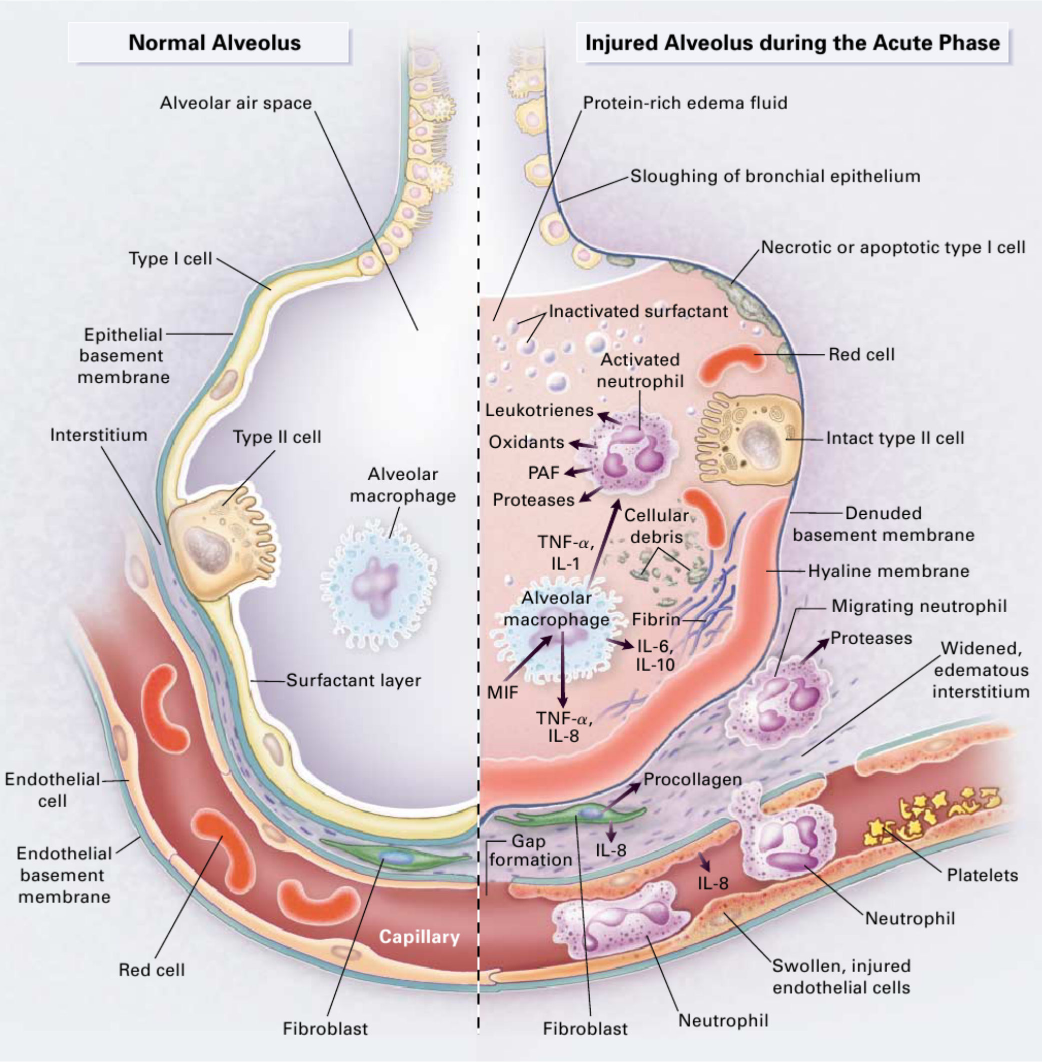

Figure 1.2.1: Comparison of normal (left) and injured (right) alveolus (from Ware and Matthay (2000)).

mographic development. Apart from being associated with considerable mortality rates, it is widely known that severe ARDS in combination with prolonged mechanical ventilation can also be associated with long-term disability, for instance persistent neuromuscular weakness (Bernard, 2005). In most surviving patients, however, pulmonary function returns to nearly normal within 6 to 12 months despite the severe lung injuries (Ware and Matthay, 2000).

Radiographic and computed tomographic scanning have demonstrated that ALI/ARDS – although affecting the lung as a whole – is mainly related to local pathologic changes on the alveolar level. The syndrome is usually progressive, i.e. distinct stages can be clearly distinguished (Ware and Matthay, 2000). The acute phase is characterized by the rapid onset of diffuse alveolar damage as shown in Figure 1.2.1. Capillary injury and disruption of the alveolar epithelium results in the increase of barrier permeability, thereby promoting flooding of the alveolar spaces with protein-rich edema fluid followed by the inactivation of surfactant. The decrease in the amount of aerated alveoli due to pulmonary edema is closely related to the overall reduction of compliance, a phenomenon commonly known as “baby lung”. Injury to type II cells impairs removal of the edema fluid and reduces the production and turnover of surfactant, thereby contributing to the characteristic surfactant abnormalities. Furthermore, neutrophils migrate to the alveolar space where they are activated by alveolar macrophages and release pro-inflammatory molecules. However, the question whether neutrophilic inflammation is the cause or the result of lung injury is not yet fully elucidated. In the so-called fibroproliferative phase (which is associated with an increased risk of death), protein-rich hyaline membranes form on the denuded basement membranes. This stage is characterized by varying degrees of interstitial fibrosis, i.e. the development of excess fibrous connective tissue (Tsushima et al., 2009). The possibly following recovery phase then involves removal of neutrophils as well as edema fluid and remodeling of the ECM. As a consequence, lung compliance increases again and hypoxemia (i.e. the decreased partial pressure of arterial oxygen) is gradually resolved. As the different stages of ALI/ARDS already suggest, the factors dominating the abnormalities in lung mechanics are assumed to vary in time. Ingenito et al. (1994) found that significant changes in parenchymal elastance and resistance occur 48 hours after the onset of severe lung injury. They concluded that surface film dysfunction and alveolar flooding dominate the early phase and parenchymal abnormalities may play a role in the later stages of acute lung diseases.

Another proposed mechanism of ALI/ARDS is atelectasis, i.e. the collapse of peripheral airspaces due to surfactant deficiency in the alveolar liquid lining or obstruction of the corresponding feeding airway. Although this notion is prevalent among many scientists and clinicians (cf. e.g. Gatto and Fluck (2004), Carney et al. (2005), and DiRocco et al. (2005)), its actual occurrence is still controversial. One reason might be the difficulty in clearly identifying these phenomena from experiments. For instance, differences in regional air distribution seen in CT images have frequently been interpreted as evidence for regional collapse of alveoli. However, Hubmayr (2002) emphasized that gradients in aeration do not necessarily imply differences in tissue expansion or alveolar size but may equally implicate pulmonary edema. Considering the well-known interdependence effects, the actual collapse of alveoli seems to be questionable since the local pressure must fall so much that edema would again be promoted. Hubmayr (2002) pointed out that there is only sparse morphometric evidence of alveolar collapse (as opposed to flooding), which, however, may be due to difficulties in the preservation of the in situ lung architecture during fixation. A clarification of this controversy is again beyond the scope of this thesis. Following Mols et al. (2006), its is assumed that collapsed and flooded alveoli might coexist in the same lung in different regions. For simplicity, the term atelectasis will be equally used for fluid filled and collapsed peripheral airspaces in the following. However, it is obvious that the basic mechanisms that initiate and mediate the progression of acute lung injury still need to be investigated in more detail.

So far, there are no methods of therapy specific to ALI/ARDS and care of patients with this syndrome remains primarily supportive and empiric (Ingenito et al., 1994). Clinical management involves prevention and aggressive treatment of infections, since the most common cause of death is uncontrolled infection with associated organ dysfunctions (MacCallum and Evans, 2004). A reduction in mortality has been observed when low-dose steroids are administered in the later phases of ALI/ARDS. All other trials of pharmacological interventions have failed to prove a positive effect on survival in large-scale trials. Because of the success of surfactant replacement therapy in IRDS patients, it has also been proposed as a treatment for ALI/ARDS. However, although a positive effect on oxygenation can be assumed according to Bernard (2005), the actual preparation, exact dosage, and delivery of synthetic surfactant still have to be investigated in more detail. Consequently, surfactant replacement is not a standard procedure for ALI/ARDS patients. The major vital supportive therapy of ALI/ARDS patients is mechanical ventilation used to maintain adequate systemic oxygenation and rest respiratory muscles (Ranieri et al., 1999). Therefore, the following sections will provide some information about this treatment along with a brief survey of ALI/ARDS-specific complications.

1.2.2 Mechanical ventilation

In intensive care medicine, mechanical ventilation is utilized to assist or replace spontaneous breathing of patients whenever oxygen supply is inadequate to maintain life. The ventilator is a pneumatically driven device that generates a controlled flow of gas into the patient's lung. Although other types of artificial respiration exist, positive pressure ventilation involving endotracheal intubation prevails in the clinical setting. Modern ventilators are electronically controlled and equipped with monitoring systems for various parameters. By choosing diverse machine settings, different patterns of respiration can be induced. According to Larsen and Ziegenfuß (2004), important variables are, for example, tidal volume, ventilation frequency, inspiratory flow, relation between inspiration and expiration time as well as end-expiratory and upper inspiratory pressure. The chosen ventilation mode in general depends on the specific disease, the available equipment, and the preferred protocols of the intensive care unit. As will be discussed also in the following section, so far no consensus on optimal ventilation strategies has been reached.

Two basic types of ventilation can be distinguished depending on the variable controlled primarily by the respirator, namely pressure or volume (Haberthür et al., 2001). In both cases, the specific target values are usually accomplished by regulating airflow. The active controlling process is in general confined to the inspiration phase, i.e. by initiating, limiting, and aborting inspiratory flow. In the subsequent no-flow-phase (the so-called inspiratory pause), a pressure plateau develops. This stage is followed by the expiration phase, which is passive in almost all common ventilation modes. This means that air flows back spontaneously due to the removal of positive tracheal pressure. Depending on the specific protocol, the end-expiratory pressure (EEP) is zero (ZEEP), negative (NEEP), or positive (PEEP). In line with the famous "open lung" concept, PEEP is usually chosen to prevent atelectasis and keep the lungs recruited in large part (Larsen and Ziegenfuß, 2004).

Although being a vital therapy for all patients undergoing surgery or suffering from ventilatory failure, Mols et al. (2006) argued that the actual process of mechanical ventilation is inherently unphysiological and artificial. After all, the mechanisms for providing the tidal volume during artificial respiration substantially differ from spontaneous breathing. The latter involves the development of a pressure gradient by means of muscular contraction. As a consequence, tracheal pressure is zero and alveolar pressure is negative. By contrast, the mechanical ventilator elevates tracheal pressure relative to the atmosphere, thereby forcing the air into the lungs. In addition to causing this substantial increase in intrapulmonal pressures, mechanical ventilation delivers uniform breaths. Normal ventilation, however, is characterized by continuously changing tidal volumes and flow rates. Although novel so-called polymorphous ventilation protocols (see e.g. Spieth et al. (2009)) attempt to mimic this intrinsic spontaneous breath-to-breath variability, they have not been fully evaluated clinically yet.

1.2.3 Complications

Artificial ventilation of patients without preexisting lung diseases (for example during anesthesia) is usually uncomplicated and not deleterious, even when high tidal volumes are utilized. According to Bates and Lutchen (2005), sub-pleural alveolar pressures are almost identical at different locations in the lung within the range of normal breathing. Hence, despite its complex structure, the lung behaves remarkably homogeneous in the healthy state. Pathology, though, invariably afflicts the lung in a heterogeneous manner which predisposes patients towards a number of complications when being mechanically ventilated. Since they are of utmost importance for the outcome of ARDS, the different side effects of artificial respiration will be briefly summarized in the following. More information (particularly on the many underlying studies) can be found e.g. in Dreyfuss and Saumon (1998), International Consensus Conferences in Intensive Care Medicine (1999), Slutsky (1999), and Oeckler and Hubmayr (2007).

In case of ARDS, three different regions of the lung can be distinguished (Gattinoni et al., 1993, 2001). Acute lung injuries occur predominantly in the dependent zones of the lung which denote the lower parts in direction of gravity. While these regions are atelectatic, the non-dependent areas are continuously open to ventilation. The transitional domains can be recruited or derecruited (i.e. aerated or atelectatic), depending on the particular point in time in the respiratory cycle and the specific ventilation protocol. When utilizing conventional ventilation strategies, the relatively normal non-dependent lung regions are at risk of overdistension. This phenomenon is commonly denoted as volutrauma and is associated with local cellular damage and a further increase in the permeability of the blood-gas barrier. Similar consequences (known as atelectrauma) are observed in the transitional domains where peripheral airspaces are repeatedly recruited and derecruited. In this context, Hubmayr (2002) defines the term “recruitment” as the aeration of previously airless regions which does not necessarily imply the reversal of collapse. Hence, the term atelectrauma is subsequently not restricted to collapse and opening of alveoli but may also refer to the repeated flooding and aeration of airspaces. It has to be noted, though, that the conventional definition of atelectrauma usually denotes the former mechanism only. However, the reinterpretation of this term is in line with the particular definition of atelectasis in section 1.2.1 and seems acceptable given the ongoing controversy. Although the existence of atelectrauma is widely accepted in the medical community and has been frequently demonstrated in animal models, the relevance to humans is still not firmly established (Moloney and Griffiths, 2004; Dirocco et al., 2006).

Both clinical and basic research have demonstrated that injurious ventilation strategies can initiate or perpetuate local and systemic inflammations (Uhlig, 2002). This so-called biotrauma plays an important role in the outcome of ARDS. In general, two basic mechanisms of biotrauma can be distinguished. First, stress failure of single cell membranes or the entire barrier due to volutrauma or atelectrauma leads to liberation and spreading of inflammatory mediators and bacteria. However, apart from physically damaging alveolar tissue, mechanical ventilation can also elicit the release of mediators in intact cells by activating stretch-induced signaling cascades. This process is also known as mechanotransduction since a mechanical stimulus is converted into chemical activity (for details see e.g. Vlahakis and Hubmayr (2003) and Kamm and Kaazempur-Mofrad (2004)). In addition to the exacerbation of preexisting injuries, inflammations can also be initiated in the formerly spared regions due to volutrauma. One involved group of inflammatory mediators are the cytokines that initiate and organize the host's response to different biological stresses (Ranieri et al., 1999). Cytokines interact with highly specific cell-surface receptors, causing a series of intracellular signaling events. If these processes are not adequately regulated, they may result in excessive amplification of the inflammatory cascade, thereby causing the uncontrolled activation of the immune system. By raising the production of pulmonary cytokines due to biotrauma and increasing the permeability of the blood-gas-barrier through volutrauma and/or atelectrauma, mechanical ventilation is likely to play an important role in the development of systemic inflammation. This might at least partly explain why most ARDS patients succumb to MODS rather than respiratory failure.

Volutrauma, atelectrauma, and biotrauma are collectively termed ventilator-associated lung injuries (VALI) and deemed among the most important factors in the pathogenesis of ARDS. Since the symptoms of VALI closely resemble those of ARDS (e.g. severe alveolar damage and inflammations), it is difficult to attribute the impairment to mechanical ventilation only (International Consensus Conferences in Intensive Care Medicine, 1999). In fact, changes in lung structure could also be due to the progression of ARDS. Consequently, the diagnosis of VALI in the clinical setting is inherently hampered. The sometimes equally used term ventilator-induced lung injuries (VILI), by contrast, usually defines acute lung injuries directly caused by mechanical ventilation in otherwise healthy animal lungs. Although the situation is inherently different, many insights into the underlying mechanisms of VALI described above were obtained from these animal experiments and the clinical relevance is now widely accepted. The development of specific ventilation strategies aimed at the protection and recovery of the lung, however, remains challenging.

According to Ware and Matthay (2000), the most appropriate method of mechanical ventilation in case of ALI has been controversial since the syndrome was first described. Although the tidal volume in normal breathing is 4 to 7 ml/kg body weight, critical care books had long recommended ventilation of ARDS patients with tidal volumes of 12 to 15 ml/kg body weight. Though this may have been suitable in case of surgery patients, it was soon found that this guideline does not hold for ARDS patients (Bernard, 2005). In 1994, the ARDS Clinical Trials Network (ARDSNet) was launched in order to investigate phenomena related to mechanical ventilation in the acutely injured lung in more detail.

In their pioneering first study (The Acute Respiratory Distress Syndrome Network, 2000), the outcomes of mechanical ventilation with 6 ml/kg and 12 ml/kg body weight were compared in 861 patients. Although the trial was initially planned for 1,000 subjects, it had to be cut short because of a striking reduction in mortality in the lower tidal volume group (31%) compared to the group treated with traditional ventilation (39.8%). The observed benefits of low-tidal volume ventilation were attributed to the protection of non-dependent airspaces against overdistension (i.e. volutrauma).

Another established recommendation for the ventilation of ARDS lungs is the maintenance of PEEP. Halter et al. (2003) stated that the noticed improvement of oxygenation is related to the prevention of flooding and/or collapse of small airways and possibly also individual alveoli during expiration. By keeping peripheral airspaces aerated throughout the respiratory cycle, damage caused by atelectrauma can potentially be impeded. Besides, PEEP may restrict the leakage of liquids from the vessels of pulmonary circulation towards the interstitial as well as the alveolar space by increasing both the perivascular and the alveolar pressure. Water already present in the alveolar space can be redistributed to the interstitium more easily. In this way, PEEP may also improve the function of the surfactant system (Larsen and Ziegenfuß, 2004). The implications of lower versus higher PEEP levels were addressed in another ARDSNet trial (Brower et al., 2004). Although oxygenation efficiency as well as lung compliance were increased in the group with higher PEEP, no benefits to survival, required ventilation time, or non-pulmonary organ function were observed. However, considering several limitations of the ARDSNet trial, Mols et al. (2006) stated that no conclusive evidence against the protective effect of an appropriately chosen PEEP could be provided and the rationale for the use of PEEP remains in general valid. However, there is again no consensus on the optimum level of PEEP in patients with ARDS (Moloney and Griffiths, 2004), although values between 5 and 15 mbar are usually utilized. Since the severity of injury varies throughout the lung, the proper selection of PEEP is further complicated.

Different alternative ventilation protocols have been formulated (e.g. alveolar recruitment maneuvers, partial liquid or high-frequency oscillatory ventilation), but none of these strategies have been shown to improve survival in randomized clinical trials (Tsushima et al., 2009). The only intervention that evidentially achieved mortality benefit has been low-tidal volume ventilation (see e.g. Amato et al. (1998)). As a consequence, many consider the ARDS Network protocol as the current standard for ventilation of ALI/ARDS patients (MacCallum and Evans, 2004). However, although providing evidence that “protective” ventilation strategies for ARDS patients can in general reduce mortality, only two distinct levels of tidal volumes were tested in this large-scale clinical trial. Hence, so far no concluding statements can be made about the optimal ventilation protocol. There is growing evidence that ventilatory variables in fact need to be adjusted individually at the bedside (Mols et al., 2006).

1.3 Objectives and outline

> *"It will probably take a multidisciplinary approach to fully elucidate alveolar mechanics [...] in both the normal and acutely injured lung."* (Gatto and Fluck, 2004)

The work described in this thesis was part of an interdisciplinary research project within the priority program "Protective artificial respiration" of the German Research Foundation (DFG). The long-term goal of this particular project is the identification of local in vivo stresses and strains in the lung during mechanical ventilation. These conditions can then be simulated experimentally in a specifically designed "bioreactor" enabling the well-defined mechanostimulation of living lung tissue slices (see Dassow et al. (2010) for details). The combination of computational models and experimental methods will help understanding how realistic mechanical forces are translated into biological responses such as pro-inflammatory gene expression. Particularly, this concept will allow for the comparison of different ventilation protocols with respect to local mechanical loadings and their corresponding biological effects. To the author's knowledge, no comparable approach aimed at quantitatively correlating mechanical stimuli and signaling responses during artificial respiration is available so far.

In this context, the main objective of the present thesis is the development of novel computational approaches enabling the detailed investigation of respiratory mechanics. Thereby, the focus will be clearly on the modeling aspects. The individual building blocks of a continuum lung model will be derived and their functionality will be demonstrated by simple numerical examples. Extensive studies based on patient-specific data, however, are beyond the scope of this work.

As already mentioned, remarkably little is known about lung mechanics even during normal breathing. This lack of understanding handicaps the investigation of pathophysiological changes in the diseased lung. Therefore, in this thesis, basic approaches to modeling the healthy lung will be developed as a first step. However, the requisites for a model of disease will always be kept in mind. Moreover, since all approaches will be built up mainly from first principles, a wide range of applicability can be assumed. The established models should be usable for both obtaining physiological insights from experimental data and testing specific hypotheses in the sense of a "virtual laboratory" in the future.

The success of any simulation strategy substantially depends on the level of detail that can be incorporated into the models. However, sophisticated models are of no practical use if not supplied with sufficient experimental data. Striking the balance of these opposing demands is among the principal tasks of an engineer. Hence, one has to formulate adequate simplifications of the real system under investigation and carefully define the resultant scope of application of the developed model. This thesis aims at providing methodologies for a detailed overall lung model that can be used to establish a better understanding of the phenomena occurring during VALI. Application of this rather complex model in the clinical setting, though, is not intended. Eventually, the insights gained by combining the developed computational models with the planned experimental investigations should be utilized to improve existing simple models that can be applied individually at the bedside.

Currently, these approaches are based on measurements of global lung mechanics only and, therefore, cannot give indication of local diseases. However, when provided with additional information obtained from detailed modeling, the simple models should help clinicians to choose patient-specific protective ventilation protocols in the future.

All methods and models devised as part of this work were implemented in the in-house finite element (FE) software platform BACI (Wall and Gee, 2010). This multi-purpose parallel research code is written in C++ and integrates open-source libraries of the trilinos project (Heroux et al., 2005). BACI has been developed jointly at the Institute for Computational Mechanics (Technische Universität München). Consequently, existing features like different element formulations or multigrid solver techniques could be easily utilized and complemented with additional implementations.

The remainder of this thesis is organized as follows. Chapter 2 will provide a short review of fundamental governing equations and relevant FE formulations. In the following chapters, the novel virtual lung model will be presented in detail.

A comprehensive alveolar model enabling the quantification of local stresses and strains will be introduced in chapter 3. Due to the poor disposability of imaging-based alveolar geometries, a new method to create artificial acinar representations suitable for FE simulations will be developed. Subsequently, the constitutive law utilized for describing alveolar tissue behavior will be presented. At the close of this chapter, a novel approach to considering surfactant film dynamics in the FE model will be devised.

Since the consideration of all 500 million alveoli is not feasible, specific approaches to establishing an overall model of lung parenchyma will be introduced in chapter 4. In this context, the alveolar micro-structure will be resolved only at certain “hot spots”, whereas a homogenized model will be utilized for the bulk of lung parenchyma. To bridge the gap between global parenchymal and local alveolar level, a nested dynamic multi-scale approach will be devised. After a short validation of the developed algorithm, its suitability for alveolar micro-structures will be demonstrated.

Chapter 5 will address the combination of the overall parenchyma model and the conducting airways to an overall continuum lung model. For this purpose, a physically motivated coupling of airflow and parenchyma volume change will be developed. The corresponding constrained fluid-structure interaction problem will be derived and specific solution procedures will be introduced. After some validating numerical examples, the novel volume-coupling approach will be shown to enable realistic simulations of coupled airflow and parenchyma deformations.

The presented computational approaches will be briefly summarized and discussed in chapter 6. Finally, a short outlook to possible and necessary enhancements of the models and future research directions will be provided.

2 Governing Equations and Finite Element Formulations

This chapter is intended to provide a basis for the development of computational models in respiratory mechanics. First, relevant continuum mechanical equations for solid dynamical problems will be reviewed. Furthermore, a few details about space and time discretization will be given. In the subsequent two sections, the governing equations and FE formulations for fluid flow on deformable domains will be addressed. Afterwards, approaches to considering the interaction of fluids and solids will be presented. Finally, two basic methods of constraint enforcement will be discussed.

2.1 Solid mechanics

The following introduction to nonlinear structural dynamics will focus on aspects necessary for the development of lung models. More extensive reviews can be found in the literature, e.g. in the standard textbooks Marsden and Hughes (1983), Ogden (1997), Holzapfel (2001), Bonet and Wood (2008), or the lecture notes of Wall et al. (2010a).

2.1.1 Kinematics

Kinematics of three-dimensional bodies

In continuum mechanics, the term kinematics denotes the mathematical description of the motion and deformation of a body. The following derivations are restricted to the total Lagrangian formulation since it is utilized exclusively in this thesis for the kinematics of solids. In this case, the reference or material configuration Ω_0^{S} denotes the domain that all points $\boldsymbol{x}_0$ of the undeformed body occupy at $t = 0$. The nonlinear map

$$\phi : \begin{cases} \Omega_0^{\mathsf{S}} & \mapsto \Omega^{\mathsf{S}} \\ \boldsymbol{x}_0 & \mapsto \boldsymbol{x} = \phi(\boldsymbol{x}_0) \end{cases} \qquad (2.1.1)$$

then completely defines the motion of the body from its reference to the current deformed configuration Ω^{S} with spatial positions $\boldsymbol{x}$ (cf. also Figure 2.1.1). The superscript S is utilized whenever there is danger of confusion with quantities of the fluid field (indicated by superscript F, cf. section 2.2) or the ALE field (identified by superscript A, cf. section 2.3).

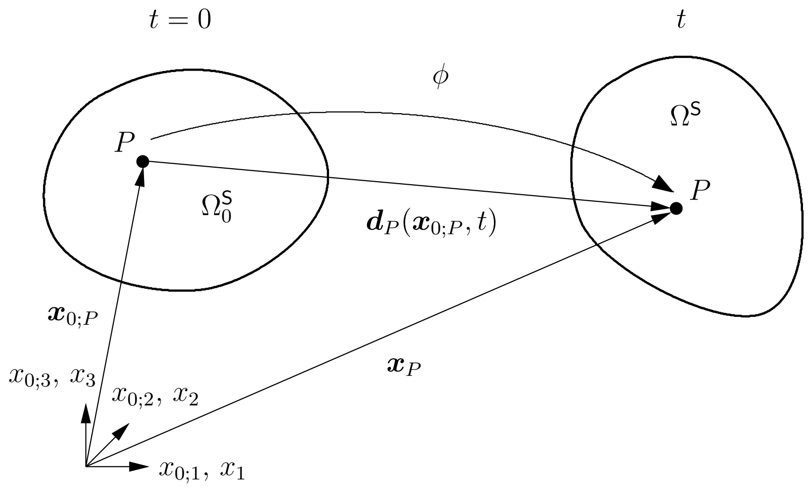

Figure 2.1.1: Total Lagrangian description of motion.

A common interpretation of the total Lagrangian formulation is that the observer describing the deformation moves with a fixed material point $\boldsymbol{x}_0$ of the body, thereby continuously determining its current position $\boldsymbol{x}$ in space.

Unless otherwise stated, a common Cartesian coordinate system is assumed for all configurations considered (see again Figure 2.1.1). Hence, the absolute displacement $\boldsymbol{d}$ of a material point $\boldsymbol{x}_0$ can be determined by

$$\boldsymbol{d}(\boldsymbol{x}_0,t) = \boldsymbol{x}(\boldsymbol{x}_0,t) - \boldsymbol{x}_0. \tag{2.1.2}$$

For a description of the time-dependent course of deformation, the material velocity $\dot{\boldsymbol{d}}$ and acceleration $\ddot{\boldsymbol{d}}$ of a point $\boldsymbol{x}_0$ are introduced based on the corresponding total derivatives of $\boldsymbol{d}$, viz.

$$\dot{\boldsymbol{d}}(\boldsymbol{x}_0,t) = \frac{\mathrm{d}\boldsymbol{d}(\boldsymbol{x}_0,t)}{\mathrm{d}t} = \left.\frac{\partial \boldsymbol{d}(\boldsymbol{x}_0,t)}{\partial t}\right|_{\boldsymbol{x}_0} = \left.\frac{\partial \boldsymbol{x}(\boldsymbol{x}_0,t)}{\partial t}\right|_{\boldsymbol{x}_0} \tag{2.1.3}$$

$$\ddot{\boldsymbol{d}}(\boldsymbol{x}_0,t) = \frac{\mathrm{d}^2\boldsymbol{d}(\boldsymbol{x}_0,t)}{\mathrm{d}t^2} = \frac{\mathrm{d}\dot{\boldsymbol{d}}(\boldsymbol{x}_0,t)}{\mathrm{d}t} = \left.\frac{\partial \dot{\boldsymbol{d}}(\boldsymbol{x}_0,t)}{\partial t}\right|_{\boldsymbol{x}_0}. \tag{2.1.4}$$

In order to characterize the volume and shape changes of a body, absolute displacements are unsuitable. For this purpose, appropriate strain measures are introduced based on the deformation gradient $\boldsymbol{F}$ given by

$$\boldsymbol{F} = \frac{\partial \boldsymbol{x}(\boldsymbol{x}_0,t)}{\partial \boldsymbol{x}_0} = \frac{\partial \boldsymbol{d}(\boldsymbol{x}_0,t)}{\partial \boldsymbol{x}_0} + \boldsymbol{I} \tag{2.1.5}$$

where $\boldsymbol{I}$ denotes the identity tensor and the derivative of a vector with respect to a vector defines a tensor. This symbolic notation will be utilized for convenience throughout this thesis. The index notation of equation (2.1.5) reads

$$F_{kL} = \frac{\partial x_k}{\partial x_{0;L}} = \frac{\partial d_k}{\partial x_{0;L}} + I_{kL}. \tag{2.1.6}$$

The deformation gradient is a two-point tensor with one basis (i.e. index) in the current and the other in the reference configuration. For simplicity, co- and contravariant components are not distinguished here and in the following unless explicitly indicated. $\boldsymbol{F}$ can be interpreted as the mapping of a tangential vector $\mathsf{d}\boldsymbol{x}_0$ in the reference state to its equivalent $\mathsf{d}\boldsymbol{x}$ in the spatial configuration via

$$\mathsf{d}\boldsymbol{x} = \boldsymbol{F} \cdot \mathsf{d}\boldsymbol{x}_0. \tag{2.1.7}$$

Due to this transformation property, $\boldsymbol{F}$ and its inverse $\boldsymbol{F}^{-1}$ are also known as push-forward and pull-back operations. The determinant of the deformation gradient, $\mathsf{det}(\boldsymbol{F})$, correlates infinitesimal volume elements of both configurations, i.e.

$$\mathsf{d}V = \mathsf{det}(\boldsymbol{F})\, \mathsf{d}V_0. \tag{2.1.8}$$

Furthermore, $\boldsymbol{F}$ also maps infinitesimal area elements between the reference and the current configuration by means of Nanson's formula

$$\boldsymbol{n}\, \mathsf{d}A = \mathsf{det}(\boldsymbol{F})\, \boldsymbol{F}^{-\mathsf{T}} \cdot \boldsymbol{n}_0\, \mathsf{d}A_0. \tag{2.1.9}$$

In this context, $\boldsymbol{n}$ and $\boldsymbol{n}_0$ denote the spatial and material unit normal vector of the area element.

$\boldsymbol{F}$ can be decomposed into a rotation tensor $\tilde{\boldsymbol{R}}$ and a stretch tensor $\tilde{\boldsymbol{U}}$, i.e.

$$\boldsymbol{F} = \tilde{\boldsymbol{R}} \cdot \tilde{\boldsymbol{U}}. \tag{2.1.10}$$

Consequently, $\boldsymbol{F}$ is not invariant with respect to rigid body rotations. By contrast, the right Cauchy-Green deformation tensor

$$\begin{aligned} \boldsymbol{C} &= \boldsymbol{F}^{\mathsf{T}} \cdot \boldsymbol{F} = \\ &= \tilde{\boldsymbol{U}}^{\mathsf{T}} \cdot \underbrace{\tilde{\boldsymbol{R}}^{\mathsf{T}} \cdot \tilde{\boldsymbol{R}}}_{\boldsymbol{I}} \cdot \tilde{\boldsymbol{U}} = \tilde{\boldsymbol{U}}^{\mathsf{T}} \cdot \tilde{\boldsymbol{U}} \end{aligned} \tag{2.1.11}$$

is a function of the stretch tensor only. Since $\boldsymbol{C}$ is unaffected by superimposed rigid body motions, this tensor field is materially objective and, therefore, particularly suited for the description of the internal state of a body. While the deformation gradient maps line elements between different configurations, $\boldsymbol{C}$ correlates their squares, i.e.

$$\mathsf{d}\boldsymbol{x} \cdot \mathsf{d}\boldsymbol{x} = \mathsf{d}\boldsymbol{x}_0 \cdot \boldsymbol{C} \cdot \mathsf{d}\boldsymbol{x}_0, \tag{2.1.12}$$

thereby quantifying also the enclosed angle. The index notation of equation (2.1.11) is given by

$$C_{KL} = F^{\mathsf{T}}_{Kk} F_{kL} \tag{2.1.13}$$

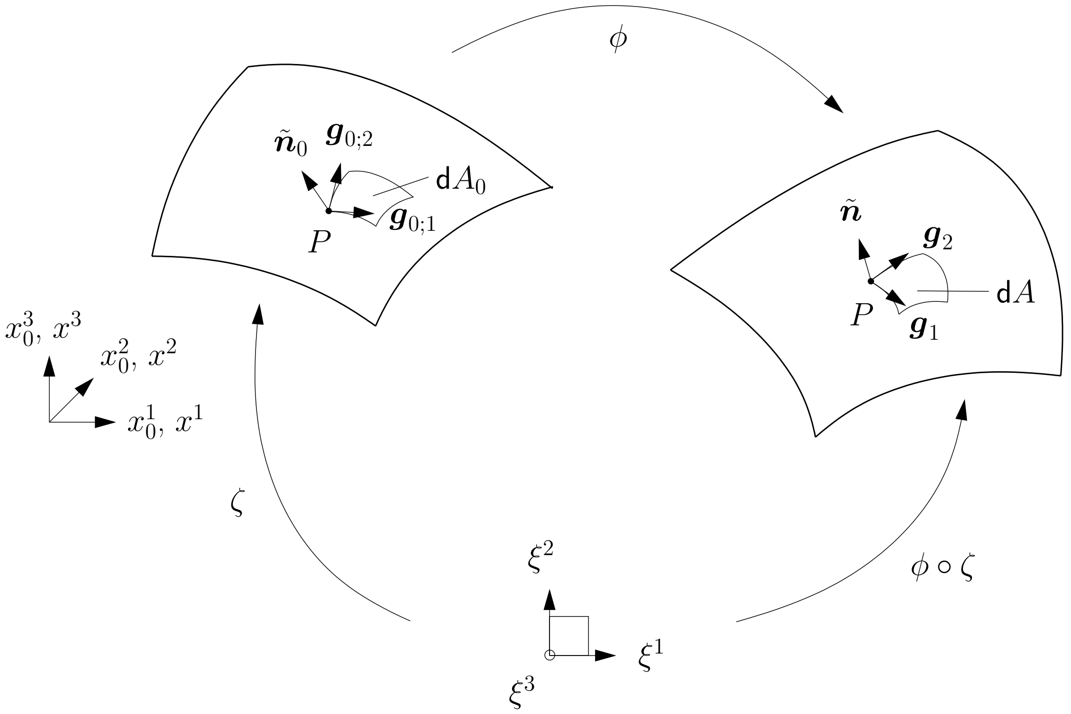

Figure 2.1.2: Mapping of an infinitesimal surface element between curvilinear coordinate space (bottom), undeformed (top left) and deformed (top right) configuration.

where Einstein summation convention is utilized. The right Cauchy-Green deformation tensor is exclusively defined in the material (i.e. reference) configuration.

Often it is desirable to ensure zero strains in the undeformed configuration (corresponding to $\boldsymbol{F} = \boldsymbol{I}$). For this purpose, the so-called Green-Lagrange strains are introduced as follows

$$\boldsymbol{E} = \frac{1}{2}(\boldsymbol{C} - \boldsymbol{I}) = \frac{1}{2}\left(\boldsymbol{F}^{\mathsf{T}} \cdot \boldsymbol{F} - \boldsymbol{I}\right). \tag{2.1.14}$$

$\boldsymbol{E}$ is a suitable nonlinear material strain measure that is commonly used in solid mechanics. However, since strains are no physical quantities, other definitions are equally possible. For instance, the so-called Euler-Almansi tensor represents a spatial strain measure given by

$$\boldsymbol{A} = \frac{1}{2}\left(\boldsymbol{I} - \boldsymbol{F}^{-\mathsf{T}} \cdot \boldsymbol{F}^{-1}\right). \tag{2.1.15}$$

Kinematics of curved surfaces

Several models presented in subsequent chapters rely on the characterization of arbitrarily curved surfaces in space. In the following, therefore, necessary expressions for surface areas and normal vectors will be derived.

The environment of a point P on a surface can be described by the tangent space with covariant basis vectors

$$\boldsymbol{g}_{0;s} = \frac{\partial \boldsymbol{x}_0}{\partial \xi^s} \tag{2.1.16}$$

in the reference configuration and

$$\boldsymbol{g}_s = \frac{\partial \boldsymbol{x}}{\partial \xi^s} \tag{2.1.17}$$

in the deformed configuration (see Figure 2.1.2). In this context, ξ^s (with $s \in \{1,2,3\}$) denote the curvilinear coordinates. The infinitesimal oriented surface area spanned by the in-plane basis vectors $\boldsymbol{g}_1$ and $\boldsymbol{g}_2$ then reads

$$\mathsf{d}\boldsymbol{A} \;=\; \boldsymbol{g}_1 \mathsf{d}\xi^1 \times \boldsymbol{g}_2 \mathsf{d}\xi^2 = \tilde{\boldsymbol{n}} \mathsf{d}\xi^1 \mathsf{d}\xi^2 \tag{2.1.18}$$

with the surface normal $\tilde{\boldsymbol{n}}$ given by

$$\tilde{\boldsymbol{n}} = \begin{pmatrix} \frac{\partial x^2}{\partial \xi^1}\frac{\partial x^3}{\partial \xi^2} - \frac{\partial x^2}{\partial \xi^2}\frac{\partial x^3}{\partial \xi^1} \\ \frac{\partial x^3}{\partial \xi^1}\frac{\partial x^1}{\partial \xi^2} - \frac{\partial x^3}{\partial \xi^2}\frac{\partial x^1}{\partial \xi^1} \\ \frac{\partial x^1}{\partial \xi^1}\frac{\partial x^2}{\partial \xi^2} - \frac{\partial x^1}{\partial \xi^2}\frac{\partial x^2}{\partial \xi^1} \end{pmatrix} = \frac{1}{\mathsf{det}\left(\bar{\boldsymbol{J}}\right)} \boldsymbol{g}^3. \tag{2.1.19}$$

In this context, $\boldsymbol{g}^3$ is the contravariant basis vector in surface normal direction and $\bar{\boldsymbol{J}}$ refers to the Jacobian of the mapping $\phi \circ \zeta$ (cf. Figure 2.1.2) defined by

$$\bar{\boldsymbol{J}} = \begin{pmatrix} \frac{\partial x^1}{\partial \xi^1} & \frac{\partial x^2}{\partial \xi^1} & \frac{\partial x^3}{\partial \xi^1} \\ \frac{\partial x^1}{\partial \xi^2} & \frac{\partial x^2}{\partial \xi^2} & \frac{\partial x^3}{\partial \xi^2} \\ \frac{\partial x^1}{\partial \xi^3} & \frac{\partial x^2}{\partial \xi^3} & \frac{\partial x^3}{\partial \xi^3} \end{pmatrix} = \begin{pmatrix} \boldsymbol{g}_1 \\ \boldsymbol{g}_2 \\ \boldsymbol{g}_3 \end{pmatrix}. \tag{2.1.20}$$

The corresponding (scalar) physical area of the infinitesimal surface is the absolute value of the oriented area given in equation (2.1.18), i.e.

$$\begin{aligned} \mathsf{d}A = |\tilde{\boldsymbol{n}}|\,\mathsf{d}\xi^1\mathsf{d}\xi^2 = \sqrt{\left(\frac{\partial x^2}{\partial \xi^1}\frac{\partial x^3}{\partial \xi^2} - \frac{\partial x^2}{\partial \xi^2}\frac{\partial x^3}{\partial \xi^1}\right)^2 + \left(\frac{\partial x^3}{\partial \xi^1}\frac{\partial x^1}{\partial \xi^2} - \frac{\partial x^3}{\partial \xi^2}\frac{\partial x^1}{\partial \xi^1}\right)^2 +} \\ \overline{+\left(\frac{\partial x^1}{\partial \xi^1}\frac{\partial x^2}{\partial \xi^2} - \frac{\partial x^1}{\partial \xi^2}\frac{\partial x^2}{\partial \xi^1}\right)^2}\,\mathsf{d}\xi^1\mathsf{d}\xi^2. \end{aligned} \tag{2.1.21}$$

Although above derivations are universally valid, the curvilinear coordinates can also be interpreted as a parameter space in line with the notation utilized for spatial discretization with FE. Therefore, equations (2.1.19) and (2.1.21) can be easily adopted for the description of element surfaces later on.

2.1.2 Definition of stresses

For defining the internal stress state of a deformed body, first the traction vector $\boldsymbol{t}^{\mathsf{S}}$ is introduced as follows

$$\boldsymbol{t}^{\mathsf{S}}(\boldsymbol{n},\boldsymbol{x},t) = \lim_{\Delta A \to 0} \frac{\Delta\tilde{\boldsymbol{r}}}{\Delta A} \tag{2.1.22}$$

where ΔA denotes an element of area with unit surface normal $\boldsymbol{n} = \frac{\tilde{\boldsymbol{n}}}{|\tilde{\boldsymbol{n}}|}$ and $\Delta\tilde{\boldsymbol{r}}$ is the resultant force acting on this area. According to Cauchy's theorem, the stresses in the deformed configuration are related to the surface traction via

$$\boldsymbol{t}^{\mathsf{S}} = \boldsymbol{\sigma}\cdot\boldsymbol{n}. \tag{2.1.23}$$

These so-called Cauchy stresses $\boldsymbol{\sigma}$ refer to an a priori unknown configuration. Therefore, alternative stress measures are often utilized in practice. For instance, the first Piola-Kirchhoff stresses $\boldsymbol{P}$ refer the resultant force to the undeformed element of surface area. Analogous to equation (2.1.23), the definition of $\boldsymbol{P}$ is given by

$$\boldsymbol{t}_0^{\mathsf{S}} = \boldsymbol{P}\cdot\boldsymbol{n}_0 \tag{2.1.24}$$

where $\boldsymbol{t}_0^{\mathsf{S}}$ denotes a pseudo-traction vector defined by

$$\boldsymbol{t}_0^{\mathsf{S}} = \frac{\mathrm{d}A}{\mathrm{d}A_0}\boldsymbol{t}^{\mathsf{S}} \tag{2.1.25}$$

and $\boldsymbol{n}_0$ is the unit normal vector of the surface in the reference configuration. The first Piola-Kirchhoff stresses can be obtained from the Cauchy stresses by applying equation (2.1.9), i.e.

$$\boldsymbol{P} = \mathrm{det}(\boldsymbol{F})\,\boldsymbol{\sigma}\cdot\boldsymbol{F}^{-\mathsf{T}}. \tag{2.1.26}$$

From the corresponding index notation,

$$P_{kL} = \mathrm{det}(\boldsymbol{F})\,\sigma_{kl}F_{lL}^{-\mathsf{T}}, \tag{2.1.27}$$

the two-point tensor characteristic of the first Piola-Kirchhoff stresses can be identified. By contrast, the second Piola-Kirchhoff tensor is a stress measure referring exclusively to the reference configuration. In this case, also the resultant force needs to be transformed to the material frame, yielding

$$\boldsymbol{S} = \boldsymbol{F}^{-1}\cdot\boldsymbol{P} = \mathrm{det}(\boldsymbol{F})\,\boldsymbol{F}^{-1}\cdot\boldsymbol{\sigma}\cdot\boldsymbol{F}^{-\mathsf{T}} \tag{2.1.28}$$

or, in index notation,

$$S_{IJ} = \mathrm{det}(\boldsymbol{F})\,F_{Ik}^{-1}\sigma_{kl}F_{lJ}^{-\mathsf{T}}. \tag{2.1.29}$$

Unlike the Cauchy stresses, both first and second Piola-Kirchhoff stresses cannot be interpreted easily. For example, the diagonal components do not correspond to normal stresses and the remaining components are not equivalent to shear stresses. However, material representations of tensorial quantities are often the preferred choice since they refer to the known reference configuration.

Any of the above introduced stress measures can be used to express the internal energy of a body. However, if a certain stress measure is chosen, the strain variable used in combination cannot be selected arbitrarily. Since stresses and strains are tensorial quantities, their components depend on their respective reference frame (e.g. the material configuration in case of Green-Lagrange strains and second Piola-Kirchhoff stresses). By contrast, the scalar value of the internal power $\mathcal{P}^{\mathsf{S}}$ is frame-invariant, i.e. objective. It can be easily shown that certain stress-strain pairs fulfill this condition, viz.

$$\mathcal{P}^{\mathsf{S}} = \int_{\Omega^{\mathsf{S}}} \boldsymbol{\sigma} : \mathscr{L}_t[\boldsymbol{A}]\,\mathsf{d}V = \int_{\Omega_0^{\mathsf{S}}} \boldsymbol{P} : \dot{\boldsymbol{F}}\,\mathsf{d}V_0 = \int_{\Omega_0^{\mathsf{S}}} \boldsymbol{S} : \dot{\boldsymbol{E}}\,\mathsf{d}V_0 \tag{2.1.30}$$

where $\mathscr{L}_t[\boldsymbol{A}]$ denotes the Lie (or objective) derivative of the Euler-Almansi strains, i.e.

$$\mathscr{L}_t[\boldsymbol{A}] = \phi\left[\frac{\mathsf{d}}{\mathsf{d}t}\left(\phi^{-1}[\boldsymbol{A}]\right)\right]. \tag{2.1.31}$$

Stresses and strains are correlated by means of a constitutive model describing the response of a material to applied loads. A popular example is the isotropic compressible Neo-Hookean law given by

$$\boldsymbol{S} = \mu_1^{\mathsf{S}}\left(\boldsymbol{I} - \boldsymbol{C}^{-1}\right) + \mu_2^{\mathsf{S}} \ln(\mathsf{det}(\boldsymbol{F}))\boldsymbol{C}^{-1}. \tag{2.1.32}$$

In this context, the so-called Lamé constants μ_1^{S} and μ_2^{S} can be referred to the Young's modulus E^{S} and the Poisson's ratio ν^{S} of the material via

$$\mu_1^{\mathsf{S}} = \frac{E^{\mathsf{S}}}{2\left(1+\nu^{\mathsf{S}}\right)}, \qquad \mu_2^{\mathsf{S}} = \frac{\nu^{\mathsf{S}} E^{\mathsf{S}}}{\left(1+\nu^{\mathsf{S}}\right)\left(1-2\nu^{\mathsf{S}}\right)}. \tag{2.1.33}$$

Further constitutive relations will be introduced in section 3.2 and chapter 4 for the characterization of alveolar and parenchymal tissue, respectively.

2.1.3 Governing equations

Conservation of mass

Introducing the spatial and reference mass densities ρ^{S} and ρ_0^{S}, i.e.

$$\rho_0^{\mathsf{S}} = \frac{\mathsf{d}V}{\mathsf{d}V_0}\rho^{\mathsf{S}} = \mathsf{det}(\boldsymbol{F})\rho^{\mathsf{S}}, \tag{2.1.34}$$

the global conservation of mass can be stated as

$$\frac{\mathsf{d}m}{\mathsf{d}t} = \frac{\mathsf{d}}{\mathsf{d}t}\int_{\Omega^{\mathsf{S}}} \rho^{\mathsf{S}}\mathsf{d}V = \frac{\mathsf{d}}{\mathsf{d}t}\int_{\Omega_0^{\mathsf{S}}} \rho_0^{\mathsf{S}}\mathsf{d}V_0 = 0. \tag{2.1.35}$$

Since the reference domain does not depend on time, the global mass conservation in the material description simplifies to

$$\int_{\Omega_0^{\mathrm{S}}} \dot{\rho}_0^{\mathrm{S}} \mathrm{d}V_0 = 0. \tag{2.1.36}$$

The spatial version of mass conservation can be reformulated using Reynold's transport theorem (cf. e.g. Belytschko et al. (2005)), i.e.

$$\frac{\mathrm{d}}{\mathrm{d}t} \int_{\Omega^{\mathrm{S}}} \rho^{\mathrm{S}} \mathrm{d}V = \int_{\Omega^{\mathrm{S}}} \left(\dot{\rho}^{\mathrm{S}} + \rho^{\mathrm{S}} \nabla \cdot \dot{\boldsymbol{d}} \right) \mathrm{d}V = 0. \tag{2.1.37}$$

In this context, "$\nabla \cdot$" denotes the spatial divergence operator. For instance, application of "$\nabla \cdot$" to a first- and second-order tensor results in

$$\nabla \cdot \dot{\boldsymbol{d}} = \dot{d}_{k,k}, \tag{2.1.38}$$

$$(\nabla \cdot \boldsymbol{\sigma})_k = \sigma_{kl,l}. \tag{2.1.39}$$

Since both equation (2.1.36) and (2.1.37) have to be fulfilled in any arbitrary subfield, the following local forms of mass conservation can be established:

$$\dot{\rho}_0^{\mathrm{S}} = 0 \tag{2.1.40}$$

$$\dot{\rho}^{\mathrm{S}} + \rho^{\mathrm{S}} \nabla \cdot \dot{\boldsymbol{d}} = 0 \tag{2.1.41}$$

Conservation of linear momentum

The conservation of linear momentum implies that the temporal change of a body's momentum is equivalent to the forces acting upon it. In the deformed configuration, this requirement can be mathematically formulated as

$$\frac{\mathrm{d}}{\mathrm{d}t} \int_{\Omega^{\mathrm{S}}} \rho^{\mathrm{S}} \dot{\boldsymbol{d}} \mathrm{d}V = \int_{\partial\Omega^{\mathrm{S}}} \boldsymbol{t}^{\mathrm{S}} \mathrm{d}A + \int_{\Omega^{\mathrm{S}}} \hat{\boldsymbol{b}}^{\mathrm{S}} \mathrm{d}V \tag{2.1.42}$$

with $\hat{\boldsymbol{b}}^{\mathrm{S}}$ referring to an arbitrary body load and $\partial\Omega^{\mathrm{S}}$ denoting the boundary of the body. Application of Reynold's transport theorem to the left-hand side of equation (2.1.42) and introduction of the spatial form of local mass conservation (2.1.41) yields

$$\begin{aligned}
\frac{\mathrm{d}}{\mathrm{d}t} \int_{\Omega^{\mathrm{S}}} \rho^{\mathrm{S}} \dot{\boldsymbol{d}} \mathrm{d}V &= \int_{\Omega^{\mathrm{S}}} \left(\dot{\rho}^{\mathrm{S}} \dot{\boldsymbol{d}} + \rho^{\mathrm{S}} \ddot{\boldsymbol{d}} + \rho^{\mathrm{S}} \dot{\boldsymbol{d}} \nabla \cdot \dot{\boldsymbol{d}} \right) \mathrm{d}V = \\
&= \int_{\Omega^{\mathrm{S}}} \left(\dot{\boldsymbol{d}} \left(\dot{\rho}^{\mathrm{S}} + \rho^{\mathrm{S}} \nabla \cdot \dot{\boldsymbol{d}} \right) + \rho^{\mathrm{S}} \ddot{\boldsymbol{d}} \right) \mathrm{d}V = \qquad (2.1.43) \\
&= \int_{\Omega^{\mathrm{S}}} \rho^{\mathrm{S}} \ddot{\boldsymbol{d}} \mathrm{d}V. \qquad (2.1.44)
\end{aligned}$$

Introducing furthermore equation (2.1.23) and making use of Gauss divergence theorem, the balance of linear momentum (2.1.42) simplifies to

$$\int_{\Omega^S} \rho^S \ddot{\boldsymbol{d}} \, \mathrm{d}V = \int_{\Omega^S} \left(\nabla \cdot \boldsymbol{\sigma} + \hat{\boldsymbol{b}}^S \right) \mathrm{d}V. \tag{2.1.45}$$

Again, relation (2.1.45) needs to be fulfilled also locally, i.e.

$$\rho^S \ddot{\boldsymbol{d}} = \nabla \cdot \boldsymbol{\sigma} + \hat{\boldsymbol{b}}^S. \tag{2.1.46}$$

After transformation of the integration domains from the current to the reference configuration and introduction of $\hat{\boldsymbol{b}}_0^S = \det(\boldsymbol{F}) \hat{\boldsymbol{b}}^S$ as well as equations (2.1.25) and (2.1.34), the material version of the balance of linear momentum (2.1.42) is determined by

$$\int_{\Omega_0^S} \rho_0^S \ddot{\boldsymbol{d}} \, \mathrm{d}V_0 = \int_{\partial\Omega_0^S} \boldsymbol{t}_0^S \, \mathrm{d}A_0 + \int_{\Omega_0^S} \hat{\boldsymbol{b}}_0^S \, \mathrm{d}V_0. \tag{2.1.47}$$

Insertion of equation (2.1.24) and application of Gauss divergence theorem allows for the following reformulation

$$\int_{\Omega_0^S} \rho_0^S \ddot{\boldsymbol{d}} \, \mathrm{d}V_0 = \int_{\Omega_0^S} \left(\nabla_0 \cdot \boldsymbol{P} + \hat{\boldsymbol{b}}_0^S \right) \mathrm{d}V_0 \tag{2.1.48}$$

with the material divergence operator defined by

$$(\nabla_0 \cdot \boldsymbol{P})_k = P_{kL,L}. \tag{2.1.49}$$

The corresponding local form is given by

$$\rho_0^S \ddot{\boldsymbol{d}} = \nabla_0 \cdot \boldsymbol{P} + \hat{\boldsymbol{b}}_0^S. \tag{2.1.50}$$

It is important to note that equation (2.1.50) still characterizes equilibrium in the deformed configuration. However, due to the transformation of vectors and tensors to the reference frame, the material approach is often more convenient and, therefore, utilized exclusively in this work. In combination with a constitutive model and the kinematical relations introduced previously, the material form of the equation of motion (2.1.50) constitutes a nonlinear coupled system of partial differential equations. The present double derivative with respect to time necessitates the specification of initial conditions for both displacements and velocities, i.e.

$$\boldsymbol{d}_0 = \boldsymbol{d}(t=0) = \hat{\boldsymbol{d}}_0 \qquad \text{in } \Omega_0^S \tag{2.1.51}$$

$$\dot{\boldsymbol{d}}_0 = \dot{\boldsymbol{d}}(t=0) = \hat{\dot{\boldsymbol{d}}}_0 \qquad \text{in } \Omega_0^S. \tag{2.1.52}$$

As with the body load, the superimposed hat identifies prescribed quantities here. The initial boundary value problem is completed by the definition of the following boundary conditions

$$\begin{aligned} \boldsymbol{d} &= \hat{\boldsymbol{d}} \qquad \text{on } \partial\Omega_{0;\mathrm{D}}^{\mathrm{S}} && (2.1.53)\\ \boldsymbol{P}\cdot\boldsymbol{n}_0 &= \hat{\boldsymbol{t}}_0 \qquad \text{on } \partial\Omega_{0;\mathrm{N}}^{\mathrm{S}} && (2.1.54) \end{aligned}$$

where $\partial\Omega_{0;\mathrm{D}}^{\mathrm{S}}$ and $\partial\Omega_{0;\mathrm{N}}^{\mathrm{S}}$ denote the Dirichlet and Neumann portions of the enclosing reference boundary with $\partial\Omega_{0;\mathrm{D}}^{\mathrm{S}} \cup \partial\Omega_{0;\mathrm{N}}^{\mathrm{S}} = \partial\Omega_{0}^{\mathrm{S}}$ and $\partial\Omega_{0;\mathrm{D}}^{\mathrm{S}} \cap \partial\Omega_{0;\mathrm{N}}^{\mathrm{S}} = 0$.

The above system of partial differential equations defines the strong form of the structural mechanics problem. Discretization with FE, however, requires the weak form as a starting point. This means that some relations are fulfilled in an integral sense only. In the present case, the essential idea is to satisfy weakly both balance equations (2.1.50) and traction boundary conditions (2.1.54). Their corresponding residuals are defined by

$$\begin{aligned} \boldsymbol{r}^{\mathrm{BE}} &= \rho_0^{\mathrm{S}}\ddot{\boldsymbol{d}} - \nabla_0\cdot\boldsymbol{P} - \hat{\boldsymbol{b}}_0^{\mathrm{S}} && \text{in } \Omega_0^{\mathrm{S}}\\ \boldsymbol{r}^{\mathrm{TBC}} &= \boldsymbol{P}\cdot\boldsymbol{n}_0 - \hat{\boldsymbol{t}}_0^{\mathrm{S}} && \text{on } \partial\Omega_{0;\mathrm{N}}^{\mathrm{S}}. \end{aligned} \qquad (2.1.55)$$

The method of weighted residuals then brings about the following weak form of equation (2.1.55)

$$\int_{\Omega_0^{\mathrm{S}}} \left(\rho_0^{\mathrm{S}}\ddot{\boldsymbol{d}} - \nabla_0\cdot\boldsymbol{P} - \hat{\boldsymbol{b}}_0^{\mathrm{S}}\right)\cdot\boldsymbol{w}\,\mathrm{d}V_0 + \int_{\partial\Omega_{0;\mathrm{N}}^{\mathrm{S}}} \left(\boldsymbol{P}\cdot\boldsymbol{n}_0 - \hat{\boldsymbol{t}}_0^{\mathrm{S}}\right)\cdot\boldsymbol{w}\,\mathrm{d}A_0 = 0 \qquad (2.1.56)$$

which is formulated in terms of a single scalar value for the entire system. The solution of the local strong equations also satisfies this weak form. $\boldsymbol{w}$ is a weighting function vector meeting the requirement

$$\boldsymbol{w} = \boldsymbol{0} \qquad \forall \boldsymbol{x}_0 \in \partial\Omega_{0;\mathrm{D}}^{\mathrm{S}}. \qquad (2.1.57)$$

The weighting functions may be associated with virtual displacements, i.e.

$$\boldsymbol{w} = \delta\boldsymbol{d}. \qquad (2.1.58)$$

The weak form (2.1.56) can then be interpreted as a virtual work expression. Integration by parts of the divergence term and insertion of equations (2.1.28) and (2.1.57) results in

$$\int_{\Omega_0^{\mathrm{S}}} \left(\rho_0^{\mathrm{S}}\ddot{\boldsymbol{d}} - \hat{\boldsymbol{b}}_0^{\mathrm{S}}\right)\cdot\delta\boldsymbol{d}\,\mathrm{d}V_0 + \int_{\Omega_0^{\mathrm{S}}} (\nabla_0\delta\boldsymbol{d})^{\mathrm{T}} : (\boldsymbol{F}\cdot\boldsymbol{S})\,\mathrm{d}V_0 - \int_{\partial\Omega_{0;\mathrm{N}}^{\mathrm{S}}} \hat{\boldsymbol{t}}_0^{\mathrm{S}}\cdot\delta\boldsymbol{d}\,\mathrm{d}A_0 = 0 \qquad (2.1.59)$$

with

$$(\nabla_0\delta\boldsymbol{d})_{kL} = \delta d_{k,L} \qquad (2.1.60)$$

denoting the material gradient operator. This relation can be further simplified to

$$\underbrace{\int_{\Omega_0^{\mathrm{S}}} \rho_0^{\mathrm{S}}\ddot{\boldsymbol{d}}\cdot\delta\boldsymbol{d}\,\mathrm{d}V_0}_{-\delta\mathcal{W}^{\mathrm{kin;S}}} + \underbrace{\int_{\Omega_0^{\mathrm{S}}} \boldsymbol{S} : \delta\boldsymbol{E}\,\mathrm{d}V_0}_{-\delta\mathcal{W}^{\mathrm{int;S}}} \underbrace{- \int_{\Omega_0^{\mathrm{S}}} \hat{\boldsymbol{b}}_0^{\mathrm{S}}\cdot\delta\boldsymbol{d}\,\mathrm{d}V_0 - \int_{\partial\Omega_{0;\mathrm{N}}^{\mathrm{S}}} \hat{\boldsymbol{t}}_0^{\mathrm{S}}\cdot\delta\boldsymbol{d}\,\mathrm{d}A_0}_{-\delta\mathcal{W}^{\mathrm{ext;S}}} = 0 \qquad (2.1.61)$$

where $\delta \boldsymbol{E}$ is obtained from the total variation of the Green-Lagrange strains given by

$$\delta \boldsymbol{E} = \frac{1}{2}\left(\left(\boldsymbol{F}^{\mathsf{T}} \cdot \nabla_0 \delta \boldsymbol{d}\right)^{\mathsf{T}} + \boldsymbol{F}^{\mathsf{T}} \cdot \nabla_0 \delta \boldsymbol{d}\right) \tag{2.1.62}$$

and advantage is taken of the symmetry of $\boldsymbol{S}$. As already indicated in equation (2.1.61), the weak form consists of a kinetic, internal, and external virtual work contribution.

Whenever an underlying energy potential $\mathcal{W}^{\mathsf{S}}$ exists, the weak form can alternatively be obtained by variation of this functional. This corresponds to the principle of minimum of total potential energy. However, since the existence of such a functional cannot be generally presumed, the universal principle of virtual work was utilized here.

2.1.4 Space and time discretization

In order to enable the numerical solution of the weak form resumed in the previous section, the equations need to be discretized in space and time. For spatial discretization, the finite element method (FEM) is utilized exclusively throughout this thesis. A detailed introduction is beyond the scope of this work but may be found in many textbooks like Hughes (2000), Belytschko et al. (2005), Zienkiewicz et al. (2005), and Zienkiewicz and Taylor (2006). The purpose of this section is to provide some basic relevant notations.

The FEM is based on the spatial approximation of continuous functions via interpolation of discrete values. For this purpose, discrete points, the so-called nodes, are introduced in the computational domain. By combining several nodes to elements, Ω_0^{S} is partitioned into a finite number nele of non-overlapping subdomains $\Omega_0^{\mathsf{S};(e)}$, viz.

$$\Omega_0^{\mathsf{S}} \approx \bigcup_{(e)=1}^{\mathsf{nele}} \Omega_0^{\mathsf{S};(e)}. \tag{2.1.63}$$

Introduction of the shape functions $\tilde{N}$ and the nodal displacements $\mathbf{d}$ allows for the following approximation of the displacements within an element

$$\boldsymbol{d}^{(e)}(\boldsymbol{x}_0, t) \approx \boldsymbol{d}^{h;(e)}(\boldsymbol{x}_0, t) = \sum_{I=1}^{\mathsf{nnod}} \tilde{N}_I(\boldsymbol{x}_0)\mathbf{d}_I(t) \tag{2.1.64}$$

where the superscript h indicates spatial discretization and nnod refers to the number of element nodes. The accelerations $\ddot{\boldsymbol{d}}$, the virtual displacements $\delta \boldsymbol{d}$, and the material representation of the element $\boldsymbol{x}_0$ are discretized equally. The shape functions utilized for interpolation are typically polynomials whose order is chosen according to the specific differentiability requirements resulting from the weak form.

The integrals in the weak form (2.1.61) can be evaluated elementwise using Gaussian quadrature (see e.g. Hughes (2000) for details). To simplify matters, $\Omega_0^{\mathsf{S};(e)}$ is mapped to a reference element geometry – for instance the normalized cube $[-1;1]^3$ – in the parameter space $\boldsymbol{\xi}$ via

$$\zeta : \quad \boldsymbol{\xi} \mapsto \boldsymbol{x}_0^{h;(e)}(\boldsymbol{\xi}) = \sum_{I=1}^{\mathsf{nnod}} N_I(\boldsymbol{\xi}) \mathbf{x}_{0;I} \tag{2.1.65}$$

where N_I is the shape function of node I in the parameter space. After assembly of the individual element contributions, the resulting spatially discretized equations of motion are given by

$$\left(\mathbf{M}^{\mathsf{S}}\ddot{\mathbf{d}} + \mathbf{f}^{\mathsf{int;S}}(\mathbf{d}) - \mathbf{f}^{\mathsf{ext;S}}\right)\delta\mathbf{d} = 0 \tag{2.1.66}$$

with the global mass matrix $\mathbf{M}^{\mathsf{S}}$, the internal force vector $\mathbf{f}^{\mathsf{int;S}}$, and the external force vector $\mathbf{f}^{\mathsf{ext;S}}$. $\delta\mathbf{d}$ and $\ddot{\mathbf{d}}$ refer to the discrete global virtual displacement and acceleration vector, respectively. Equation (2.1.66) has to hold for arbitrary $\delta\mathbf{d}$, i.e.

$$\mathbf{M}^{\mathsf{S}}\ddot{\mathbf{d}} + \mathbf{f}^{\mathsf{int;S}}(\mathbf{d}) - \mathbf{f}^{\mathsf{ext;S}} = \mathbf{0}. \tag{2.1.67}$$

In order to consider viscous damping, the semi-discrete equations of motions (2.1.67) are sometimes extended to

$$\mathbf{M}^{\mathsf{S}}\ddot{\mathbf{d}} + \mathbf{D}^{\mathsf{S}}\dot{\mathbf{d}} + \mathbf{f}^{\mathsf{int;S}}(\mathbf{d}) - \mathbf{f}^{\mathsf{ext;S}} = \mathbf{0} \tag{2.1.68}$$

where $\dot{\mathbf{d}}$ denote the global, spatially discrete velocities discretized analogous to the displacements (2.1.64) and $\mathbf{D}$ refers to a damping matrix given e.g. by

$$\mathbf{D}^{\mathsf{S}} = c_{\mathsf{M}}\mathbf{M}^{\mathsf{S}} + c_{\mathsf{K}}\mathbf{K}_0^{\mathsf{S}}. \tag{2.1.69}$$

In this context, c_{M}, c_{K} are empirical parameters and $\mathbf{K}_0^{\mathsf{S}}$ refers to the initial tangential stiffness matrix introduced in the following section. This so-called Rayleigh ansatz is a simple, widely used phenomenological approach to viscous damping.

For time discretization of equation (2.1.68), the generalized-α method introduced by Chung and Hulbert (1993) is utilized here. This one-step integration scheme is based on Newmark-like approximations in the time domain. Hence, the approximate velocities $\mathbf{v}_{n+1} \approx \dot{\mathbf{d}}\,(t_{n+1})$ and accelerations $\mathbf{a}_{n+1} \approx \ddot{\mathbf{d}}\,(t_{n+1})$ at the end of a discrete time step $[t_n, t_{n+1}]$, i.e. at time t_{n+1}, can be formulated in terms of known quantities at t_n and the unknown end-displacements $\mathbf{d}_{n+1}$ only

$$\mathbf{v}_{n+1}(\mathbf{d}_{n+1}) = \frac{\bar{\gamma}}{\bar{\beta}\Delta t}(\mathbf{d}_{n+1} - \mathbf{d}_n) - \frac{\bar{\gamma} - \bar{\beta}}{\bar{\beta}}\mathbf{v}_n - \frac{\bar{\gamma} - 2\bar{\beta}}{2\bar{\beta}}\Delta t\,\mathbf{a}_n \tag{2.1.70}$$

$$\mathbf{a}_{n+1}(\mathbf{d}_{n+1}) = \frac{1}{\bar{\beta}\Delta t^2}(\mathbf{d}_{n+1} - \mathbf{d}_n) - \frac{1}{\bar{\beta}\Delta t}\mathbf{v}_n - \frac{1 - 2\bar{\beta}}{2\bar{\beta}}\mathbf{a}_n \tag{2.1.71}$$

with $\bar{\gamma} \in [0,1], \bar{\beta} \in [0, \frac{1}{2}]$, and time step size Δt. Introducing these approximations in equation (2.1.68) would result in the discrete equilibrium equations at the end of the current time step t_{n+1}. The key idea of the generalized-α method is a modification of the time point at which these discretized equations of motion are set up. The evaluation point is shifted from t_{n+1} to generalized mid-points $t_{n+1-\alpha_{\mathsf{f}}}$ and $t_{n+1-\alpha_{\mathsf{m}}}$, respectively. Corresponding mid accelerations, velocities, displacements, and external forces are then given by linear combinations of the corresponding start and end vector, i.e.

$$\mathbf{d}_{n+1-\alpha_\mathrm{f}} = (1-\alpha_\mathrm{f})\,\mathbf{d}_{n+1} + \alpha_\mathrm{f}\mathbf{d}_n \tag{2.1.72}$$

$$\mathbf{v}_{n+1-\alpha_\mathrm{f}} = (1-\alpha_\mathrm{f})\,\mathbf{v}_{n+1} + \alpha_\mathrm{f}\mathbf{v}_n \tag{2.1.73}$$

$$\mathbf{a}_{n+1-\alpha_\mathrm{m}} = (1-\alpha_\mathrm{m})\,\mathbf{a}_{n+1} + \alpha_\mathrm{m}\mathbf{a}_n \tag{2.1.74}$$

$$\mathbf{f}^{\mathrm{ext;S}}_{n+1-\alpha_\mathrm{f}} = (1-\alpha_\mathrm{f})\,\mathbf{f}^{\mathrm{ext;S}}_{n+1} + \alpha_\mathrm{f}\mathbf{f}^{\mathrm{ext;S}}_n. \tag{2.1.75}$$

The spectral radius of a time integration method is a measure of numerical dissipation. Thereby, a smaller spectral radius corresponds to greater algorithmic damping. Although controllable dissipation in the high-frequency domain is desired, it should be achieved without inducing excessive damping in the important low-frequency domain. Hence, the spectral radius has to decrease smoothly with increasing frequency. This demand poses several restrictions on the parameters of the generalized-α scheme. Introducing ρ_∞ as the user-defined value of the spectral radius in the high-frequency limit, the optimal choice of algorithmic parameters is given by

$$\alpha_\mathrm{f} = \frac{\rho_\infty}{\rho_\infty + 1}, \qquad \alpha_\mathrm{m} = \frac{2\rho_\infty - 1}{\rho_\infty + 1} \tag{2.1.76}$$

$$\bar{\beta} = \frac{1}{4}(1-\alpha_\mathrm{m}+\alpha_\mathrm{f})^2 \qquad \bar{\gamma} = \frac{1}{2} - \alpha_\mathrm{m} + \alpha_\mathrm{f}. \tag{2.1.77}$$

In this case, the resulting time integration scheme is second-order accurate and stable. For the simulations in this work, ρ_∞ is chosen to be 0.7.

The discrete linear momentum balance finally reads

$$\mathbf{M}^\mathrm{S}\mathbf{a}_{n+1-\alpha_\mathrm{m}} + \mathbf{D}^\mathrm{S}\mathbf{v}_{n+1-\alpha_\mathrm{f}} + \mathbf{f}^{\mathrm{int;S}}\left(\mathbf{d}_{n+1-\alpha_\mathrm{f}}\right) - \mathbf{f}^{\mathrm{ext;S}}_{n+1-\alpha_\mathrm{f}} = \mathbf{0}. \tag{2.1.78}$$

2.1.5 Linearization

The system of nonlinear equations (2.1.78) is solved iteratively with the help of Newton's method. In a given iteration step i, the residual of the discrete linear momentum balance can be defined as follows

$$\mathbf{r}^{\mathrm{effdyn;S}}\left(\mathbf{d}^i_{n+1}\right) = \mathbf{M}^\mathrm{S}\mathbf{a}^i_{n+1-\alpha_\mathrm{m}} + \mathbf{D}^\mathrm{S}\mathbf{v}^i_{n+1-\alpha_\mathrm{f}} + \mathbf{f}^{\mathrm{int;S}}\left(\mathbf{d}^i_{n+1-\alpha_\mathrm{f}}\right) - \mathbf{f}^{\mathrm{ext;S}}_{n+1-\alpha_\mathrm{f}}. \tag{2.1.79}$$

The linearized form of the residual (2.1.79) is obtained by expanding $\mathbf{r}^{\mathrm{effdyn;S}}$ in a Taylor series around the current solution $\mathbf{d}^i_{n+1}$ and truncating it after the linear term, i.e.

$$\mathrm{Lin}\,\mathbf{r}^{\mathrm{effdyn;S}}\left(\mathbf{d}^i_{n+1}\right) = \mathbf{r}^{\mathrm{effdyn;S}}\left(\mathbf{d}^i_{n+1}\right) + \underbrace{\left.\frac{\partial \mathbf{r}^{\mathrm{effdyn;S}}\left(\mathbf{d}_{n+1}\right)}{\partial \mathbf{d}_{n+1}}\right|^i}_{\mathbf{K}^{\mathrm{effdyn;S}}\left(\mathbf{d}^i_{n+1}\right)} \Delta\mathbf{d}^{i+1}_{n+1}. \tag{2.1.80}$$

Using Newmark's approximations as well as equations (2.1.72), (2.1.73), and (2.1.74),

$\mathbf{K}^{\mathrm{effdyn;S}}$ is obtained as

$$\begin{aligned}\mathbf{K}^{\mathrm{effdyn;S}}\left(\mathbf{d}_{n+1}^{i}\right) &= \left.\frac{\partial \mathbf{r}^{\mathrm{effdyn;S}}\left(\mathbf{d}_{n+1}\right)}{\partial \mathbf{d}_{n+1}}\right|^{i} = \\ &= \left[\frac{1-\alpha_{\mathrm{m}}}{\beta \Delta t^{2}}\mathbf{M}^{\mathrm{S}} + \frac{(1-\alpha_{\mathrm{f}})\gamma}{\beta \Delta t}\mathbf{D}^{\mathrm{S}} + (1-\alpha_{\mathrm{f}})\,\mathbf{K}^{\mathrm{S}}\left(\mathbf{d}_{n+1-\alpha_{\mathrm{f}}}\right)\right]^{i}. \end{aligned} \tag{2.1.81}$$

For simplicity, the external forces were assumed to be independent of the unknown displacements here. Therefore, the tangential stiffness matrix $\mathbf{K}^{\mathrm{S}}$ is simply given by

$$\mathbf{K}^{\mathrm{S}}\left(\mathbf{d}_{n+1-\alpha_{\mathrm{f}}}\right) = \left.\frac{\partial \mathbf{f}^{\mathrm{int;S}}\left(\mathbf{d}_{n+1-\alpha_{\mathrm{f}}}\right)}{\partial \mathbf{d}_{n+1-\alpha_{\mathrm{f}}}}\right|^{i}. \tag{2.1.82}$$

In equilibrium, the residual and its linearized form need to vanish. From

$$\mathrm{Lin}\,\mathbf{r}^{\mathrm{effdyn;S}}\left(\mathbf{d}_{n+1}^{i}\right) \overset{!}{=} 0, \tag{2.1.83}$$

the following linear system of equations is obtained

$$\mathbf{K}^{\mathrm{effdyn;S}}\left(\mathbf{d}_{n+1}^{i}\right)\Delta\mathbf{d}_{n+1}^{i+1} = -\mathbf{r}^{\mathrm{effdyn;S}}\left(\mathbf{d}_{n+1}^{i}\right). \tag{2.1.84}$$

After solution of equation (2.1.84) for $\Delta\mathbf{d}_{n+1}^{i+1}$, the displacement vector can be updated as follows

$$\mathbf{d}_{n+1}^{i+1} = \mathbf{d}_{n+1}^{i} + \Delta\mathbf{d}_{n+1}^{i+1}. \tag{2.1.85}$$

The iterative procedure is aborted, i.e. $\mathbf{d}_{n+1}^{i+1} = \mathbf{d}_{n+1}$, when a user-specified convergence criterion for the residual (2.1.79) is met.

2.2 Fluid mechanics

For the development of an overall lung model, airflow in the conducting passages needs to be considered. This section should, therefore, provide a succinct overview of the governing equations for incompressible flows within the context of the FEM. More detailed information on the theoretical background and appropriate numerical methods can be found e.g. in Wall (1999), Gresho and Sani (2000), Donea and Huerta (2003), Förster (2007), and Gamnitzer (2010).

2.2.1 Kinematics and constitutive relations

The kinematics of flow problems is often characterized with the help of an Eulerian approach. In this case, a figurative observer is situated at a fixed spatial point and describes the properties of fluid particles passing by. In contrast to the Lagrangian approach described in section 2.1.1, the Eulerian formulation easily facilitates the treatment of large distortions in fluid motion. However, the detection of free surfaces or interfaces between different media is intricate. To overcome this problem, an Arbitrary Lagrangian Eulerian (ALE) approach combining the advantages of both kinematical formulations can be utilized. The key concept of the ALE formulation is the introduction of a computational mesh that can move independently of the velocity of the material particles. The mapping between the location of a particular point in the ALE reference system specified by χ and its position in the spatial frame is then given by

$$\varphi(\chi,t): \quad \chi \mapsto \boldsymbol{x}(\chi,t). \tag{2.2.1}$$

The absolute fluid velocity is again the material time derivative of the spatial position, i.e.

$$\boldsymbol{u} = \frac{\mathsf{d}\boldsymbol{x}}{\mathsf{d}t} = \left.\frac{\partial \boldsymbol{x}(\chi,t)}{\partial t}\right|_{\chi} + \frac{\partial \boldsymbol{x}(\chi,t)}{\partial \chi}\frac{\partial \chi}{\partial t}. \tag{2.2.2}$$

Introducing the ALE grid velocity

$$\boldsymbol{u}^{\mathsf{A}} = \left.\frac{\partial \boldsymbol{x}(\chi,t)}{\partial t}\right|_{\chi} \tag{2.2.3}$$

and the convective velocity

$$\boldsymbol{c} = \boldsymbol{u} - \boldsymbol{u}^{\mathsf{A}}, \tag{2.2.4}$$

the material time derivative of a given quantity f can then be determined by

$$\begin{aligned}
\frac{\mathsf{d}f(\chi,t)}{\mathsf{d}t} &= \left.\frac{\partial f(\chi,t)}{\partial t}\right|_{\chi} + \frac{\partial f(\chi,t)}{\partial \boldsymbol{x}}\frac{\partial \boldsymbol{x}}{\partial \chi}\frac{\partial \chi}{\partial t} = \\
&= \left.\frac{\partial f(\chi,t)}{\partial t}\right|_{\chi} + \left(\boldsymbol{u} - \boldsymbol{u}^{\mathsf{A}}\right)\cdot\nabla f(\chi,t) = \\
&= \left.\frac{\partial f(\chi,t)}{\partial t}\right|_{\chi} + \boldsymbol{c}\cdot\nabla f(\chi,t) = \qquad (2.2.5)\\
&= \mathring{f} + \boldsymbol{c}\cdot\nabla f(\chi,t). \qquad (2.2.6)
\end{aligned}$$

According to this fundamental ALE equation, the material time derivative of f depends on a temporal change of f in the reference frame and a convective term accounting for the relative motion of this system.

Another important kinematic quantity is the strain rate tensor given by

$$\boldsymbol{\epsilon}(\boldsymbol{u}) = \frac{1}{2}\left(\nabla\boldsymbol{u} + (\nabla\boldsymbol{u})^{\mathsf{T}}\right). \tag{2.2.7}$$

Based on this definition, the following constitutive relation can be assumed for an incompressible Newtonian fluid

$$\boldsymbol{\sigma} = 2\mu^{\mathsf{F}}\boldsymbol{\epsilon}(\boldsymbol{u}) - \bar{p}\boldsymbol{I} \tag{2.2.8}$$

where μ^{F} is the dynamic viscosity and $\bar{p}$ refers to the hydrostatic pressure.

2.2.2 Governing equations

The incompressible Navier-Stokes equations utilized for modeling airflow are based on the local conservation of mass and linear momentum. Since the procedures for setting up this system of equations are comparable to the ones presented in section 2.1.3, the detailed derivations are spared here. Defining the kinematic viscosity

$$\nu^{\mathsf{F}} = \frac{\mu^{\mathsf{F}}}{\rho} \tag{2.2.9}$$

and the kinematic pressure

$$p = \frac{\bar{p}}{\rho}, \tag{2.2.10}$$

the resulting density-scaled strong form of the incompressible Navier-Stokes equations in the deformed domain Ω^{F} is given by

$$\begin{aligned} \mathring{\boldsymbol{u}} + \boldsymbol{c} \cdot \nabla \boldsymbol{u} - 2\nu^{\mathsf{F}} \nabla \cdot \boldsymbol{\epsilon}(\boldsymbol{u}) + \nabla p &= \hat{\boldsymbol{b}}^{\mathsf{F}} && (2.2.11)\\ \nabla \cdot \boldsymbol{u} &= 0 && (2.2.12) \end{aligned}$$

with initial and boundary conditions

$$\begin{aligned} \boldsymbol{u}_0 = \boldsymbol{u}(t=0) = \hat{\boldsymbol{u}}_0 &\qquad \text{in } \Omega^{\mathsf{F}} && (2.2.13)\\ \boldsymbol{u} = \hat{\boldsymbol{u}} &\qquad \text{on } \partial\Omega^{\mathsf{F}}_{\mathsf{D}} && (2.2.14)\\ \frac{1}{\rho}\boldsymbol{\sigma} \cdot \boldsymbol{n} = \hat{\boldsymbol{t}}^{\mathsf{F}} &\qquad \text{on } \partial\Omega^{\mathsf{F}}_{\mathsf{N}} && (2.2.15)\\ \boldsymbol{u} \cdot \boldsymbol{n} = \boldsymbol{u}^{\mathsf{A}} \cdot \boldsymbol{n} &\qquad \text{on } \partial\Omega^{\mathsf{F}}_{\mathsf{B}}. && (2.2.16) \end{aligned}$$

In this context, equation (2.2.16) ensures that no fluid particles cross a deformable boundary or material interface $\partial\Omega^{\mathsf{F}}_{\mathsf{B}}$. The special case $\boldsymbol{u} = \boldsymbol{u}^{\mathsf{A}}$ corresponds to a local Lagrangian description of $\partial\Omega^{\mathsf{F}}_{\mathsf{B}}$ (Wall, 1999). In order to guarantee a well-posed problem, the prescribed velocity field (2.2.13) has to satisfy the continuity condition (2.2.12). The same requirement applies to equation (2.2.14) in case of solely Dirichlet bounded problems. More details on mathematically permissible boundary conditions of the Navier-Stokes equations can be found e.g. in Gresho and Sani (2000).

Introducing the virtual velocities $\delta\boldsymbol{u}$ (with $\delta\boldsymbol{u} = \boldsymbol{0}$ on $\partial\Omega^{\mathsf{F}}_{\mathsf{D}}$) and the virtual pressure δp, the weak form of equations (2.2.11) and (2.2.12) reads

$$\begin{aligned} \int_{\Omega^{\mathsf{F}}} \mathring{\boldsymbol{u}} \cdot \delta\boldsymbol{u} \, \mathrm{d}V + \int_{\Omega^{\mathsf{F}}} (\boldsymbol{c} \cdot \nabla \boldsymbol{u}) \cdot \delta\boldsymbol{u} \, \mathrm{d}V - \int_{\Omega^{\mathsf{F}}} \left(2\nu^{\mathsf{F}} \nabla \cdot \boldsymbol{\epsilon}(\boldsymbol{u})\right) \cdot \delta\boldsymbol{u} \, \mathrm{d}V + \int_{\Omega^{\mathsf{F}}} \nabla p \cdot \delta\boldsymbol{u} \, \mathrm{d}V +& \\ + \int_{\Omega^{\mathsf{F}}} (\nabla \cdot \boldsymbol{u}) \delta p \, \mathrm{d}V = \int_{\Omega^{\mathsf{F}}} \hat{\boldsymbol{b}}^{\mathsf{F}} \cdot \delta\boldsymbol{u} \, \mathrm{d}V.& \qquad (2.2.17) \end{aligned}$$

Integration by parts of the viscosity as well as pressure gradient terms and consideration of the symmetry of the strain rate tensor results in

$$\int_{\Omega^{\mathsf{F}}} \mathring{\boldsymbol{u}} \cdot \delta \boldsymbol{u} \,\mathsf{d}V + \int_{\Omega^{\mathsf{F}}} (\boldsymbol{c} \cdot \nabla \boldsymbol{u}) \cdot \delta \boldsymbol{u} \,\mathsf{d}V + \int_{\Omega^{\mathsf{F}}} 2\nu^{\mathsf{F}} \boldsymbol{\epsilon}(\boldsymbol{u}) : \boldsymbol{\epsilon}(\delta \boldsymbol{u}) \,\mathsf{d}V - \int_{\Omega^{\mathsf{F}}} p \nabla \cdot \delta \boldsymbol{u} \,\mathsf{d}V + \\ + \int_{\Omega^{\mathsf{F}}} (\nabla \cdot \boldsymbol{u}) \delta p \,\mathsf{d}V = \int_{\Omega^{\mathsf{F}}} \hat{\boldsymbol{b}}^{\mathsf{F}} \cdot \delta \boldsymbol{u} \,\mathsf{d}V + \int_{\partial \Omega^{\mathsf{F}}_{\mathsf{N}}} \hat{\boldsymbol{t}}^{\mathsf{F}} \cdot \delta \boldsymbol{u} \,\mathsf{d}A. \quad (2.2.18)$$

In contrast to the weak form of the solid mechanics problem (2.1.61), equation (2.2.18) does not correspond to a virtual work $\delta\mathcal{W}$ but can be interpreted as a virtual power expression $\delta\mathcal{P}$.

2.2.3 Space and time discretization

For discretization in space of equation (2.2.18), the FEM is utilized again. After mapping to the parameter space denoted by $\boldsymbol{\xi}$, the velocity and the pressure within each element (e) can be approximated by

$$\boldsymbol{u}^{(e)}(\boldsymbol{\xi},t) \approx \boldsymbol{u}^{h;(e)}(\boldsymbol{\xi},t) = \sum_{I=1}^{\mathsf{nnod}} N^{\mathsf{u}}_I(\boldsymbol{\xi}) \mathbf{u}_I(t) \quad (2.2.19)$$

$$p^{(e)}(\boldsymbol{\xi},t) \approx p^{h;(e)}(\boldsymbol{\xi},t) = \sum_{I=1}^{\mathsf{nnod}} N^{\mathsf{p}}_I(\boldsymbol{\xi}) \mathbf{p}_I(t) \quad (2.2.20)$$

with velocity and pressure shape functions N^{u} and N^{p}, respectively. The corresponding virtual counterparts are discretized analogously. In general, the polynomial orders of N^{u} and N^{p} cannot be chosen independently of each other. In order to prevent spurious pressure oscillations and guarantee optimal convergence, the so-called inf–sup or LBB condition has to be fulfilled (see e.g. Gresho and Sani (2000) for more details). To put it simply, this constraint means that the polynomial order of N^{p} has to be lower than the one of N^{u}. However, the LBB condition can be circumvented by introducing specific stabilization terms, thereby facilitating equal-order interpolation of pressure and velocity. Since this alternative is very convenient with regard to computational implementation, the equal order approach with $N^{\mathsf{u}} = N^{\mathsf{p}} = N$ is utilized exclusively in this work. Corresponding stabilization techniques will be addressed briefly in the following subsection.

Introduction of equations (2.2.19), (2.2.20), and their virtual counterparts into the weak form (2.2.18) results in the following semi-discrete system of equations

$$\begin{aligned} \left[\mathbf{M}^{\mathsf{F}}\left(\mathbf{d}^{\mathsf{A}}\right)\mathring{\mathbf{u}} + \mathbf{N}^{\mathsf{F}}\left(\mathbf{u},\mathbf{d}^{\mathsf{A}}\right)\mathbf{u} + \mathbf{G}^{\mathsf{F}}\left(\mathbf{d}^{\mathsf{A}}\right)\mathbf{p}\right]\delta\mathbf{u} &= \mathbf{f}^{\mathsf{F;ext}}\left(\mathbf{d}^{\mathsf{A}}\right)\delta\mathbf{u} && (2.2.21) \\ \left(\mathbf{G}^{\mathsf{F}}\left(\mathbf{d}^{\mathsf{A}}\right)\right)^{\mathsf{T}}\mathbf{u}\,\delta\mathbf{p} &= \mathbf{0} && (2.2.22) \end{aligned}$$

where $\mathbf{M}^{\mathsf{F}}$ is the fluid mass matrix, $\mathbf{N}^{\mathsf{F}}$ represents the linear viscous and nonlinear convective terms, $\mathbf{G}^{\mathsf{F}}$ refers to the discrete gradient operator, and $\mathbf{f}^{\mathsf{F}}_{\mathsf{ext}}$ constitutes the external forces. Since the Navier-Stokes equations have been formulated on a deforming domain

Ω^{F}, all terms depend on the mesh positions denoted by $\mathbf{d}^{\mathsf{A}}$. Equations (2.2.21) and (2.2.22) have to hold for arbitrary $\delta\mathbf{u}$ and $\delta\mathbf{p}$. Consequently, the semi-discrete forms of the linear momentum balance and the continuity equation are obtained as

$$\begin{aligned} \mathbf{M}^{\mathsf{F}}\left(\mathbf{d}^{\mathsf{A}}\right)\mathring{\mathbf{u}} + \mathbf{N}^{\mathsf{F}}\left(\mathbf{u},\mathbf{d}^{\mathsf{A}}\right)\mathbf{u} + \mathbf{G}^{\mathsf{F}}\left(\mathbf{d}^{\mathsf{A}}\right)\mathbf{p} &= \mathbf{f}^{\mathsf{F;ext}}\left(\mathbf{d}^{\mathsf{A}}\right) && (2.2.23)\\ \left(\mathbf{G}^{\mathsf{F}}\left(\mathbf{d}^{\mathsf{A}}\right)\right)^{\mathsf{T}}\mathbf{u} &= \mathbf{0}. && (2.2.24) \end{aligned}$$

The fluid acceleration $\mathring{\mathbf{u}}$ is approximated using the one-step-θ method, i.e.

$$\frac{\mathbf{u}_{n+1} - \mathbf{u}_n}{\Delta t} = \theta\,\mathring{\mathbf{u}}_{n+1} + (1-\theta)\,\mathring{\mathbf{u}}_n. \tag{2.2.25}$$

Within this work, θ is chosen to be 0.66. Insertion of relation (2.2.25) into (2.2.23) and multiplication with Δt yields

$$\begin{aligned} &\left[\mathbf{M}^{\mathsf{F}}\left(\mathbf{d}^{\mathsf{A}}_{n+1}\right) + \theta\Delta t\mathbf{N}^{\mathsf{F}}\left(\mathbf{u}_{n+1},\mathbf{d}^{\mathsf{A}}_{n+1}\right)\right]\mathbf{u}_{n+1} + \theta\Delta t\mathbf{G}^{\mathsf{F}}\left(\mathbf{d}^{\mathsf{A}}_{n+1}\right)\mathbf{p}_{n+1} = \\ &\qquad = \mathbf{M}^{\mathsf{F}}\left(\mathbf{d}^{\mathsf{A}}_{n+1}\right)\left[\mathbf{u}_n + (1-\theta)\Delta t\mathring{\mathbf{u}}_n\right] + \theta\Delta t\mathbf{f}^{\mathsf{F;ext}}\left(\mathbf{d}^{\mathsf{A}}_{n+1}\right). \end{aligned} \tag{2.2.26}$$

In above system of equations, a discrete representation of the mesh positions is assumed. More details on the corresponding time integration scheme will be provided in section Section 2.3.

Although equation (2.2.26) is still a nonlinear problem, the discrete form of the incompressible Navier-Stokes equations can be written for illustrative purposes in compact matrix format as

$$\begin{bmatrix} \mathbf{M}^{\mathsf{F}} + \theta\Delta t\mathbf{N}^{\mathsf{F}} & \theta\Delta t\mathbf{G}^{\mathsf{F}} \\ \left(\mathbf{G}^{\mathsf{F}}\right)^{\mathsf{T}} & \mathbf{0} \end{bmatrix}_{n+1} \begin{bmatrix} \mathbf{u} \\ \mathbf{p} \end{bmatrix}_{n+1} = \begin{bmatrix} \mathbf{M}^{\mathsf{F}}\left[\mathbf{u}_n + (1-\theta)\Delta t\mathring{\mathbf{u}}_n\right] + \theta\Delta t\mathbf{f}^{\mathsf{F;ext}}_{n+1} \\ \mathbf{0} \end{bmatrix}. \tag{2.2.27}$$

The continuity equation can be interpreted as a constraint enforced by the pressure. In section 2.5.1, a similar system of equations will be derived for general constrained problems in the context of the Lagrange multiplier method.

2.2.4 Stabilization

As already indicated in the previous section, the chosen equal-order interpolation of pressure and velocity violates the LBB condition. As a consequence, the system of equations becomes singular. Another source of instability is the insufficient resolution of boundary layers in case of convection-dominated flows. Spurious velocity oscillations emanating from the unresolved high gradients tend to spread over the entire domain, thereby globally disturbing the velocity solution. Thus, whenever flow problems with considerable convective transport are encountered and/or the LBB condition is violated, the FE formulation needs to be stabilized. For this purpose, additional terms weighted with problem-specific parameters are included in the discrete form of the incompressible Navier-Stokes equations. A detailed survey of different stabilization techniques and the choice of adequate stabilization parameters can be found e.g. in Wall (1999), Förster (2007), and Gamnitzer (2010).

Within this thesis, three different types of stabilization terms are utilized. To enable equal-order interpolation, the pressure stabilizing Petrov-Galerkin (PSPG) method (Hughes et al., 1986) is employed. This approach is based on the relaxation of the incompressibility constraint such that LBB incompatible spaces can be used. Convection stabilization is achieved by means of the streamline upwind Petrov-Galerkin (SUPG) approach (Brooks and Hughes, 1982). Practically, the SUPG term increases the fluid's viscosity in flow direction, thereby smoothing the velocity field and preventing spurious oscillations. Furthermore, an additional term for the stabilization of the continuity equation is introduced (Franca and Hughes, 1988). Inclusion of this bulk viscosity term is invariably advantageous in view of stability, particularly in case of higher Reynolds numbers (Wall, 1999).

2.2.5 Linearization

The residuals of the stabilized linear momentum balance (marked by index m) and continuity equation (labeled by c) are defined by

$$\begin{aligned}\mathbf{r}^{\mathsf{F;m}}_{\mathsf{stab}}\left(\mathbf{u}_{n+1},\mathbf{p}_{n+1},\mathbf{d}^{\mathsf{A}}_{n+1}\right) = {} & \left[\mathbf{M}^{\mathsf{F}}\left(\mathbf{d}^{\mathsf{A}}_{n+1}\right)+\theta\Delta t\mathbf{N}^{\mathsf{F}}\left(\mathbf{u}_{n+1},\mathbf{d}^{\mathsf{A}}_{n+1}\right)\right]\mathbf{u}_{n+1}+\theta\Delta t\mathbf{G}^{\mathsf{F}}\left(\mathbf{d}^{\mathsf{A}}_{n+1}\right)\mathbf{p}_{n+1}- \\ & -\mathbf{M}^{\mathsf{F}}\left(\mathbf{d}^{\mathsf{A}}_{n+1}\right)\left[\mathbf{u}_n+(1-\theta)\Delta t\mathring{\mathbf{u}}_n\right]-\theta\Delta t\mathbf{f}^{\mathsf{F;ext}}\left(\mathbf{d}^{\mathsf{A}}_{n+1}\right)+\mathscr{S}^{\mathsf{m}}\left(\mathbf{u}_{n+1},\mathbf{p}_{n+1},\mathbf{d}^{\mathsf{A}}_{n+1}\right)\overset{!}{=}\mathbf{0}\end{aligned} \tag{2.2.28}$$

$$\mathbf{r}^{\mathsf{F;c}}_{\mathsf{stab}}\left(\mathbf{u}_{n+1},\mathbf{p}_{n+1},\mathbf{d}^{\mathsf{A}}_{n+1}\right)=\left(\mathbf{G}^{\mathsf{F}}\left(\mathbf{d}^{\mathsf{A}}_{n+1}\right)\right)^{\mathsf{T}}\mathbf{u}_{n+1}+\mathscr{S}^{\mathsf{c}}\left(\mathbf{u}_{n+1},\mathbf{p}_{n+1},\mathbf{d}^{\mathsf{A}}_{n+1}\right)\overset{!}{=}\mathbf{0}. \tag{2.2.29}$$

In this context, $\mathscr{S}^{\mathsf{m}}$ and $\mathscr{S}^{\mathsf{c}}$ denote the additional stabilization terms. The nonlinearities present in equations (2.2.28) and (2.2.29) stem from the convective term in $\mathbf{N}^{\mathsf{F}}$, the stabilization terms, and the dependencies on the grid displacements. The unknown state $(\mathbf{u}_{n+1},\mathbf{p}_{n+1})$ at the end of the current time step is again determined iteratively by means of Newton's method. The corresponding linearized equations in a given iteration step i are given by

$$\left(\frac{\partial\mathbf{r}^{\mathsf{F;m}}_{\mathsf{stab}}}{\partial\mathbf{u}}\right)^i_{n+1}\Delta\mathbf{u}^{i+1}_{n+1}+\left(\frac{\partial\mathbf{r}^{\mathsf{F;m}}_{\mathsf{stab}}}{\partial\mathbf{p}}\right)^i_{n+1}\Delta\mathbf{p}^{i+1}_{n+1}+\left(\frac{\partial\mathbf{r}^{\mathsf{F;m}}_{\mathsf{stab}}}{\partial\mathbf{d}^{\mathsf{A}}}\right)^i_{n+1}\Delta\mathbf{d}^{\mathsf{A;i+1}}_{n+1}=-\left(\mathbf{r}^{\mathsf{F;m}}_{\mathsf{stab}}\right)^i_{n+1} \tag{2.2.30}$$

$$\left(\frac{\partial\mathbf{r}^{\mathsf{F;c}}_{\mathsf{stab}}}{\partial\mathbf{u}}\right)^i_{n+1}\Delta\mathbf{u}^{i+1}_{n+1}+\left(\frac{\partial\mathbf{r}^{\mathsf{F;c}}_{\mathsf{stab}}}{\partial\mathbf{p}}\right)^i_{n+1}\Delta\mathbf{p}^{i+1}_{n+1}+\left(\frac{\partial\mathbf{r}^{\mathsf{F;c}}_{\mathsf{stab}}}{\partial\mathbf{d}^{\mathsf{A}}}\right)^i_{n+1}\Delta\mathbf{d}^{\mathsf{A;i+1}}_{n+1}=-\left(\mathbf{r}^{\mathsf{F;c}}_{\mathsf{stab}}\right)^i_{n+1} \tag{2.2.31}$$

or, in compact matrix format,

$$\begin{bmatrix}\mathbf{K}^{\mathsf{F}}_{\mathsf{uu}} & \mathbf{K}^{\mathsf{F}}_{\mathsf{up}} & \mathbf{K}^{\mathsf{F}}_{\mathsf{ud^A}} \\ \mathbf{K}^{\mathsf{F}}_{\mathsf{pu}} & \mathbf{K}^{\mathsf{F}}_{\mathsf{pp}} & \mathbf{K}^{\mathsf{F}}_{\mathsf{pd^A}}\end{bmatrix}^i_{n+1}\begin{bmatrix}\Delta\mathbf{u} \\ \Delta\mathbf{p} \\ \Delta\mathbf{d}^{\mathsf{A}}\end{bmatrix}^{i+1}_{n+1}=-\begin{bmatrix}\mathbf{r}^{\mathsf{F;m}}_{\mathsf{stab}} \\ \mathbf{r}^{\mathsf{F;c}}_{\mathsf{stab}}\end{bmatrix}^i_{n+1}. \tag{2.2.32}$$

Detailed information on the involved linearizations can be found in Gamnitzer (2010).

In order to ease the notation introduced above (particularly in the context of fluid-structure interaction problems discussed in section 2.4), the momentum and continuity equations are henceforth not differentiated anymore. Likewise, velocity and pressure degrees of freedom (DOFs) are subsequently combined in the vector $\mathbf{u}$, thereby eliminating $\mathbf{p}$ as a separate vector of unknowns. Furthermore, the index stab can be dropped in the following due to the exclusive use of stabilized fluid formulations. The overall fluid problem is, thus, simply given by

$$\mathbf{K}^{\mathsf{F};i}\Delta\mathbf{u}_{n+1}^{i+1} = -\mathbf{r}^{\mathsf{F};i}. \tag{2.2.33}$$

The new solution guess can then be obtained as

$$\mathbf{u}_{n+1}^{i+1} = \mathbf{u}_{n+1}^{i} + \Delta\mathbf{u}_{n+1}^{i+1}. \tag{2.2.34}$$

The Newton loop is terminated, i.e. $\mathbf{u}_{n+1}^{i+1} = \mathbf{u}_{n+1}$, if user-defined convergence criteria for the residuals (2.2.28) and (2.2.29) are satisfied.

2.3 ALE mesh motion algorithm

The ALE formulation of the incompressible Navier-Stokes equations necessitates the definition of the mapping φ (2.2.1). In case of the fluid-structure interaction problems considered here, the boundary of the ALE mesh is coupled to the Lagrangian mesh of the flanking structures and an Eulerian mesh at the in- and outflow portions. Within the domain, the ALE mesh is in general allowed to deform arbitrarily, although a uniform distortion is commonly preferred. For the description of the domain mesh motion, different approaches have been developed. Within this work, the ALE field is treated as a linear pseudo-structure with pseudo-stiffness matrix $\mathbf{K}^{\mathsf{A}}$ (for details see e.g. Wall (1999)). Consequently, the following linear problem needs to be solved for $\mathsf{d}_{\mathsf{I}}^{\mathsf{A}}$

$$\mathbf{K}_{\mathsf{II}}^{\mathsf{A}}\mathsf{d}_{\mathsf{I}}^{\mathsf{A}} = -\mathbf{K}_{\mathsf{IB}}^{\mathsf{A}}\mathsf{d}_{\mathsf{B}}^{\mathsf{A}} \tag{2.3.1}$$

where the indices I and B mark the interior domain and the boundary, respectively. In general, subscripts indicate the respective dimensions of the involved submatrices of $\mathbf{K}^{\mathsf{A}}$. For example, the number of rows in $\mathbf{K}_{\mathsf{IB}}^{\mathsf{A}}$ equals the number of interior ALE DOFs whereas the number of columns corresponds to the number of boundary ALE DOFs. The known forces resulting from the prescribed boundary deformation were shifted to the right-hand side of the linear problem (2.3.1).

For the determination of the convective velocity $\mathbf{c}$, the ALE grid velocity $\mathbf{u}^{\mathsf{A}}$ needs to be determined. In this thesis, a one-step theta scheme is utilized for time integration of equation (2.2.3). Consequently, the resulting discrete mesh velocity is given by

$$\mathsf{u}_{n+1}^{\mathsf{A}} = \frac{\mathsf{d}_{n+1}^{\mathsf{A}} - \mathsf{d}_{n}^{\mathsf{A}}}{\theta\Delta t} - \frac{1-\theta}{\theta}\mathsf{u}_{n}^{\mathsf{A}}. \tag{2.3.2}$$

More details on requirements regarding the update of mesh positions and velocities are provided e.g. in Wall (1999) and Förster (2007).

2.4 Fluid-structure interaction

When simulating airflow in the deformable conducting passages, fluid-structure interaction (FSI) phenomena need to be considered. An extensive survey and comparison of related solution methods can be found in Küttler (2009). In summary, FSI approaches can be classified according to their specific coupling algorithms. The main representatives are the so-called partitioned and monolithic algorithms, although different intermediate methods also exist.

Partitioned FSI approaches are based on the staggered solution of the individual fields. Interaction effects are taken into account by means of a transfer of loads and boundary deformations between the independent field solvers. In this context, one way staggered and iterative staggered schemes can be distinguished. Utilization of the latter approach enables convergence of the field solutions to an equilibrium state. By contrast, the one way staggered scheme is based on one solution per field and time step only. Consequently, the FSI coupling conditions are usually not exactly satisfied in this case. Partitioned FSI approaches are very flexible with respect to the formulation and solution methods of the involved problems. Hence, existing field-specific software packages can be easily combined. Furthermore, the decomposition of the overall problem into smaller blocks comes along with reduced memory requirements, albeit at the expense of increased computing time. Details on the theoretical background, methodological aspects, and implementation of partitioned methods can be found e.g. in Wall (1999), Förster (2007), and Küttler (2009).

Monolithic FSI approaches are based on the solution of the fully coupled nonlinear FSI problem within one global Newton loop. Consequently, the individual field variables, i.e. fluid velocities, ALE mesh positions, and solid displacements, are determined simultaneously. In contrast to the partitioned schemes, monolithic methods inherently require the development of specific solution techniques since the application of field-specific "black-box" solvers is not possible. This implies a reduced flexibility of the monolithic schemes as compared with the partitioned ones. However, solver robustness and efficiency is in general improved considerably. In Küttler et al. (2010), monolithic approaches were found to be the best choice for complex biological problems involving the coupling of incompressible flows and soft tissue. Therefore, monolithic schemes are utilized exclusively in this thesis. Accordingly, the following considerations are restricted to this kind of coupling algorithm.

The overall residual of the monolithic FSI problem is given by

$$\mathbf{r}_{n+1}^{\mathsf{FSI}} = \mathbf{r}^{\mathsf{FSI}}\left(\mathbf{d}_{n+1}, \mathbf{u}_{n+1}, \mathbf{d}_{n+1}^{\mathsf{A}}\right) \overset{!}{=} \mathbf{0} \tag{2.4.1}$$

where $\mathbf{u}_{n+1}$ was introduced in section 2.2.5 as the discrete vector of fluid velocities and pressures. The contributions of the single field equations to $\mathbf{r}_{n+1}^{\mathsf{FSI}}$ were already derived in sections 2.1–2.3. In addition, two kinematic coupling conditions need to be satisfied at the FSI interface. In the following, the different meshes at the FSI interface are assumed to be conforming. In this case, solid and ALE meshes need to coincide at any time, i.e.

$$\mathbf{d}_{\mathsf{B};n+1} = \mathbf{d}^{\mathsf{A}}_{\mathsf{B};n+1}, \tag{2.4.2}$$

where the index B marks the interface. Furthermore, solid displacements and fluid velocities are coupled at the interface. Förster (2007) derived the following relation

$$\mathbf{u}_{\mathsf{B};n+1} = 2\frac{\mathbf{d}_{\mathsf{B};n+1} - \mathbf{d}_{\mathsf{B};n}}{\Delta t} - \mathbf{u}_{\mathsf{B};n}. \tag{2.4.3}$$

This trapezoidal rule for the interface velocity correctly preserves the size of the fluid domain and is exact for every fluid time integration scheme that assumes constant accelerations within the time step Δt. Rearrangement of equation (2.4.3) yields the subsequent expression for the increments of fluid velocities

$$\Delta\mathbf{u}_{\mathsf{B};n+1} = \underbrace{\frac{2}{\Delta t}}_{\tau} \Delta\mathbf{d}_{\mathsf{B};n+1} - 2\mathbf{u}_{\mathsf{B};n}. \tag{2.4.4}$$

Integration of the kinematic coupling conditions into the field equations allows for the statement of a global linearized FSI problem, i.e.

$$\begin{bmatrix} \mathbf{K}^{\mathsf{SS}}_{\mathsf{II}} & \mathbf{K}^{\mathsf{SS}}_{\mathsf{IB}} & \mathbf{0}^{\mathsf{SF}}_{\mathsf{II}} & \mathbf{0}^{\mathsf{SA}}_{\mathsf{II}} \\ \mathbf{K}^{\mathsf{SS}}_{\mathsf{BI}} & \mathbf{K}^{\mathsf{SS}}_{\mathsf{BB}} + \rho^{\mathsf{F}}\left(\tau\mathbf{K}^{\mathsf{FF}}_{\mathsf{BB}} + \mathbf{K}^{\mathsf{FA}}_{\mathsf{BB}}\right) & \rho^{\mathsf{F}}\mathbf{K}^{\mathsf{FF}}_{\mathsf{BI}} & \rho^{\mathsf{F}}\mathbf{K}^{\mathsf{FA}}_{\mathsf{BI}} \\ \mathbf{0}^{\mathsf{FS}}_{\mathsf{II}} & \tau\mathbf{K}^{\mathsf{FF}}_{\mathsf{IB}} + \mathbf{K}^{\mathsf{FA}}_{\mathsf{IB}} & \mathbf{K}^{\mathsf{FF}}_{\mathsf{II}} & \mathbf{K}^{\mathsf{FA}}_{\mathsf{II}} \\ \mathbf{0}^{\mathsf{AS}}_{\mathsf{II}} & \mathbf{K}^{\mathsf{AS}}_{\mathsf{IB}} & \mathbf{0}^{\mathsf{AF}}_{\mathsf{II}} & \mathbf{K}^{\mathsf{AA}}_{\mathsf{II}} \end{bmatrix}^{i}_{n+1} \begin{bmatrix} \Delta\mathbf{d}_{\mathsf{I}} \\ \Delta\mathbf{d}_{\mathsf{B}} \\ \Delta\mathbf{u}_{\mathsf{I}} \\ \Delta\mathbf{d}^{\mathsf{A}}_{\mathsf{I}} \end{bmatrix}^{i+1}_{n+1} = - \begin{bmatrix} \mathbf{r}^{\mathsf{S}}_{\mathsf{I}} \\ \mathbf{r}^{\mathsf{S}}_{\mathsf{B}} + \rho^{\mathsf{F}}\mathbf{r}^{\mathsf{F}}_{\mathsf{B}} \\ \mathbf{r}^{\mathsf{F}}_{\mathsf{I}} \\ \mathbf{r}^{\mathsf{A}}_{\mathsf{I}} \end{bmatrix}^{i}_{n+1}. \tag{2.4.5}$$

For the sake of clarity, contributions of solid and fluid fields are highlighted in pink and blue, respectively. As a consequence, the “overlap” of the distinct field equations at the interface can be easily identified. The dimensions of the involved submatrices are characterized by means of subscripts in combination with superscripts. This notation can be illustrated using the example of $\mathbf{K}^{\mathsf{FA}}_{\mathsf{II}}$ which results from the linearization of the incompressible Navier-Stokes equations with respect to the mesh positions. The number of rows in $\mathbf{K}^{\mathsf{FA}}_{\mathsf{II}}$ corresponds to the number of “interior” fluid DOFs whereas the number of columns is equivalent to the number of “interior” ALE DOFs. In this context, the “interior” DOFs comprise all DOFs not situated along the FSI interface. Hence, fluid in- and outflow boundaries are, for example, also part of this subset. To simplify matters, the subscript effdyn employed usually to identify the effective dynamic residual or stiffness matrix in solid mechanics is abandoned here.

When combining fluid and solid contributions at the FSI interface, the scaling of the fluid residual with $\frac{1}{\rho^{\mathsf{F}}}$ (cf. equations (2.2.11) and (2.2.12)) needs to be taken into account. Furthermore, the factor τ introduced in equation (2.4.4) for the transformation of interface velocity increments into displacement increments needs to be included. In the first Newton step, the dependency of $\Delta\mathbf{u}_{\mathsf{B};n+1}$ on the absolute velocity of the old time step $\mathbf{u}_{\mathsf{B};n}$ also needs to be considered, i.e.

$$\left(\mathbf{r}^{\mathsf{FSI}}\right)^0_{n+1} = \begin{bmatrix} \mathbf{r}^{\mathsf{S}}_{\mathsf{I}} \\ \mathbf{r}^{\mathsf{S}}_{\mathsf{B}} + \rho^{\mathsf{F}}\mathbf{r}^{\mathsf{F}}_{\mathsf{B}} \\ \mathbf{r}^{\mathsf{F}}_{\mathsf{I}} \\ \mathbf{r}^{\mathsf{A}}_{\mathsf{I}} \end{bmatrix}^0_{n+1} - 2 \begin{bmatrix} \mathbf{0} \\ \rho^{\mathsf{F}}\left(\mathbf{K}^{\mathsf{FF}}_{\mathsf{BB}}\right)^0_{n+1}\mathbf{u}_{\mathsf{B};n} \\ \left(\mathbf{K}^{\mathsf{FF}}_{\mathsf{IB}}\right)^0_{n+1}\mathbf{u}_{\mathsf{B};n} \\ \mathbf{0} \end{bmatrix}. \tag{2.4.6}$$

For $i \neq 0$, the global linearized FSI problem (2.4.5) can be written in a more compact form as

$$\begin{bmatrix} \mathbf{K}^{\mathsf{SS}}_{\mathsf{II}} & \mathbf{K}^{\mathsf{SS}}_{\mathsf{IB}} & \mathbf{0}^{\mathsf{SF}}_{\mathsf{II}} & \mathbf{0}^{\mathsf{SA}}_{\mathsf{II}} \\ \mathbf{K}^{\mathsf{SS}}_{\mathsf{BI}} & \mathbf{K}^{\mathsf{SS}}_{\mathsf{BB}} + \underset{\sim}{\underline{\mathbf{K}}}^{\mathsf{FF}}_{\mathsf{BB}} + \underline{\mathbf{K}}^{\mathsf{FA}}_{\mathsf{BB}} & \underline{\mathbf{K}}^{\mathsf{FF}}_{\mathsf{BI}} & \underline{\mathbf{K}}^{\mathsf{FA}}_{\mathsf{BI}} \\ \mathbf{0}^{\mathsf{FS}}_{\mathsf{II}} & \underset{\sim}{\mathbf{K}}^{\mathsf{FF}}_{\mathsf{IB}} + \mathbf{K}^{\mathsf{FA}}_{\mathsf{IB}} & \mathbf{K}^{\mathsf{FF}}_{\mathsf{II}} & \mathbf{K}^{\mathsf{FA}}_{\mathsf{II}} \\ \mathbf{0}^{\mathsf{AS}}_{\mathsf{II}} & \mathbf{K}^{\mathsf{AS}}_{\mathsf{IB}} & \mathbf{0}^{\mathsf{AF}}_{\mathsf{II}} & \mathbf{K}^{\mathsf{AA}}_{\mathsf{II}} \end{bmatrix}^i_{n+1} \begin{bmatrix} \Delta\mathbf{d}_{\mathsf{I}} \\ \Delta\mathbf{d}_{\mathsf{B}} \\ \Delta\mathbf{u}_{\mathsf{I}} \\ \Delta\mathbf{d}^{\mathsf{A}}_{\mathsf{I}} \end{bmatrix}^{i+1}_{n+1} = - \begin{bmatrix} \mathbf{r}^{\mathsf{S}}_{\mathsf{I}} \\ \mathbf{r}^{\mathsf{S}}_{\mathsf{B}} + \underline{\mathbf{r}}^{\mathsf{F}}_{\mathsf{B}} \\ \mathbf{r}^{\mathsf{F}}_{\mathsf{I}} \\ \mathbf{r}^{\mathsf{A}}_{\mathsf{I}} \end{bmatrix}^i_{n+1} \tag{2.4.7}$$

where the following abbreviations are utilized for different scalings of arbitrary vectors or matrices **#**

$$\underline{\#} = \rho^{\mathsf{F}}\# \qquad \underset{\sim}{\#} = \tau\# \qquad \underset{\sim}{\underline{\#}} = \rho^{\mathsf{F}}\tau\#. \tag{2.4.8}$$

The kinematic coupling condition (2.4.4) can of course also be reformulated such that the interface velocities are retained in the overall system, whereas the interface displacements are converted. Both alternatives are in general equivalent but may exhibit different numerical behavior. In case of non-conforming meshes at the interface, the coupling conditions need to be properly adapted (cf. e.g. Klöppel et al. (2011) for a dual mortar formulation).

Details on the solution of the linear system (2.4.7) are given in Küttler (2009) and can also be found in section 5.3 where specific procedures suitable for FSI problems subject to constraints will be derived.

2.5 Constrained problems

In the following, two different methods of constraint enforcement utilized for the formulation of (nearly) incompressible materials as well as the coupling of airway and parenchyma models will be briefly discussed. The presented approaches are well-known e.g. from optimization or contact problems. Accordingly, further details can be found in standard textbooks, see e.g. Strang (1986), Hughes (2000), and Luenberger (2003).

To simplify matters, subsequent derivations are based on a conservative solid problem. In this case, a stable equilibrium solution is found by minimizing an underlying potential $\mathcal{W}$.

The constrained problem can then be formulated as

$$\min \mathcal{W}(\boldsymbol{d}) \text{ subject to } C(\boldsymbol{d}) = 0 \tag{2.5.1}$$

where $C(\boldsymbol{d}) = 0$ is the constraint on the system.

2.5.1 Lagrange multiplier method

In this most classical approach, an additional unknown variable – the Lagrange multiplier λ – is introduced. The modified potential $\mathcal{W}^{\mathsf{LM}}$ is then given by the sum of the objective function $\mathcal{W}$ and the constraint equation C weighted by the Lagrange multiplier λ:

$$\mathcal{W}^{\mathsf{LM}}(\mathbf{d},\lambda) = \mathcal{W}(\mathbf{d}) + \lambda C(\mathbf{d}) \tag{2.5.2}$$

The total variation of the overall potential (2.5.2) reads

$$\begin{aligned} \delta\mathcal{W}^{\mathsf{LM}}(\mathbf{d},\lambda) &= \delta\mathcal{W}(\mathbf{d}) + \delta(\lambda C(\mathbf{d})) = \\ &= \left(\frac{\partial\mathcal{W}(\mathbf{d})}{\partial\mathbf{d}} + \lambda\frac{\partial C(\mathbf{d})}{\partial\mathbf{d}}\right)\delta\mathbf{d} + C(\mathbf{d})\delta\lambda. \end{aligned} \tag{2.5.3}$$

Since both the displacements $\mathbf{d}$ and the Lagrange multiplier λ represent primary unknowns, equation (2.5.3) corresponds to a mixed variational formulation. The solution of this saddle point problem is on the one hand a minimum of $\mathcal{W}^{\mathsf{LM}}$ with respect to the displacements $\mathbf{d}$ and on the other hand a maximum of $\mathcal{W}^{\mathsf{LM}}$ with respect to the Lagrange multiplier λ (Strang, 1986). The corresponding linearized problem can be stated as follows

$$\begin{bmatrix} \mathbf{K}^{\mathsf{LM}} & \mathbf{B}^{\mathsf{T}} \\ \mathbf{B} & \mathbf{0} \end{bmatrix} \begin{bmatrix} \Delta\mathbf{d} \\ \Delta\lambda \end{bmatrix} = -\begin{bmatrix} \mathbf{r}_{\mathsf{d}}^{\mathsf{LM}} \\ \mathbf{r}_{\lambda}^{\mathsf{LM}} \end{bmatrix} \tag{2.5.4}$$

with

$$\mathbf{r}_{\mathsf{d}}^{\mathsf{LM}} = \frac{\partial\mathcal{W}(\mathbf{d})}{\partial\mathbf{d}} + \lambda\frac{\partial C(\mathbf{d})}{\partial\mathbf{d}}, \tag{2.5.5}$$

$$\mathbf{r}_{\lambda}^{\mathsf{LM}} = C(\mathbf{d}), \tag{2.5.6}$$

$$\mathbf{K}^{\mathsf{LM}} = \frac{\partial}{\partial\mathbf{d}}\left(\frac{\partial(\mathcal{W}(\mathbf{d}) + \lambda C(\mathbf{d}))}{\partial\mathbf{d}}\right), \tag{2.5.7}$$

and

$$\mathbf{B} = \frac{\partial C(\mathbf{d})}{\partial\mathbf{d}}. \tag{2.5.8}$$

The main advantage of the Lagrange multiplier method is that it allows for the exact satisfaction of the imposed constraint. In return, an additional unknown, i.e. the Lagrange multiplier, has to be introduced into the global system. Furthermore, the system matrix of the linearized problem (2.5.4) is not positive-definite because of the zeroes on the diagonal. Solving saddle point problems iteratively therefore poses some numerical difficulties. This subject will be addressed in more detail in section 5.3.

2.5.2 Penalty method

The second approach is based on enforcing the constraint by means of a penalty term. In this case, the modified potential $\mathcal{W}^{\mathsf{P}}$ is given by

$$\mathcal{W}^{\mathsf{P}}(\mathbf{d}) = \mathcal{W}(\mathbf{d}) + \frac{1}{2}\epsilon\left(C(\mathbf{d})\right)^2 \tag{2.5.9}$$

Here, ϵ is no additional unknown but an unphysical parameter penalizing a violation of $C(\mathbf{d}) = 0$. The total variation of the overall potential (2.5.9) is determined by

$$\begin{aligned} \delta\mathcal{W}^{\mathsf{P}} &= \delta\mathcal{W}(\mathbf{d}) + \epsilon C(\mathbf{d})\,\delta C(\mathbf{d}) = \\ &= \left(\frac{\partial\mathcal{W}(\mathbf{d})}{\partial\mathbf{d}} + \epsilon C(\mathbf{d})\frac{\partial C(\mathbf{d})}{\partial\mathbf{d}}\right)\delta\mathbf{d}. \end{aligned} \tag{2.5.10}$$

The corresponding linearized problem simply reads

$$\mathbf{K}^{\mathsf{P}}\Delta\mathbf{d} = -\mathbf{r}_{\mathsf{d}}^{\mathsf{P}} \tag{2.5.11}$$

with

$$\mathbf{r}_{\mathsf{d}}^{\mathsf{P}} = \frac{\partial\mathcal{W}(\mathbf{d})}{\partial\mathbf{d}} + \epsilon C(\mathbf{d})\frac{\partial C(\mathbf{d})}{\partial\mathbf{d}} \tag{2.5.12}$$

and

$$\mathbf{K}^{\mathsf{P}} = \frac{\partial}{\partial\mathbf{d}}\left(\frac{\partial\mathcal{W}(\mathbf{d})}{\partial\mathbf{d}}\right) + \epsilon C(\mathbf{d})\frac{\partial}{\partial\mathbf{d}}\left(\frac{\partial C(\mathbf{d})}{\partial\mathbf{d}}\right) + \epsilon\frac{\partial C(\mathbf{d})}{\partial\mathbf{d}}\left(\frac{\partial C(\mathbf{d})}{\partial\mathbf{d}}\right)^{\mathsf{T}}. \tag{2.5.13}$$

It can be shown that for $\epsilon \to \infty$, the solution of the Lagrange multiplier approach is recovered. However, a large number for ϵ leads to an ill-conditioned numerical problem. In general, the choice of the penalty parameter is problem-specific and somewhat arbitrary. At the end of the day, an adequate trade-off between accuracy and stability needs to be found.

A major advantage of the penalty method over the Lagrange multiplier approach is the fact that no additional unknowns enter the global system (2.5.10). Given that the original Jacobian is positive-definite – as is the case for the conservative problem assumed here –, then the augmented system is also positive-definite. Due to its easy implementation, the penalty method is widely used, e.g. in the context of elasticity, where the incompressible case is approximated by employing a slightly compressible formulation.

After having surveyed relevant governing equations and general FE formulations, the computational models developed specifically for the investigation of respiratory mechanics will be presented in the following chapters.

3 Alveolar Model

"Make things as simple as possible – but not simpler." (Albert Einstein)

A consistent feature of all mechanisms of VALI identified so far is that the injury manifests itself at the alveolar level. Thus, improving ventilation strategies in order to prevent VALI requires a detailed knowledge of alveolar mechanics. However, as already mentioned in the introductory chapter, experimental investigations in literature come up with conflicting results. Again, this may be attributed to different preparation and imaging techniques. In order to gain more insights into involved phenomena, a three-dimensional computational model considering the geometrical and mechanical properties of alveoli was developed as part of this thesis. Subsequently, a brief overview of existing alveolar models, their particular fields of application, and limitations will be given. More details on individual aspects will be provided in the respective sections of this chapter.

Perhaps one of the most frequently repeated figures in discussions of alveolar mechanics is the Y-tube with two unequal bubbles attached. This model is utilized in many textbooks to claim that, without intervention, a small alveolus ought to collapse into its larger neighbor. This phenomenon is attributed to the Laplace-Young law stating that the pressure inside a body with curved surface is inversely proportional to the radius given that the surface stress is constant. The effect of the surfactant lining is then assumed to alter the surface stresses of alveoli of different radii such that Laplace's law is exactly counteracted at any volume. Prange (2003) elegantly demonstrated, though, that the application of Laplace's law to individual alveoli is a misconception of anatomy and a misapplication of physics. Not only are alveoli rather polygonal in shape, they also share common walls with interalveolar pores. Consequently, transalveolar pressure differences are very unlikely to develop. The fact that the "collapsing bubble" model is still in the minds of some physicians is probably due to the insufficient cross linking of medical and engineering sciences.

In fact, the modeling of alveolar mechanics has made substantial progress over the last decades. Mead et al. (1970), for instance, established a relationship between transpulmonary pressure and the stresses distending individual regions of the lung. Despite a number of simplifying assumptions, their general findings concerning interdependence effects and lung stability were pioneering. Unfortunately, however, the most frequently cited aspect of their work is a simplistic sample calculation concerning the pressure required to expand an atelectatic region. Although the limitations of this particular analysis were already pointed out in the original paper, the estimated opening pressure is now widely established in the medical community.

More recent approaches to investigating the mechanical properties of alveoli were based on the application of the FEM. Dale et al. (1980) and Kowe et al. (1986), for instance, compared simulated alveolar pressure-volume characteristics with curves determined experimentally for the lung as a whole. Kimmel and Budiansky (1990) calculated macroscopic elastic moduli of lung parenchyma based on a simple model of an isolated alveolus. A survey of these early approaches can be found e.g. in Stamenovic (1990). A more advanced FE model was proposed by Gefen et al. (1999) who analyzed the distribution of stresses within individual alveolar septa of normal and simulated diseased lungs. The most comprehensive alveolar model so far has been established by Denny and Schroter in a series of publications (Denny and Schroter, 1995, 1997, 2000, 2006). Although they did not claim their model to be a precise representation of the micro-mechanics of actual lung parenchyma, it exhibited a sufficient level of realism to draw meaningful general conclusions under a range of conditions. Hence, the influence of various parameters on alveolar duct recoil could be investigated. In this context, dynamic effects and non-uniform parenchyma distortion were also considered. The focus of these studies, though, was on the macroscopic behavior of the alveolar duct model and no statements regarding local stresses and strains in alveolar septa could be made.

Depending on the particular objective of the studies mentioned above, different geometric representations of alveoli and alveolar ducts were employed. Furthermore, distinct aspects of alveolar mechanics were included in the models. In general, it is not only necessary to investigate soft tissue characteristics but also the influence of the surfactant film on the overall behavior, both as a direct component of lung recoil and through distortion of alveolar geometry. Previous alveolar models, however, usually focused on only one of these two aspects. Dale et al. (1980), for example, modeled an alveolus as a network of fibers without considering either the effect of interfacial phenomena or an underlying ground substance. Some subsequent approaches based on the work of Kowe et al. (1986) retained the idea of reducing alveolar soft tissue to a network of fibers while additionally considering surface tension effects. Partly, also dynamic surfactant models were employed in this context, e.g. in Denny and Schroter (2000) and Denny and Schroter (2006). Other attempts concentrated on the modeling of continuum tissue mechanics whereas interfacial phenomena were treated in a simplified manner (Karakaplan et al., 1980) or even totally neglected (Gefen et al., 1999, 2001). Contrary to the afore mentioned approaches, the alveolar model developed as part of this thesis (cf. Wiechert et al. (2009)) combines a detailed constitutive law for alveolar soft tissue with an elaborate dynamic surfactant model. In particular, the interaction of tissue and interfacial forces is taken into account.

The remainder of this chapter is organized as follows. First, the generation of alveolar geometries applicable to computational simulations will be addressed. Subsequently, a continuum constitutive model previously developed for arteries will be adopted for alveolar tissue. After a general discussion of interfacial phenomena, the chapter will close with the presentation of a novel approach to considering surfactant film dynamics in the computational model.

3.1 Artificial Morphology

Realistic representations of alveoli are important if dependable statements regarding local stresses and strains are required. Obtaining the necessary geometric information, however, still remains a very challenging task. Subsequently, different approaches to investigating alveolar morphology will be briefly discussed.

Previously, casting techniques were utilized to gain knowledge about the general structure of the acinus (see e.g. Hansen and Ampaya (1975), Schreider and Raabe (1981), and Haefeli-Bleuer and Weibel (1988)). However, geometries suitable for computational simulations could not be obtained by this means.

More recently, different microscopy techniques were utilized to characterize the organization of alveolar tissue. Brewer et al. (2003) and Cavalcante et al. (2005), for example, employed fluorescent microscopy for visualization of alveoli in isolated tissue strips. Perlman and Bhattacharya (2007) applied real-time confocal microscopy to isolated, perfused rat lungs in order to view single alveoli in a 2 µm-thick optical section below the pleural surface. Carney et al. (2005) and Dirocco et al. (2006) performed in vivo videomicroscopy to obtain photomicrographs of the outer face of subpleural alveoli. A further development of this technique was reported by Stahl et al. (2006) who developed a novel endoscopic device to enable measurement and control of the pressure applied to the pleural surface under view.

A major drawback of all microscopy approaches, however, is the inherent restriction to two-dimensional views. Although attempts to reconstruct alveoli based on photographs of different sections were reported (cf. e.g. Mercer et al. (1987), Mercer and Crapo (1987), and Berend et al. (1991)), these procedures are unlikely to provide an adequate basis for detailed FE modeling. The first suitable three-dimensional dataset for human alveoli was obtained by Watz et al. (2005). They excised, fixated, and stained specimens from different regions of autopsy lungs before imaging with μ-CT. Recently, Popp et al. (2006) performed real-time three-dimensional imaging of isolated, perfused, and ventilated rabbit lungs by means of optical coherence tomography.

All approaches mentioned so far served to either characterize alveolar tissue with regard to morphological and mechanical properties or investigate specific medical problems. However, the data obtained in these studies have not been used for computational simulations. The first realistic FE models were proposed by Gefen et al. (1999) who digitized a scanning electron micrograph of mouse lung parenchyma to yield a geometric replica of a typical two-dimensional alveolar sac. Local strain distributions in realistic three-dimensional rat alveoli were investigated for the first time by Rausch et al. (2011a). The underlying acinar geometry was obtained by means of a synchrotron-based X-ray tomographic microscopy technique described in detail in Schittny et al. (2008).

In the long term, utilization of imaging-based alveolar geometries is definitely desirable. So far, however, realistic representations are only available for excised small animal lungs. Therefore, finding ways to create artificial acinar geometries, particularly for the human lung, still seems to be worthwhile. Apart from providing flexibility with respect to the modeled species, artificial representations usually have the advantage of being easy to handle, e.g. concerning FE meshing. However, it has to be assured that the simplification of the complex, irregular geometric features is justifiable. Thus, in the future, the simpler artificial models need to be validated by comparing with the results obtained from realistic (i.e. imaging-based) geometries.

In the past, various approaches to generating artificial acinar representations were developed. To study screening phenomena, i.e. the effectivity of diffusion in the acinus, Sapoval et al. (2002) introduced a simplified two-dimensional model based on the space-filling Hilbert curve. Kitaoka et al. (2000) proposed an acinar model based on an assemblage of cubic cells representing alveolar ducts and alveoli. Connections between different cells were established by means of a labyrinthine algorithm ensuring minimum path lengths within the assemblage. Felici et al. (2003) utilized this set-up to investigate above mentioned screening phenomena in a more realistic geometry. Although models based on the labyrinthine algorithm were shown to be in good agreement with published morphological data, acinar geometries were locally fairly unrealistic. Especially if the mechanical behavior of pulmonary alveoli is to be investigated, this is a very significant drawback. A more authentic shape for alveolar ducts based on a quadrangular prism was proposed by Kitaoka et al. (2007). Each square was divided into four parts which were shifted alternatively inside and outside. Secondary septa were attached at the edges of the deformed parts, so that overall eight alveoli were generated within one duct. By combining several alveolar ducts by means of the labyrinthine algorithm, a spring-hinge parenchyma model was developed and employed in simplified simulations of alveolar dynamics.

Other frequently used shapes for alveolar ducts and alveoli are different polyhedra. Frankus and Lee (1974) and Kimmel and Budiansky (1990), for instance, proposed utilization of the dodecahedron since the angle between any two intersecting planes is close to the reported angle of 120° between alveolar walls. However, when assembled into a cluster of many units, the dodecahedron is not space-filling, i.e. the formation of alveolar ducts and acinar structures without leaving any voids is not possible. Therefore, the so-called tetrakaidecahedron seems to be a more appropriate choice for approximating alveolar structures. This space-filling 14-sided Archimedean polyhedron is constructed from a regular octahedron by removal of six right square pyramids, one from each point (see Figure 3.1.1). The resulting tetrakaidecahedron has 8 regular hexagonal faces, 6 square faces, 24 vertices, and 36 edges. Remarkably, most common shapes of alveoli found in photographs of parenchymal micro-structures are of hexagonal and rectangular type (Fung, 1988). Among all space-filling polyhedra of the same volume, the 14-hedron has the minimum surface-to-volume ratio, which is an important factor in the stability of alveoli under the action of surface tension (Fung, 1975). It has to be noted, though, that the tetrakaidecahedron has three orthogonal planes of symmetry in its undistorted state. Hence, the truncated octahedron is in general not structurally isotropic. However, Denny and Schroter (2006) demonstrated that corresponding alveolar models have very similar elastic properties when distorted in different directions.

Tetrakaidecahedra were widely used as a geometric description for pulmonary alveoli and alveolar ducts in the literature. However, usually only geometries based on single alveoli as in Dale et al. (1980) and Kowe et al. (1986) or simple assemblages of alveoli were employed, cf. e.g. Denny and Schroter (1995), Denny and Schroter (1997), Denny and

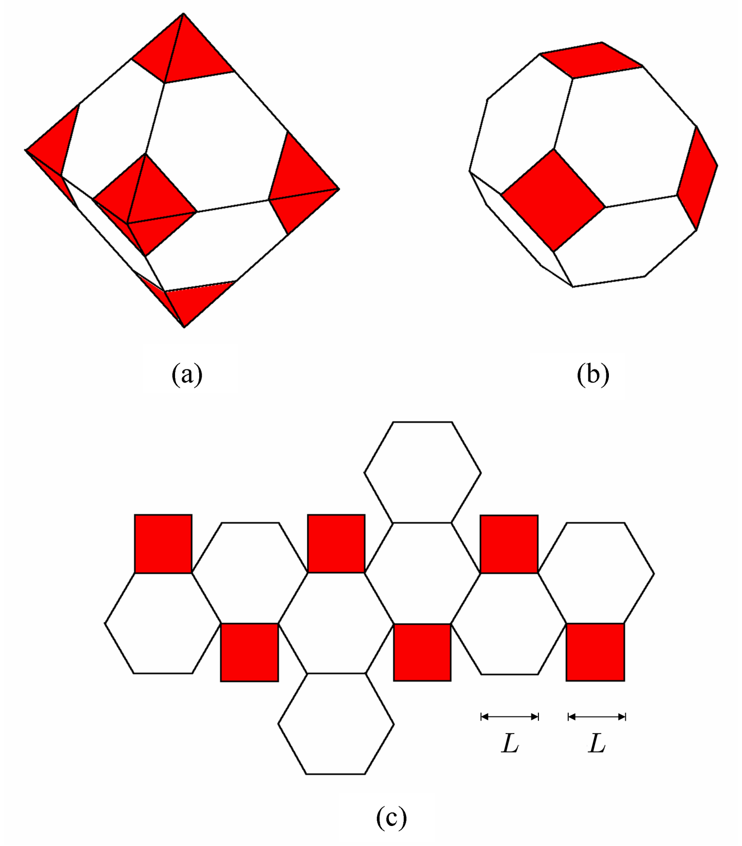

Figure 3.1.1: Tetrakaidecahedral geometry. (a) Construction by truncation of regular octahedron. (b) Three-dimensional view of tetrakaidecahedron. (c) Introduction of characteristic length L in developed view of tetrakaidecahedron.

Schroter (2000), and Denny and Schroter (2006). In the latter case, fixed arrangements of single cells opened to a straight conducting unit were utilized. A more elaborate approach to forming acinar structures based on tetrakaidecahedral alveoli was proposed by Fung (1988) and utilized by Sznitman and Heimsch (2009) to investigate respiratory flow phenomena and gravitational deposition. The basic unit of Fung's artificial acinus was a single tetrakaidecahedron which was referred to as an order-1 polyhedron. By connecting a central order-1 polyhedron with 14 identical surrounding tetrakaidecahedra, a so-called order-2 polyhedron was formed. Alveolar ducts were then constructed by connecting several order-2 polyhedra with each other or with respiratory bronchioles. Since order-2 polyhedra are not exactly space-filling, some isolated order-1 polyhedra had to be specifically connected to the ductal structure. Despite the good correlation with available morphometric data, therefore, the generation of acinar structures appeared somehow arbitrary. A different approach to creating artificial alveolar geometries was suggested by Burrowes (2005). Although the employed Voronoi meshing technique sounds promising in general, the underlying procedure was not explained satisfyingly and, thus, the generation process again seemed rather discretionary.

To overcome the shortcomings of previous approaches, an alternative method for generating artificial acinar representations has been developed as part of this work (cf. also Wall et al. (2010b)). Briefly, the labyrinthine algorithm introduced by Kitaoka et al. (2000) for cubic cells has been extended to tetrakaidecahedral geometries. In the following, the labyrinthine algorithm will be briefly summarized. It will be shown that a simple modification of the connection rules to account for the geometric characteristics of tetrakaidecahedra is not sufficient to ensure minimal path lengths within the acinus. For that purpose, a new approach to formulating optimal interalveolar connections will be proposed. After an illustration of the versatility of the developed procedure, a comparison of an artificial acinar model with silicone rubber casts of human lungs will be drawn.

3.1.1 Original labyrinthine algorithm

In general, a labyrinthine algorithm enables the creation of a network of interconnected cells. Point of origin is an a priori defined assemblage of identical initially closed cells. By successively opening faces, connections of all cells to a given starting cell are established. Assuming that the design of peripheral airspaces is guided by effective gas transport, the generated paths should have minimal length. Hence, certain connection rules are introduced to ensure that detours are precluded and each cell is passed only once except at branching points. Thereby, optimality of paths through the assemblage is already guaranteed after the first passage of all cells. By contrast, alternative approaches are usually based on the incremental optimization of a given random configuration (cf. e.g. Denny and Schroter (1996) for a corresponding annealing algorithm).

In the following, the general procedure of the labyrinthine algorithm introduced by Kitaoka et al. (2000) will be shortly summarized by means of a simple example (see Figure 3.1.2). If a cell is affiliated in the course of the labyrinth creation, it is stored in a queue. In every step, the first cell in the queue can actively create a path to one of its neighbors that are not already passed. Thereby, directions pointing from the starting cell to the center of the assemblage are pioritized. If there are several priority cells, one of them can be chosen randomly. If, otherwise, priority directions are lacking, then a cell is selected randomly from non-priority directions. After having established the connection, the active cell and the newly affiliated cell are moved to the end of the queue. However, if the active cell has no other unpassed admissible neighbors, it is deleted from the queue. This procedure is repeated until the queue is worn out.

For square and cubic base cells, the concept of priority directions effectively ensures optimal path lengths in the created artificial acinus. In case of tetrakaidecahedral base cells, however, the labyrinthine algorithm needs to be appropriately adapted to account for the more complicated geometry.

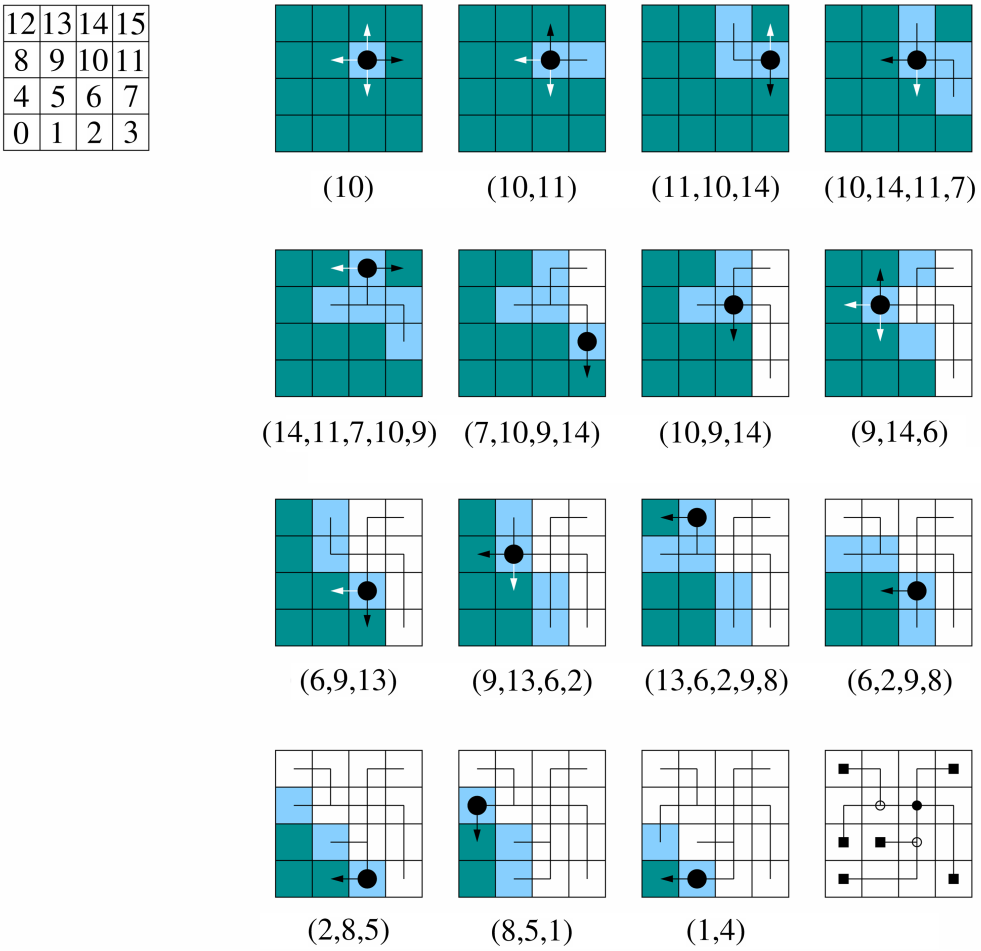

12	13	14	15
8	9	10	11
4	5	6	7
0	1	2	3

(10) (10,11) (11,10,14) (10,14,11,7)

(14,11,7,10,9) (7,10,9,14) (10,9,14) (9,14,6)

(6,9,13) (9,13,6,2) (13,6,2,9,8) (6,2,9,8)

(2,8,5) (8,5,1) (1,4)

Figure 3.1.2: Example of a simple two-dimensional labyrinth with quadratic base cells numbered as shown on the left-hand side. Cyan cells are not yet passed, light blue cells are members of the queue and white cells are already affiliated but have no admissible neighbors and are therefore deleted from the queue. Black arrows show chosen directions whereas white arrows indicate possible other connections. Queue vectors for the corresponding steps are given below the individual figures. The symbols •, ○, and ▪ in the final labyrinth denote starting cell, branching, and dead end cells, respectively.

3.1.2 Extension to truncated octahedra

Basic notation

Before extending the original labyrinthine algorithm to tetrakaidecahedral cells, some basic notations have to be introduced. To simplify the search of neighbor cells, utilization of cell center coordinates is beneficial. However, since the coordinate system only serves for a characterization of cells in the process of pathway generation, it does not have to

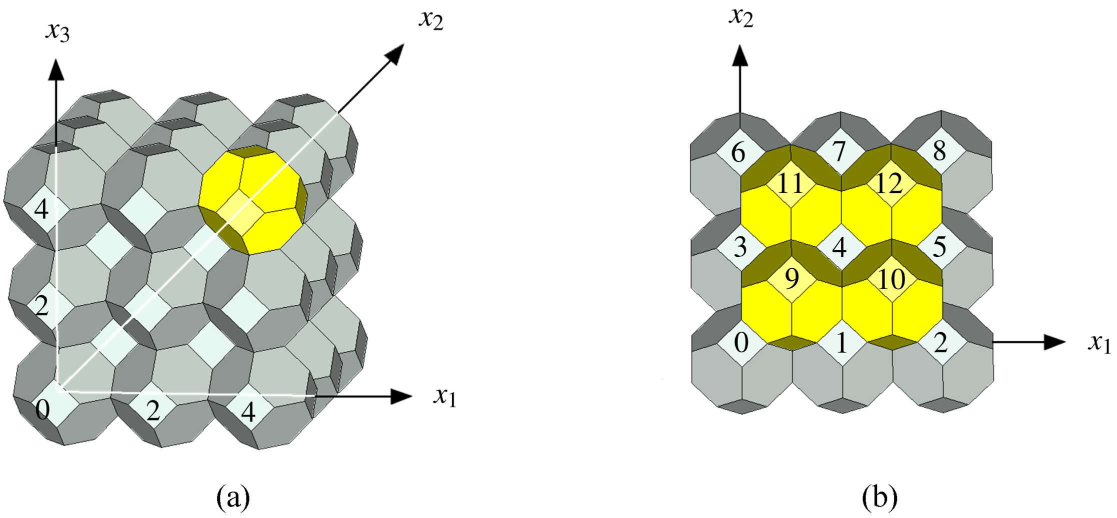

(a) (b)

Figure 3.1.3: (a) Definition of coordinate system employed for later labyrinth generation. (b) Illustration of cell numbering for one main (marked in gray) and one ancillary (marked in yellow) plane of the assemblage shown in (a).

reflect realistic physical dimensions. Hence, for simplicity, it is defined such that the center coordinates of each cell can be characterized by three integers (cf. Figure 3.1.3(a)). In space-filling assemblages of truncated octahedra, cells are either located on main or ancillary planes as shown in Figure 3.1.3. In this context, the staggered ancillary planes fill the space between two consecutive main planes. As shown in Figure 3.1.3(a), cells on main planes are denoted by even coordinates whereas cells on ancillary planes exhibit odd coordinates.

With these definitions, the coordinates of all neighboring cells $\boldsymbol{x}^{\mathsf{N}} = \left(x_1^{\mathsf{N}}, x_2^{\mathsf{N}}, x_3^{\mathsf{N}}\right)$ of a given active cell $\boldsymbol{x}^{\mathsf{A}} = \left(x_1^{\mathsf{A}}, x_2^{\mathsf{A}}, x_3^{\mathsf{A}}\right)$ can be simply calculated to

$$x_k^{\mathsf{N}} = x_k^{\mathsf{A}} + a_k \tag{3.1.1}$$

with $k \in \{1,2,3\}$ and $a_k \in \{-2,-1,0,1,2\}$. Thereby, the different components of $\boldsymbol{a}$ have to go well together, i.e. even and odd numbers must not be combined. Otherwise, equation (3.1.1) does not yield a valid cell (cf. Figure 3.1.3). If the given cell is situated along the boundary, the domain of a_k has to be appropriately adapted.

Sometimes it is more convenient to address an individual cell by a unique *ID*. For this purpose, cells are numbered consecutively starting from 0 in the coordinate origin. In Figure 3.1.3(b), this numbering scheme is illustrated by the example of the first main and ancillary plane of a small assemblage. Consequently, each cell can be identified either by its *ID* or by its cell center coordinates. For instance, the highlighted cell in Figure 3.1.3(a) possesses the *ID* 28 and the coordinates $(4,4,0)$. A convenient way to convert between cell *ID* and center coordinates (and vice versa) is presented in Appendix A.1.

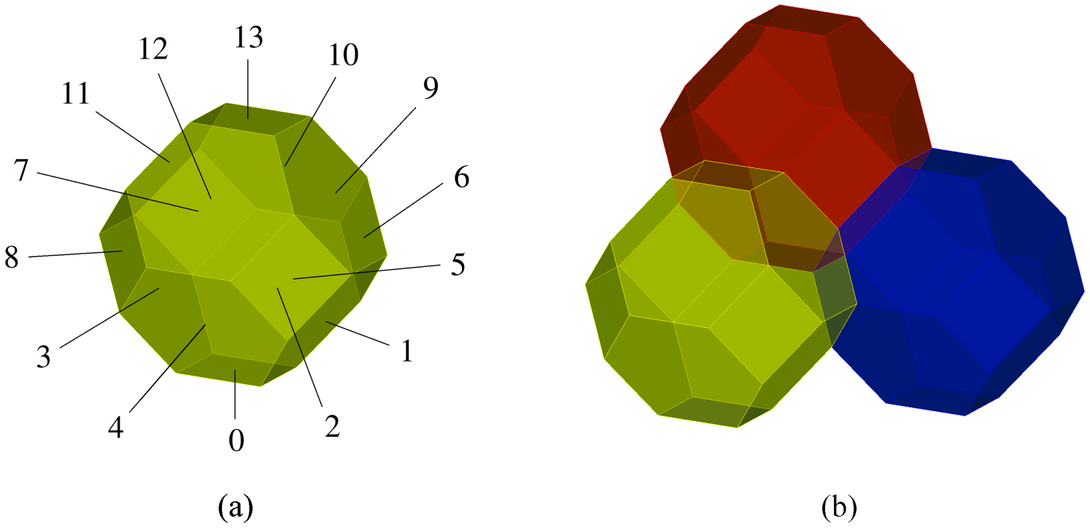

Figure 3.1.4: (a) Local surface IDs for tetrakaidecahedral cell. (b) Exemplary connection of three tetrakaidecahedra. Corresponding connecting surfaces are (in the respective local numbering scheme) 10/4 (connection of yellow and red cell), 6/8 (connection of yellow and blue cell), and 11/1 (connection of blue and red cell).

For the later generation of three-dimensional geometries, the surfaces between connected alveoli have to be deleted. To enable the unique identification of these connecting surfaces, a local numbering scheme for each cell is introduced as shown in Figure 3.1.4.

Concept of priority directions

In case of square and cubic cells, the pathway from one cell to each of its neighbors is of equal length. For tetrakaidecahedral cells, however, two kinds of connections have to be distinguished as a consequence of the more complicated geometry. If neighboring cells are connected via square faces this connection is subsequently denoted as straight. The corresponding path between cell centers is $2\sqrt{2}L$ long with L being the length of the edges of the tetrakaidecahedron (cf. Figure 3.1.1(c)). By contrast, the distance between centers of cells connected via hexagonal faces is $\sqrt{6}L$. In the following, these pathways are referred to as diagonal.

Without violating the concept of priority directions, different pathways are conceivable connecting two given cells. This finding is demonstrated in the top row of Figure 3.1.5, where possible connections between cell A and cell E are displayed. The shortest way takes course along the diagonal connecting A and D, whereas the orthogonal path via cell B and C is longer because it involves the passing of an additional cell.

Since diagonal and orthogonal pathways are not equally long, overall path lengths may differ even if the number of intermediate cells is equal. An illustrative example is provided in the bottom row of Figure 3.1.5. Here, the path connecting A and D via C is shorter

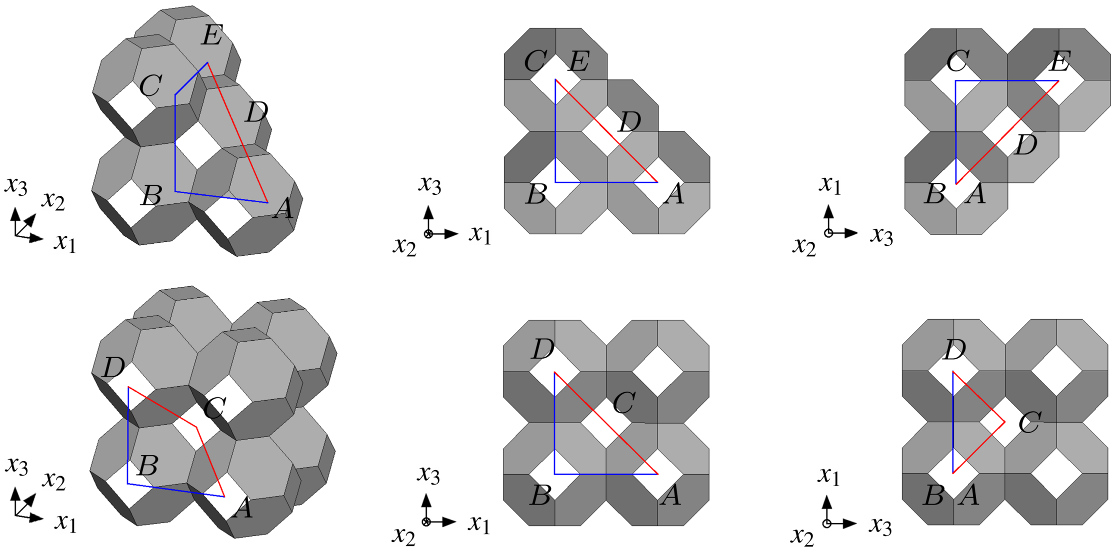

Figure 3.1.5: Comparison of different pathways connecting two cells. Top: Different path lengths arising from different numbers of connections. Bottom: Different path lengths due to different lengths of straight and diagonal connections in spite of equal numbers of intermediate cells.

than the orthogonal connection via B, even if the concept of priority directions is partially violated due to the change in one coordinate direction. This strongly suggests that diagonal pathways should be generally preferred whereas pathways running orthogonally with respect to the previous path should be prohibited. Therefore, if overall minimal path length should be preserved, the conventional concept of priority directions has to be modified.

To account for the characteristics of tetrakaidecahedral cells discussed above, three categories of possible pathways have to be distinguished. First, a preferred (meaning diagonal) path in priority directions can be defined. The second class of pathways is composed of diagonal paths exhibiting one non-priority coordinate direction and is called the group of preferred directions. Eventually, if neither preferred priority nor preferred directions are available, then a direction can be chosen from so-called admissible priority directions. Here, priority directions are said to be admissible if they do not process orthogonally to the previous pathway.

As can be seen in the very simple case of 35 tetrakaidecahedra in Figure 3.1.6, the modified algorithm nevertheless fails in preserving optimal path length. The highlighted pathway in Figure 3.1.6(a) is larger than the optimal one depicted in Figure 3.1.6(b) due to two non-diagonal connections. Thus, even if all requirements are met, minimal path length can not be guaranteed. Since the creation of labyrinths is a random process, potentially only pathways with lengths greater than the minimal one are generated. In Figure 3.1.7, overall path lengths of networks created in 100 consecutive runs of the modified labyrinthine algorithm were evaluated. Interestingly, none of the created labyrinths matched an optimal configuration (which would have an overall path length of $230.9\,L$).

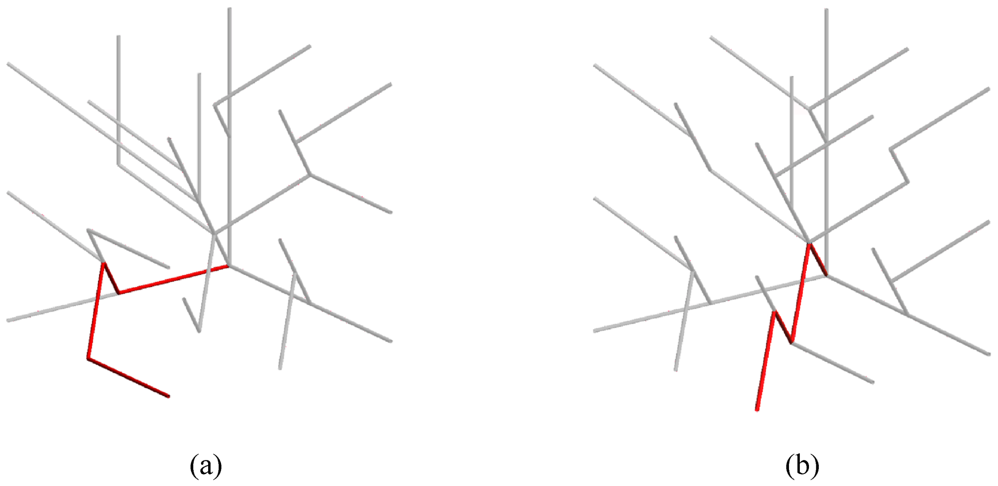
(a) (b)

Figure 3.1.6: Comparison of the configuration obtained by means of the adapted algorithm (a) and the optimal configuration (b) in case of an ensemble of 35 tetrakaidecahedra. For the sake of clarity, only cell center connections are displayed here.

To conclude, an extension of the concept of priority directions fails to ensure minimal path lengths in tetrakaidecahedral assemblages. Therefore, a novel connection rule that was developed as part of this work will be introduced in the following section.

Explicit check for optimality

To ensure that a chosen new cell N can be connected to the active cell A in an optimal way, all possible pathways to this cell have to be compared. Introducing P^{A} as the path length from the starting cell S to A, the length of the path to N via A can be calculated by

$$P^{\mathsf{N}} = P^{\mathsf{A}} + \begin{cases} 2\sqrt{2}L & \text{for straight connection} \\ \sqrt{6}L & \text{for diagonal connection.} \end{cases} \tag{3.1.2}$$

The other cells in the queue might not be located in direct adjacency of N. In this case, the shortest path to N via a queue cell C includes as many connections in diagonal direction as possible. To determine the exact number of diagonal connections along the optimal path between C with $\boldsymbol{x}^{\mathsf{C}} = \left(x_1^{\mathsf{C}}, x_2^{\mathsf{C}}, x_3^{\mathsf{C}}\right)$ and N with $\boldsymbol{x}^{\mathsf{N}} = \left(x_1^{\mathsf{N}}, x_2^{\mathsf{N}}, x_3^{\mathsf{N}}\right)$, first the differences in corresponding coordinates have to be evaluated, i.e.

$$\Delta x_1 = x_1^{\mathsf{N}} - x_1^{\mathsf{C}} \tag{3.1.3}$$

$$\Delta x_2 = x_2^{\mathsf{N}} - x_2^{\mathsf{C}} \tag{3.1.4}$$

$$\Delta x_3 = x_3^{\mathsf{N}} - x_3^{\mathsf{C}}. \tag{3.1.5}$$

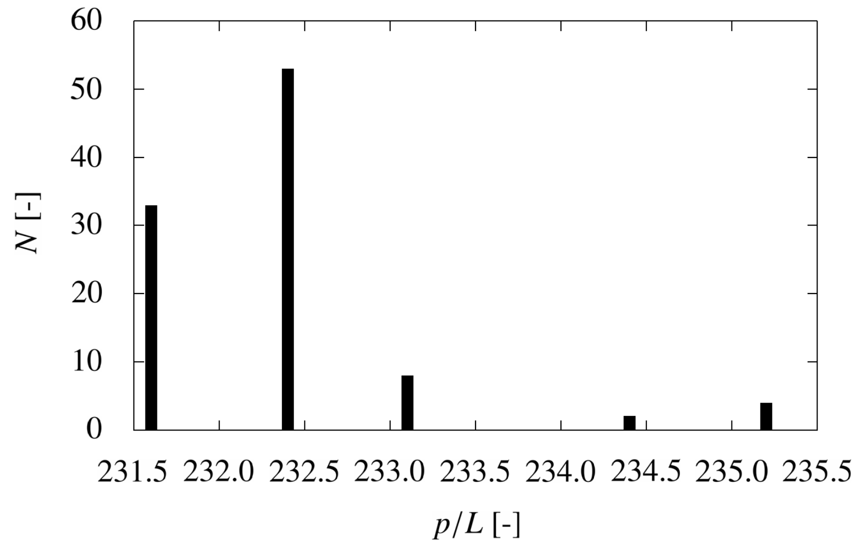

Figure 3.1.7: Evaluation of overall dimensionless path length p/L for 100 runs of the modified conventional labyrinthine algorithm in case of 35 tetrakaidecahedral base cells. N denotes the respective occurrences of individual path lengths.

Note that Δx_1, Δx_2, and Δx_3 are defined as integer parameters. The maximum and minimum absolute coordinate differences are then given by

$$\Delta v_{\mathsf{max}} = \mathsf{max}\left\{|\Delta x_1|,\, |\Delta x_2|,\, |\Delta x_3|\right\} \tag{3.1.6}$$

$$\Delta v_{\mathsf{min}} = \mathsf{min}\left\{|\Delta x_1|,\, |\Delta x_2|,\, |\Delta x_3|\right\} \tag{3.1.7}$$

whereas the absolute value of the remaining difference in coordinates is denoted by Δv_{mid}. Using these definitions, the number of diagonal and straight connections along the optimal pathway between C and N can be determined by

$$n_{\mathsf{diag}} = \Delta v_{\mathsf{mid}} \tag{3.1.8}$$

$$n_{\mathsf{straight}} = \frac{1}{2}\left(\Delta v_{\mathsf{max}} - \Delta v_{\mathsf{mid}}\right). \tag{3.1.9}$$

Consequently, the overall path length to N via C results in

$$\tilde{P}^{\mathsf{N}} = P^{\mathsf{C}} + 2\sqrt{2}L \cdot n_{\mathsf{straight}} + \sqrt{6}L \cdot n_{\mathsf{diag}}. \tag{3.1.10}$$

If none of the alternative path lengths $\tilde{P}^{\mathsf{N}}$ is smaller than P^{N}, i.e. $\tilde{P}^{\mathsf{N}}_{\mathsf{min}} > P^{\mathsf{N}}$, then N can be connected to A. Otherwise another cell has to be selected from the range of neighbors. In case that either no other adjacent cell is at hand or can be connected optimally, A is deleted from the queue and its successor is activated. The general procedure is summarized in Algorithm 3.1.

Algorithm 3.1 Labyrinthine algorithm for tetrakaidecahedral ensembles.

```
Define dimensions of assemblage and starting cell $\mathsf{S}$
Calculate individual cell coordinates $\bar{\mathbf{C}}$ (A.1.3), (A.1.4)/(A.1.6), (A.1.5)/(A.1.7)
Determine $ID$s of neighbors of each cell $\bar{\mathbf{N}}$ (3.1.1), (A.1.11)
Define possible connecting surfaces $\bar{\mathbf{S}}$
Construct vector of active cells in queue $\bar{\mathbf{q}} = [\mathsf{S}]$ and vector of passed cells $\bar{\mathbf{p}} = []$
Initialize vector of path lengths $\bar{\mathbf{l}}$ and list of deleted surfaces per cell $\bar{\mathbf{D}}$

while length($\bar{\mathbf{p}}$) $\neq$ total number of cells:
    Set active cell $\mathsf{A} = \bar{\mathbf{q}}[0]$ (*)
    for all $\mathsf{N}$ in $\bar{\mathbf{N}}[\mathsf{A}]$:
        if $\mathsf{N} \in \bar{\mathbf{p}}$:
            Delete $\mathsf{N}$ from $\bar{\mathbf{N}}[\mathsf{A}]$ and connecting surface from $\bar{\mathbf{S}}$
    if $\bar{\mathbf{N}}[\mathsf{A}] = []$:
        Delete $\mathsf{A}$ from $\bar{\mathbf{q}}$ and continue with (*)
    else:
        Initialize $P^{\mathsf{N}}$ and $\tilde{P}^{\mathsf{N}}_{\mathsf{min}}$
        while $P^{\mathsf{N}} > \tilde{P}^{\mathsf{N}}_{\mathsf{min}}$:
            Randomly choose new cell $\mathsf{N}$ from $\bar{\mathbf{N}}[\mathsf{A}]$
            Calculate $P^{\mathsf{N}}$ (3.1.2)
            Initialize $\tilde{P}^{\mathsf{N}}_{\mathsf{min}}$
            for all $\mathsf{C}$ in $\bar{\mathbf{q}}$:
                Calculate $\tilde{P}^{\mathsf{N}}$ (3.1.10)
                if $\tilde{P}^{\mathsf{N}} < \tilde{P}^{\mathsf{N}}_{\mathsf{min}}$:
                    $\tilde{P}^{\mathsf{N}}_{\mathsf{min}} = \tilde{P}^{\mathsf{N}}$
            if $P^{\mathsf{N}} > \tilde{P}^{\mathsf{N}}_{\mathsf{min}}$:
                Delete $\mathsf{N}$ from $\bar{\mathbf{N}}[\mathsf{A}]$ and connecting surface from $\bar{\mathbf{S}}$
                if $\bar{\mathbf{N}}[\mathsf{A}] = []$:
                    Delete $\mathsf{A}$ from $\bar{\mathbf{q}}$ and continue with (*)
            else:
                Append $\mathsf{N}$ to $\bar{\mathbf{p}}$ and connecting surfaces to $\bar{\mathbf{D}}[\mathsf{A}]$ and $\bar{\mathbf{D}}[\mathsf{N}]$
                Store $P^{\mathsf{N}}$ in $\bar{\mathbf{l}}$
                Move $\mathsf{A}$ from first to last position in $\bar{\mathbf{q}}$
                Append $\mathsf{N}$ to $\bar{\mathbf{q}}$
```

Examples

In Figures 3.1.8, 3.1.9, and 3.1.10, the universality of the presented new labyrinthine algorithm is illustrated. For the sake of clarity, the surrounding tetrakaidecahedra are again left out and only the pathways connecting the cell centers are displayed. The new labyrinthine algorithm enables the generation of random configurations with optimal mean path length and applies for arbitrary starting points and assemblage sizes.

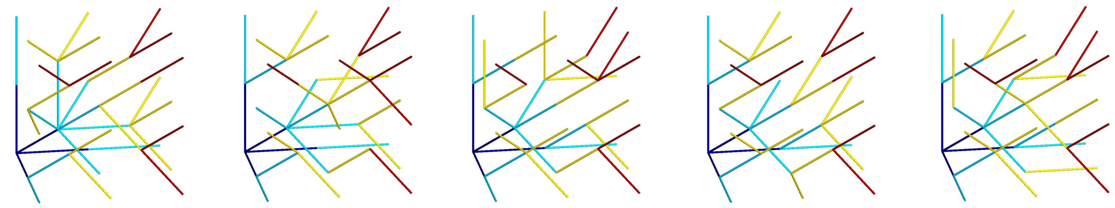

Figure 3.1.8: Different realizations of optimal pathways through an assemblage of 35 tetrakaidecahedral base cells. Colors indicate distances to the starting cell with blue denoting proximal and red meaning distal.

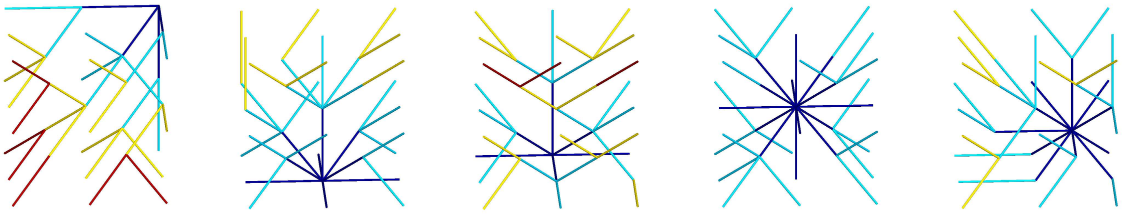

Figure 3.1.9: Optimal pathways through an assemblage of 35 tetrakaidecahedral base cells with different starting points. Colors indicate distances to the starting cell with blue denoting proximal and red meaning distal.

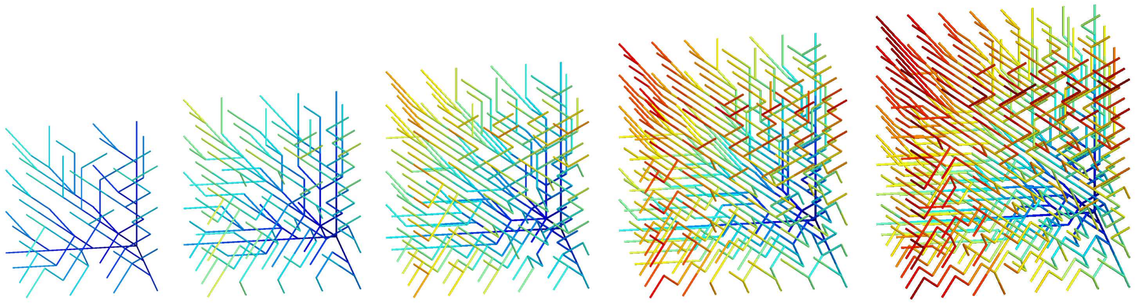

Figure 3.1.10: Optimal pathways through tetrakaidecahedral assemblages of different sizes. Colors indicate distances to the starting cell with blue denoting proximal and red meaning distal.

For a comparison with published anatomical data, the mean longitudinal path length within an assemblage of 3514 cells ($22 \cdot 13 \cdot 7$ on the main planes) was calculated. The starting point was located at a vertex and an edge length $L = 0.082$ mm was chosen in line with Denny and Schroter (1997). In this case, a mean longitudinal path length of 4.17 mm from the fourth acinar generation after the transitional bronchiole to the termination in the alveolar sacs was obtained. It is noteworthy that the mean longitudinal path length is not the same as the overall path length since only dead-end cells are included in the calculation. Assuming that the average path length in the first three generations is equal to 3.4 mm (Haefeli-Bleuer and Weibel, 1988), the mean longitudinal path length from the transitional bronchiole to the alveolar sacs was determined as 7.57 mm. The deviation of this result from the longitudinal path length measured in silicone rubber casts by Haefeli-Bleuer and Weibel (1988) was approximately 4.9%.

3.1.3 Generation of three-dimensional acinar geometries

Information provided by the labyrinthine algorithm regarding connections between cells of acini or subacini can be directly used for the generation of three-dimensional geometries (see Figures 3.1.11(a) and 3.1.11(b)). In this context, the characteristic length L of the tetrakaidecahedron (cf. Figure 3.1.1(c)) as well as the wall thickness t can be chosen depending on the species to be modeled. This flexibility is a major advantage of the presented methodology.

In a first step, the mid planes of the artificial alveoli are constructed. Thereby, surfaces between connected cells (see Algorithm 3.1) are omitted. Based on that, interior and exterior surfaces are created by intersecting planes parallel to the mid surfaces at intervals of $\frac{t}{2}$. A specific procedure is then employed to construct the alveolar entrance rings by intersecting planes owned by connected alveoli. The mechanical properties of these regions are – depending on the species – significantly different than those of the remaining alveolar wall. The developed approach enables the specific handling of these entrance rings, which is beneficial e.g. for the definition of constitutive models and material parameters. A detailed overview of the generation of three-dimensional acinar geometries is given in Appendix A.2.

Finally, batch files specific to preprocessing programs such as GiD or CUBIT are generated. In this way, the created objects can be easily imported and prepared for computational simulations. The acinar models can be structurally meshed with hexahedral elements in a straightforward manner as illustrated in Figure 3.1.11(c).

An obvious drawback of the created artificial geometry is that all alveoli or alveolar ducts are of the same shape and size. This characteristic is inconsistent with morphological measurements provided e.g. in Haefeli-Bleuer and Weibel (1988). A better agreement with the in vivo situation can be attained by simply introducing statistical fluctuations of the vertex positions during the generation of the three-dimensional geometry. In the scope of this work, however, only regular tetrakaidecahedral shapes have been utilized.

3.2 Alveolar soft tissue behavior

For the determination of stresses and strains in individual alveolar walls, an accurate description of lung tissue behavior is indispensable. To frame the requirements of a suitable constitutive law, the properties of lung parenchyma as assessed from experiments will be

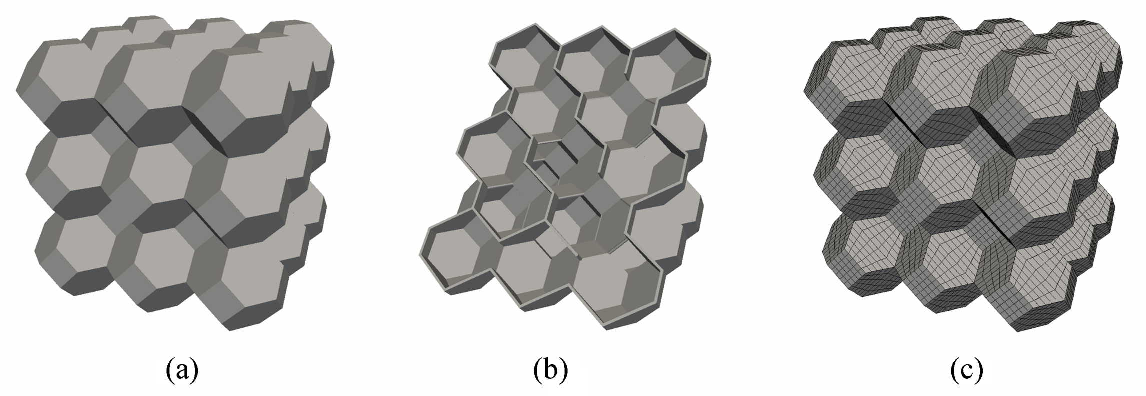

Figure 3.1.11: Three-dimensional geometry of an assemblage of 35 alveoli based on information provided by the labyrinthine algorithm. (a) Outside view. (b) Clipped view illustrating interalveolar connections. (c) View of generated FE mesh.

discussed in the following. After a survey of existing material models for alveolar tissue, selected constitutive equations developed for other soft biological tissues will be briefly reviewed. Thereupon, the material model chosen within the scope of this thesis will be presented in more detail. A brief remark on the consideration of residual stresses will conclude this section.

3.2.1 Survey of experimental results

The characteristics of lung parenchyma have been investigated extensively in literature. However, none of these studies have been able to provide information about the behavior of individual alveolar walls. At most, alveolar properties have been deduced from experiments with larger tissue strips based on very simple model assumptions. Although available data are not directly applicable to the alveolar model developed within this thesis, selected studies will be surveyed subsequently in order to illustrate experimental capabilities and define the requirements of suitable constitutive models.

Several investigations were aimed at the characterization of the overall behavior of lung tissue. Fukaya et al. (1968) were the first to perform tension tests on small cat lung tissue strips in vitro. The obtained length-tension curves were highly nonlinear and hysteretic, i.e. with a pathway different on extension and release. Furthermore, time-dependent phenomena like stress relaxation and recovery were observed. Sugihara et al. (1971) demonstrated that the maximum extensibility of human lung tissue diminishes with aging and the presence of diffuse lung diseases. Tai and Lee (1981) studied the dependency of the mechanical behavior of dog parenchyma on the location within the lung and the direction of force application. They concluded that the common assumption of isotropy and homogeneity in gross modeling of lung deformation is justified. First approximate elastic constants of dog lung tissue were derived by Hoppin et al. (1975) from three-axial tension tests. A more elaborate approach was proposed recently by Rausch et al. (2011b) who investigated the material behavior of viable precision-cut rat lung slices. In contrast to most other studies, also transversal deformations were recorded, thereby enabling the fitting of more complicated three-dimensional constitutive models.

Other studies were concerned with analyzing the influence of the different constituents of alveolar tissue (cf. also section 1.1.2.2) on the overall behavior. For instance, Yuan et al. (1997) showed that interstitial cells within normal lung parenchyma do not directly affect tissue stiffness at the macroscopic level and may contribute to tissue resistance by less than 12%. Hence, the macroscopic elastic and dissipative properties are mainly dominated by the connective tissue fibers. In a later study, the respective roles of collagen and elastin were investigated by examining the properties of tissue strips before and after treatment with elastase and collagenase (Yuan et al., 2000). Corresponding data suggested that both collagen and elastin contribute to tissue elasticity during normal breathing. Besides, it was demonstrated that the elastance coefficient of the tissue strip is far less than that of the fibers alone. This phenomenon was attributed to a pronounced network effect. Al Jamal et al. (2001) studied the influence of the glycosaminoglycans (GAGs) in the ground substance on the visco-elastic behavior of lung tissue. The observed effect of the GAGs was attributed to their interactions with the cell membrane or other ECM molecules. The mechanical interaction between proteoglycans and collagen fibers was analyzed by Cavalcante et al. (2005). They hypothesized that the proteoglycans (which can resist compression and shear) stabilize the fiber network and contribute to lung elasticity at low to medium lung volumes. Using a two-dimensional hexagonal network model of the alveolar structure, they also roughly estimated the Young's modulus of a single alveolar wall and a collagen fiber.

In summary, many insights into the properties of lung parenchyma have been gained. However, there still remain large gaps in the understanding of how precisely the rheological behavior of alveolar tissue is related to the properties of its constituents and their respective interaction. Hence, when developing a constitutive model, inappropriate complexity should be avoided.

3.2.2 Outline of existing modeling approaches

Several attempts to model alveolar soft tissue behavior have been reported in the literature. In this context, two basic approaches can be distinguished. The first alternative is based on the assumption that the resistance to deformation is provided solely by the supporting fiber network. Corresponding models approximate alveolar tissue by an arrangement of discrete elements representing the connective tissue fibers without considering the effect of the surrounding ground substance. For instance, Maksym et al. (1998) idealized individual septal walls in lung tissue strips by a two-dimensional network of elastin and collagen fibers arranged in parallel. Elastin was represented by a linear spring, whereas collagen was modeled by a stiff string extending without resistance until taut. Corresponding "knee lengths" of the collagen fibers (i.e. the lengths at which the individual strings become taut) were distributed according to an inverse power law. Dale et al. (1980) modeled a single alveolus as a symmetric arrangement of pin-jointed bars which were constrained to lie in planes corresponding to the faces of a tetrakaidecahedron. A similar approach was pursued by Kimmel and Budiansky (1990) who, however, utilized an analytical approach based on a dodecahedral alveolar geometry. In the alveolar duct model of Denny and Schroter (1995), elastin and collagen fibers were arranged along the edges and surface diagonals of individual tetrakaidecahedral alveoli. The density and distribution of both fiber types could be varied separately, thereby easily facilitating the study of diseases such as emphysema in which a degradation of predominantly elastin occurs. While elastin fiber bundles were assumed to obey a simple linear material law, the behavior of collagen fibers was modeled using an exponential stress-strain relationship. In later studies (Denny and Schroter, 2000, 2006), viscous effects were taken into account by introducing a transient relaxation function into afore mentioned fiber models. In all discrete approaches discussed so far, only few individual fibers with an arbitrarily chosen orientation represented the complex network structure. As opposed to this, the tissue model proposed by Bates (1998) was based on the summed effects of many randomly interacting fibers. When suddenly stretched uniaxially, the fibers aligned themselves preferentially in the strain direction before slowly reverting back to random orientation due to thermal motion.

The second alternative is to model the alveolar wall as a continuum by integrating over the properties of its constituents. Frankus and Lee (1974), for example, approximated alveolar tissue by a plane membrane material derived from isotropically distributed pseudo-fibers. These fictitious structures represented the composite material found in the alveolar wall and, hence, were not synonymous with real tissue fibers. A membrane material was also proposed by Karakaplan et al. (1980). However, they formulated a material model based on a phenomenological strain energy density function (SEF). As the name suggests, this kind of constitutive law describes distinct macroscopic phenomena which can be observed in experiments without requiring a detailed knowledge of the underlying micro-structure. Consequently, related parameters in general do not possess a clear physical interpretation like the elastic modulus of a collagen fiber. However, they can be determined by fitting the model to corresponding experimental data. Gefen et al. (1999), for instance, suggested a constitutive law based on a one-dimensional polynomial stress-stretch relation. Corresponding parameters were determined from uni-axial tension tests performed by Sugihara et al. (1971). Another more micro-structurally motivated – albeit still phenomenological – approach to characterizing alveolar tissue behavior was introduced by Lanir (1983) who utilized a SEF for fibrous connective tissues.

Over the last decade, various models have been developed for other soft biological materials such as arterial or aortic tissues. Although specific properties are likely to be distinct, there are a number of common characteristics. This can be attributed to the presence of similar micro-structural constituents. Therefore, it seems possible to adapt some of these material models to alveolar tissue. For instance, Humphrey and Yin (1987) developed a model that synthesized certain desirable features from phenomenological and micro-structurally motivated approaches. They assumed that many soft tissues can be idealized as being composed of a homogeneous matrix and various families of non-interacting densely distributed fibers. In this context, each fiber family was allowed to possess different material properties and orientations. The SEF was then formulated as the sum of matrix and fiber contributions. The same concept was employed by Holzapfel et al. (2000)

for a constitutive model of arterial tissue. The two mechanically relevant layers (i.e. the media and the adventitia) were treated as orthotropic fiber-reinforced materials whose orientations were obtained from a statistical analysis of histological sections. Balzani et al. (2006) showed that the proposed SEFs for the matrix material and the fiber families satisfy general polyconvexity conditions (cf. Ball (1977)), thereby ensuring a numerically stable and physically reasonable material model. In the same study, a general construction principle for polyconvex constitutive models suitable for the description of various biological soft tissues was formulated. Since collagen fibers are usually not perfectly aligned even if a prevalent direction exists, Gasser et al. (2006) introduced a generalized version of the Holzapfel model by incorporating a parameter characterizing the dispersion of collagen fiber orientations. Ehret and Itskov (2007) proposed an alternative polyconvex SEF for collagenous tissues such as coronary arteries and the abdominal aorta. To control the anisotropic behavior, they introduced specific weight factors into the fiber functions. Zulliger et al. (2003) expanded the idea of structural SEFs by including also the volume fractions of both elastin and collagen contained in arterial tissue. The parameters of the novel SEF had the physical meaning of the elastic moduli of collagen and elastin, the collagen waviness, and the collagen fiber angle. Maceri et al. (2010) developed a multi-level model for soft collagenous tissues with regular fiber arrangement. Their formulation was based on few parameters which were directly related to histological information. The resulting constitutive model accounted for effects on the nano-, micro-, and macro-scale of the tissue. Application to several tissues such as tendon and ligaments showed good agreement with experimental data. Another hierarchical approach proposed by Tang et al. (2009) established a link between nano-scale collagen features and material properties at larger tissue scales. A quantitative comparison between simulation results and experimental measurements, however, has not been performed yet.

After having discussed different approaches to modeling the mechanical behavior of biological materials, a constitutive law suitable for the intended application has to be chosen. The discrete models discussed above are out of question since they oversimplify the complex structure of lung tissue. By contrast, the multi-level approaches proposed recently seem to complicate the alveolar model without being supported by appropriate data concerning e.g. the exact amount and three-dimensional distribution of fibers. To find a compromise between structural accuracy and mathematical simplicity, it seems reasonable to start with a well-established phenomenological constitutive law that is based on general micro-structural information.

3.2.3 Constitutive model for alveolar tissue

In the experimental studies discussed in section 3.2.1, time-dependent phenomena such as stress relaxation and recovery were observed. As a first step, however, viscous effects are neglected and alveolar tissue is assumed to be hyperelastic. In this case, the material response can be determined based on a SEF Ψ defined per unit reference volume such that

$$\boldsymbol{S} = 2\frac{\partial \Psi}{\partial \boldsymbol{C}}. \tag{3.2.1}$$

Since biological tissues (like many other materials) are characterized by a quite different behavior with regard to volumetric and isochoric deformations, it is beneficial to define the following multiplicative split of the deformation gradient $\boldsymbol{F}$ into dilatational and distortional parts

$$\boldsymbol{F} = \left(J^{1/3}\boldsymbol{I}\right) \cdot \bar{\boldsymbol{F}}. \tag{3.2.2}$$

In this context, $\bar{\boldsymbol{F}}$ refers to the isochoric part of the deformation gradient, J is the determinant of $\boldsymbol{F}$, and, hence, $J^{1/3}\boldsymbol{I}$ denotes the volumetric part of $\boldsymbol{F}$. The isochoric right Cauchy-Green tensor is then defined by

$$\bar{\boldsymbol{C}} = \bar{\boldsymbol{F}}^{\mathsf{T}} \cdot \bar{\boldsymbol{F}}. \tag{3.2.3}$$

Based on this split, the following decoupled form of the SEF is postulated

$$\Psi(\boldsymbol{C}) = U(J) + \bar{\Psi}(\bar{\boldsymbol{C}}) \tag{3.2.4}$$

with U and $\bar{\Psi}$ being the volumetric and the isochoric contributions to the overall strain energy density, respectively. In the following, specific functions suitable for the description of alveolar soft tissue behavior will be proposed.

Although a phenomenological model has been chosen in this work, as much information about the underlying micro-structure as possible should be included. As already discussed in section 1.1.2.2, the constituents of alveolar tissue exhibit significantly different mechanical properties. The chosen material model should enable a distinction of the corresponding contributions to the overall energy. In line with the model presented by Holzapfel et al. (2000) for arterial tissue, $\bar{\Psi}$ is proposed to consist of two main parts related to the major stress-bearing elements. It seems reasonable to adapt this approach as well as the individual SEFs also for alveolar tissue albeit hard experimental evidence for this choice is missing.

The first part of the SEF $\bar{\Psi}^{\mathsf{gs}}$ represents mainly the elastin fiber system and the amorphous ground substance. Following Holzapfel et al. (2000), Holzapfel et al. (2004), and Gasser et al. (2006), $\bar{\Psi}^{\mathsf{gs}}$ is approximated by an isochoric Neo-Hookean model, i.e.

$$\bar{\Psi}^{\mathsf{gs}}\left(\bar{I}_1\right) = c\left(\bar{I}_1 - 3\right). \tag{3.2.5}$$

In this context, $c > 0$ is a shear modulus-like parameter and $\bar{I}_1$ is the first principal invariant of the isochoric right Cauchy-Green tensor defined by

$$\bar{I}_1 = \mathsf{tr}\left(\bar{\boldsymbol{C}}\right) \tag{3.2.6}$$

with $\mathsf{tr}(\bar{\boldsymbol{C}})$ denoting the trace of $\bar{\boldsymbol{C}}$.

The second contribution to the isochoric SEF is related to the collagen fiber network. Following Gasser et al. (2006), collagen fiber directions are assumed to be distributed around a preferential direction $\boldsymbol{a}$ according to an orientation density function $\hat{\rho}$. To allow for a coordinate-invariant formulation of the constitutive equations in the presence of anisotropy, a general structural tensor $\boldsymbol{H}$ can be introduced as follows

$$\boldsymbol{H} = \eta \boldsymbol{I} + (1 - 3\eta)\, \boldsymbol{a} \otimes \boldsymbol{a}. \tag{3.2.7}$$

The parameter η is given by

$$\eta = \frac{1}{4} \int_0^{\pi} \hat{\rho}\left(\hat{\theta}\right) \sin^3\left(\hat{\theta}\right) \mathrm{d}\hat{\theta} \tag{3.2.8}$$

where $\hat{\theta}$ denotes the angle between a fiber and the preferential orientation $\boldsymbol{a}$. Experimental results of Sobin et al. (1988) and Toshima et al. (2004) suggest that fiber orientation in alveolar tissue is rather random. Consequently, lung parenchyma can be treated as a homogeneous, isotropic continuum. According to Gasser et al. (2006), η is equal to $\frac{1}{3}$ in this case. Based on the general structural tensor $\boldsymbol{H}$, an additional so-called mixed invariant $\bar{J}_4$ of the isochoric right Cauchy-Green tensor can be introduced as follows

$$\bar{J}_4 = \mathrm{tr}\left(\boldsymbol{H} \cdot \bar{\boldsymbol{C}}\right) = \frac{1}{3} \bar{I}_1. \tag{3.2.9}$$

$\bar{J}_4$ in general denotes the square of the stretch in fiber direction given that affine kinematics can be presumed. It has to be noted, though, that this assumption is not in line with the experimentally observed network effect in lung tissue (Yuan et al., 2000) that, according to theoretical studies of Chandran and Barocas (2006), potentially leads to a three-fold decrease of fiber stresses compared to the macroscopic stress. However, bearing in mind that the proposed constitutive model is still a phenomenological one, introduction of more complex approaches to considering realistic fiber behavior seems to be pointless here. Hence, for simplicity, the validity of affine kinematics is presumed in the following. Consequently, it seems reasonable to formulate the SEF representing the contribution of the collagen fibers based on $\bar{J}_4$. Due to the highly nonlinear behavior of collagen, exponential functions are widely used in biomechanical modeling since the pioneering work of Fung (1967). For instance, the SEF proposed by Holzapfel et al. (2000) and Gasser et al. (2006) for the collagen fibers in arterial tissue reads

$$\bar{\Psi}^{\mathrm{fib}}\left(\bar{J}_4\right) = \delta \frac{k_1}{2k_2} \left\{ \exp\left[k_2 \left(\bar{J}_4 - 1 \right)^2 \right] - 1 \right\} \tag{3.2.10}$$

with $k_1 \geq 0$ being a stress-like parameter, $k_2 > 0$ denoting a dimensionless parameter, $\delta = 0$ for $\bar{J}_4 < 1$, and $\delta = 1$ for $\bar{J}_4 \geq 1$. This case distinction is necessary since $\bar{J}_4 < 1$ characterizes a shortening of the fibers which are assumed to have no compressive strength. Introducing the mixed invariant (3.2.9) into the fiber SEF (3.2.10) yields

$$\bar{\Psi}^{\mathrm{fib}}\left(\bar{I}_1\right) = \delta \frac{k_1}{2k_2} \left\{ \exp\left[k_2 \left(\frac{1}{3} \bar{I}_1 - 1 \right)^2 \right] - 1 \right\} \tag{3.2.11}$$

with $\delta = 0$ for $\bar{I}_1 < 3$ and $\delta = 1$ for $\bar{I}_1 \geq 3$. This isotropic variant is chosen as the collagen fiber SEF for alveolar tissue. Except for a different coefficient, the fiber function (3.2.11) essentially equals the SEF introduced by Delfino et al. (1997) for the description of arterial tissue. Remarkably, Sansour (2008) found that formulating anisotropic fiber SEFs like (3.2.10) based on $\bar{\boldsymbol{C}}$ instead of $\boldsymbol{C}$ may lead to unphysical results. He demonstrated that, in the compressible anisotropic case, any spherical state of stress produces a change of both volume and shape, even if the volumetric stress is assumed to depend solely on J. Furthermore, he argued that utilization of the isochoric deformations in fiber-related expressions causes spurious multi-dimensional fiber stresses. Therefore, he suggested to formulate any anisotropic fiber function using the original (i.e. complete) right Cauchy-Green tensor. Although in the limiting case of incompressibility, both alternative fiber SEFs coincide, associated volumetric stresses still differ in the presence of anisotropy. However, since the collagen fiber function chosen for alveolar tissue is isotropic, the split of deformations is permissible in any case and, hence, retained in equation (3.2.11).

After introduction of the isochoric SEFs, now the volumetric contribution will be briefly discussed. Due to their high water content, biological soft tissues are commonly assumed to be incompressible. In this case, $U(J)$ can be interpreted as an additional kinematic constraint potential with the hydrostatic pressure p as a Lagrange multiplier. Exact satisfaction of the incompressibility condition, therefore, involves a mixed FE approach including displacement and pressure DOFs. However, as already indicated in section 2.5.2, the incompressible case can also be approximated by employing a slightly compressible formulation based on a penalty method. Due to its ease of implementation, this concept is widely spread and, therefore, also chosen for the modeling of the volumetric behavior of alveolar tissue. Within this thesis, the following volumetric SEF introduced by Balzani et al. (2006) was implemented

$$U(J) = \epsilon_1 \left(J^{2\epsilon_2} + \frac{1}{J^{2\epsilon_2}} - 2 \right) \tag{3.2.12}$$

where $\epsilon_1 > 0$ is the penalty parameter and $\epsilon_2 > 1$ acts as a parameter controlling the shape of the function. For $\epsilon_1 \to \infty$, the penalty function (3.2.12) ensures vanishing volumetric deformations. In practice, ϵ_1 is a problem-specific parameter chosen sufficiently large to satisfy the incompressibility constraint approximately, but small enough to prevent ill-conditioning of the numerical problem.

Finally, the overall SEF for alveolar tissue takes the following form

$$\Psi\left(\bar{I}_1, J\right) = \bar{\Psi}^{\mathsf{gs}}\left(\bar{I}_1\right) + \bar{\Psi}^{\mathsf{fib}}\left(\bar{I}_1\right) + U\left(J\right). \tag{3.2.13}$$

It is noteworthy that each part fulfills the principles of objectivity as well as the requirements of polyconvexity and a stress-free reference state.

Based on equations (3.2.1) and (3.2.13), the corresponding second Piola-Kirchhoff stress tensor can be specified for a given deformation state. It has to be noted that the determination of $\boldsymbol{S}$ involves differentiation of the SEF with respect to the original right Cauchy-Green tensor $\boldsymbol{C}$. For this purpose, the following relations between the isochoric invariants utilized in equation (3.2.13) and the corresponding invariants of $\boldsymbol{C}$ need to be defined

$$I_3 = \det(\boldsymbol{C}) = J^2, \qquad I_1 = \mathrm{tr}(\boldsymbol{C}) = \bar{I}_1 J^{2/3} = \bar{I}_1 I_3^{1/3}. \tag{3.2.14}$$

The second Piola-Kirchhoff stresses then read

$$\begin{aligned} \boldsymbol{S} &= 2\frac{\partial \Psi}{\partial \boldsymbol{C}} = 2\left[\frac{\partial \Psi}{\partial \bar{I}_1}\frac{\partial \bar{I}_1}{\partial I_1}\frac{\partial I_1}{\partial \boldsymbol{C}} + \left(\frac{\partial \Psi}{\partial \bar{I}_1}\frac{\partial \bar{I}_1}{\partial I_3} + \frac{\partial \Psi}{\partial J}\frac{\partial J}{\partial I_3}\right)\frac{\partial I_3}{\partial \boldsymbol{C}}\right] = \\ &= 2\left[\frac{\partial \Psi}{\partial \bar{I}_1} I_3^{-1/3}\boldsymbol{I} + \left(-\frac{1}{3}\frac{\partial \Psi}{\partial \bar{I}_1} I_1 I_3^{-4/3} + \frac{1}{2}\frac{\partial \Psi}{\partial J} I_3^{-1/2}\right) I_3 \boldsymbol{C}^{-1}\right] \end{aligned} \tag{3.2.15}$$

where the derivatives of I_1 and I_3 with respect to $\boldsymbol{C}$ can be found e.g. in Holzapfel (2001) and differentiation of the overall SEF (3.2.13) with respect to the invariants of $\bar{\boldsymbol{C}}$ yields

$$\frac{\partial \Psi}{\partial J} = 2\epsilon_1\epsilon_2\left(I_3^{\epsilon_2} - I_3^{-\epsilon_2}\right) I_3^{-1/2} \tag{3.2.16}$$

$$\frac{\partial \Psi}{\partial \bar{I}_1} = c + \delta\frac{1}{3}k_1 \exp\left(k_2 \mathcal{Q}^2\right)\mathcal{Q}. \tag{3.2.17}$$

In this context, the following abbreviation is introduced for the sake of lucidity

$$\mathcal{Q} = \left(\frac{1}{3}\bar{I}_1 - 1\right) = \left(\frac{1}{3}I_1 I_3^{-1/3} - 1\right). \tag{3.2.18}$$

Differentiation of the second Piola-Kirchhoff stresses (3.2.15) with respect to the Green-Lagrange strains yields the associated elasticity tensor

$$\boldsymbol{\mathcal{C}} = \frac{\partial \boldsymbol{S}}{\partial \boldsymbol{E}} = 2\frac{\partial \boldsymbol{S}}{\partial \boldsymbol{C}} = 4\frac{\partial^2 \Psi}{\partial \boldsymbol{C}\partial \boldsymbol{C}}. \tag{3.2.19}$$

The most general form of $\boldsymbol{\mathcal{C}}$ in terms of the principal invariants of $\boldsymbol{C}$ can be found in Holzapfel (2001). In the present case, the elasticity tensor reduces to

$$\boldsymbol{\mathcal{C}} = \delta_1 \boldsymbol{I}\otimes\boldsymbol{I} + \delta_3\left(\boldsymbol{I}\otimes\boldsymbol{C}^{-1} + \boldsymbol{C}^{-1}\otimes\boldsymbol{I}\right) + \delta_6 \boldsymbol{C}^{-1}\otimes\boldsymbol{C}^{-1} + \delta_7 \boldsymbol{C}^{-1}\odot\boldsymbol{C}^{-1} \tag{3.2.20}$$

with the symbols $\otimes$ and $\odot$ denoting tensor products given by

$$(\boldsymbol{I}\otimes\boldsymbol{I})_{JKLM} = I_{JK} I_{LM} \tag{3.2.21}$$

$$\left(\boldsymbol{C}^{-1}\odot\boldsymbol{C}^{-1}\right)_{JKLM} = \frac{1}{2}\left(C_{JL}^{-1}C_{KM}^{-1} + C_{JM}^{-1}C_{KL}^{-1}\right) \tag{3.2.22}$$

and the coefficients δ_1, δ_3, δ_6, and δ_7 defined by

$$\delta_1 = \delta\frac{4}{9}k_1 \exp\left(k_2\mathcal{Q}^2\right) I_3^{-2/3}\left(2k_2\mathcal{Q}^2 + 1\right), \tag{3.2.23}$$

$$\delta_3 = -\frac{4}{3}c I_3^{-1/3} - \delta\frac{4}{27}k_1 \exp\left(k_2\mathcal{Q}^2\right) I_3^{-2/3}\left(I_1 + 2k_2 I_1 \mathcal{Q}^2 + 3I_3^{1/3}\mathcal{Q}\right), \tag{3.2.24}$$

$$\delta_6 = \frac{4}{9} c I_1 I_3^{-1/3} + \delta \frac{4}{81} k_1 \mathsf{exp}\left(k_2 \mathcal{Q}^2\right) I_1 I_3^{-2/3} \left(I_1 + 2k_2 I_1 \mathcal{Q}^2 + 3 I_3^{1/3} \mathcal{Q}\right) + \\ + 4\epsilon_1 \epsilon_2^2 \left(I_3^{\epsilon_2} + I_3^{-\epsilon_2}\right), \quad (3.2.25)$$

$$\delta_7 = \frac{4}{3} c I_1 I_3^{-1/3} + \delta \frac{4}{9} k_1 \mathsf{exp}\left(k_2 \mathcal{Q}^2\right) I_1 I_3^{-1/3} \mathcal{Q} - 4\epsilon_1 \epsilon_2 \left(I_3^{\epsilon_2} - I_3^{-\epsilon_2}\right). \quad (3.2.26)$$

Due to the lack of data for individual alveolar walls, the material model introduced above was fitted to experimental stress-strain curves published in Al Jamal et al. (2001) for lung tissue sheets (Röhrnbauer, 2006). As a consequence, current parameters model a homogenized continuum of alveolar tissue and air rather than a single alveolar interseptum. The parameters found for ground substance and fiber function were $c = 1$ kPa, $k_1 = 13.5$ kPa, $k_2 = 76.5$ and the penalty parameters were chosen to be $\epsilon_1 = 10$ kPa, $\epsilon_2 = 1.0$. A more realistical approach to determining material constants was employed by Karakaplan et al. (1980) who chose the parameters for their alveolar duct FE model such that its predictions matched experimental results obtained from triaxial tension tests on larger specimens (Hoppin et al., 1975). A similar procedure that is currently under way will be briefly addressed in section 6. For the time being, however, the parameters given above are utilized.

The resulting contributions of the individual functions to the overall potential in case of uniaxial tension can be seen in Figure 3.2.1. The principal stretches are denoted by $\Lambda_1 = \Lambda_2$ perpendicular to and Λ_3 in load direction. The presented ground substance function is compared to a standard Neo-Hookean material governed by the following SEF

$$\Psi^{\mathsf{NH}}(I_1) = c\,(I_1 - 3) \quad (3.2.27)$$

with c chosen to be identical to the homonymous parameter of the ground substance function.

The influence of the different material parameters on the uniaxial stress-strain behavior is illustrated in Figure 3.2.2. Plots show the relationship between the principal stretch Λ and the Cauchy stress σ in load direction in case of perfect incompressibility. In each plot, one constitutive parameter is varied, whereas the other two are kept constant. Clearly, elastin fibers and ground substance (represented by the parameter c) control the material response in the lower stretch regime rather, whereas k_1 and k_2 (the parameters of the collagen function) govern the behavior at higher strains.

Although the constitutive model adapted here for alveolar walls is widely accepted in soft tissue mechanics, it has to be again emphasized that viscous effects are likely to play an important role. Fortunately, the developed alveolar model is by no means restricted to the presented material law. Hence, extensions to visco-elasticity can be integrated in the future.

3.2.4 Remark on residual stresses

It is well-known that most soft biological tissues are not stress-free in their unloaded configuration. For instance, after cutting in radial direction, excised arterial segments spring

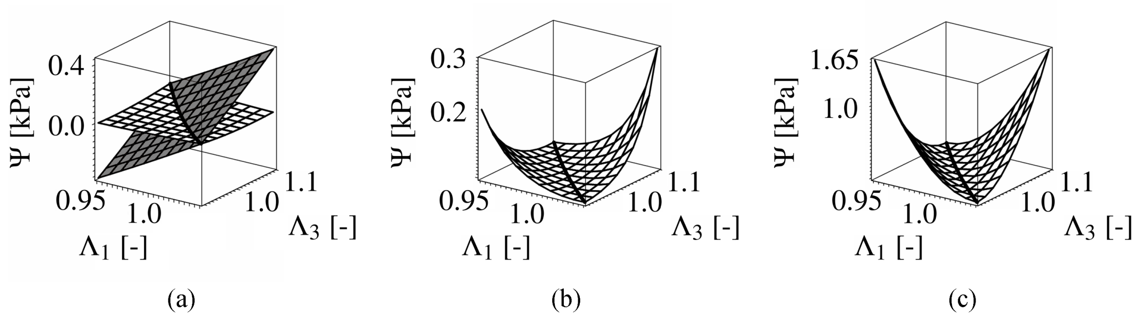

Figure 3.2.1: Contributions to the overall potential depending on the stretches $\Lambda_1 = \Lambda_2$ and Λ_3. The thick black curve indicates the incompressible state of uniaxial deformation in each plot. (a) Potential of the ground substance $\bar{\Psi}^{\mathrm{gs}}$ (white) compared to a standard Neo-Hookean material Ψ^{NH} (gray). (b) Potential of the collagen fiber network $\bar{\Psi}^{\mathrm{fib}}$. (c) Potential of the penalty function U.

open into sectors corresponding to their zero-stress state (Fung, 1981). The consideration of so-called residual stresses is essential for the determination of both realistic stresses and strains. Therefore, in their simulation of arterial behavior, Holzapfel et al. (2000) started with the open sector of an idealized artery which was then closed by an initial bending to arrive at the load-free, but stressed cylindrical configuration. In case of alveolar tissue, the relevance of residual stresses is not definitively proven. Due to the small dimensions of alveolar walls, experiments demonstrating a “spring open” effect are not feasible. In many photomicrographs of excised lung tissue in the literature, alveolar walls seem to be buckled. For instance, Gil et al. (1979) studied the geometry of peripheral airspaces in air- and saline-filled rabbit lungs. In the latter case, interfacial phenomena are absent and alveolar morphology is governed predominantly by tissue tensions. They found that alveolar septa in saline-filled lungs appear undulated at low and medium inflation levels, suggesting that substantial parts of the connective tissue network are at their resting lengths. However, Fung (1981) argued that the observed wrinkling of alveolar tissue is an artifact attributed to the incomplete fixation of elastin fibers. If the tissue is fixed in a state of tension, e.g. in the inflated lung, and then sectioned in the absence of loads, the residual stresses in the elastin are released and the fibers shrink to their length at a zero-stress state. The fixed part of the tissue is then wrinkled by the shortening of the elastin fibers. Consequently, no conclusions with regard to the presence of residual stresses can be drawn from these photomicrographs. Likewise, Sobin et al. (1988) reported that in many hundreds slices of quick-frozen lung tissue, they found no fibers folding or pleating.

Since the question as to whether residual stresses are present in lung tissue cannot be answered conclusively, it seems reasonable to assume that alveolar walls are stress-free in the unloaded configuration. In the in vivo situation, however, alveolar tissue is always prestressed by the negative pleural pressure that keeps the lungs expanded. The exact amount of prestress in individual alveolar walls, though, is not known. Therefore, any approach to imposing an imprinted stress state due to pleural pressure directly in the alveolar model seems to be futile. However, the computational model developed within this thesis is not

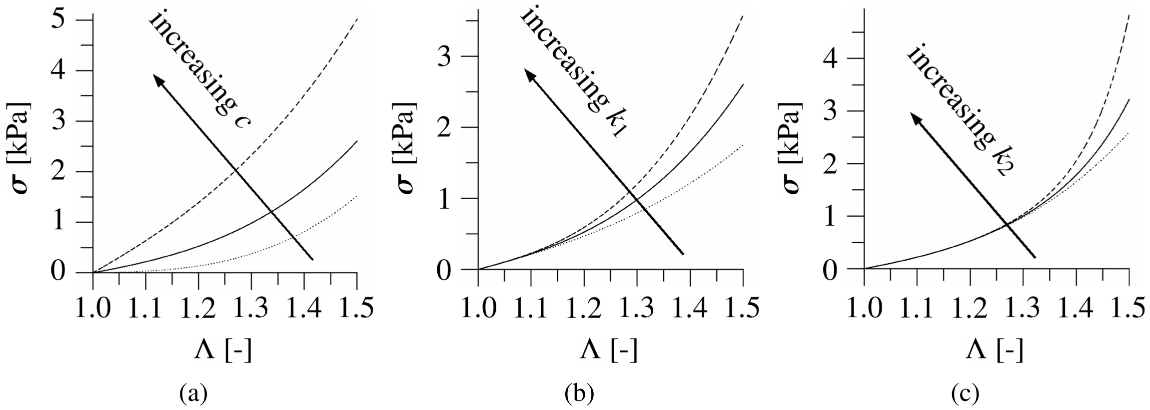

Figure 3.2.2: Influence of material parameters on the appearance of the stress-stretch curve in case of uniaxial tension. (a) Variation of parameter c (dotted line: $c = 0.1$ kPa; solid line: $c = 1$ kPa; dashed line: $c = 3$ kPa). (b) Variation of parameter k_1 (dotted line: $k_1 = 30$ kPa; solid line: $k_1 = 76.5$ kPa; dashed line: $k_1 = 130$ kPa). (c) Variation of parameter k_2 (dotted line: $k_2 = 13.5$; solid line: $k_2 = 200$; dashed line: $k_2 = 500$).

restricted to the alveolar level but, eventually, comprises the lung as a whole. Hence, pleural pressure can be applied to the overall parenchyma model presented in chapter 4 using a prestressing technique as proposed by Gee et al. (2010). Their modified updated Lagrangian formulation (MULF) was shown to yield physically meaningful results on complex three-dimensional models of aortic aneurysms. In this case, the geometry obtained from medical imaging is also not stress-free but represents a predeformed spatial configuration loaded by the blood pressure. To account for this prestressing, they performed a load-controlled calculation where the structure does not deform but builds up an imprinted deformation gradient and, thereby, also an initial stress state which is in equilibrium with the imposed blood pressure. In the future, MULF – which is available in the FE code BACI – can be applied to the developed multi-scale parenchyma model to account for the effect of pleural pressure. This methodology will enable the simulation of physiologically reasonable stresses also in locally resolved alveoli.

3.3 Interfacial phenomena

As already discussed in section 1.1.2.3, alveolar walls are covered by a continuous surfactant film which is assumed to influence the overall mechanical behavior significantly. In order to ensure that the developed computational model is of predictive value, the interaction of tissue and liquid lining mechanics needs to be considered. In this section, a corresponding computational framework will be derived. After a short introduction into the fundamentals of interfacial phenomena, a novel approach to considering general surface stress effects in the context of the FEM will be proposed. Subsequently, an elaborate surfactant model enabling the determination of local surface stresses will be presented. Important features of the presented methodology will be illustrated by selected numerical examples.

3.3.1 The concept of surface stress

All interfacial phenomena originate from complex molecular interactions between different phases. Molecules at an interface are in an energetically unfavorable state compared to those in the bulk due to reduced intermolecular attractions. As a consequence, surface stresses arise that tend to minimize the surface area and, by this means, also the interfacial energy. Surface phenomena manifest themselves in many ways such as the surface tension of water, the separation of two immiscible liquids after shaking, or the resulting contact angle when a droplet of water is placed on a solid surface (Hills, 1999). In this section, a short summary of existing terminology will be given. A more detailed introduction into the physics of surfaces can be found e.g. in Butt et al. (2003).

When considering interfacial effects, different mechanisms of surface area change have to be distinguished. In case of an ideal liquid, the area per molecule A_{mol} always remains constant and the number of interfacial molecules N_{mol} changes proportional to the surface area (cf. Figure 3.3.1(a)). For an ideal solid, however, this so-called plastic area change is not the only possible process since relaxation occurs much slower and, more importantly, only after a yield strength is exceeded. Therefore, elastic changes of surface area can also occur. In this case, the distance between neighboring molecules – and, thus, also the area per molecule A_{mol} – changes while the number of interfacial molecules N_{mol} remains constant (see Figure 3.3.1(b)).

To consider this in more detail, a simple example will be discussed in the following. In case of a one-dimensional interface, the overall scalar interface strain reads

$$\varepsilon = \frac{\mathsf{d}A}{A} = \varepsilon_{\mathsf{p}} + \varepsilon_{\mathsf{e}} \tag{3.3.1}$$

where A denotes the surface "area" and ε_{p}, ε_{e} refer to the plastic and elastic surface strains, respectively. With each surface molecule, an excess energy E_{mol} can be associated. In a one-component system, the surface tension $\hat{\gamma}$ equals the specific free surface energy, i.e.

$$\hat{\gamma} = \frac{E_{\mathsf{mol}}}{A_{\mathsf{mol}}} = \frac{N_{\mathsf{mol}} E_{\mathsf{mol}}}{A}. \tag{3.3.2}$$

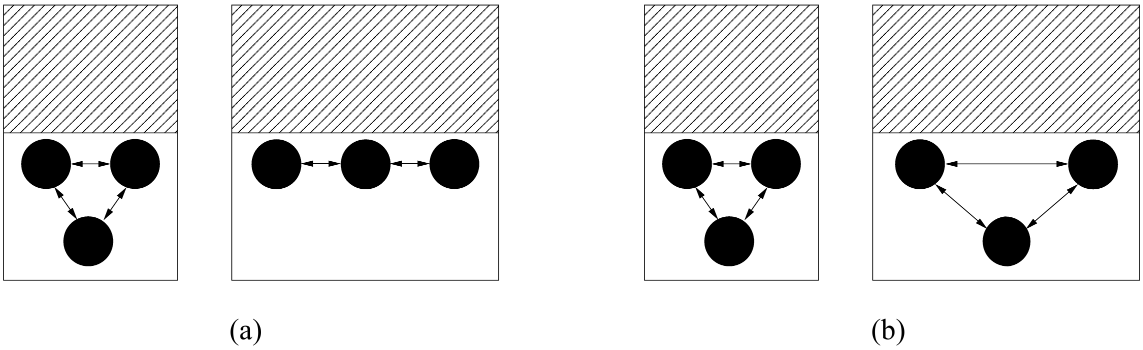

Figure 3.3.1: Different mechanisms of surface area change. (a) Ideally plastic area change with constant area per molecule A_{mol} and variable number of interfacial molecules N_{mol}. (b) Ideally elastic area change with constant number of interfacial molecules N_{mol} and variable area per molecule A_{mol}.

This central thermodynamic quantity corresponds to the reversible work required to create unit area of surface at constant temperature, volume, and chemical potentials (Vermaak et al., 1968). Based on the surface tension (3.3.2), the infinitesimal increase in free energy related to the stretching of an interface equals

$$\begin{aligned} \mathrm{d}\mathcal{W}^{\mathsf{surf}} &= \mathrm{d}(N_{\mathsf{mol}}E_{\mathsf{mol}}) = \left(\hat{\gamma} + \frac{\partial\hat{\gamma}}{\partial A}A\right)\mathrm{d}A = \left(\hat{\gamma} + \frac{\partial\hat{\gamma}}{\partial\varepsilon}\right)\mathrm{d}A = \\ &= \gamma\,\mathrm{d}A \end{aligned} \tag{3.3.3}$$

where γ denotes the surface stress given by

$$\gamma = \hat{\gamma} + \frac{\partial\hat{\gamma}}{\partial\varepsilon}. \tag{3.3.4}$$

This most general relation between surface stress and surface tension simplifies to

$$\gamma_{\mathsf{p}} = \hat{\gamma} \tag{3.3.5}$$

in case of an ideally plastic area change or

$$\gamma_{\mathsf{e}} = \hat{\gamma} + \frac{\partial\hat{\gamma}}{\partial\varepsilon_{\mathsf{e}}} \tag{3.3.6}$$

if the area change is purely elastic.

In the general multi-dimensional case, surface stresses are tensorial quantities, whereas surface tension is a scalar. However, within this work only isotropic interfacial effects are considered so that equations (3.3.3) and (3.3.4) are sufficient for the characterization of surface energy changes. The surface stress can then be interpreted as a force per unit length of exposed edge which must be applied to a terminating surface in order to keep it in equilibrium (Vermaak et al., 1968). That is why γ has often been referred to as

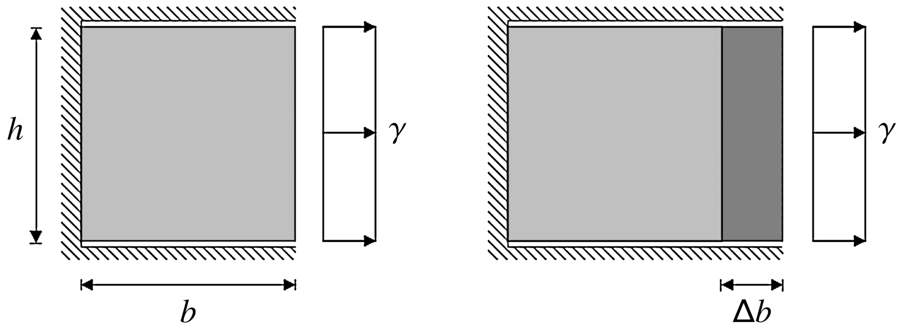

Figure 3.3.2: Surface change of a planar surface constrained along three edges. The absolute value of the surface force resultant is γh and, correspondingly, the surface work done equals $\gamma h \Delta b = \gamma \Delta A$.

"surface tension", thereby contributing to the widely spread confusion in the literature. γ is tangential to the interface and, in the isotropic case, perpendicular to every cut edge (see Figure 3.3.2).

The effect of interface curvature can be illustrated using the example of a spherical droplet. If the radius r is increased by an increment $\mathsf{d}r$, the droplet's volume and surface area changes are given by

$$\mathsf{d}V = \frac{4}{3}\pi(r+\mathsf{d}r)^3 - \frac{4}{3}\pi r^3 \approx 4\pi r^2 \mathsf{d}r \tag{3.3.7}$$

$$\mathsf{d}A = 4\pi(r+\mathsf{d}r)^2 - 4\pi r \approx 8\pi r \mathsf{d}r \tag{3.3.8}$$

where higher order terms in $\mathsf{d}r$ have been neglected. The associated variation of the interfacial energy (3.3.3) needs to be compensated by a pressure difference p between the two phases, i.e.

$$\gamma \mathsf{d}A = p \mathsf{d}V. \tag{3.3.9}$$

Introduction of $\mathsf{d}V$ (3.3.7) and $\mathsf{d}A$ (3.3.8) into relation (3.3.9) then yields the well-known Laplace-Young equation for a spherical interface

$$p = \frac{2\gamma}{r}. \tag{3.3.10}$$

By mistake, this relation has frequently been used to deduce $\hat{\gamma}$ from experiments. Despite converse claims, however, measurements of surface stress, but not surface tension, are possible from the effect of hydrostatic pressure if the area change is not purely plastic (Vermaak et al., 1968). This finding also has to be considered when experimental results concerning the interfacial properties of surfactant should be assessed.

After this short general introduction into interfacial phenomena, now the computational modeling in the context of the FEM can be addressed.

3.3.2 Coupling of solid and interfacial mechanics

In the literature, different approaches to modeling multi-phase problems including the effects of surface stresses have been proposed. Olson and Kock (1994), for instance, simply added the additional surface work (3.3.3) to the existing variational formulation for inviscid fluids. In most other computational fluid dynamics (CFD) models, though, a modified traction boundary condition based on the generalized Laplace-Young equation has been applied at the interface, i.e.

$$\boldsymbol{\sigma} \cdot \boldsymbol{n} = -p_{\mathrm{int}}\boldsymbol{n} = -p_{\mathrm{ext}}\boldsymbol{n} + \kappa\gamma\boldsymbol{n} \qquad (3.3.11)$$

with κ denoting the interface curvature (cf. e.g. Chessa and Belytschko (2003) and Dettmer and Peric (2005)). Although above formulation is equivalent to the surface work in case of curved interfaces (see equation (3.3.9) for a verification in the spherical case), the treatment of planar surfaces is not possible with this approach. Furthermore, direct computation of κ is difficult for linear FE shape functions since the involved second derivatives vanish in the element interiors. According to Gross and Reusken (2007), however, inadequate approximation of the surface force terms often leads to unphysical oscillations of the velocity vector at the interface. Adami et al. (2010) avoided the calculation of the surface curvature in their smoothed particle hydrodynamics (SPH) model by rewriting the surface traction as a gradient of a stress tensor. This tensor was defined in a transition region between the two phases which approximated the actual, sharp interface. In the resulting continuous surface force model, tangential surface stress gradient forces were additionally considered. These so-called Marangoni forces were also considered by Wei et al. (2005) in their simplified two-dimensional model of an alveolus partially filled with liquid.

The CFD approaches mentioned above are based on the explicit modeling and discretization of all liquid phases involved. The alveolar model developed within this thesis, however, is primarily aimed at quantifying in vivo stresses and strains in the septal walls. Therefore, the detailed modeling of the covering fluid film is of little interest, except inasmuch as it influences the overall behavior. Due to its small thickness, the main effect of the liquid lining on alveolar mechanics can essentially be attributed to interfacial phenomena. Assuming that the impact of the solid-liquid interface is negligible, considerations can be restricted to the surface stresses in the surfactant layer. Following this line of argument, two basic modeling strategies have been established in the past. The first one is based on adding the liquid-gas interfacial energy to the SEF of alveolar tissue (see e.g. Lanir (1983) and Kowalczyk and Kleiber (1994)). This easy-to-implement approach is, however, restricted to membrane discretizations of the alveolar septa. In case of a continuum tissue model, the additional SEF would also be taken into account in the bulk of the walls, thereby spuriously increasing the surface force resultant. The second strategy involves the formulation of an interface FE accounting for the surface stresses in the surfactant layer. This approach originally proposed by Karakaplan et al. (1980) has been applied in several models of individual alveoli and alveolar ducts (cf. e.g. Kowe et al. (1986) and Denny and Schroter (1997)). So far, however, only triangular (i.e. planar) interface elements have been utilized in combination with discrete fiber models (cf. section 3.2.2).

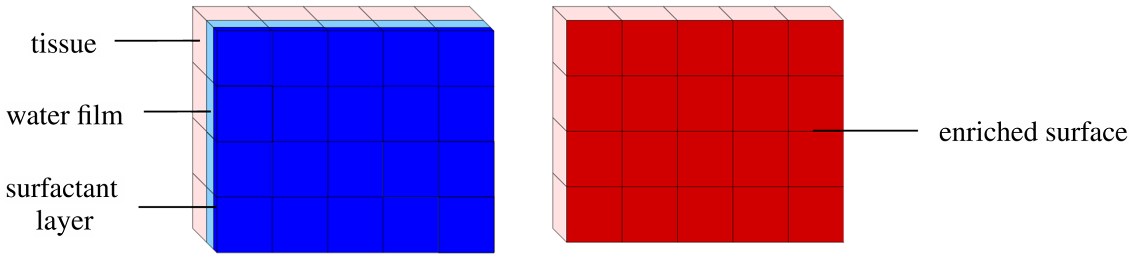

Figure 3.3.3: Left: Schematic of the actual configuration including FE discretization of the alveolar wall, aqueous fluid film, and covering surfactant layer. Right: Simplified FE model based on including the interfacial energy of the surfactant layer in the surface of the alveolar wall.

As part of this work, the basic concept of a surface stress element has been developed further and integrated in the alveolar model. Since an isolated surface stress element as suggested by Karakaplan et al. (1980) degenerates to an ideal point without appropriate boundary conditions, it seems more sensible to establish a direct coupling between bulk and interface mechanics. That is why the novel approach proposed here is based on including the interfacial energy of the surfactant layer in the surfaces of the alveolar wall model (see Figure 3.3.3). According to equation (3.3.3), the corresponding additional infinitesimal work done by the surface stresses γ is defined by

$$\mathsf{d}\mathcal{W}^{\mathsf{surf}} = \gamma\,\mathsf{d}A \tag{3.3.12}$$

with $\mathsf{d}A$ representing the change in infinitesimal interface area in the deformed configuration. In this context, the surface area of the surfactant-air interface and the alveolar wall are assumed to be identical due to the small thickness of the liquid lining. The overall surface work can be determined by integrating $\mathsf{d}\mathcal{W}^{\mathsf{surf}}$ (3.3.12), i.e.

$$\mathcal{W}^{\mathsf{surf}} = \int_{A_0}^{A} \gamma\,\mathsf{d}A^* \tag{3.3.13}$$

where A and A_0 denote the current and reference surface area, respectively. Hence, the limits in equation (3.3.13) already indicate that integration is performed over area changes and not the current surface area. After discretization in space, the surface work for an individual element located at the alveolar surface correspondingly reads

$$\mathcal{W}^{\mathsf{surf}(e)} = \int_{A_0^{(e)}}^{A^{(e)}} \gamma^{(e)}\mathsf{d}A^* \tag{3.3.14}$$

where γ is assumed to be constant within the surface element. Although a continuous distribution of surface stresses is also possible, this approach – which follows the original formulation of Karakaplan et al. (1980) – has been chosen here for simplicity. The variation of the overall surface work (3.3.14) then takes the following form

$$\delta\mathcal{W}^{\mathsf{surf}(e)} = \frac{\partial}{\partial\mathbf{d}^{(e)}}\left(\int_{A_0^{(e)}}^{A^{(e)}} \gamma^{(e)}\mathrm{d}A^*\right)\delta\mathbf{d}^{(e)} = \\ = \frac{\partial}{\partial A^{(e)}}\left(\int_{A_0^{(e)}}^{A^{(e)}} \gamma^{(e)}\mathrm{d}A^*\right)\frac{\partial A^{(e)}}{\partial\mathbf{d}^{(e)}}\delta\mathbf{d}^{(e)}. \tag{3.3.15}$$

Application of the fundamental theorem of calculus to equation (3.3.15) yields

$$\delta\mathcal{W}^{\mathsf{surf}(e)} = \gamma^{(e)}\frac{\partial A^{(e)}}{\partial\mathbf{d}^{(e)}}\delta\mathbf{d}^{(e)} = \mathbf{f}^{\mathsf{surf(e)}}\delta\mathbf{d}^{(e)} \tag{3.3.16}$$

where $\mathbf{f}^{\mathsf{surf(e)}}$ has been introduced as the surface stress resultant vector. At the alveolar wall surface, the equilibrium equation (2.1.78) is complemented by $\mathbf{f}^{\mathsf{surf(e)}}$ evaluated at the generalized mid-point. In this context, the following approximation of the surface stresses is made

$$\gamma^{(e)}_{n+1-\alpha_\mathrm{f}} = (1-\alpha_\mathrm{f})\gamma^{(e)}_{n+1} + \alpha_\mathrm{f}\gamma^{(e)}_{n}. \tag{3.3.17}$$

Accordingly, the index notation of $\mathbf{f}^{\mathsf{surf}(e)}_{n+1-\alpha_\mathrm{f}}$ at node I is given by

$$\left(\mathsf{f}^{\mathsf{surf}}_{I;r}\right)^{(e)}_{n+1-\alpha_\mathrm{f}} = \left(\gamma\frac{\partial A}{\partial\mathsf{d}_{I;r}}\right)^{(e)}_{n+1-\alpha_\mathrm{f}} \tag{3.3.18}$$

with r denoting the respective coordinate direction.

The iterative solution of the modified equilibrium equation by means of Newton's method necessitates the linearization of the surface force (3.3.18). In addition to the nonlinearity of the interfacial area A, a possible nonlinearity of $\gamma^{(e)}$ also needs to be taken into account (cf. equation (3.3.4)). The derivative of the surface stresses (3.3.17) with respect to the nodal displacements at the generalized mid-point in general reads

$$\left(\frac{\partial\gamma}{\partial\mathbf{d}}\right)^{(e)}_{n+1-\alpha_\mathrm{f}} = (1-\alpha_\mathrm{f})\frac{\partial\gamma^{(e)}_{n+1}}{\partial\mathbf{d}^{(e)}_{n+1-\alpha_\mathrm{f}}}. \tag{3.3.19}$$

For the sake of lucidity, the nonlinear iteration step is omitted here. In view of the surfactant constitutive model presented in detail in section 3.3.3, a reformulation of equation (3.3.19) in terms of the interfacial area is convenient, i.e.

$$\left(\frac{\partial\gamma}{\partial\mathbf{d}}\right)^{(e)}_{n+1-\alpha_\mathrm{f}} = (1-\alpha_\mathrm{f})\frac{\partial\gamma^{(e)}_{n+1}}{\partial A^{(e)}_{n+1}}\frac{\partial A^{(e)}_{n+1}}{\partial\mathbf{d}^{(e)}_{n+1}}\underbrace{\frac{\partial\mathbf{d}^{(e)}_{n+1}}{\partial\mathbf{d}^{(e)}_{n+1-\alpha_\mathrm{f}}}}_{(1-\alpha_\mathrm{f})^{-1}} = \\ = \left(\frac{\partial\gamma}{\partial A}\right)^{(e)}_{n+1}\left(\frac{\partial A}{\partial\mathbf{d}}\right)^{(e)}_{n+1}. \tag{3.3.20}$$

The overall surface stress contribution to the effective dynamic stiffness matrix (2.1.81) is then obtained as

$$\begin{aligned}\left(\mathsf{K}^{\mathsf{surf}}_{(I;r)(J;s)}\right)^{(e)}_{n+1} &= (1-\alpha_{\mathrm{f}})\left(\mathsf{K}^{\mathsf{surf}}_{(I;r)(J;s)}\right)^{(e)}_{n+1-\alpha_{\mathrm{f}}} = \\ &= (1-\alpha_{\mathrm{f}})\left(\left(\gamma\frac{\partial^2 A}{\partial \mathsf{d}_{I;r}\partial \mathsf{d}_{J;s}}\right)_{n+1-\alpha_{\mathrm{f}}} + \left(\frac{\partial\gamma}{\partial A}\frac{\partial A}{\partial \mathsf{d}_{J;s}}\right)_{n+1}\left(\frac{\partial A}{\partial \mathsf{d}_{I;r}}\right)_{n+1-\alpha_{\mathrm{f}}}\right)^{(e)}.\end{aligned} \quad (3.3.21)$$

In contrast to previous interface FE formulations, the restriction to triangular surface discretizations is lifted here. Following the derivations in section 2.1.1, the area of the arbitrarily curved surface of an alveolar wall element is in general given by

$$A^{(e)} = \int_{-1}^{1}\int_{-1}^{1}\sqrt{\tilde{n}_1^2+\tilde{n}_2^2+\tilde{n}_3^2}\,\mathsf{d}\xi_1\mathsf{d}\xi_2 = \int_{-1}^{1}\int_{-1}^{1}|\tilde{\boldsymbol{n}}|\,\mathsf{d}\xi_1\mathsf{d}\xi_2. \quad (3.3.22)$$

The derivative of the element surface area with respect to the displacement in s-direction at node I reads

$$\left(\frac{\partial A}{\partial \mathsf{d}_{I;s}}\right)^{(e)} = \int_{-1}^{1}\int_{-1}^{1}\frac{\partial|\tilde{\boldsymbol{n}}|}{\partial \mathsf{d}_{I;s}}\mathsf{d}\xi_1\mathsf{d}\xi_2 \quad (3.3.23)$$

with

$$\frac{\partial|\tilde{\boldsymbol{n}}|}{\partial \mathsf{d}_{I;s}} = \frac{1}{|\tilde{\boldsymbol{n}}|}\left(\tilde{n}_r\frac{\partial\tilde{n}_r}{\partial \mathsf{d}_{I;s}} + \tilde{n}_t\frac{\partial\tilde{n}_t}{\partial \mathsf{d}_{I;s}}\right). \quad (3.3.24)$$

Thereby, the directions $r,s,t \in \{1,2,3\}$ are mutually distinct, i.e. $s \neq r$, $t \neq r$, and $s \neq t$. By way of example, the derivative of $\tilde{n}_r$ with respect to the displacement $d_{I;s}$ is given by

$$\frac{\partial\tilde{n}_r}{\partial \mathsf{d}_{I;s}} = \mathscr{E}_{rst}\frac{\partial}{\partial \mathsf{d}_{I;s}}\left(\frac{\partial x_s}{\partial\xi_1}\frac{\partial x_t}{\partial\xi_2} - \frac{\partial x_s}{\partial\xi_2}\frac{\partial x_t}{\partial\xi_1}\right). \quad (3.3.25)$$

The distinction of co- and contravariant components is dropped here for simplicity. $\mathscr{E}_{rst}$ corresponds to the Levi-Civita symbol defined by

$$\mathscr{E}_{rst} = \begin{cases} 0 & \text{if } r=s \text{ or } s=t \text{ or } r=t \\ 1 & \text{if } (r,s,t) \text{ is } (1,2,3) \text{ or } (2,3,1) \text{ or } (3,1,2) \text{ (even permutation)} \\ -1 & \text{if } (r,s,t) \text{ is } (3,2,1) \text{ or } (2,1,3) \text{ or } (1,3,2) \text{ (odd permutation).} \end{cases} \quad (3.3.26)$$

Introducing

$$\frac{\partial x_s}{\partial\xi_l} = \sum_{J=1}^{\mathsf{nnod}}\left(\frac{\partial N_J}{\partial\xi_l}\mathsf{x}_{J;s}\right) = \sum_{J=1}^{\mathsf{nnod}}\left[\frac{\partial N_J}{\partial\xi_l}(\mathsf{x}_{0;J;s}+\mathsf{d}_{J;s})\right] \quad (3.3.27)$$

into equation (3.3.25) finally results in

$$\frac{\partial\tilde{n}_r}{\partial \mathsf{d}_{I;s}} = \mathscr{E}_{rst}\left(\frac{\partial N_I}{\partial\xi_1}\sum_{J=1}^{\mathsf{nnod}}\left(\frac{\partial N_J}{\partial\xi_2}\mathsf{x}_{J;t}\right) - \frac{\partial N_I}{\partial\xi_2}\sum_{J=1}^{\mathsf{nnod}}\left(\frac{\partial N_J}{\partial\xi_1}\mathsf{x}_{J;t}\right)\right). \quad (3.3.28)$$

The derivative of $\tilde{n}_t$ with respect to the displacement $\mathsf{d}_{I;s}$ can be determined analogously.

For the calculation of the stiffness matrix (3.3.21), the second derivative of the surface area with respect to the displacements is needed. From equation (3.3.23), this term is determined by

$$\left(\frac{\partial^2 A}{\partial \mathsf{d}_{I;s} \partial \mathsf{d}_{J;t}}\right)^{(e)} = \int_{-1}^{1} \int_{-1}^{1} \frac{\partial^2 |\tilde{\boldsymbol{n}}|}{\partial \mathsf{d}_{I;s} \partial \mathsf{d}_{J;t}} \mathsf{d}\xi_1 \mathsf{d}\xi_2 \tag{3.3.29}$$

with

$$\frac{\partial^2 |\tilde{\boldsymbol{n}}|}{\partial \mathsf{d}_{I;s} \partial \mathsf{d}_{J;t}} = -\frac{1}{|\tilde{\boldsymbol{n}}|} \frac{\partial |\tilde{\boldsymbol{n}}|}{\partial \mathsf{d}_{I;s}} \frac{\partial |\tilde{\boldsymbol{n}}|}{\partial \mathsf{d}_{J;t}} + \frac{1}{|\tilde{\boldsymbol{n}}|} \left(\frac{\partial \tilde{n}_r}{\partial \mathsf{d}_{I;s}} \frac{\partial \tilde{n}_r}{\partial \mathsf{d}_{J;t}} + \tilde{n}_r \frac{\partial^2 \tilde{n}_r}{\partial \mathsf{d}_{I;s} \partial \mathsf{d}_{J;t}} \right). \tag{3.3.30}$$

The second derivative of $\tilde{n}_r$ is given by

$$\frac{\partial^2 \tilde{n}_r}{\partial \mathsf{d}_{I;s} \partial \mathsf{d}_{J;t}} = \mathscr{E}_{rst} \left(\frac{\partial N_I}{\partial \xi_1} \frac{\partial N_J}{\partial \xi_2} - \frac{\partial N_I}{\partial \xi_2} \frac{\partial N_J}{\partial \xi_1} \right). \tag{3.3.31}$$

In practice, the index pairs utilized above are substituted by global DOF identifiers. Introducing $\mathsf{ndim} = 3$ as the number of spatial dimensions, the global ID z can be determined from $(I;r)$ via

$$(I;r) \rightarrow z = \mathsf{ndim} \cdot I + r. \tag{3.3.32}$$

The methodology developed for considering the effect of interfacial energy applies to essentially any kind of thin liquid film. In case of an ideal fluid lining, some expressions simplify due to the constancy of surface stresses. For the more complicated surfactant film, corresponding derivations are presented in the following.

3.3.3 Modeling of surface active agents

Due to their particular amphiphilic structure, surfactant molecules in the aqueous alveolar lining migrate to the liquid-gas interface where they form a buffer zone between the two phases (cf. Figure 1.1.5). As a consequence, the free energy of the surfactant-solvent system is significantly decreased (Otis et al., 1994). The effective surface stress depends on the interfacial concentration of surfactant, which is governed by various factors including the rate and the history of the surface strain. During breathing, the liquid lining cyclically expands and contracts, resulting in a periodic variation in interfacial surfactant concentration and, thereby, also surface stress. When plotted against interfacial area, the surface stress typically forms a hysteresis loop, revealing the complex nonlinear behavior of surfactant.

Several surfactant constitutive models allowing for the determination of the surface stress have been reported in the literature. In many cases, separate pseudo-elastic functions for the inflation and deflation paths of selected hysteresis loops have been utilized. This approach was pursued by Kimmel and Budiansky (1990) who assumed γ to be uniform over the faces of their dodecahedron model, but permitted to vary with the total surface area. By comparing their simulation results with experimentally derived pressure-volume curves, the parameter for the deflation branch was derived. Kowe et al. (1986) formulated the surface stresses as exponential functions of local area changes. A similar path-dependent model was also utilized by Denny and Schroter in their first studies on alveolar duct models (Denny and Schroter, 1995, 1997). A major drawback of these pseudo-elastic functions is the fact that usually only one experimentally derived hysteresis loop is fitted. Hence, utilization of these functions for surface area ratios other than the measured one necessitates scaling of the curves (cf. e.g. Kojic et al. (2006)). Moreover, consideration of different surface area strain rates is in general not possible.

More accurate models have been developed based on the consideration of time-dependent surfactant transport between bulk film and interface. For example, Archie (1973) suggested an inverse relation between the interfacial surfactant concentration calculated from a diffusion equation and the surface stress. However, his simplified model was aimed at predicting spatial average values for the lung as a whole and not for individual alveoli. Wei et al. (2005) combined semianalytical and numerical techniques to determine the flow field and sorption-controlled surfactant transport in a thick fluid film subject to prescribed breathing motions. The surface stress was then assumed to be a linear function of the calculated surfactant concentration. For characterizing the steady-state oscillatory behavior of surfactant, Otis et al. (1994) proposed a transport model considering adsorption, desorption, and squeeze-out processes. To relate surfactant concentration and surface stress, they formulated a piecewise linear relation. Due to its good agreement with experimental measurements, the Otis model has been widely used for simulating surfactant dynamics. For instance, Denny and Schroter utilized this approach in their later studies on alveolar duct mechanics (Denny and Schroter, 2000, 2006). Morris et al. (2001) extended the Otis model to allow for diffusion processes in the liquid phase. Recently, Adami et al. (2010) additionally included diffusion of surfactant on the interface in their detailed model of the alveolar liquid lining. A slightly different approach was followed by Krueger and Gaver (2000) who claimed that the consideration of multilayer dynamics is necessary to mimic the ultralow surface stresses of surfactant. They established an analytical model for a bilayer system including also film collapse and respreading. A rather complicated piecewise defined equation of state was proposed to correlate the surfactant concentration and the corresponding surface stress. In contrast to the purely adsorption-limited approach proposed by Otis et al. (1994), the latter more sophisticated models enable the consideration of varying bulk surfactant concentrations due to transport processes.

For the alveolar model developed within this thesis, a suitable compromise between accuracy and simplicity must be found. Pseudo-elastic functions that need to be adapted to each particular application are deemed inappropriate. Therefore, a transport model is chosen to reasonably describe dynamic surfactant behavior during ventilation. As noted by Krueger and Gaver (2000), the qualitative agreement of the Otis model with experimental data demonstrates that significant properties of the hysteresis loop can be attributed to adsorption and desorption alone. In this work, therefore, the Otis model is favored over the more complex approaches considering diffusion or multi-layer phenomena. Subsequently, the chosen model and its implementation in the context of the FE approach presented in section 3.3.2 will be discussed in more detail.

Originally, the Otis model was developed for simulating γ-A measurements of the semi-

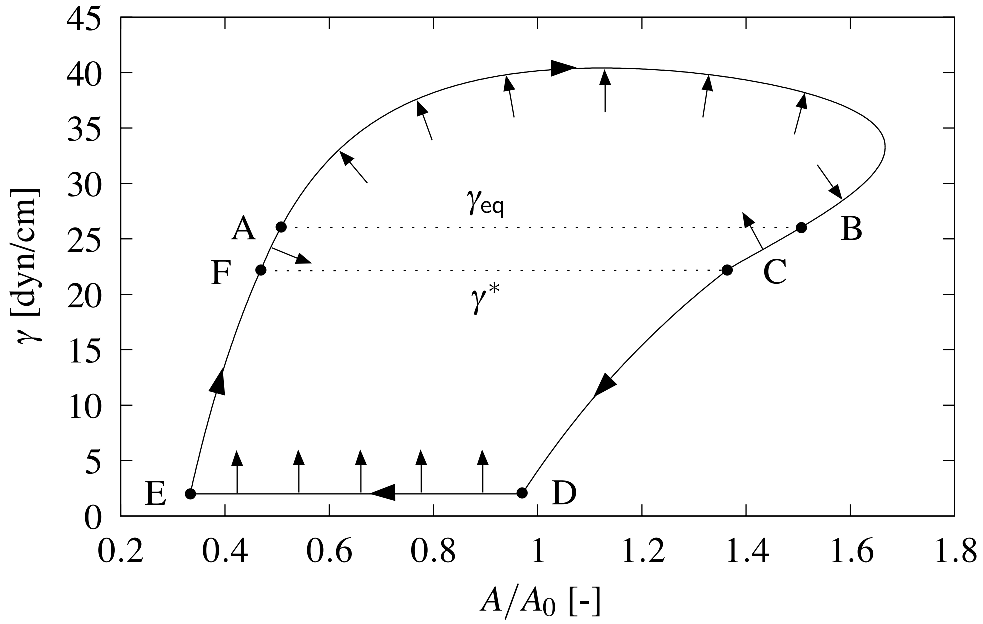

Figure 3.3.4: Typical surface stress versus normalized area loop demonstrating surfactant transport mechanisms in the different regimes. First regime ($\gamma \geq \gamma^*$): kinetic adsorption (segment A-B) or desorption (segments B-C and F-A). Second regime ($\gamma_{\mathrm{min}} < \gamma < \gamma^*$): insoluble monolayer (segments C-D and E-F). Third regime ($\gamma = \gamma_{\mathrm{min}}$): squeeze-out (segment D-E). The direction of the loop is indicated by tangential arrow heads. Outward and inward normal arrows represent transport of surfactant to the interface (i.e. adsorption) and from the interface (i.e. desorption/squeeze-out), respectively.

synthetic surfactant TA performed using a pulsating bubble surfactometer (PBS). A small spherical bubble of air was formed at the lower end of a 0.4 mm capillary in a suspension containing surfactant. The bubble volume was cycled while measuring the current bubble pressure. From the Laplace-Young equation (3.3.10), the corresponding surface stress γ was determined. A typical surface stress vs. normalized area loop (generated using the model described in the following) is shown in Figure 3.3.4. As already mentioned, Otis et al. (1994) assumed that transport of surfactant is adsorption-limited, i.e. diffusional processes occur on a time scale much shorter than those for sorption. As a consequence, the bulk suspension is considered to be well mixed at any time at a constant bulk concentration $\bar{C}$. The kinetics of surfactant transport is defined by three interfacial concentration (Γ) regimes. Γ can be thought of as the mass of surfactant or the number of occupied binding sites per unit interfacial area.

Within the first regime, Γ is less than the maximum equilibrium concentration Γ^* and surfactant transport is modeled using Langmuir kinetics. This approach is based on the assumption that all adsorption sites are equivalent and intermolecular interactions in the adsorbed layer can be neglected. Hence, the probability of adsorption to an empty site does not depend on the presence of molecules at the surrounding sites (von Bahr, 2003).

Consequently, adsorption is proportional to the number of available sites on the interface $\Gamma^* - \Gamma$ whereas desorption is proportional to the number of occupied sites Γ. After normalization with Γ^*, the temporal development of the mass of interfacial surfactant molecules ΓA can then be modeled as

$$\begin{aligned}\frac{\mathrm{d}}{\mathrm{d}t}\left(\frac{\Gamma A}{\Gamma^*}\right) &= A\left(\alpha_1 \bar{C}\left(1-\frac{\Gamma}{\Gamma^*}\right)-\alpha_2\frac{\Gamma}{\Gamma^*}\right) = \\ &= \alpha_1\bar{C}A - \alpha_1\bar{C}\left(\frac{\Gamma}{\Gamma^*}A\right) - \alpha_2\left(\frac{\Gamma}{\Gamma^*}A\right). \qquad (3.3.33)\end{aligned}$$

Here, α_1 and α_2 are the adsorption and desorption coefficient, respectively, whereas $\bar{C}$ refers to the constant bulk concentration of surfactant molecules in the hypophase. At equilibrium, there is no interfacial mass flux and equation (3.3.33) reduces to

$$\frac{\Gamma_{\mathrm{eq}}}{\Gamma^*} = \frac{\alpha_1\bar{C}}{\alpha_1\bar{C}+\alpha_2} \qquad (3.3.34)$$

with Γ_{eq} denoting the equilibrium surfactant concentration. During cyclic loading, however, the normalized mass of surfactant at the interface periodically changes. For time discretization of equation (3.3.33), the Backward Euler approach is utilized in this work. Hence, the corresponding discrete form reads

$$\frac{\Delta\left(\frac{\Gamma A}{\Gamma^*}\right)_{n+1}}{\Delta t} = \alpha_1\bar{C}A_{n+1} - \alpha_1\bar{C}\left(\frac{\Gamma A}{\Gamma^*}\right)_{n+1} - \alpha_2\left(\frac{\Gamma A}{\Gamma^*}\right)_{n+1}. \qquad (3.3.35)$$

Introducing

$$\Delta\left(\frac{\Gamma A}{\Gamma^*}\right)_{n+1} = \left(\frac{\Gamma A}{\Gamma^*}\right)_{n+1} - \left(\frac{\Gamma A}{\Gamma^*}\right)_{n} \qquad (3.3.36)$$

and solving for the normalized mass of surfactant at t_{n+1} yields

$$\left(\frac{\Gamma A}{\Gamma^*}\right)_{n+1} = \frac{\frac{1}{\Delta t}\left(\frac{\Gamma A}{\Gamma^*}\right)_n + \alpha_1\bar{C}A_{n+1}}{\frac{1}{\Delta t}+\alpha_1\bar{C}+\alpha_2}. \qquad (3.3.37)$$

Mutual division by the current interfacial area A_{n+1} finally results in

$$\left(\frac{\Gamma}{\Gamma^*}\right)_{n+1} = \frac{\frac{1}{\Delta t}\left(\frac{\Gamma A}{\Gamma^*}\right)_n + \alpha_1\bar{C}A_{n+1}}{A_{n+1}\left(\frac{1}{\Delta t}+\alpha_1\bar{C}+\alpha_2\right)}. \qquad (3.3.38)$$

For relating the surface stress γ to the nondimensionalized surfactant concentration, Otis et al. (1994) proposed a linear isotherm. Its time-discrete form is defined by

$$\gamma_{n+1} = \gamma_0 - m_1\left(\frac{\Gamma}{\Gamma^*}\right)_{n+1} \qquad (3.3.39)$$

where γ_0 is the reference surface tension of water and m_1 refers to the experimentally derived isotherm slope for the first regime. By means of equations (3.3.38) and (3.3.39), the upper portion of the γ-A loop (segment F-C in Figure 3.3.4) is completely defined. Within this Langmuir regime, surfactant adsorbs to the interface if $\gamma > \gamma_{\mathsf{eq}}$ (corresponding to $\Gamma < \Gamma_{\mathsf{eq}}$) whereas desorption occurs if $\gamma < \gamma_{\mathsf{eq}}$ (conforming with $\Gamma > \Gamma_{\mathsf{eq}}$). For the determination of the consistent tangent stiffness matrix (3.3.21), the surface stress needs to be differentiated with respect to the interfacial area. From equations (3.3.38) and (3.3.39), the corresponding time-discrete derivative is determined by

$$\left(\frac{\partial\gamma}{\partial A}\right)_{n+1} = -m_1 \frac{\partial}{\partial A_{n+1}} \left(\frac{\Gamma}{\Gamma^*}\right)_{n+1} \tag{3.3.40}$$

with

$$\frac{\partial}{\partial A_{n+1}} \left(\frac{\Gamma}{\Gamma^*}\right)_{n+1} = -\frac{\frac{1}{\Delta t}\left(\frac{\Gamma A}{\Gamma^*}\right)_n}{(A_{n+1})^2\left(\frac{1}{\Delta t} + \alpha_1 \bar{C} + \alpha_2\right)}. \tag{3.3.41}$$

Morris et al. (2001) found that in certain situations, the surface stress remains constant at its minimum equilibrium value γ^* while the film is compressed. Hence, the system is unable to reach sufficient interfacial surfactant concentration to enter the next regime. While the compression of the interface raises the concentration by compacting the surface film, it is lowered due to simultaneous desorption of molecules from the interface. The identification of this mechanism could be important for the design of surfactant replacements. Increasing the adsorption rate (which has been considered beneficial for a long time) in general also increases the desorption rate, thereby carrying the risk of surface stresses stagnating at a relatively high level.

Within the second regime, surfactant concentrations range between the maximum equilibrium and the absolute maximum concentration ($\Gamma^* < \Gamma < \Gamma_{\mathsf{max}}$). In this interval, no exchange of surfactant material with the subphase is assumed to occur, so that the monolayer is modeled as insoluble (segments C-D and E-F in Figure 3.3.4). Consequently, the normalized surfactant mass is constant, i.e.

$$\frac{\mathsf{d}\left(\frac{\Gamma A}{\Gamma^*}\right)}{\mathsf{d}t} = 0. \tag{3.3.42}$$

After discretization in time, equation (3.3.42) can be rewritten as

$$\Delta\left(\frac{\Gamma A}{\Gamma^*}\right)_{n+1} = 0. \tag{3.3.43}$$

Introduction of relation (3.3.36) then allows for the determination of the current nondimensionalized surfactant concentration

$$\left(\frac{\Gamma}{\Gamma^*}\right)_{n+1} = \left(\frac{\Gamma}{\Gamma^*}\right)_n \frac{A_n}{A_{n+1}}. \tag{3.3.44}$$

Hence, the concentration changes merely due to variations of interfacial area. Again, surface stresses can be calculated with the help of a linear isotherm. For the second regime, this equation of state is given in its discrete form by

$$\gamma_{n+1} = \gamma^* - m_2\left(\left(\frac{\Gamma}{\Gamma^*}\right)_{n+1} - 1\right) \tag{3.3.45}$$

with m_2 denoting the isotherm slope for the second regime. The time-discrete derivative of the surface stress with respect to the interfacial area is then obtained from equations (3.3.44) and (3.3.45) as

$$\left(\frac{\partial\gamma}{\partial A}\right)_{n+1} = -m_2\frac{\partial}{\partial A_{n+1}}\left(\frac{\Gamma}{\Gamma^*}\right)_{n+1} \tag{3.3.46}$$

with

$$\begin{aligned}\frac{\partial}{\partial A_{n+1}}\left(\frac{\Gamma}{\Gamma^*}\right)_{n+1} &= -\left(\frac{\Gamma}{\Gamma^*}\right)_n \frac{A_n}{(A_{n+1})^2} = \\ &= -\frac{\left(\frac{\Gamma}{\Gamma^*}\right)_{n+1}}{A_{n+1}}.\end{aligned} \tag{3.3.47}$$

Following Morris et al. (2001), the adsorption and desorption coefficient are allowed to drop continuously to zero when approaching Γ^* to facilitate a smooth transition between the Langmuir and the insoluble regime, i.e.

$$\bar{\alpha}_1 = \frac{\alpha_1}{\varsigma}\left(1 - \frac{\Gamma}{\Gamma^*}\right) \qquad \text{if } \frac{\Gamma}{\Gamma^*} > 1 - \varsigma \tag{3.3.48}$$

$$\bar{\alpha}_2 = \frac{\alpha_2}{\varsigma}\left(1 - \frac{\Gamma}{\Gamma^*}\right) \qquad \text{if } \frac{\Gamma}{\Gamma^*} > 1 - \varsigma. \tag{3.3.49}$$

Here, ς is an arbitrarily chosen small number defining the range of concentrations in which the sorption parameters diminish to zero. According to Morris et al. (2001), the specific value of ς does not significantly affect the results of the model except in direct vicinity of the phase transition between both regimes. In the simulations presented within this work, ς was chosen to be 0.02, corresponding to a linear decrease of α_1 and α_2 between $\frac{\Gamma}{\Gamma^*} = 0.98$ and $\frac{\Gamma}{\Gamma^*} = 1.0$.

In the third regime (segment D-E in Figure 3.3.4), Γ equals the maximum concentration Γ_{max} and, accordingly, the surface stress reaches its minimum. Consequently, the following relations hold

$$\left(\frac{\Gamma}{\Gamma^*}\right)_{n+1} = \frac{\Gamma_{\mathsf{max}}}{\Gamma^*} \tag{3.3.50}$$

$$\frac{\partial}{\partial A_{n+1}}\left(\frac{\Gamma}{\Gamma^*}\right)_{n+1} = 0, \tag{3.3.51}$$

$$\gamma_{n+1} = \gamma_{\mathsf{min}}, \tag{3.3.52}$$

$$\left(\frac{\partial\gamma}{\partial A}\right)_{n+1} = 0. \tag{3.3.53}$$

$\alpha_1\bar{C}$ [μs^{-1}]	1.0
α_2 [μs^{-1}]	0.016
m_1 [dyn/cm]	48.0
m_2 [dyn/cm]	140.0
γ_{min} [dyn/cm]	2.0
γ_0 [dyn/cm]	70.0

Table 3.1: Surfactant model parameters utilized within this work.

Since any further decrease of the interfacial area results in a “squeeze-out” of molecules to the bulk fluid, this part of the hysteresis loop is often also referred to as the film collapse regime. Both the second and the third regime can only be reached during dynamic loading. However, while the insoluble state can be maintained during contraction (segment C-D in Figure 3.3.4) as well as extension (segment E-F in Figure 3.3.4) of the interfacial area A, film collapse can only occur if A is compressed. As soon as the interfacial area increases again, the second regime is entered (point E in Figure 3.3.4).

Otis et al. (1994) determined the material constants of the presented model by fitting the simulated γ-A loops to data obtained from their PBS measurements. A summary of parameters utilized in this thesis is given in Table 3.1. Since the accuracy of the PBS is reduced in the low surface stress region (Veldhuizen and Haagsman, 2000), γ_{min} was taken to be 2.0 dyn/cm following Denny and Schroter (2000) rather than 10.0 dyn/cm as proposed by Otis et al. (1994). Figures 3.3.5-3.3.10 illustrate the influence of the distinct parameters on the resulting hysteresis loops when interfacial area is cycled sinusoidally according to

$$A(t) = 1 + \frac{\Delta A}{A_0}\sin\left(2\pi\frac{t}{T}\right) \tag{3.3.54}$$

with $T = 3$ s being the cycle duration, A_0 denoting the original surface area, and $\frac{\Delta A}{A_0} = 0.33$ referring to the nondimensionalized amplitude of area change. In each plot, the solid line corresponds to the standard choice of parameters according to Table 3.1. In Figures 3.3.11 and 3.3.12, different area amplitudes ΔA and cycle times T have been prescribed. The appearance of the simulated γ-A loops varies significantly for different material parameters or prescribed dynamic loadings. Since it is very unlikely that pseudo-elastic functions could model similar effects, the application of the more complicated surfactant transport model seems to be justified. Another particular advantage of the Otis model is the physical meaning of involved material constants. In the literature, several studies addressed pathological changes in the chemical composition of surfactant in ARDS and other diseases (see e.g. Gregory et al. (1991) and Griese (1999)). Corresponding results could be combined with experimental data concerning the specific effect of each constituent (cf. Morris (1998) and Ingenito et al. (1999)), thereby enabling qualitative predictions for the altered behavior of surfactant under cyclic loading in the ARDS lung.

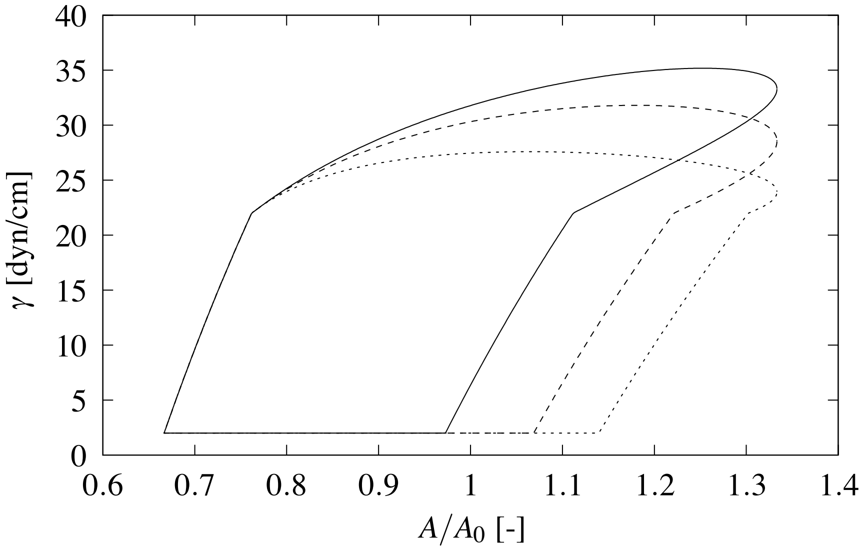

Figure 3.3.5: Surface stresses depending on normalized interfacial area for different choices of $\alpha_1\bar{C}$ (solid line: $\alpha_1\bar{C} = 1.0\,\mu s^{-1}$; dashed line: $\alpha_1\bar{C} = 2.0\,\mu s^{-1}$; dotted line: $\alpha_1\bar{C} = 5.0\,\mu s^{-1}$).

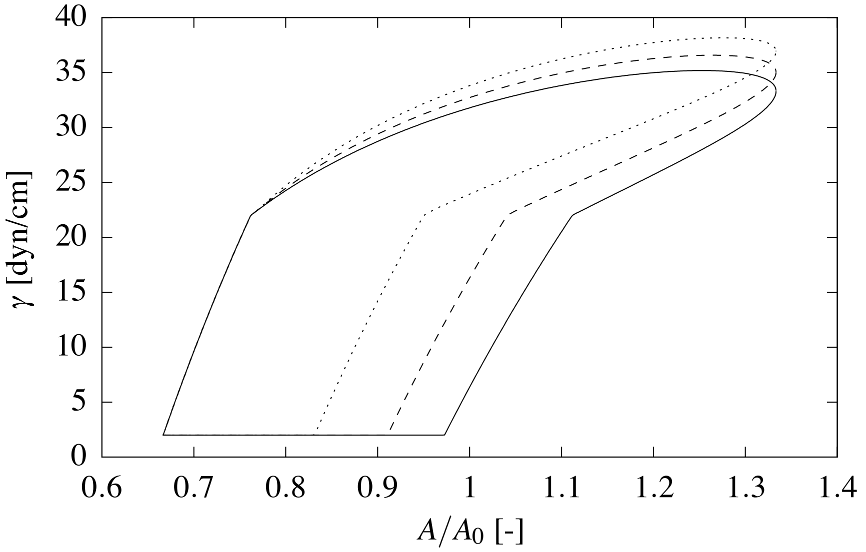

Figure 3.3.6: Surface stresses depending on normalized interfacial area for different choices of α_2 (solid line: $\alpha_2 = 0.016\,\mu s^{-1}$; dashed line: $\alpha_2 = 0.1\,\mu s^{-1}$; dotted line: $\alpha_2 = 0.2\,\mu s^{-1}$).

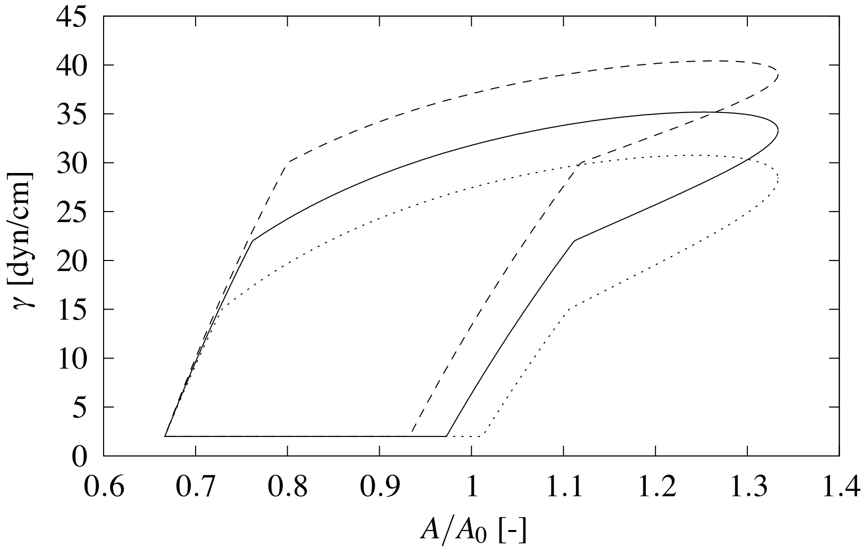

Figure 3.3.7: Surface stresses depending on normalized interfacial area for different choices of m_1 (dashed line: $m_1 = 40$ dyn/cm; solid line: $m_1 = 48$ dyn/cm; dotted line: $m_1 = 55$ dyn/cm).

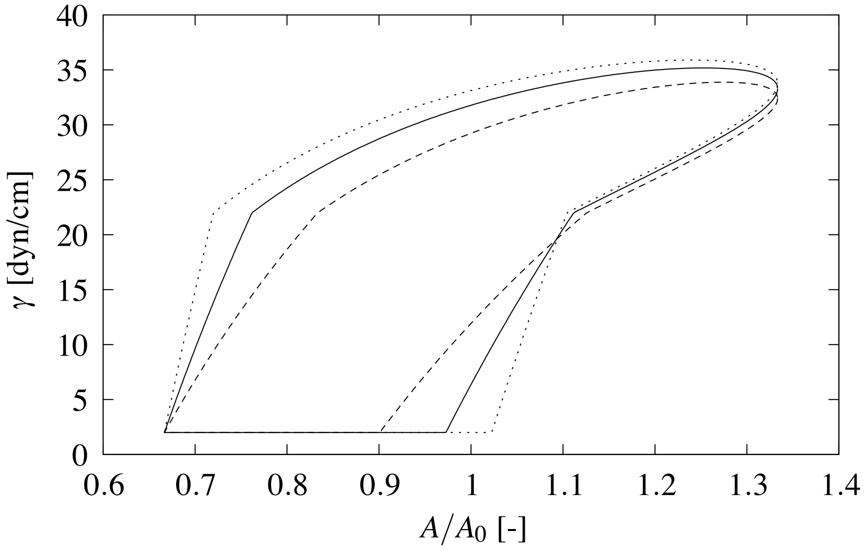

Figure 3.3.8: Surface stresses depending on normalized interfacial area for different choices of m_2 (dashed line: $m_2 = 80$ dyn/cm; solid line: $m_2 = 140$ dyn/cm; dotted line: $m_2 = 250$ dyn/cm).

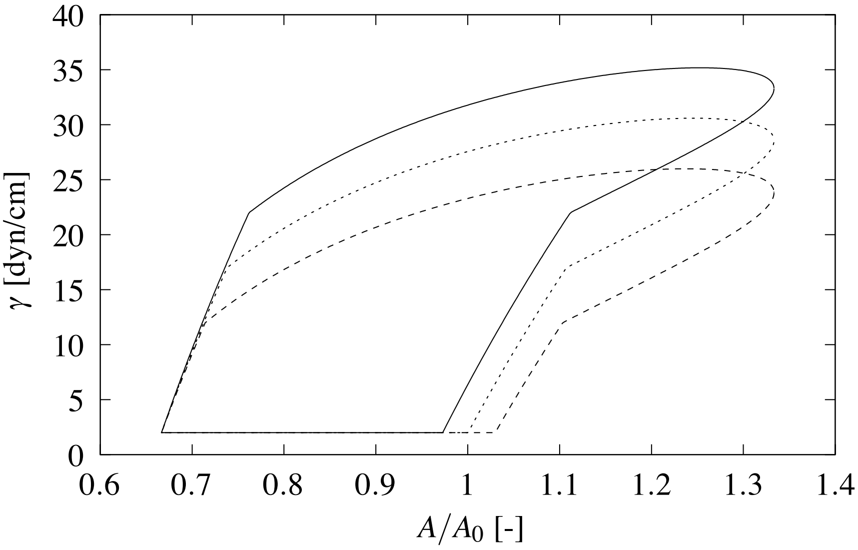

Figure 3.3.9: Surface stresses depending on normalized interfacial area for different choices of γ_0 (dashed line: $\gamma_0 = 60$ dyn/cm; dotted line: $\gamma_0 = 65$ dyn/cm; solid line: $\gamma_0 = 70$ dyn/cm).

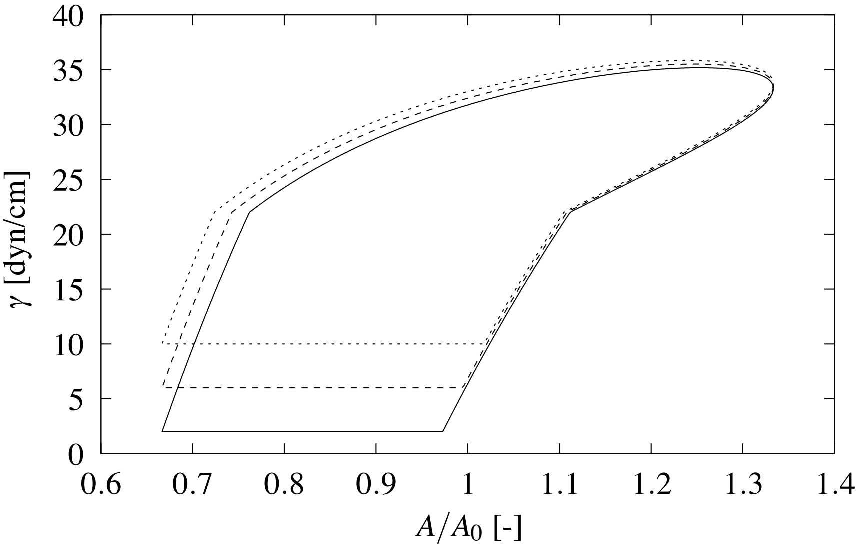

Figure 3.3.10: Surface stresses depending on normalized interfacial area for different choices of γ_{min} (solid line: $\gamma_{\mathsf{min}} = 2$ dyn/cm; dashed line: $\gamma_{\mathsf{min}} = 6$ dyn/cm; dotted line: $\gamma_{\mathsf{min}} = 10$ dyn/cm).

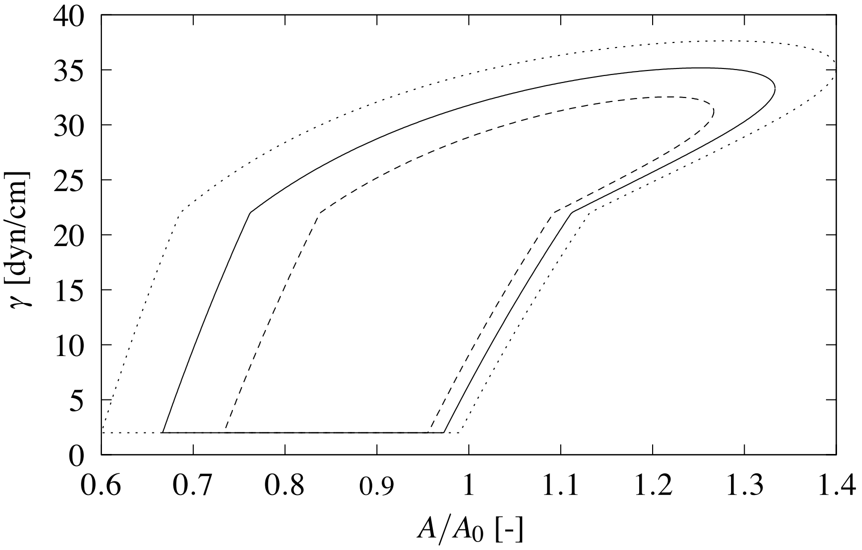

Figure 3.3.11: Surface stresses depending on normalized interfacial area for different choices of $\Delta A/A_0$ (dashed line: $\Delta A/A_0$ = 0.27; solid line: $\Delta A/A_0$ = 0.33; dotted line: dA/A_0 = 0.4).

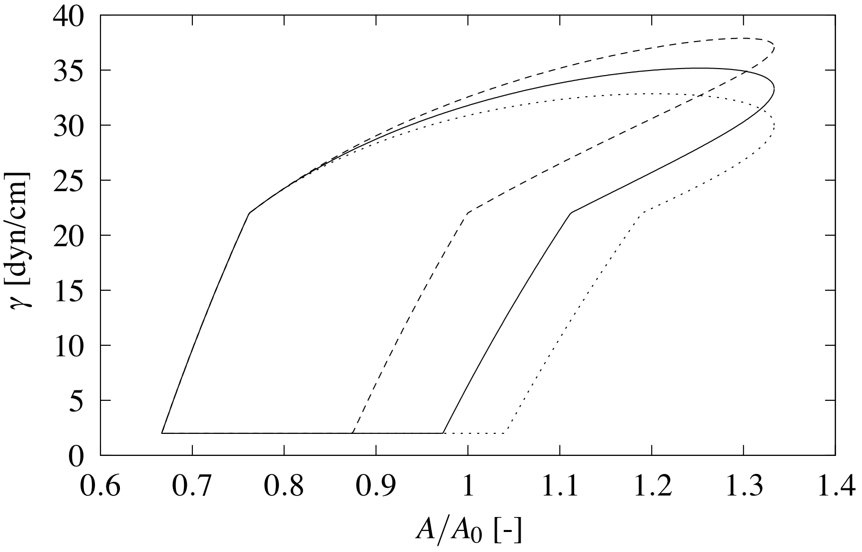

Figure 3.3.12: Surface stresses depending on normalized interfacial area for different choices of T (dashed line: $T = 1.5$ s; solid line: $T = 3.0$ s; dotted line: $T = 5.0$ s).

As already indicated above, the model is intended to predict the steady-state behavior of an ideally spherical bubble with spatially constant surfactant concentration under cyclic loading. In an irregularly shaped alveolus, however, temporarily distinct surfactant concentrations may develop over the interface due to locally different area changes. Instead of constraining the liquid lining to a spatially constant surface stress, the relationships established in Otis et al. (1994) are used here for the description of local – i.e. elementwise – changes in surfactant concentrations and surface stresses. It has to be noted that for application of Newton's method, $\gamma^{(e)}$ and $\left(\frac{\partial \gamma}{\partial A}\right)^{(e)}$ have to be computed in every nonlinear iteration step. Furthermore, both $A^{(e)}$ and $\left(\frac{\Gamma}{\Gamma^*}\right)^{(e)}$ of the last time step need to be stored to calculate the current surfactant concentration. Details on the integration of the surface stress contribution into the nonlinear dynamic framework introduced in section 2.1 are provided in Algorithms 3.2-3.4.

To illustrate some features of the presented model, selected numerical examples will be discussed in the following. In all cases, first the equilibrium surface stresses were gradually applied (cf. Algorithm 3.2) before the cyclic loading was initiated. In Figure 3.3.13, the deformation of a cuboid with two-sided surfactant lining is shown. The cuboid was constrained on the bottom surface, whereas the top surface was loaded by a sinusoidally varying pressure after application of equilibrium surface stresses. For simplicity, only vertical displacements were admitted. A comparison of the deformation states obtained using different interface discretization clearly demonstrates the mesh independency of simulation results.

Figure 3.3.14 displays the simulated distribution of normalized surfactant concentrations in an alveolus during sinusoidal pressure loading. Locally different concentrations developed depending on the corresponding change in interfacial area. In reality, gradients in surface stresses cause so-called Marangoni flows on the interface. Although a direct exchange of surfactant molecules between neighboring interface elements has not been explicitly considered in the numerical model, the nodal surface stress resultants allow for an indirect compensation. For instance, during inflation, elements with lower surfactant concentrations exhibit larger contracting forces $\mathbf{f}^{\mathsf{surf(e)}}$. As a consequence, the increase in interfacial area is impeded compared to those elements with higher concentrations. According to Figure 3.3.11, a smaller amplitude of area change is associated with reduced surface stresses during inflation since surfactant adsorption is promoted. Therefore, local concentration gradients balance out implicitly if there is enough time for accommodation. In the absence of dynamic interfacial area changes, the concentration in all elements should ultimately reach the equilibrium value Γ_{eq}. However, the presented approach only partly allows for the modeling of this behavior. Figure 3.3.15 shows the development of the normalized surfactant concentration in a single interface element over simulated time steps. After gradual application of the equilibrium surface stress (cf. Algorithm 3.2), the steady state was reached after approximately two loops of area change. The interfacial area was then instantaneously fixed at different points in the sixth loop. The equilibrium state could only be recovered from the first regime, whereas concentrations were trapped in the others. This behavior directly resulted from the specific formulation of the surfactant model. In both the second and the third regime, a change of state inherently necessitates a variation

Algorithm 3.2 Consideration of surfactant surface stresses in alveolar FE model.

```
for each element $(e)$:
    $\Gamma^{(e)}_{n=0} = \Gamma_{\mathsf{eq}}$, $\gamma^{(e)}_{n=0} = \gamma_{\mathsf{eq}}$ (arbitrary choice)
    Calculate $A^{(e)}_{n=0} = A^{(e)}_{0}$ (3.3.22), $\left(\frac{\partial A}{\partial \mathbf{d}}\right)^{(e)}_{n=0} = \left(\frac{\partial A_0}{\partial \mathbf{d}}\right)^{(e)}$ (3.3.23)

Starting phase (gradual application of equilibrium surface stresses):
for each time step $[t_n, t_{n+1}]$ with $t_n \leq t_s$:
    for each Newton iteration $i$ until convergence:
        for each element $(e)$:
            Determine $A^{(e)i+1}_{n+1-\alpha_{\mathsf{f}}}$ (3.3.22), $\left(\frac{\partial A}{\partial \mathbf{d}}\right)^{(e)i+1}_{n+1-\alpha_{\mathsf{f}}}$(3.3.23), and $\left(\frac{\partial^2 A}{\partial \mathbf{d}^2}\right)^{(e)i+1}_{n+1-\alpha_{\mathsf{f}}}$ (3.3.29)
            Compute $\left(\frac{\partial A}{\partial \mathbf{d}}\right)^{(e)i+1}_{n+1}$ (3.3.23)
            $\gamma^{(e)i+1}_{n+1} = \gamma_{\mathsf{eq}}$ and $\left(\frac{\partial \gamma}{\partial A}\right)^{(e)i+1}_{n+1} = 0$
            Calculate scaling factor $\hat{s}$ from user-defined time curve ($\hat{s}(t_s) = 1.0$)
            Compute and assemble $\hat{s} \cdot \left(\mathbf{f}^{\mathsf{surf}}\right)^{(e)i+1}_{n+1}$ (3.3.18), $\hat{s} \cdot \left(\mathbf{K}^{\mathsf{surf}}\right)^{(e)i+1}_{n+1}$ (3.3.21)
        Add $\hat{s} \cdot \left(\mathbf{f}^{\mathsf{surf}}\right)^{i+1}_{n+1}$ to (2.1.79) and $\hat{s} \cdot \left(\mathbf{K}^{\mathsf{surf}}\right)^{i+1}_{n+1}$ to (2.1.81)
        Solve linear system (2.1.84) for $\Delta\mathbf{d}^{i+1}_{n+1}$ and update $\mathbf{d}^{i+1}_{n+1}$ (2.1.85)
        Check for convergence and update $i$
    Update $n$

Dynamic loading phase:
for each time step $[t_n, t_{n+1}]$ with $t_n > t_s$:
    for each Newton iteration $i$:
        for each element $(e)$:
            Determine $A^{(e)i+1}_{n+1-\alpha_{\mathsf{f}}}$ (3.3.22), $\left(\frac{\partial A}{\partial \mathbf{d}}\right)^{(e)i+1}_{n+1-\alpha_{\mathsf{f}}}$(3.3.23), and $\left(\frac{\partial^2 A}{\partial \mathbf{d}^2}\right)^{(e)i+1}_{n+1-\alpha_{\mathsf{f}}}$ (3.3.29)
            Compute $\left(\frac{\partial A}{\partial \mathbf{d}}\right)^{(e)i+1}_{n+1}$ (3.3.23)
            Calculate $\left(\frac{\Gamma}{\Gamma^*}\right)^{(e)i+1}_{n+1}$ and $\left(\frac{\partial(\Gamma/\Gamma^*)}{\partial A}\right)^{(e)i+1}_{n+1}$ $\leadsto$ Algorithm 3.3
            Determine $\gamma^{(e)i+1}_{n+1}$ and $\left(\frac{\partial \gamma}{\partial A}\right)^{(e)i+1}_{n+1}$ $\leadsto$ Algorithm 3.4
            Compute $\gamma^{(e)i+1}_{n+1-\alpha_{\mathsf{f}}}$ (3.3.17)
            Compute and assemble $\left(\mathbf{f}^{\mathsf{surf}}\right)^{(e)i+1}_{n+1}$ (3.3.18), $\left(\mathbf{K}^{\mathsf{surf}}\right)^{(e)i+1}_{n+1}$ (3.3.21)
        Add $\left(\mathbf{f}^{\mathsf{surf}}\right)^{i+1}_{n+1}$ to (2.1.79) and $\left(\mathbf{K}^{\mathsf{surf}}\right)^{i+1}_{n+1}$ to (2.1.81)
        Solve linear system (2.1.84) for $\Delta\mathbf{d}^{i+1}_{n+1}$ and update $\mathbf{d}^{i+1}_{n+1}$ (2.1.85)
        Check for convergence and update $i$
    Update $n$
```

Algorithm 3.3 Computation of element interfacial surfactant concentration and its derivative at t_{n+1}.

```
if $\left(\frac{\Gamma^{(e)}}{\Gamma^*}\right)_n \leq 1.0$:
    if $\left(\frac{\Gamma^{(e)}}{\Gamma^*}\right)_n > 0.98$:
        Determine modified sorption coefficients (3.3.48), (3.3.49)
    $\left(\frac{\Gamma^{(e)}}{\Gamma^*}\right)_{n+1}^{(e)i+1}, \left(\frac{\partial(\Gamma/\Gamma^*)}{\partial A}\right)_{n+1}^{(e)i+1} \rightsquigarrow$ (3.3.38), (3.3.41)
else if $1.0 < \left(\frac{\Gamma^{(e)}}{\Gamma^*}\right)_n < \frac{\Gamma_{\mathsf{max}}}{\Gamma^*}$:
    $\left(\frac{\Gamma^{(e)}}{\Gamma^*}\right)_{n+1}^{(e)i+1}, \left(\frac{\partial(\Gamma/\Gamma^*)}{\partial A}\right)_{n+1}^{(e)i+1} \rightsquigarrow$ (3.3.44), (3.3.47)
else:
    if $A_{n+1}^{(e)i+1} < A_n^{(e)}$:
        $\left(\frac{\Gamma^{(e)}}{\Gamma^*}\right)_{n+1}^{(e)i+1}, \left(\frac{\partial(\Gamma/\Gamma^*)}{\partial A}\right)_{n+1}^{(e)i+1} \rightsquigarrow$ (3.3.50), (3.3.51)
    else:
        $\left(\frac{\Gamma^{(e)}}{\Gamma^*}\right)_{n+1}^{(e)i+1}, \left(\frac{\partial(\Gamma/\Gamma^*)}{\partial A}\right)_{n+1}^{(e)i+1} \rightsquigarrow$ (3.3.44), (3.3.47)
Validity check:
if $\left(\frac{\Gamma^{(e)}}{\Gamma^*}\right)_{n+1} > \frac{\Gamma_{\mathsf{max}}}{\Gamma^*}$:
    $\left(\frac{\Gamma^{(e)}}{\Gamma^*}\right)_{n+1} = \frac{\Gamma_{\mathsf{max}}}{\Gamma^*}$
```

Algorithm 3.4 Computation of element surface stress and its derivative at t_{n+1}.

```
if $\left(\frac{\Gamma^{(e)}}{\Gamma^*}\right)_{n+1}^{(e)i+1} \leq 1.0$:
    $\gamma_{n+1}^{(e)i+1}, \left(\frac{\partial\gamma}{\partial A}\right)_{n+1}^{(e)i+1} \rightsquigarrow$ (3.3.39), (3.3.40)
else if $1.0 < \left(\frac{\Gamma^{(e)}}{\Gamma^*}\right)_{n+1}^{(e)i+1} < \frac{\Gamma_{\mathsf{max}}}{\Gamma^*}$:
    $\gamma_{n+1}^{(e)i+1}, \left(\frac{\partial\gamma}{\partial A}\right)_{n+1}^{(e)i+1} \rightsquigarrow$ (3.3.45), (3.3.46)
else:
    $\gamma_{n+1}^{(e)i+1}, \left(\frac{\partial\gamma}{\partial A}\right)_{n+1}^{(e)i+1} \rightsquigarrow$ (3.3.52), (3.3.53)
```

of interfacial area. This shortcoming of the model, however, seems acceptable considering the intended application of use. During both normal breathing and mechanical ventilation, the assumption of a constantly changing alveolar surface area is justified.

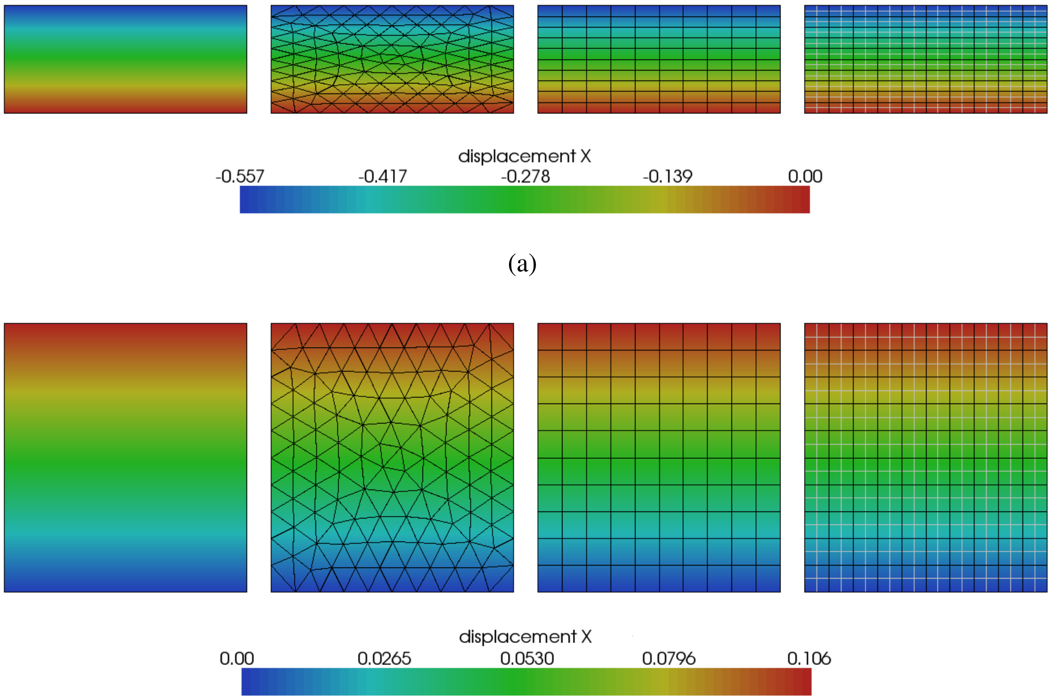

(a)

(b)

Figure 3.3.13: Mesh independency of simulation results. Each interface was meshed with (from left to right) a single 4-noded quadrilateral, 213 3-noded triangles, 100 4-noded, and 100 9-noded quadrilaterals, respectively. (a) Deformation state after application of equilibrium surfactant concentration. (b) Deformation state under maximum load.

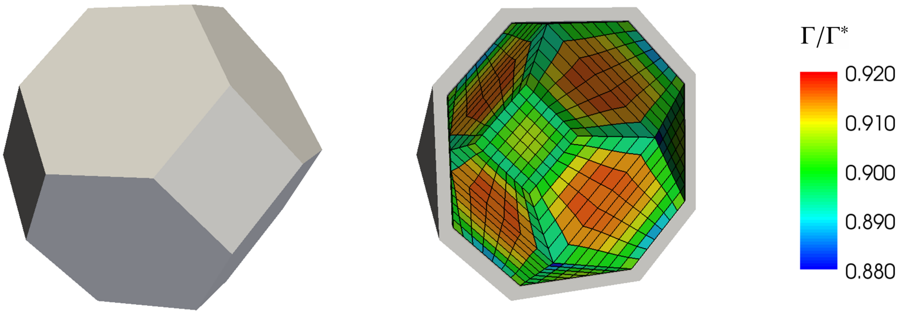

Figure 3.3.14: Left: Geometry of simulated artificial alveolus. Right: Clipped view showing a snapshot of the distribution of normalized element surfactant concentrations during sinusoidal pressure loading.

As already indicated above, a few loops of interfacial area changes are usually necessary before the steady state is reached. Depending on the arbitrarily chosen initial state, different intermediate configurations are adopted which are, however, in general not physio-

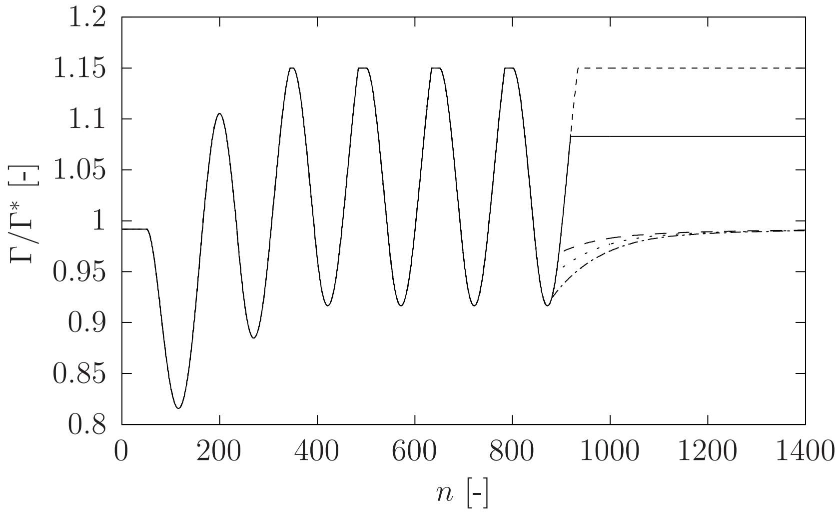

Figure 3.3.15: Development of surfactant concentrations in a single element over simulated time steps. When fixing the interfacial area, equilibrium surfactant concentration was only recovered from the first regime (widely dashed, dotted, and dash-dotted lines), whereas concentrations were trapped in the second (solid line) and third (closely dashed line) regimes, respectively.

logically relevant. Reasonable predictions of alveolar behavior are, therefore, not possible until the course of surfactant concentrations has become stationary. Apart from the chosen material parameters, the exact number of required preceding loops also depends on the dynamic loading conditions. Figure 3.3.16 shows the course of the normalized surfactant concentration in a single element over several simulated cycles for two different prescribed area amplitudes $\Delta A/A_0$. The dashed horizontal lines correspond to the step-wise application of the equilibrium surfactant concentration in the beginning of the simulations. In case of the smaller $\Delta A/A_0$, seven loops were required before the process levels off, whereas the steady state was attained already in the second cycle in the example with the larger value of $\Delta A/A_0$. Corresponding lead times must be taken into account when evaluating simulation results.

After having investigated some important implications of the chosen surfactant model, the influence of the liquid lining on the overall mechanical behavior will now be illustrated by means of a simple numerical example (cf. Figure 3.3.17). Single artificial alveoli (edge length $L = 60.0\,\mu\text{m}$, wall thickness $t = 8.0\,\mu\text{m}$) were loaded by a sinusoidally varying hydrostatic pressure given by

$$p = \frac{p_{\text{max}}}{2}\left[1 + \sin\left(\frac{2\pi t}{T} - \frac{\pi}{2}\right)\right] \tag{3.3.55}$$

with $p_{\text{max}} = 600\,\text{Pa}$, $T = 3.0\,\text{s}$. For the description of soft tissue behavior, the material model presented in section 3.2.3 was utilized. On the interior surfaces, three different surface configurations were prescribed. The first alveolus was assumed to be completely

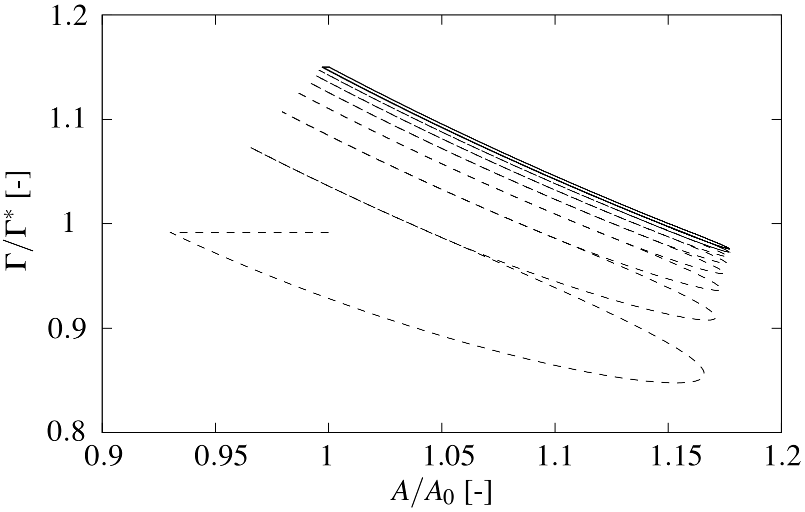

(a)

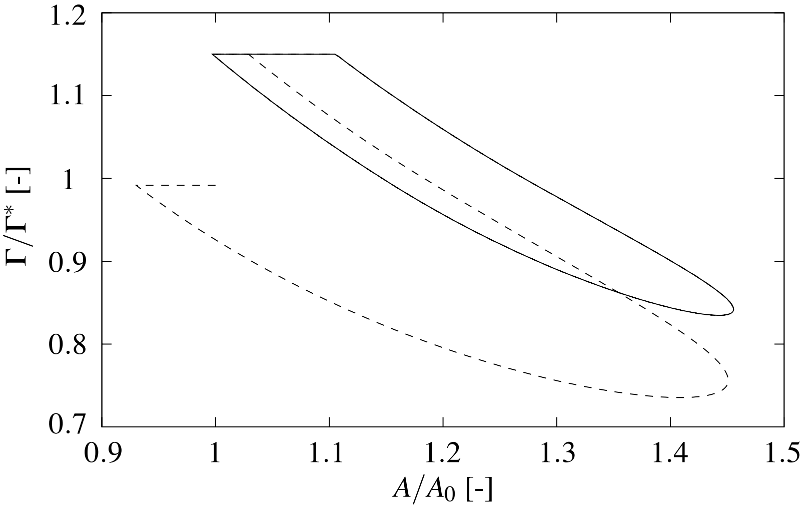

(b)

Figure 3.3.16: Reaching the steady state (solid line) for surfactant concentration changes in case of a (a) small and (b) large prescribed amplitude of area change.

filled with liquid, hence no interfacial phenomena were considered in this case (see Figure 3.3.17(c)). The second alveolus was lined by a surfactant layer with parameters given in Table 3.1 (see Figure 3.3.17(d)). In the third alveolus, a water lining with constant surface tension ($\hat{\gamma} = 70.0$ dyn/cm) was modeled to simulate surfactant deficiency in a gas-filled alveolus (cf. Figure 3.3.17(e)). The differences in the overall deformation states affirmed the importance of considering interfacial phenomena in alveolar mechanics. A comparison of the results for surfactant and water films demonstrated the efficiency of surfactant in decreasing the surface stress of the aqueous hypophase, thereby reducing

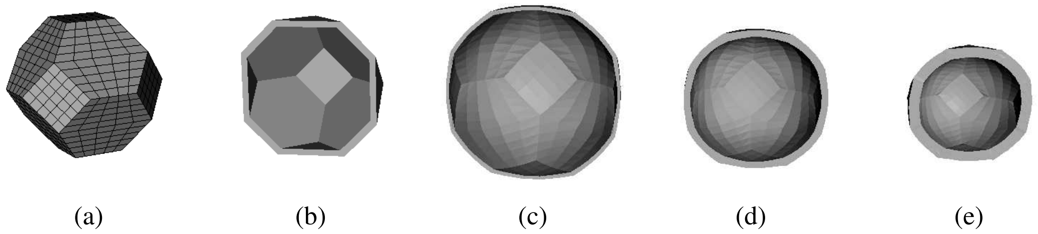
(a) (b) (c) (d) (e)

Figure 3.3.17: Single alveolus with different interfacial configurations under sinusoidally varying hydrostatic pressure. (a) Undeformed geometry with mesh. (b) Section of undeformed geometry. (c)-(e) Sections of deformed geometries under maximum load in case of (c) tissue alone, (d) tissue coupled with surfactant, and (e) tissue coupled with water film on the interior surface (each 1.5 times exaggerated).

the overall stiffness of alveoli. This already provides an indication of the altered alveolar behavior in the ARDS lung where surfactant may be partly or even completely disabled.

Since available experimental data almost exclusively stem from animal experiments, the question whether the effect of interfacial phenomena is species-dependent is crucial. It is known that all mammals exhibit comparable surface stresses at the air-liquid interface (Lum and Mitzner, 1987). Because the retractive interfacial forces decrease with increasing radius of curvature, larger lungs could be expected to be more compliant than smaller ones. This presumption was supported by simulations comparing the effect of different liquid linings on maximum inflation states in human and hamster alveoli (Wiechert et al., 2008). For simplicity, identical tissue behavior was assumed in both cases. In reality, however, alveolar wall composition is also highly species-dependent (Mercer et al., 1994). Larger alveoli are characterized by a higher amount of connective tissue and a more dispersed distribution of fibers throughout the septal walls (cf. section 1.1.2.2 and references therein). According to Mercer and Crapo (1990), this increase in tissue stiffness may reflect the need to compensate for the reduced lung recoil due to surface stresses. In consequence of the complex interplay of tissue and interfacial mechanics, the overall mechanical behavior is potentially independent of the individual alveolar size. However, although general considerations support this theory, detailed investigations remain to be done.

4 Multi-Scale Model of Lung Parenchyma

> *“Almost all problems in science and engineering are multiscale in nature.”* (E et al., 2007)

In the preceding chapter, an extensive computational model of individual alveoli has been derived. So far, however, the statement of appropriate boundary conditions has not been addressed. Although neighboring lung regions are known to be highly interdependent (Mead et al., 1970), this effect was completely neglected in previous alveolar models. Due to the lack of physiologically reasonable boundary conditions, clinically relevant predictions of local stresses and strains in alveoli have not been feasible up to now.

One possibility to overcome this problem is to consider lung parenchyma as a whole instead of restricting analyses to isolated alveolar domains. In this case, the formulation of suitable boundary conditions is straightforward. For instance, pleural pressure (cf. e.g. West (2008) for the definition of a corresponding profile) or a deformation state obtained from four-dimensional CT imaging can be applied at the surface of the lungs.

In the literature, several approaches to simulating the overall behavior of lung tissue can be found. In all cases, parenchyma has been approximated as a homogeneous and isotropic continuum. Although anisotropy may be present at the alveolar level where the alveolar ducts exhibit distinct axes, the orientation of respiratory units is rather random on a larger scale (Frankus and Lee, 1974; Hoppin et al., 1975). Hence, the assumption of homogeneity and isotropy at the parenchymal level is justified (at least for the healthy lung).

In general, two distinct kinds of global parenchyma models can be distinguished. The first class of approaches focuses on the solid part. Lanir (1983), for example, derived constitutive equations for lung tissue on the basis of a stochastic approach to the micro-structure. Alveolar walls were approximated by membranes with a given orientation density function. Assuming affine deformations on both levels, the macroscopic stresses were then derived from the algebraic sum of the elastic potentials of all alveolar membranes within a unit volume. Other models (cf. e.g. Vawter (1980), Stamenovic and Wilson (1985), and Gao et al. (2006)) were based on describing the mechanical behavior of lung parenchyma by means of phenomenological SEFs. The most recent material model of this kind was proposed by Rausch et al. (2011b). They conducted uniaxial tension tests on living lung tissue prepared from isolated rat lungs. An inverse analysis was then performed to optimize the material parameters of different combinations and recombinations of existing SEFs. By comparing the best-fits of the tested SEFs, an optimal constitutive model was identified (cf. also Figure 4.0.1).

The second class of approaches is based on the combined description of homogenized tissue deformation and airflow. For instance, Owen and Lewis (2001) proposed a viscoelastic porous medium model of lung parenchyma. For determining macroscopic airflow, pressure, and tissue deformation, volume averaging was performed over a cubic unit cell without considering specific features of alveolar geometry. The theoretical solution obtained was applied and extended by Lande and Mitzner (2006) to derive a general formula for the overall impedance of the lung. Another approach based on the theory of porous media was developed by Kowalczyk and Kleiber (1994). They modeled the solid phase representing the lung tissue as a nonlinearly elastic, highly deformable continuum. To account for the effect of the surfactant film, a pseudo-elastic surface stress function (cf. section 3.3.3) was considered.

Although the parenchyma models addressed above are capable of reproducing global lung tissue behavior, a link to the alveolar level is completely missing. However, in order to allow for the determination of local stresses and strains involved in the development of VALI, the complex micro-structure has to be taken into account. The need for resolving the realistic alveolar morphology was confirmed by a study of Rausch et al. (2011a). They found that local strains in individual alveolar walls can reach a multiple of the prescribed global value, thereby rendering statements about overall strains pointless. However, explicitly modeling all 500 million alveoli present in the human respiratory system is not feasible. In this thesis, therefore, a combination of two complementary approaches is proposed. Novel multi-scale techniques are utilized to resolve the alveolar micro-structure only at certain “hot spots”, whereas lung parenchyma is modeled as a homogenized continuum otherwise (see Figure 4.0.1 for a schematic overview).

For the bulk of lung tissue, utilization of an existing approach is suggested. Since the interaction of airflow and tissue deformation will be considered separately in chapter 5, the global parenchyma model can be confined to the solid phase. In this regard, the phenomenological SEF introduced by Rausch et al. (2011b) is considered as the most convenient approach. To bridge the gap between the global parenchymal and the local alveolar level in regions of particular interest, a suitable multi-scale model needs to be formulated. The remainder of this chapter is devoted to this specific topic. In the following, a brief overview of existing micro-macro methods will be provided. Afterwards, a novel approach extending available methods to coupled and dynamic scenarios inherent to (mechanical) ventilation will be presented. Since the micro-level (i.e. alveolar) stresses and strains are of particular interest for the intended application, a concurrent coupling of scales will be proposed. After defining the governing equations on both levels as well as appropriate scale bridging conditions, some information concerning the computational implementation will be provided. The chapter is completed by selected numerical examples which validate the developed approach and illustrate its applicability to lung parenchyma.

4.1 Survey of existing micro-macro approaches

Over the last decades, there has been increasing interest in modeling multi-scale phenomena in both solid and fluid mechanics. The particular complexity inherent in these kinds of

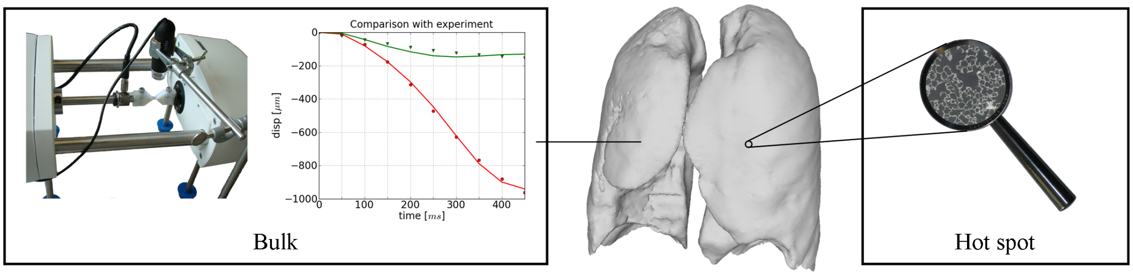

Figure 4.0.1: Schematic of the intended parenchyma model. For the bulk of lung tissue, a phenomenological constitutive model fitted to experimental data (Rausch et al., 2011b) is employed (left-hand side). At a hot spot, a multi-scale approach is utilized to zoom in on the local alveolar micro-structure (right-hand side).

problems is due to the interplay of effects on different length (and possibly time) scales. In case of a multi-phase material, for instance, the macroscopic behavior is governed by the morphology and the properties of its micro-constituents. Another well-known example for multi-scale problems is turbulent flow. For high Reynolds numbers, eddies develop that break up into smaller and smaller structures in a cascade-process. In order to allow for an accurate prediction of material or flow behavior, actually all phenomena down to the smallest scale of interest need to be taken into account. However, as in the case of the lung with its 500 million individual alveoli, this approach is impractical in most cases due to limited computational resources. Therefore, a plethora of different so-called multi-scale methods has been developed in the past. As a matter of principle, these approaches aim for integrating fine-scale effects in a coarse-scale model while avoiding a direct numerical simulation of the completely resolved micro-structure. By combining information available on different levels, advantage can be taken of both the simplicity of a macroscopic description and the accuracy of a fine-scale model.

Due to the variety of (commonly problem-specific) methods, the field of multi-scale approaches is too wide a subject to be surveyed extensively in this thesis. A comprehensive review and taxonomy of different existing methodologies can be found e.g. in Gravemeier et al. (2008). The subsequent overview will be confined to a specific class of methods that is deemed suitable for the intended scope of application. Particularly, approaches based on the detailed discretization (as opposed to a mere approximation) of the micro-structure will be reviewed. These so-called micro-macro approaches fall within the scope of the heterogeneous multi-scale method (HMM) proposed by E et al. (2007). Simply put, the HMM is a framework for designing multi-scale approaches that can be applied to problems for which the macroscopic model is either only partly known or valid only on part of the physical domain. In both cases, the missing information on the global level is obtained by solving problems locally on finer scales. Hence, the HMM can also be interpreted as an adaptive model refinement that allows to efficiently move between different scales. Usually, there is a distinct gap in the scale spectrum of the HMM, i.e. only a finite number of different levels is covered. In most cases, two scales are considered explicitly, namely

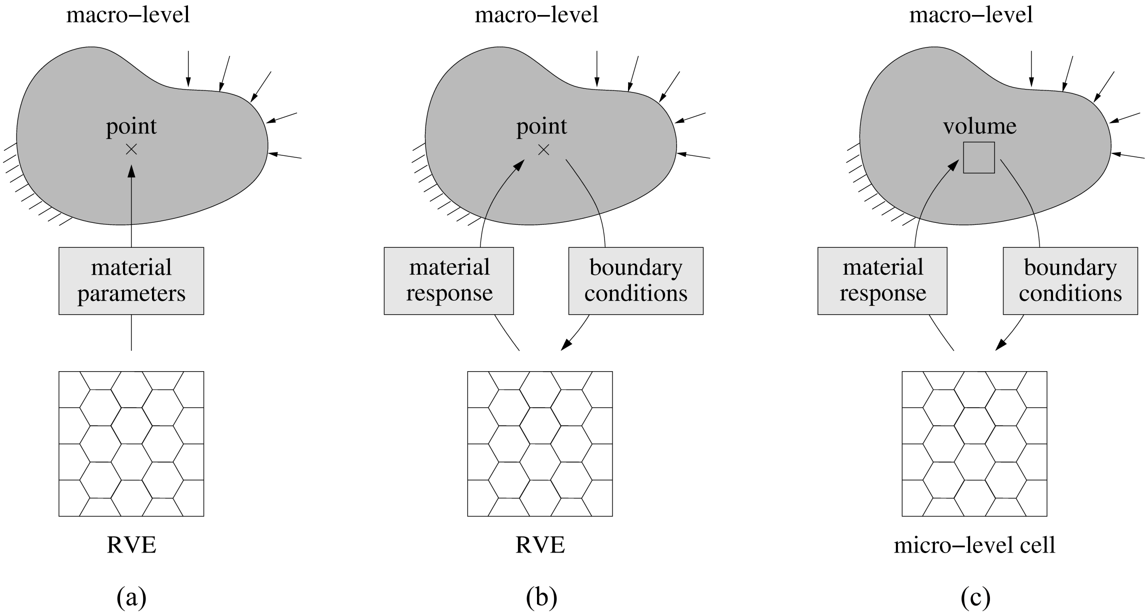

Figure 4.1.1: Basic types of micro-macro approaches. (a) Sequential homogenization. (b) Concurrent homogenization. (c) Concurrent volume-coupled approach.

the macroscopic level (also known as the coarse-scale or macro-level) and a representative fine-scale. In the following, this level will often be referred to as the micro-scale regardless of the actual characteristic size. The models at the different levels can be of very different nature, e.g. continuum mechanics on the macro-level and molecular dynamics on the micro-scale. Concerning the coupling of the individual levels, two basic strategies have to be distinguished. In the following, corresponding approaches will be briefly discussed using the example of a micro-heterogeneous solid.

The first type of scale bridging is also known as sequential homogenization (cf. Figure 4.1.1(a)). To describe the effective macroscopic behavior, a suitable phenomenological constitutive model is chosen. The constants of this equivalent homogeneous substitute material are determined from calculations on representative volume elements (RVEs) of the heterogeneous micro-structure in a preprocessing step. Details on related analytical and computational approaches can be found e.g. in Nemat-Nasser and Hori (1999), Zohdi and Wriggers (2005), and references therein. In the linear elastic regime, sequential homogenization analyses are well-established and provide accurate estimates for the effective macroscopic elasticity tensor. In the nonlinear realm, however, making reasonable assumptions concerning the macro-level constitutive behavior can be very difficult. Even for combinations of relatively simple materials on the micro-level, it may not be possible to predict the explicit form of the macroscopic constitutive equation in advance. Although some promising approaches have been proposed (see e.g. Temizer and Zohdi (2006) for the construction of a pre-computed effective "material map"), homogenization in the presence of nonlinearities is still a less developed field. Another major drawback of sequential multi-scale methods is their inherent "bottom-up" characteristic. Since microscopic processes are considered only a preprocessing step, the current state of the micro-structure is unknown during simulation of the macro-level response.

If the micro-scale solution itself is of particular interest, macro- and micro-level need to be linked together “on-the-fly”. This kind of scale bridging is typical for concurrent multi-scale approaches based on the simultaneous simulation of the mutually coupled scales. In this case, detailed current micro-structural information can be introduced in the macroscopic analysis. Over the years, different concurrent approaches have been developed. In case of the so-called computational homogenization, each macro-level integration point is implicitly identified with an RVE representing the micro-structure in its vicinity. The local macroscopic mechanical behavior can then be represented via the average response of the RVE (cf. Figure 4.1.1(b)). In contrast to sequential homogenization procedures, concurrent methods dispense with any constitutive assumption on the macro-level. Instead, the effective stresses at a macro-level point are determined by solving the boundary value problem (BVP) of the associated RVE for each macroscopic deformation state. Corresponding methods are suitable for arbitrary micro-level geometries as well as material behavior and enable the consideration of nonlinearities on both scales. Basic principles of this class of multi-scale approaches have been introduced for example in Suquet (1985), Terada and Kikuchi (1995), and Smit et al. (1998). Further and more recent developments can be found e.g. in Michel et al. (1999), Feyel and Chaboche (2000), Ghosh et al. (2001), Terada and Kikuchi (2001), Kouznetsova et al. (2001), Miehe (2003), Peric et al. (2010), and Geers et al. (2010). In general, any modeling technique is possible on the micro-scale (e.g. molecular dynamics (E et al., 2007), Voronoi cell approaches (Ghosh et al., 2001), or Fast Fourier Transform models (Michel et al., 1999)). For computational homogenization methods based on a FE discretization of both macro- and micro-level problems, the term FE^2 has been coined. Corresponding approaches have been employed for a wide range of applications, e.g. biomechanical modeling of human eye tissues (Grytz, 2008), thermo-mechanical analysis of heterogeneous solids (Oezdemir et al., 2008), solidification (Lee and Sundararaghavan, 2009), and thermo-mechanical contact problems (Temizer and Wriggers, 2010).

The improved description of the coarse-scale behavior by means of a detailed solution of the micro-level BVP comes along with high computational costs. Therefore, usage of concurrent multi-scale models in critical regions only while reverting to classical constitutive laws in non-critical domains was proposed by Ghosh et al. (2001). Another option is utilization of model reduction methods for solving the micro-level problem (Yvonnet and He, 2007). This approach (also known as the reduced model multi-scale method or R3M) was shown to lower computing times and storage requirements significantly.

Both sequential and computational homogenization methods inherently assume a strict separation of scales (cf. Figure 4.1.2). Since fine-scale dimensions are supposed to be infinitely small compared to the characteristic coarse-scale size, macroscopic fields are uniform over the RVE and standard local continuum mechanics concepts hold. As a consequence, macro-scale stresses rely on the first gradient of displacements only. Therefore, corresponding approaches are also commonly known as first-order methods. Although being a versatile strategy to describe the behavior of micro-heterogeneous materials on different scales, first-order homogenization techniques suffer two major disadvantages. First,

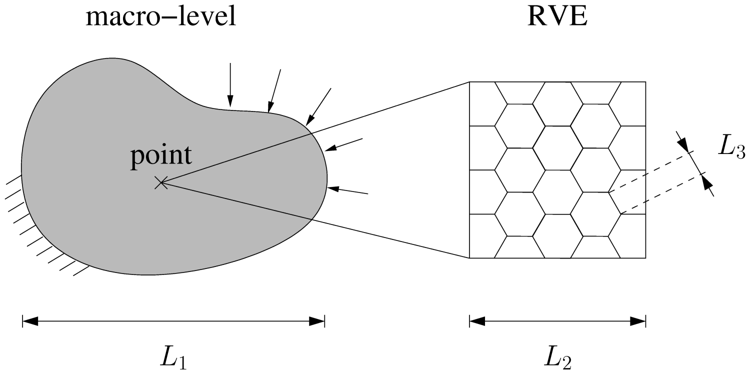

Figure 4.1.2: Concept of scale separation: $L_1 \gg L_2 \gg L_3$, where L_k ($k \in \{1,2,3\}$) denotes a scale-specific characteristic dimension or wave length.

geometrical size effects cannot be simulated since the macro-level solution is insensitive to the absolute dimensions of the micro-structure (Kouznetsova et al., 2004). The second difficulty arises from the intrinsic assumption of uniformity of the macroscopic fields over the RVE (Kouznetsova, 2002). This hypothesis is not admissible in critical regions of high gradients, where the macroscopic fields can vary rapidly. In case of localization phenomena, for instance, the scale separation assumption breaks down and first-order schemes exhibit both macro-level mesh and micro-scale sample size dependency (Gitman, 2006).

To overcome these drawbacks, so-called higher-order or non-local approaches have been proposed (see e.g. Kouznetsova (2002), Feyel (2003), and Kouznetsova et al. (2004)). These methods are based on an enhanced continuum formulation on the macro-scale, while the micro-level BVP remains classical. Although the scale bridging still happens pointwise, the coupling involves strain gradients and higher order stresses. Thereby, non-uniform macroscopic deformation fields within the RVE can be considered and a micro-structural length scale parameter automatically enters the macro-level problem. As a consequence, the macro-scale mesh sensitivity of simulation results for localization problems is resolved. Unfortunately, however, non-local multi-scale approaches also exhibit several disadvantages. First, the micro-scale size dependency cannot be handled since the length scale parameter is always proportional to the size of the microscopic sample (Gitman, 2006). Besides, the implementation of higher-order schemes is considerably more involved compared to a first-order approach. After all, the proper description of the macro-level requires a full higher-order equilibrium formulation. Suitable FE formulations must be based either on C^1-continuous interpolation functions or mixed approaches introducing an additional second-order tensor field (Kouznetsova et al., 2004). Furthermore, closed-form constitutive relations for higher-order continua are difficult to formulate and contain a large number of parameters (Feyel, 2003). Although this problem is bypassed by a concurrent multi-scale approach, utilization of phenomenological material models in non-critical regions of the macroscopic domain is complicated.

A conceptually different class of concurrent multi-scale methods is based on a volume-coupled scale bridging (cf. e.g Ibrahimbegovic and Markovic (2003), Gitman (2006), and

Hund and Ramm (2007)). These approaches abandon the idea that the finite micro-scale cell size is linked to an infinitely small macro-level material point. Instead, the dimensions of the micro-level sample are chosen identical to the size of its associated macro-scale element (see Figure 4.1.1(c)). The overall solution is then composed of a coarse- and a fine-scale part. Due to the unique coupling of micro-scale cell and macro-level mesh sizes, corresponding approaches do not rely on the definition of an RVE anymore. Hence, in contrast to the concurrent methods discussed before, the cell size dependency of the solution in case of localization problems is overcome. However, this benefit comes at the cost of a completely resolved micro-structure. Therefore, volume-coupled approaches can be interpreted as domain decomposition methods rather than classical heterogeneous multi-scale procedures. Ideally, the micro-structure is fully resolved in regions of high macroscopic field gradients only, whereas point-coupled multi-scale schemes are utilized in more uniformly deformed parts of the domain (Ghosh et al., 2001).

In contrast to spatial multi-scale methods, temporal multi-scale approaches have received relatively little attention so far. However, it is well-known that spatial and temporal scales are tightly coupled in many cases. The so-called “gap-tooth scheme” (Samaey et al., 2005) or the “divide-and-conquer” multi-scale method (Gravemeier and Wall, 2008) are among the few coherent multi-scale methods in space *and* time. Key idea behind these approaches is to solve small-scale problems in a subset of the domain over short time intervals. Macroscopic information is then recovered by interpolation in space and extrapolation in time. This strategy is particularly suitable if the time scale separation is particularly pronounced, e.g. in case of molecular dynamics simulations on the micro-level. In the present application, though, the time scale of interest (i.e. the breathing cycle) is equal on both the overall parenchyma and the local alveolar level. Therefore, corresponding space-time multi-scale methods are not pursued in the following.

After having discussed different micro-macro methods, an approach suitable for the application to lung parenchyma has to be proposed now. Obviously, sequential methods are out of the question since they do not provide detailed information on the current state of the micro-structure. After all, the determination of local alveolar stresses and strains during ventilation is the primary purpose of the developed overall lung model. Therefore, utilization of a concurrent multi-scale approach is indispensable here. Resolving the alveolar micro-structure completely over large domains of lung parenchyma, however, seems to be impracticable. Therefore, a point-coupled scheme is preferred to a volume-coupled method. Since a pronounced separation of scales can be assumed and localization phenomena are not to be expected, application of a complicated higher-order approach currently appears to be unnecessary. Moreover, as the combination with classical constitutive models in the bulk of lung parenchyma is complicated, non-local continuum formulations are deemed inconvenient here. Considering all arguments brought forward so far, a first-order computational homogenization method seems to be the most reasonable choice. So far, corresponding approaches were restricted to static and mostly two-dimensional problems. Breathing, however, is a three-dimensional and highly dynamic process. Therefore, a novel method extending existing first-order schemes to three-dimensional dynamic scenarios was devised as part of this work (cf. Wiechert and Wall (2010)). In the following, the developed FE^2 approach, its implementation, and application to lung parenchyma will be presented.

4.2 Dynamic first-order FE^2 approach

As already indicated in the previous section, computational homogenization is based on the determination of the macroscopic constitutive response by means of the adequate definition and solution of an associated micro-level BVP. In this context, the following basic building blocks can be distinguished: (i) definition of a representative sample of the underlying micro-structure; (ii) formulation of the macroscopic nonlinear BVP; (iii) determination and application of micro-scale boundary conditions based on known macroscopic data (macro-micro transition); (iv) formulation of the microscopic nonlinear BVP; (v) calculation of the macroscopic stress and constitutive tensor by averaging over the RVE (micro-macro transition). This classification applies to essentially any computational homogenization method. The differences in distinct approaches result from varying implementations of the individual building blocks. When comparing first- and higher-order schemes, for instance, modules (ii), (iii), and (v) differ, whereas the other components are equal. Subsequently, the building blocks of the developed dynamic FE^2 approach will be introduced in detail. The main difference as compared to existing static methods results from the time-dependent formulation of the macro-level problem. In order to ensure a consistent information transfer between scales, the micro-level BVP and the transition procedures will be properly restated. Albeit not being specific to the novel approach, some guidelines concerning the identification of the micro-structural RVE will also be provided for the sake of completeness.

4.2.1 Definition of the RVE

The sensible definition of an RVE of the micro-structure is crucial for any homogenization approach. Particularly in the nonlinear regime, the behavior may be very sensitive to the chosen sample size (Terada et al., 2000). Although the meaning of the term RVE seems to be quite self-explanatory at first sight, several distinct interpretations can be found in the literature. Without any claim to completeness, some relevant definitions will be surveyed subsequently.

One of the first RVE specifications was given by Hill (1963) who argued that representative samples have to be entirely typical of the whole micro-structure on average. Accordingly, different microscopic “realizations” should exhibit a statistically similar micro-structure (Shan and Gokhale, 2002). According to Kouznetsova (2002), however, sample sizes that rigorously satisfy this condition are rarely utilized in actual homogenization analyses.

A less stringent condition states that an RVE is the smallest volume that is sufficiently representative for the effective macroscopic properties of interest. Particular caution has to be exercised to capture the overall material symmetries. For instance, small sample sizes often exhibit pronounced anisotropy, although the macroscopic behavior may in fact be isotropic (Temizer and Zohdi, 2006).

Whenever precise knowledge of microscopic quantities is also important, the sample should be chosen such that predicted micro-structural stress and strain distributions are representative (Terada et al., 2000; Shan and Gokhale, 2002). During the homogenization process, oscillations in microscopic quantities usually cancel out. As a consequence, fluctuations in micro-scale properties are significantly more pronounced than variations in the corresponding macroscopic counterparts. Hence, RVE size requirements based on this criterion are much stricter compared to those resulting from an analysis of effective properties.

Another well-known prerequisite is that effective moduli obtained by averaging over the RVE should be independent of the nature of applied boundary conditions (i.e. displacement versus traction control), as long as they are "macroscopically uniform" (Hill, 1963). Later on, this requirement was expanded by Shan and Gokhale (2002) from the effective properties also to the microscopic fields. In both cases, the sample has to contain a sufficiently large number of micro-heterogeneities (i.e. $L_2 \gg L_3$, cf. Figure 4.1.2) and must be large enough to have small boundary field fluctuations relative to its size (Zohdi and Wriggers, 2005). In practice, however, this requirement is frequently circumvented by utilization of periodic boundary conditions (see section 4.2.3).

The bottom line of the RVE definitions discussed so far is that the larger the micro-structural sample, the better the quality of the prediction. However, there are also several factors limiting the feasible maximum size of the RVE. First, the micro-structural volume must be small compared to the macroscopic structure (i.e. $L_1 \gg L_2$, cf. Figure 4.1.2). Otherwise, the RVE cannot be regarded as a point on the macro-level anymore. Besides, computing time and memory requirements also play an important role. This issue has to be considered particularly in case of concurrent approaches based on the repetitive solution of microscopic BVPs in each macro-level Gauss point. In practice, therefore, the smallest possible size of the micro-structural sample has to be chosen.

Details on specific procedures for the determination of appropriate RVE sizes can be found e.g. in Shan and Gokhale (2002), Gitman (2006), and Temizer and Zohdi (2006). In general, the parameters of interest are compared on successively larger samples until they converge with respect to a specified criterion. Although corresponding analyses have not been performed for lung parenchyma yet, it is subsequently assumed that an alveolar RVE exists[1] and its optimum size is known.

4.2.2 Dynamic macro-level problem

As already mentioned, the developed multi-scale model of lung parenchyma should account for transient effects inherent to (mechanical) ventilation. On the macro-level, therefore, a nonlinear dynamic problem has to be formulated. Corresponding weak and discrete forms have already been derived in section 2.1.3. Accordingly, the material description of the macroscopic principle of virtual work is given by

$$\begin{aligned}\delta\mathcal{W}_{\mathrm{M};0} = &\int_{\Omega_{\mathrm{M};0}} \rho_{\mathrm{M};0}\, \ddot{\boldsymbol{d}}_{\mathrm{M}} \cdot \delta\boldsymbol{d}_{\mathrm{M}}\, \mathrm{d}V_0 + \int_{\Omega_{\mathrm{M};0}} \boldsymbol{S}_{\mathrm{M}} : \delta\boldsymbol{E}_{\mathrm{M}}\, \mathrm{d}V_0 - \int_{\Omega_{\mathrm{M};0}} \hat{\boldsymbol{b}}_{\mathrm{M};0} \cdot \delta\boldsymbol{d}_{\mathrm{M}}\, \mathrm{d}V_0 - \\ &- \int_{\partial\Omega_{\mathrm{M};0;\mathrm{N}}} \boldsymbol{t}_{\mathrm{M};0} \cdot \delta\boldsymbol{d}_{\mathrm{M}}\, \mathrm{d}A_0 \overset{!}{=} 0\end{aligned} \tag{4.2.1}$$

---

[1] An RVE does not exist, for instance, in case of softening when the material loses its statistical homogeneity (Gitman, 2006). However, occurrence of this type of phenomena is not expected here.

with appropriate initial and boundary conditions. In this context, subscript M refers to macro-scale quantities. For the sake of clarity, the superscript S introduced in section 2.1 to denote solid mechanical quantities is dropped here and in the following. The macroscopic reference density $\rho_{\mathrm{M};0}$ and the second Piola-Kirchhoff stresses $\boldsymbol{S}_{\mathrm{M}}$ are highlighted in yellow and blue, respectively.

After discretization of the weak form (4.2.1) in space and time, the nonlinear discrete equation of motion (cf. equation (2.1.78)) is obtained. Linearization then yields the following system of equations at the macroscopic iteration step i_{M}

$$\mathbf{K}^{\mathrm{effdyn}}_{\mathrm{M}}\left(\mathbf{d}^{i_{\mathrm{M}}}_{\mathrm{M};n+1}\right)\Delta\mathbf{d}^{i_{\mathrm{M}}+1}_{\mathrm{M};n+1} = -\mathbf{r}^{\mathrm{effdyn}}_{\mathrm{M}}\left(\mathbf{d}^{i_{\mathrm{M}}}_{\mathrm{M};n+1}\right) \tag{4.2.2}$$

with the dynamic residual defined by

$$\begin{aligned}\mathbf{r}^{\mathrm{effdyn}}_{\mathrm{M}}\left(\mathbf{d}^{i_{\mathrm{M}}}_{\mathrm{M};n+1}\right) = \mathbf{M}_{\mathrm{M}}\,\mathbf{a}^{i_{\mathrm{M}}}_{\mathrm{M};n+1-\alpha_{\mathrm{m}}} + \mathbf{D}_{\mathrm{M}}\,\mathbf{v}^{i_{\mathrm{M}}}_{\mathrm{M};n+1-\alpha_{\mathrm{f}}} + \mathbf{f}^{\mathrm{int}}_{\mathrm{M}}\left(\mathbf{d}^{i_{\mathrm{M}}}_{\mathrm{M};n+1-\alpha_{\mathrm{f}}}\right) - \\ - \mathbf{f}^{\mathrm{ext}}_{\mathrm{M};n+1-\alpha_{\mathrm{f}}}\end{aligned} \tag{4.2.3}$$

and the effective dynamic stiffness matrix given by

$$\mathbf{K}^{\mathrm{effdyn}}_{\mathrm{M}}\left(\mathbf{d}^{i_{\mathrm{M}}}_{\mathrm{M};n+1}\right) = \left[\frac{1-\alpha_{\mathrm{m}}}{\beta\Delta t^2}\,\mathbf{M}_{\mathrm{M}} + \frac{(1-\alpha_{\mathrm{f}})\gamma}{\beta\Delta t}\,\mathbf{D}_{\mathrm{M}} + (1-\alpha_{\mathrm{f}})\,\mathbf{K}_{\mathrm{M}}\left(\mathbf{d}_{\mathrm{M};n+1-\alpha_{\mathrm{f}}}\right)\right]^{i_{\mathrm{M}}} \tag{4.2.4}$$

Again, a Rayleigh ansatz is utilized to consider viscous damping. Since the mass matrix $\mathbf{M}_{\mathrm{M}}$ and the internal force vector $\mathbf{f}^{\mathrm{int};i_{\mathrm{M}}}_{\mathrm{M};n+1-\alpha_{\mathrm{f}}}$ are based on $\rho_{\mathrm{M};0}$ and $\boldsymbol{S}^{i_{\mathrm{M}}}_{\mathrm{M};n+1;-\alpha_{\mathrm{f}}}$, they are also marked in yellow and blue, respectively. The tangent stiffness matrix $\mathbf{K}^{i_{\mathrm{M}}}_{\mathrm{M};n+1-\alpha_{\mathrm{f}}}$ involves the constitutive matrix $\boldsymbol{\mathcal{C}}^{i_{\mathrm{M}}}_{\mathrm{M};n+1-\alpha_{\mathrm{f}}}$ (i.e. the derivative of $\boldsymbol{S}^{i_{\mathrm{M}}}_{\mathrm{M};n+1-\alpha_{\mathrm{f}}}$ with respect to the Green-Lagrange strains $\boldsymbol{E}^{i_{\mathrm{M}}}_{\mathrm{M};n+1-\alpha_{\mathrm{f}}}$), whereas the damping matrix $\mathbf{D}_{\mathrm{M}}$ is composed of the mass matrix and the initial stiffness matrix $\mathbf{K}_{\mathrm{M};0}$. To demonstrate their indirect dependency on $\rho_{\mathrm{M};0}$ or $\boldsymbol{S}^{i_{\mathrm{M}}}_{\mathrm{M};n+1-\alpha_{\mathrm{f}}}$, $\mathbf{D}_{\mathrm{M}}$ and $\mathbf{K}^{i_{\mathrm{M}}}_{\mathrm{M};n+1-\alpha_{\mathrm{f}}}$ are highlighted in green.

Classical single-scale simulations are based on deriving the marked quantities from a phenomenological constitutive law. In the FE^2 approach, however, $\rho_{\mathrm{M};0}$, $\boldsymbol{S}^{i_{\mathrm{M}}}_{\mathrm{M};n+1-\alpha_{\mathrm{f}}}$, and $\boldsymbol{\mathcal{C}}^{i_{\mathrm{M}}}_{\mathrm{M};n+1-\alpha_{\mathrm{f}}}$ are directly computed from the RVE associated with the local Gauss integration point. In the following sections, this approach will be presented in detail.

4.2.3 Macro-micro scale transition

Each RVE can be thought of as an infinitely small sample cut out of the micro-structure in the vicinity of the macroscopic Gauss integration point. When applying the consistent internal forces, the micro-structural deformation state of the RVE can be determined exactly. In practice, however, these forces are unknown since the surrounding micro-structure is not resolved explicitly. Therefore, approximate boundary conditions need to be deduced from the current macro-level state in a so-called macro-micro transition.

To simplify the following considerations, the geometric center of the RVE – which corresponds to the macroscopic Gauss point – is assumed to be located at the origin of the reference frame. In this case, the current position $\boldsymbol{x}_{\mathsf{m}}$ of any material point $\boldsymbol{x}_{0;\mathsf{m}}$ of the RVE is given by

$$\boldsymbol{x}_{\mathsf{m}} = \boldsymbol{F}_{\mathsf{M}} \cdot \boldsymbol{x}_{0;\mathsf{m}} + \tilde{\boldsymbol{w}}_{\mathsf{m}} \left(\boldsymbol{x}_{0;\mathsf{m}} \right) \tag{4.2.5}$$

with subscript m identifying micro-scale quantities and $\boldsymbol{F}_{\mathsf{M}}$ denoting the deformation gradient at the associated macroscopic Gauss integration point. $\tilde{\boldsymbol{w}}_{\mathsf{m}}$ refers to the non-homogeneous (or non-affine) fine-scale contribution to the deformation. These so-called displacement fluctuations directly result from the presence of heterogeneities on the micro-level. The choice of suitable boundary conditions is essential for the accurate determination of $\tilde{\boldsymbol{w}}_{\mathsf{m}}$ and, thereby, also the averaged stresses and constitutive tensors passed back to the macro-level BVP.

In homogenization analyses, three basic types of boundary conditions are of practical interest, viz. (i) homogeneous displacements, (ii) periodic displacements, or (iii) uniform tractions. Resultant boundary displacement fluctuations are (i) zero, (ii) periodic, or (iii) unconstrained. Corresponding to the degree of the imposed kinematical constraint, prescription of homogeneous boundary displacements gives the stiffest RVE response, whereas utilization of traction boundary conditions produces the most compliant solution. Accordingly, employment of periodic boundary displacements in general yields intermediate results. Strictly speaking, periodic boundary conditions are valid only for perfectly periodic media. It has been shown, though, that even for non-periodic materials, application of these boundary conditions provides the most expedient effective response under a wide range of conditions (Zohdi and Wriggers, 2005). Therefore, many FE^2 models are based on periodic displacement boundary conditions on the micro-scale (cf. e.g. Kouznetsova et al. (2001), Feyel (2003), Kouznetsova et al. (2004), and Oezdemir et al. (2008)).

However, when the sample is arbitrarily large compared to the present heterogeneities, it can be argued that the behavior is in the limit independent of the boundary conditions (Hill, 1972). Hence, the advantages of one boundary condition over another diminish as the sample size increases (see e.g. Terada et al. (2000) and Peric et al. (2010) for numerical examples attesting this convergence). As a first step, therefore, it seems reasonable to focus on the simplest of the three alternatives. In contrast to the homogeneous displacement boundary conditions, the kinematical constraints involved in uniform traction and periodic boundary conditions are rather non-conventional. This is due to the fact that corresponding conditions cannot be described in terms of either fully constrained or completely free nodal DOFs (Peric et al., 2010). Although several approaches to imposing these kinds of constraints in a deformation-driven procedure have been proposed in the literature (cf. e.g. Kouznetsova (2002), Miehe and Koch (2002), Miehe (2003), Somer et al. (2009), and Peric et al. (2010)), homogeneous displacement boundary conditions will be utilized exclusively within this work for simplicity.

In this case, equation (4.2.5) reduces to

$$\boldsymbol{x}_{\mathsf{m};\partial\Omega_{\mathsf{m}}} = \boldsymbol{F}_{\mathsf{M}} \cdot \boldsymbol{x}_{0;\mathsf{m};\partial\Omega_{\mathsf{m}}} \tag{4.2.6}$$

at the RVE boundary $\partial\Omega_{\mathsf{m}}$. Using a more convenient matrix notation, the boundary deformation of the RVE in the i_{M}-th macro-scale iteration at $t_{n+1-\alpha_{\mathrm{f}}}$ is, thus, given by

$$\boldsymbol{x}^{i_{\mathsf{M}}}_{\mathsf{m};n+1-\alpha_{\mathrm{f}};\partial\Omega_{\mathsf{m}}} = \mathbb{D}^{\mathsf{T}}\mathbf{F}^{i_{\mathsf{M}}}_{\mathsf{M};n+1-\alpha_{\mathrm{f}}}. \tag{4.2.7}$$

In this context, $\mathbb{D}$ is a matrix containing the positions of the undeformed RVE boundary nodes, i.e.

$$\mathbb{D} = \begin{bmatrix} x_{0;\mathsf{m};1;1} & 0 & 0 & x_{0;\mathsf{m};2;1} & 0 & 0 & \cdots \\ 0 & x_{0;\mathsf{m};1;2} & 0 & 0 & x_{0;\mathsf{m};2;2} & 0 & \cdots \\ 0 & 0 & x_{0;\mathsf{m};1;3} & 0 & 0 & x_{0;\mathsf{m};2;3} & \cdots \\ x_{0;\mathsf{m};1;2} & 0 & 0 & x_{0;\mathsf{m};2;2} & 0 & 0 & \cdots \\ 0 & x_{0;\mathsf{m};1;3} & 0 & 0 & x_{0;\mathsf{m};2;3} & 0 & \cdots \\ 0 & 0 & x_{0;\mathsf{m};1;1} & 0 & 0 & x_{0;\mathsf{m};2;1} & \cdots \\ x_{0;\mathsf{m};1;3} & 0 & 0 & x_{0;\mathsf{m};2;3} & 0 & 0 & \cdots \\ 0 & x_{0;\mathsf{m};1;1} & 0 & 0 & x_{0;\mathsf{m};2;1} & 0 & \cdots \\ 0 & 0 & x_{0;\mathsf{m};1;2} & 0 & 0 & x_{0;\mathsf{m};2;2} & \cdots \end{bmatrix}, \tag{4.2.8}$$

with $x_{0;\mathsf{m};I;r}$ being the r-th component of the reference position vector of node I. $\mathbf{F}^{i_{\mathsf{M}}}_{\mathsf{M};n+1-\alpha_{\mathrm{f}}}$ is the macro-scale deformation gradient given in Voigt's notation by

$$\mathbf{F}^{i_{\mathsf{M}}}_{\mathsf{M};n+1-\alpha_{\mathrm{f}}} = \begin{bmatrix} F_{11} \\ F_{22} \\ F_{33} \\ F_{12} \\ F_{23} \\ F_{31} \\ F_{13} \\ F_{21} \\ F_{32} \end{bmatrix}^{i_{\mathsf{M}}}_{\mathsf{M};n+1-\alpha_{\mathrm{f}}}. \tag{4.2.9}$$

Depending on the specific element technology utilized on the macro-level to prevent locking, the actual macroscopic deformation gradient may not be directly accessible. If, for example, an enhanced assumed strain (EAS) formulation involving a modification of the Green-Lagrange strains is employed, a consistent deformation gradient has to be recalculated. It seems suitable to assume that the EAS approach affects the stretch tensor only. Hence, the unaltered rotation tensor can be computed from the original deformation gradient

$$\boldsymbol{F}_{\mathsf{M}} = \tilde{\boldsymbol{R}}_{\mathsf{M}} \cdot \tilde{\boldsymbol{U}}_{\mathsf{M}} \tag{4.2.10}$$

by means of a singular value decomposition. The modified stretch tensor $\tilde{\boldsymbol{U}}^{\mathsf{EAS}}_{\mathsf{M}}$ itself is determined from the enhanced Green-Lagrange strains

$$\boldsymbol{E}^{EAS}_{\mathsf{M}} = \frac{1}{2}\left(\left(\tilde{\boldsymbol{U}}^{\mathsf{EAS}}_{\mathsf{M}}\right)^{\mathsf{T}} \cdot \tilde{\boldsymbol{U}}^{\mathsf{EAS}}_{\mathsf{M}} - \boldsymbol{I}\right) \tag{4.2.11}$$

via another singular value decomposition. A possible (although not unique) consistent deformation gradient is then given by

$$\boldsymbol{F}_{\mathrm{M}}^{EAS} = \tilde{\boldsymbol{R}}_{\mathrm{M}} \cdot \tilde{\boldsymbol{U}}_{\mathrm{M}}^{\mathrm{EAS}}. \tag{4.2.12}$$

By contrast, approaches based on the direct modification of the deformation gradient (e.g. the so-called F-bar method (De Souza Neto et al., 1996)) can be utilized on the macro-level without necessitating additional computational effort.

The boundary constraint (4.2.6) can be enforced directly by adequate modification of the RVE linear system introduced in section 4.2.4. Alternatively, a formulation based on the Lagrange multiplier approach (cf. e.g. Miehe (2003)) or the penalty method (see e.g. Temizer and Wriggers (2008)) is also possible. In this work, the first option is chosen since it enables exact satisfaction of the boundary condition without introducing additional unknowns.

It is important to remember that the definition of reasonable boundary conditions for alveolar simulations is one of the main reasons to develop a multi-scale model of lung parenchyma. The macro-micro transition discussed previously can be interpreted as an embedding of individual alveolar ensembles into a global lung parenchyma model. Thereby, the influence of the unresolved surrounding micro-structure is incorporated via the macro-level in a simplified way.

4.2.4 Quasi-static micro-level problem

After having derived suitable boundary conditions from the macro-level, the local micro-scale problem can now be addressed in more detail. In the following, the RVE is supposed to be devoid of any discontinuities, whereas the presence of voids is not excluded. Furthermore, its is assumed that the microscopic material behavior can be described by phenomenological constitutive models given in general by

$$\boldsymbol{S}_{\mathrm{m}} = \boldsymbol{g}(\boldsymbol{E}_{\mathrm{m}}^{i_{\mathrm{M}}}, \boldsymbol{x}_{0;\mathrm{m}}^{i_{\mathrm{M}}}, \Xi_{\mathrm{m}}^{i_{\mathrm{M}}}, t) \tag{4.2.13}$$

with $\Xi_{\mathrm{m}}^{i_{\mathrm{M}}}$ denoting possible internal variables. Within this work, only convex problems satisfying material and structural stability conditions on the micro-level are considered.

Since inertial effects are already fully taken into account on the macro-scale (cf. equation (4.2.1)), a quasi-static formulation is chosen for the micro-level problem. The corresponding weak form is then defined by

$$\int_{\Omega_{\mathrm{m};0}} \boldsymbol{S}_{\mathrm{m}}^{i_{\mathrm{M}}} \cdot \delta\boldsymbol{E}_{\mathrm{m}} \mathrm{d}V_0 - \int_{\Omega_{\mathrm{m};0}} \hat{\boldsymbol{b}}_{\mathrm{m};0}^{i_{\mathrm{M}}} \cdot \delta\boldsymbol{d}_{\mathrm{m}} \mathrm{d}V_0 - \int_{\partial\Omega_{\mathrm{m};0;\mathrm{N}}} \hat{\boldsymbol{t}}_{\mathrm{m};0}^{i_{\mathrm{M}}} \cdot \delta\boldsymbol{d}_{\mathrm{m}} \mathrm{d}A_0 = 0 \tag{4.2.14}$$

where the dependence on the coarse-scale iteration index i_{M} comes about due to the boundary conditions stated in (4.2.7). From the equivalence of the virtual work on micro- and macro-level (see also section 4.2.5), Peric et al. (2010) deduced that the contributions of the body force and surface traction fields have to vanish. Hence, no micro-level forces are permitted except the reaction forces associated with the imposed kinematical constraints. Consequently, the weak form (4.2.14) reduces to

$$\delta\mathcal{W}_{\mathrm{m};0} = \int_{\Omega_{\mathrm{m};0}} \boldsymbol{S}_{\mathrm{m}}^{i_{\mathrm{M}}} : \delta\boldsymbol{E}_{\mathrm{m}}\,\mathrm{d}V_0 = 0. \tag{4.2.15}$$

After spatial discretization with FE, equation (4.2.15) can be simply reformulated as

$$\mathbf{f}_{\mathrm{m}}^{\mathrm{int}}\left(\mathbf{d}_{\mathrm{m}}^{i_{\mathrm{M}}}\right) = \mathbf{0} \tag{4.2.16}$$

with $\mathbf{d}_{\mathrm{m}}^{i_{\mathrm{M}}}$ as the global vector of displacements and $\mathbf{f}_{\mathrm{m}}^{\mathrm{int};i_{\mathrm{M}}}$ denoting the global vector of internal forces on the micro-level.

Due to the mutual coupling of scales, a pseudo time step as well as a generalized mid-point $t_{n+1-\alpha_{\mathrm{f}}}$ need to be introduced also on the micro-level. By this means, equilibrium can be evaluated at the same physical point in time and information can be transferred between the scales consistently. For solving the nonlinear problem (4.2.16), Newton's method is again utilized. The linearized system at the pseudo generalized mid-point is then given by

$$\mathbf{K}_{\mathrm{m}}^{\mathrm{effdyn}}\left(\mathbf{d}_{\mathrm{m};n+1}^{i_{\mathrm{M}};i_{\mathrm{m}}}\right)\Delta\mathbf{d}_{\mathrm{m};n+1}^{i_{\mathrm{M}};i_{\mathrm{m}}+1} = -\mathbf{r}_{\mathrm{m}}^{\mathrm{effdyn}}\left(\mathbf{d}_{\mathrm{m};n+1}^{i_{\mathrm{M}};i_{\mathrm{m}}}\right) \tag{4.2.17}$$

where superscript i_{m} indicates the micro-level iteration step which is strictly distinct from the coarse-scale iteration step i_{M}. From equation (4.2.16), the micro-scale residual of linear momentum balance can be identified as

$$\mathbf{r}_{\mathrm{m}}^{\mathrm{effdyn}}\left(\mathbf{d}_{\mathrm{m};n+1}^{i_{\mathrm{M}};i_{\mathrm{m}}}\right) = \mathbf{f}_{\mathrm{m}}^{\mathrm{int}}\left(\mathbf{d}_{\mathrm{m};n+1-\alpha_{\mathrm{f}}}^{i_{\mathrm{M}};i_{\mathrm{m}}}\right). \tag{4.2.18}$$

The corresponding effective "dynamic" stiffness matrix for the quasi-static problem reduces to

$$\mathbf{K}_{\mathrm{m}}^{\mathrm{effdyn}}\left(\mathbf{d}_{\mathrm{m};n+1}^{i_{\mathrm{M}};i_{\mathrm{m}}}\right) = \left.\frac{\partial\mathbf{r}_{\mathrm{m}}^{\mathrm{effdyn}}\left(\mathbf{d}_{\mathrm{m};n+1}\right)}{\partial\mathbf{d}_{\mathrm{m};n+1}}\right|^{i_{\mathrm{M}};i_{\mathrm{m}}} = (1-\alpha_{\mathrm{f}})\,\mathbf{K}_{\mathrm{m}}\left(\mathbf{d}_{\mathrm{m};n+1-\alpha_{\mathrm{f}}}^{i_{\mathrm{M}};i_{\mathrm{m}}}\right) \tag{4.2.19}$$

with $\mathbf{K}_{\mathrm{m}}$ denoting the current fine-scale tangential stiffness matrix at $t_{n+1-\alpha_{\mathrm{f}}}$. Introducing furthermore

$$\Delta\mathbf{d}_{\mathrm{m};n+1-\alpha_{\mathrm{f}}}^{i_{\mathrm{M}};i_{\mathrm{m}}+1} = (1-\alpha_{\mathrm{f}})\,\Delta\mathbf{d}_{\mathrm{m};n+1}^{i_{\mathrm{M}};i_{\mathrm{m}}+1}, \tag{4.2.20}$$

the subsequent linear system of equations on the micro-scale is obtained

$$\mathbf{K}_{\mathrm{m}}\left(\mathbf{d}_{\mathrm{m};n+1-\alpha_{\mathrm{f}}}^{i_{\mathrm{M}};i_{\mathrm{m}}}\right)\Delta\mathbf{d}_{\mathrm{m};n+1-\alpha_{\mathrm{f}}}^{i_{\mathrm{M}};i_{\mathrm{m}}+1} = -\mathbf{f}_{\mathrm{m}}^{\mathrm{int}}\left(\mathbf{d}_{\mathrm{m};n+1-\alpha_{\mathrm{f}}}^{i_{\mathrm{M}};i_{\mathrm{m}}}\right). \tag{4.2.21}$$

For convenience, all quantities are expressed at the pseudo generalized mid-point. Solving equation (4.2.21) for $\Delta\mathbf{d}_{\mathrm{m};n+1-\alpha_{\mathrm{f}}}^{i_{\mathrm{M}};i_{\mathrm{m}}+1}$ then allows for the update of the displacements at $t_{n+1-\alpha_{\mathrm{f}}}$, i.e.

$$\mathbf{d}_{\mathrm{m};n+1-\alpha_{\mathrm{f}}}^{i_{\mathrm{M}};i_{\mathrm{m}}+1} = \mathbf{d}_{\mathrm{m};n+1-\alpha_{\mathrm{f}}}^{i_{\mathrm{M}};i_{\mathrm{m}}} + \Delta\mathbf{d}_{\mathrm{m};n+1-\alpha_{\mathrm{f}}}^{i_{\mathrm{M}};i_{\mathrm{m}}+1}. \tag{4.2.22}$$

The iterative procedure is aborted, i.e. $\mathbf{d}_{\mathrm{m};n+1-\alpha_{\mathrm{f}}}^{i_{\mathrm{M}};i_{\mathrm{m}}+1} = \mathbf{d}_{\mathrm{m};n+1-\alpha_{\mathrm{f}}}^{i_{\mathrm{M}}}$, when a user-specified micro-level convergence criterion is met. In some cases, convergence of the RVE problem is critical and macro-scale time step sizes have to be chosen very small. Alternatively, a substepping scheme based on a step-wise application of the macroscopic deformation gradient can be utilized (Somer et al., 2009). This procedure was shown to substantially increase the robustness and efficiency of the numerical solution on the micro-level.

For the converged RVE problem, effective macroscopic stresses and constitutive tensors at iteration step i_M can be determined by volume averaging (see section 4.2.5). After having reached a converged state on the macro-level as well, fine-scale displacements – as well as any history variables, e.g. time-dependent surface stresses – have to be updated to the end of the pseudo time step t_{n+1} as follows

$$\mathbf{d}_{\mathsf{m};n+1} = \frac{\mathbf{d}_{\mathsf{m};n+1-\alpha_\mathsf{f}} - \alpha_\mathsf{f}\,\mathbf{d}_{\mathsf{m};n}}{1-\alpha_\mathsf{f}}. \tag{4.2.23}$$

Micro-level deformations and internal variables need to be stored in every macroscopic Gauss point, thereby requiring a large amount of computational resources in practical applications.

4.2.5 Micro-macro scale transition

Once the micro-scale BVP associated with the i_M-th macroscopic iteration at $t_{n+1-\alpha_\mathsf{f}}$ is solved, local stresses and strains are available. In a next step, global quantities needed for the formulation of the macro-level problem (cf. section 4.2.2) can be derived in a so-called micro-macro scale transition.

In experiments, the mechanical behavior is usually characterized based on measured loads or mean displacements at the surfaces of a representative sample. Therefore, Hill (1972) proposed that the macro-variables in homogenization analyses should also be defined in terms of surface data alone. Although it is not necessary that these macro-variables are unweighted volume averages of their microscopic counterparts, he argued that quantities possessing this particular property are naturally the easiest to handle analytically in the transition between scales. Since the deformation gradient and the first Piola-Kirchhoff stresses meet this criterion, Hill (1972) concluded that their averages are acceptable as macro-variables.

Subsequently, corresponding expressions for $\boldsymbol{F}_\mathsf{M}$ and $\boldsymbol{P}_\mathsf{M}$ will be derived. For this purpose, an alternative representation of $\boldsymbol{F}$ is introduced, i.e.

$$\boldsymbol{F} = \frac{\partial \boldsymbol{x}}{\partial \boldsymbol{x}_0} = \left(\nabla_0 \cdot (\boldsymbol{I} \otimes \boldsymbol{x})\right)^\mathsf{T}. \tag{4.2.24}$$

By making use of Gauss divergence theorem, the macroscopic deformation gradient is then obtained as

$$\boldsymbol{F}_\mathsf{M} = \frac{1}{V_{0;\mathsf{m}}} \int_{\Omega_{\mathsf{m};0}} \boldsymbol{F}_\mathsf{m}\,\mathsf{d}V_0 = \frac{1}{V_{0;\mathsf{m}}} \int_{\Omega_{\mathsf{m};0}} \left(\nabla_0 \cdot (\boldsymbol{I} \otimes \boldsymbol{x}_\mathsf{m})\right)^\mathsf{T} \mathsf{d}V_0 = \frac{1}{V_{0;\mathsf{m}}} \int_{\partial\Omega_{\mathsf{m};0}} \boldsymbol{x}_\mathsf{m} \otimes \boldsymbol{n}_{0;\mathsf{m}}\,\mathsf{d}A_0 \tag{4.2.25}$$

with RVE reference volume $V_{0;\mathrm{m}}$ including also all interior holes. It has to be noted that the equivalence of volume and boundary integrals as stated in equation (4.2.25) is valid in the absence of RVE discontinuities only. Otherwise, the volume average has to be complemented by corresponding surface integrals (Bayreuther, 2004). Due to the assumptions made in section 4.2.4, the homogeneous displacement boundary conditions employed in the macro-micro transition fulfill relation (4.2.25) without further modifications.

In case of the first Piola-Kirchhoff stresses, the correlation between volume and surface integrals can be derived by making use of the following expression

$$\nabla_0 \cdot (\boldsymbol{P}_\mathrm{m} \otimes \boldsymbol{x}_{0;\mathrm{m}}) = (\nabla_0 \cdot \boldsymbol{P}_\mathrm{m}) \otimes \boldsymbol{x}_{0;\mathrm{m}} + \boldsymbol{P}_\mathrm{m} \cdot (\nabla_0 \boldsymbol{x}_{0;\mathrm{m}}) \tag{4.2.26}$$

with $\nabla_0 \boldsymbol{x}_{0;\mathrm{m}} = \boldsymbol{I}$. Recalling furthermore that there are no inertial and body forces on the micro-level, i.e. $\nabla_0 \cdot \boldsymbol{P}_\mathrm{m} = \boldsymbol{0}$, equation (4.2.26) reduces to

$$\boldsymbol{P}_\mathrm{m} = \nabla_0 \cdot (\boldsymbol{P}_\mathrm{m} \otimes \boldsymbol{x}_{0;\mathrm{m}}). \tag{4.2.27}$$

The macroscopic first Piola-Kirchhoff stresses are then given by

$$\begin{aligned} \boldsymbol{P}_\mathrm{M} &= \frac{1}{V_{0;\mathrm{m}}} \int_{\Omega_{\mathrm{m};0}} \boldsymbol{P}_\mathrm{m} \, \mathrm{d}V_0 = \frac{1}{V_{0;\mathrm{m}}} \int_{\Omega_{\mathrm{m};0}} \nabla_0 \cdot (\boldsymbol{P}_\mathrm{m} \otimes \boldsymbol{x}_{0;\mathrm{m}}) \, \mathrm{d}V_0 = \\ &= \frac{1}{V_{0;\mathrm{m}}} \int_{\partial\Omega_{\mathrm{m};0}} (\boldsymbol{P}_\mathrm{m} \otimes \boldsymbol{x}_{0;\mathrm{m}}) \cdot \boldsymbol{n}_{0;\mathrm{m}} \, \mathrm{d}A_0 = \frac{1}{V_{0;\mathrm{m}}} \int_{\partial\Omega_{\mathrm{m};0}} \boldsymbol{f}_{\mathrm{m;B}} \otimes \boldsymbol{x}_{0;\mathrm{m}} \, \mathrm{d}A_0 \end{aligned} \tag{4.2.28}$$

where $\boldsymbol{f}_{\mathrm{m;B}}$ is the vector of boundary forces. Note that equation (4.2.28) is valid in general since local equilibrium at possible inner surfaces and discontinuities implies that corresponding surface integrals always vanish.

In order to allow for a consistent transition between scales, the so-called Hill-Mandel condition has to be satisfied. Essentially, this criterion implies that the volume average of the variational work on the fine-scale equals the local variational work on the coarse-scale (Hill, 1963), i.e.

$$\delta \mathcal{W}_{\mathrm{m};0} = \delta \mathcal{W}_{\mathrm{M};0}. \tag{4.2.29}$$

It can be easily verified that this requirement is a priori fulfilled in case of the chosen set of macro-variables. To this end, the volume average of the virtual work on the micro-level is first expressed in terms of RVE surface quantities as follows

$$\delta \mathcal{W}_{\mathrm{m};0} = \frac{1}{V_{0;\mathrm{m}}} \int_{\Omega_{\mathrm{m};0}} \boldsymbol{P}_\mathrm{m} : \delta \boldsymbol{F}_\mathrm{m} \mathrm{d}V_0 = \frac{1}{V_{0;\mathrm{m}}} \int_{\partial\Omega_{\mathrm{m};0}} \boldsymbol{f}_{\mathrm{m;B}} \cdot \delta \boldsymbol{x} \, \mathrm{d}A_0. \tag{4.2.30}$$

Introduction of the homogeneous displacement boundary condition (4.2.6) then yields

$$\begin{aligned} \delta \mathcal{W}_{\mathrm{m};0} &= \frac{1}{V_{0;\mathrm{m}}} \int_{\partial\Omega_{\mathrm{m};0}} \boldsymbol{f}_{\mathrm{m;B}} \cdot (\delta \boldsymbol{F}_\mathrm{M} \cdot \boldsymbol{x}_{0;\mathrm{m}}) \mathrm{d}A_0 = \frac{1}{V_{0;\mathrm{m}}} \int_{\partial\Omega_{\mathrm{m};0}} \boldsymbol{f}_{\mathrm{m;B}} \otimes \boldsymbol{x}_{0;\mathrm{m}} \, \mathrm{d}A_0 : \delta \boldsymbol{F}_\mathrm{M} = \\ &= \boldsymbol{P}_\mathrm{M} : \delta \boldsymbol{F}_\mathrm{M} = \delta \mathcal{W}_{\mathrm{M};0}. \end{aligned} \tag{4.2.31}$$

By contrast, the volume averages of second Piola-Kirchhoff stresses and Green-Lagrange strains do not satisfy the Hill-Mandel condition and are, therefore, not suitable for the scale transition (Temizer and Zohdi, 2006). Therefore, in line with many other micro-macro approaches (cf. e.g. Kouznetsova (2002), Miehe (2003), and Temizer and Zohdi (2006)), the recommendation of Hill is followed here, although the general formulation of the BVPs on both scales is based on $\boldsymbol{S}$ and $\boldsymbol{E}$.

For a discrete expression of the macroscopic first Piola-Kirchhoff stress (4.2.28), it is beneficial to split the micro-scale equilibrium equations (i.e. the converged version of equation (4.2.17), therefore dropping the iteration index i_m) into prescribed boundary (with index B) and unconstrained interior (with index I) DOFs as follows

$$\begin{bmatrix} \mathbf{K}^{i\mathrm{M}}_{\mathrm{m;BB}} & \mathbf{K}^{i\mathrm{M}}_{\mathrm{m;BI}} \\ \mathbf{K}^{i\mathrm{M}}_{\mathrm{m;IB}} & \mathbf{K}^{i\mathrm{M}}_{\mathrm{m;II}} \end{bmatrix} \cdot \begin{bmatrix} \Delta\mathbf{d}^{i\mathrm{M}}_{\mathrm{m};n+1-\alpha_\mathrm{f};\mathrm{B}} \\ \Delta\mathbf{d}^{i\mathrm{M}}_{\mathrm{m};n+1-\alpha_\mathrm{f};\mathrm{I}} \end{bmatrix} = \begin{bmatrix} \mathbf{f}^{i\mathrm{M}}_{\mathrm{m};n+1-\alpha_\mathrm{f};\mathrm{B}} \\ \mathbf{0} \end{bmatrix}. \tag{4.2.32}$$

The macro-level first Piola-Kirchhoff stress in Voigt's notation then simply reads

$$\mathbf{P}^{i\mathrm{M}}_{\mathrm{M};n+1-\alpha_\mathrm{f}} = \frac{1}{V_{0;\mathrm{m}}}\,\mathbb{D}\,\mathbf{f}^{i\mathrm{M}}_{\mathrm{m};n+1-\alpha_\mathrm{f};\mathrm{B}} \tag{4.2.33}$$

with $\mathbb{D}$ given in equation (4.2.8). The second Piola-Kirchhoff stresses $\boldsymbol{S}^{i\mathrm{M}}_{\mathrm{M};n+1-\alpha_\mathrm{f}}$ needed for the chosen macro-level formulation (cf. also section 4.2.2) can be obtained based on the well-known continuum mechanics relation

$$\boldsymbol{S} = \boldsymbol{F}^{-1}\cdot\boldsymbol{P}. \tag{4.2.34}$$

For application of Newton's method on the macro-scale, the consistent tangent stiffness has to be computed. In a first step, therefore, a constitutive matrix relating first Piola-Kirchhoff stresses and the deformation gradient at the generalized mid-point can be calculated from equation (4.2.33), viz.

$$\begin{aligned} \boldsymbol{\mathcal{A}}^{i\mathrm{M}}_{\mathrm{M};n+1-\alpha_\mathrm{f}} &= \frac{\partial\mathbf{P}^{i\mathrm{M}}_{\mathrm{M};n+1-\alpha_\mathrm{f}}}{\partial\mathbf{F}^{i\mathrm{M}}_{\mathrm{M};n+1-\alpha_\mathrm{f}}} = \frac{1}{V_{0;\mathrm{m}}}\,\mathbb{D}\,\frac{\partial\mathbf{f}^{i\mathrm{M}}_{\mathrm{m};n+1-\alpha_\mathrm{f};\mathrm{B}}}{\partial\mathbf{d}^{i\mathrm{M}}_{\mathrm{m};n+1-\alpha_\mathrm{f};\mathrm{B}}}\,\frac{\partial\mathbf{d}^{i\mathrm{M}}_{\mathrm{m};n+1-\alpha_\mathrm{f};\mathrm{B}}}{\partial\mathbf{F}^{i\mathrm{M}}_{\mathrm{M};n+1-\alpha_\mathrm{f}}} & (4.2.35) \\ &= \frac{1}{V_{0;\mathrm{m}}}\,\mathbb{D}\,\tilde{\mathbf{K}}^{i\mathrm{M}}_{\mathrm{m;BB}}\,\mathbb{D}^\mathrm{T} & (4.2.36) \end{aligned}$$

with $\tilde{\mathbf{K}}^{i\mathrm{M}}_{\mathrm{m;BB}}$ relating micro-scale boundary displacements and respective forces as follows

$$\tilde{\mathbf{K}}^{i\mathrm{M}}_{\mathrm{m;BB}}\cdot\Delta\mathbf{d}^{i\mathrm{M}}_{\mathrm{m};n+1-\alpha_\mathrm{f};\mathrm{B}} = \mathbf{f}^{i\mathrm{M}}_{\mathrm{m};n+1-\alpha_\mathrm{f};\mathrm{B}}. \tag{4.2.37}$$

$\tilde{\mathbf{K}}^{i\mathrm{M}}_{\mathrm{m;BB}}$ can be determined from the linear system (4.2.32) by static condensation of the interior DOFs

$$\tilde{\mathbf{K}}^{i\mathrm{M}}_{\mathrm{m;BB}} = \tilde{\mathbf{K}}_{\mathrm{m;BB}}\left(\mathbf{d}^{i\mathrm{M}}_{\mathrm{m};n+1-\alpha_\mathrm{f}}\right) = \mathbf{K}^{i\mathrm{M}}_{\mathrm{m;BB}} - \mathbf{K}^{i\mathrm{M}}_{\mathrm{m;BI}}\left(\mathbf{K}^{i\mathrm{M}}_{\mathrm{m;II}}\right)^{-1}\mathbf{K}^{i\mathrm{M}}_{\mathrm{m;IB}}. \tag{4.2.38}$$

Since the macro-level problem is formulated in terms of second Piola-Kirchhoff stresses and Green-Lagrange strains, the constitutive tensor $\mathscr{C}$ relating $\boldsymbol{S}$ and $\boldsymbol{E}$ has to be determined. For this purpose, it is convenient to switch from Voigt's notation to a tensorial representation. Introducing $\mathscr{A}$ as the tensor form of $\boldsymbol{\mathcal{A}}$, the following relation is obtained based on the chain rule

$$\begin{aligned} \mathscr{A} &= \frac{\partial \boldsymbol{P}}{\partial \boldsymbol{F}} = \frac{\partial (\boldsymbol{F} \cdot \boldsymbol{S})}{\partial \boldsymbol{F}} = \boldsymbol{F} \cdot \frac{\partial \boldsymbol{S}}{\partial \boldsymbol{E}} \cdot \frac{\partial \boldsymbol{E}}{\partial \boldsymbol{F}} + \frac{\partial \boldsymbol{F}}{\partial \boldsymbol{F}} \cdot \boldsymbol{S} = \\ &= \boldsymbol{F} \cdot \mathscr{C} \cdot \boldsymbol{F}^{\mathsf{T}} + \boldsymbol{I} \otimes \boldsymbol{S}. \end{aligned} \tag{4.2.39}$$

Hence, the desired constitutive tensor is given in index notation by

$$\begin{aligned} \mathscr{C}_{IJKL} &= \frac{1}{4} \Big[F^{-1}_{Ir} \left(\mathscr{A}_{rJsL} - I_{rs} S_{JL} \right) F^{-\mathsf{T}}_{sK} + F^{-1}_{Jr} \left(\mathscr{A}_{rIsL} - I_{rs} S_{IL} \right) F^{-\mathsf{T}}_{sK} + \\ &+ F^{-1}_{Ir} \left(\mathscr{A}_{rJsK} - I_{rs} S_{JK} \right) F^{-\mathsf{T}}_{sL} + F^{-1}_{Jr} \left(\mathscr{A}_{rIsK} - I_{rs} S_{IK} \right) F^{-\mathsf{T}}_{sL} \Big] \end{aligned} \tag{4.2.40}$$

where a symmetrization is performed in order to comply with the minor symmetries of $\mathscr{C}$, i.e.

$$\mathscr{C}_{IJKL} = \mathscr{C}_{JIKL} = \mathscr{C}_{JILK} = \mathscr{C}_{IJLK}. \tag{4.2.41}$$

Based on equation (4.2.40), the sought constitutive matrix in Voigt's notation $\boldsymbol{\mathcal{C}}^{i_{\mathrm{M}}}_{\mathrm{M};n+1-\alpha_{\mathrm{f}}}$ can be defined in a straightforward manner.

It is noteworthy that the determination of the consistent constitutive tensor necessitates the computation of a Schur complement (cf. equation (4.2.38)). Therefore, this procedure is computationally very expensive in practice. Since the tangential stiffness matrix does not change the physical result but only the convergence behavior, approximations are in general possible. For instance, a modified Newton approach could be utilized. In this case, the stiffness matrix is evaluated only once at the beginning of the time step and kept constant during the nonlinear iteration process. Alternatively, a perturbation technique based on a forward difference approximation of the tangent modulus could be employed (cf. e.g. Miehe (1996)). This procedure essentially reduces the determination of the tangent moduli to multiple stress computations based on a perturbed deformation gradient. In the present case, though, this approach would necessitate the solution of six nonlinear micro-level BVPs per macroscopic Gauss point and iteration. Another option is the application of Jacobian-free Newton-Krylov methods to obtain the macro-level solution (see e.g. Knoll and Keyes (2004) for a concise survey). Primary motivation for the development of these approaches has been the ability to perform a Newton iteration without explicitly forming the tangential stiffness matrix. In fact, Krylov solvers (cf. section 5.3) require the action of the Jacobian only in form of matrix-vector products, which may be approximated by

$$\mathbf{K}\mathbf{z} \approx -\frac{1}{\upsilon} \left[\mathbf{r}(\mathbf{d} + \upsilon \mathbf{z}) - \mathbf{r}(\mathbf{d}) \right] \tag{4.2.42}$$

where $\mathbf{r}$ is the residual vector and υ denotes a small perturbation. In contrast to the perturbation technique addressed before, equation (4.2.42) involves the evaluation of only one additional residual in a perturbed state. It has to be noted, though, that utilization of any approximation to the stiffness matrix renders Newton's method inexact, thereby drop-

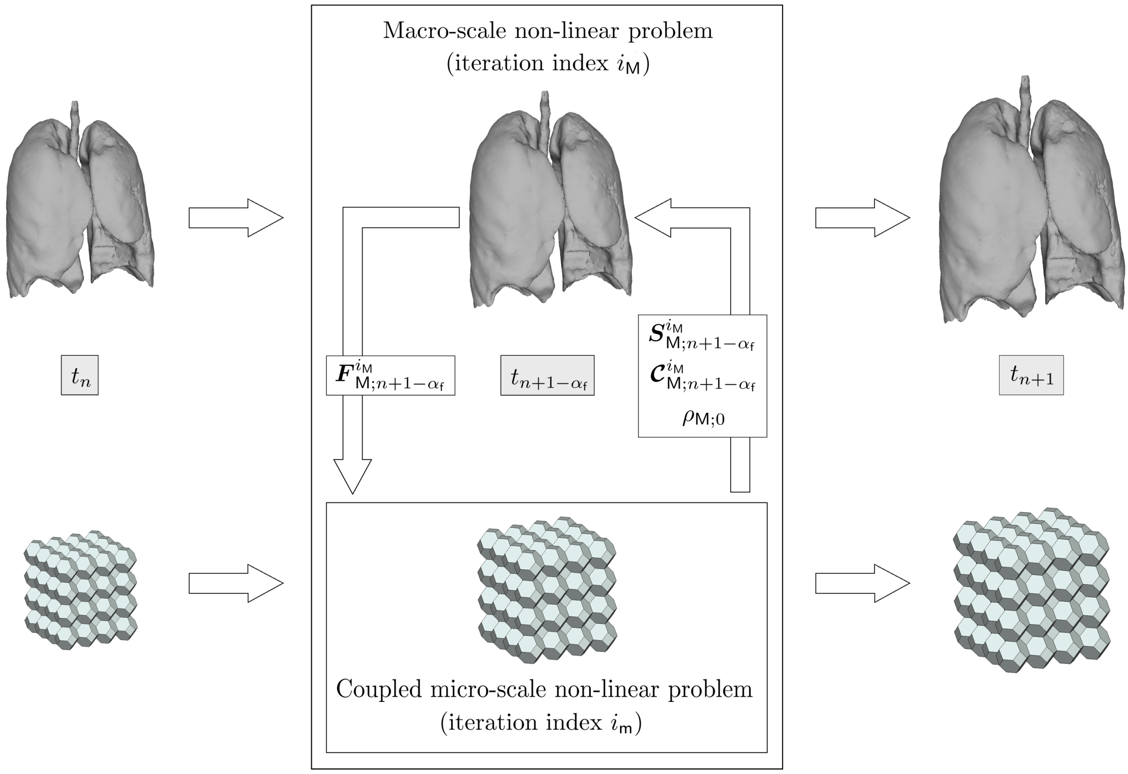

Figure 4.2.1: Schematic overview of the nested dynamic multi-scale method for a given time step $[t_n, t_{n+1}]$.

ping its quadratic convergence behavior. Increasing the number of macroscopic iterations, however, comes along with high computational costs since the nonlinear micro-level problems have to be solved more often. Hence, it is highly doubtful that application of these techniques really pays off. Therefore, in all simulations performed within this work, a consistent constitutive tensor is determined as outlined above.

The final step in the micro-macro transition consists in calculation of the reference density $\rho_{\mathsf{M};0}$ needed for the macro-level consistent mass matrix via

$$\rho_{\mathsf{M};0} = \frac{1}{V_{0;\mathsf{m}}} \int_{\Omega_{\mathsf{m};0}} \rho_{\mathsf{m};0} \mathsf{d}V_0. \qquad (4.2.43)$$

In contrast to the stresses and the constitutive tensor, this quantity needs to be computed only once and not in every coarse-scale iteration step.

With this, all macro-variables of interest have been derived and the macroscopic system of equations can be solved. Thereupon, all steps discussed in sections 4.2.2-4.2.5 are repeated until convergence is achieved on the macro-scale. The presented nested multi-scale approach is sketched in Figure 4.2.1 and summarized in detail in Algorithm 4.1.

Algorithm 4.1 Nested dynamic multi-scale approach.

```
for each time step $\in [t_n, t_{n+1}]$:
    Explicit predictor for $\mathbf{d}^{i_\mathsf{M}=0}_{\mathsf{M};n+1} \rightsquigarrow \mathbf{d}^{i_\mathsf{M}=0}_{\mathsf{M};n+1-\alpha_\mathsf{f}}$ (2.1.72), $\mathbf{v}^{i_\mathsf{M}=0}_{\mathsf{M};n+1-\alpha_\mathsf{f}}$ (2.1.73),
                                  $\mathbf{a}^{i_\mathsf{M}=0}_{\mathsf{M};n+1-\alpha_\mathsf{m}}$ (2.1.74)
    Compute $\mathbf{f}^{\mathsf{ext}}_{\mathsf{M};n+1-\alpha_\mathsf{f}}$ (2.1.75)
    Compute $\mathbf{r}^{\mathsf{effdyn}}_{\mathsf{M}}\left(\mathbf{d}^{i_\mathsf{M}=0}_{\mathsf{M};n+1}\right)$ (4.2.3), $\mathbf{K}^{\mathsf{effdyn}}_{\mathsf{M}}\left(\mathbf{d}^{i_\mathsf{M}=0}_{\mathsf{M};n+1}\right)$ (4.2.4):
        for each Gauss integration point:
            if application of multi-scale approach:
                Prescribe boundary displacements (4.2.6)
                Compute $\mathbf{f}^{\mathsf{int}}_{\mathsf{m}}\left(\mathbf{d}^{i_\mathsf{M}=0;i_\mathsf{m}=0}_{\mathsf{m};n+1-\alpha_\mathsf{f}}\right)$ and $\mathbf{K}_{\mathsf{m}}\left(\mathbf{d}^{i_\mathsf{M}=0;i_\mathsf{m}=0}_{\mathsf{m};n+1-\alpha_\mathsf{f}}\right)$
                for each iteration $i_\mathsf{m}$ until fine-scale convergence:
                    Solve (4.2.21) for $\Delta\mathbf{d}^{i_\mathsf{M}=0;i_\mathsf{m}+1}_{\mathsf{m};n+1-\alpha_\mathsf{f}}$ and update $\mathbf{d}^{i_\mathsf{M}=0;i_\mathsf{m}+1}_{\mathsf{m};n+1-\alpha_\mathsf{f}}$ (4.2.22)
                    Compute $\mathbf{f}^{\mathsf{int}}_{\mathsf{m}}\left(\mathbf{d}^{i_\mathsf{M}=0;i_\mathsf{m}+1}_{\mathsf{m};n+1-\alpha_\mathsf{f}}\right)$ and $\mathbf{K}_{\mathsf{m}}\left(\mathbf{d}^{i_\mathsf{M}=0;i_\mathsf{m}+1}_{\mathsf{m};n+1-\alpha_\mathsf{f}}\right)$
                    Check for fine-scale convergence and update $i_\mathsf{m}$
                Calculate $\boldsymbol{S}^{i_\mathsf{M}=0}_{\mathsf{M};n+1-\alpha_\mathsf{f}}$ (4.2.34), $\boldsymbol{\mathcal{C}}^{i_\mathsf{M}=0}_{\mathsf{M};n+1-\alpha_\mathsf{f}}$ (4.2.40)
            else
                Calculate $\boldsymbol{S}^{i_\mathsf{M}=0}_{\mathsf{M};n+1-\alpha_\mathsf{f}}$, $\boldsymbol{\mathcal{C}}^{i_\mathsf{M}=0}_{\mathsf{M};n+1-\alpha_\mathsf{f}}$ from empirical constitutive law
    for each iteration $i_\mathsf{M}$ until coarse-scale convergence:
        Solve (2.1.84) for $\Delta\mathbf{d}^{i_\mathsf{M}+1}_{\mathsf{M};n+1}$ and update $\mathbf{d}^{i_\mathsf{M}+1}_{\mathsf{M};n+1}$ (2.1.85)
        $\rightsquigarrow \mathbf{d}^{i_\mathsf{M}+1}_{\mathsf{M};n+1-\alpha_\mathsf{f}}$ (2.1.72), $\mathbf{v}^{i_\mathsf{M}+1}_{\mathsf{M};n+1-\alpha_\mathsf{f}}$ (2.1.73), $\mathbf{a}^{i_\mathsf{M}+1}_{\mathsf{M};n+1-\alpha_\mathsf{m}}$ (2.1.74)
        Compute $\mathbf{r}^{\mathsf{effdyn}}_{\mathsf{M}}\left(\mathbf{d}^{i_\mathsf{M}+1}_{\mathsf{M};n+1}\right)$ (4.2.3), $\mathbf{K}^{\mathsf{effdyn}}_{\mathsf{M}}\left(\mathbf{d}^{i_\mathsf{M}+1}_{\mathsf{M};n+1}\right)$ (4.2.4):
            for each Gauss integration point:
                if application of multi-scale approach:
                    Prescribe boundary displacements (4.2.6)
                    Compute $\mathbf{f}^{\mathsf{int}}_{\mathsf{m}}\left(\mathbf{d}^{i_\mathsf{M}+1;i_\mathsf{m}=0}_{\mathsf{m};n+1-\alpha_\mathsf{f}}\right)$ and $\mathbf{K}_{\mathsf{m}}\left(\mathbf{d}^{i_\mathsf{M}+1;i_\mathsf{m}=0}_{\mathsf{m};n+1-\alpha_\mathsf{f}}\right)$
                    for each iteration $i_\mathsf{m}$ until fine-scale convergence:
                        Solve (4.2.21) for $\Delta\mathbf{d}^{i_\mathsf{M}+1;i_\mathsf{m}+1}_{\mathsf{m};n+1-\alpha_\mathsf{f}}$
                        Update $\mathbf{d}^{i_\mathsf{M}+1;i_\mathsf{m}+1}_{\mathsf{m};n+1-\alpha_\mathsf{f}}$ (4.2.22)
                        Compute $\mathbf{f}^{\mathsf{int}}_{\mathsf{m}}\left(\mathbf{d}^{i_\mathsf{M}+1;i_\mathsf{m}+1}_{\mathsf{m};n+1-\alpha_\mathsf{f}}\right)$ and $\mathbf{K}_{\mathsf{m}}\left(\mathbf{d}^{i_\mathsf{M}+1;i_\mathsf{m}+1}_{\mathsf{m};n+1-\alpha_\mathsf{f}}\right)$
                        Check for fine-scale convergence and update $i_\mathsf{m}$
                    Calculate $\boldsymbol{S}^{i_\mathsf{M}+1}_{\mathsf{M};n+1-\alpha_\mathsf{f}}$ (4.2.34), $\boldsymbol{\mathcal{C}}^{i_\mathsf{M}+1}_{\mathsf{M};n+1-\alpha_\mathsf{f}}$ (4.2.40)
                else
                    Calculate $\boldsymbol{S}^{i_\mathsf{M}=0}_{\mathsf{M};n+1-\alpha_\mathsf{f}}$, $\boldsymbol{\mathcal{C}}^{i_\mathsf{M}=0}_{\mathsf{M};n+1-\alpha_\mathsf{f}}$ from empirical constitutive law
        Check for coarse-scale convergence and update $i_\mathsf{M}$
    for each Gauss integration point:
        if application of multi-scale approach:
            Update $\mathbf{d}_{\mathsf{m};n+1}$ (4.2.23) and potential internal micro-variables
    Update $n$
```

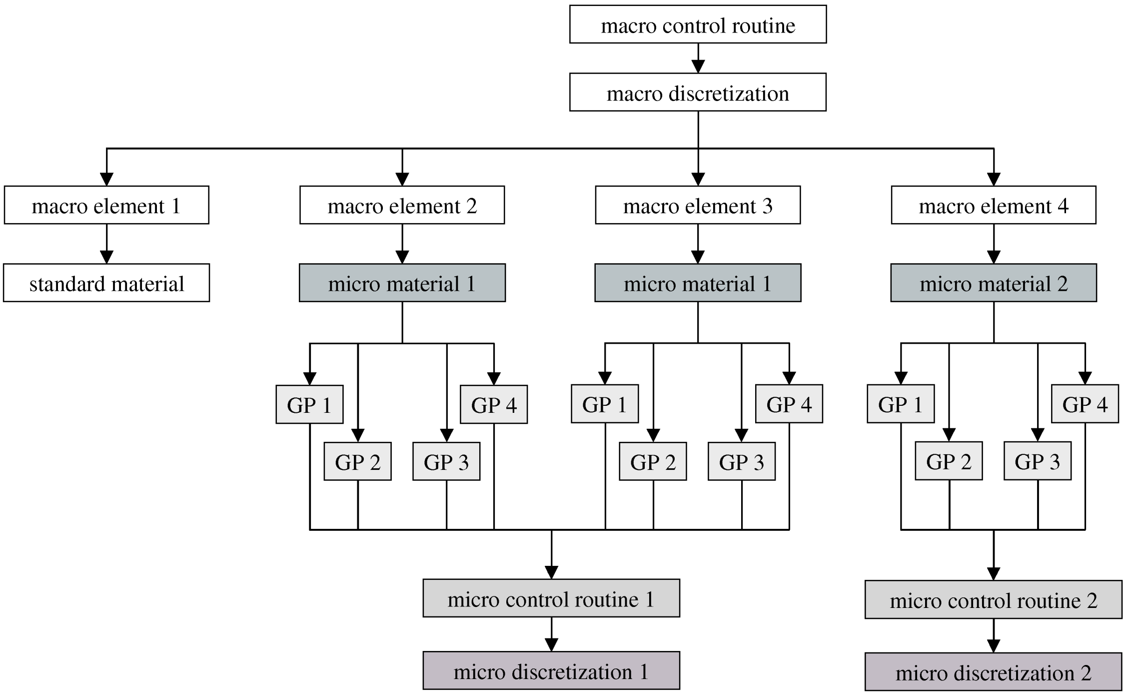

Figure 4.3.1: Basic organization of the multi-scale implementation in BACI.

4.3 Implementation details

In contrast to standard constitutive models, the implementation of a nested multi-scale approach is significantly more involved. Particularly, if a multi-purpose FE code like BACI should be utilized, the reasonable organization of data structures is essential. In Figure 4.3.1, a schematic overview of the basic code architecture is given.

On the macro-level, the dynamic simulation is governed by a corresponding control routine including time and nonlinear iteration loops. For setting up corresponding internal forces, mass and stiffness matrices, the macroscopic discretization has to be accessed. Apart from defining the topology of the mesh, this class provides functions for evaluating all kinds of element integrals.

Each individual macro-element refers to a specific material. As indicated in Figure 4.3.1, both standard constitutive models (macro element 1) and multi-scale schemes (macro elements 2-4) can be employed within one simulation. By defining distinct classes of so-called micro materials, different RVEs can be associated with the macro elements. In Figure 4.3.1, accordingly, the same RVE is applied in macro elements 2 and 3, whereas a different realization of the micro-structure is assumed in macro element 4. The possibility of assigning distinct RVEs to different locations in the macroscopic domain is particularly important when heterogeneous lung damages have to be considered. In this case, the alveolar morphology, material, and surfactant behavior may vary significantly in different lung regions.

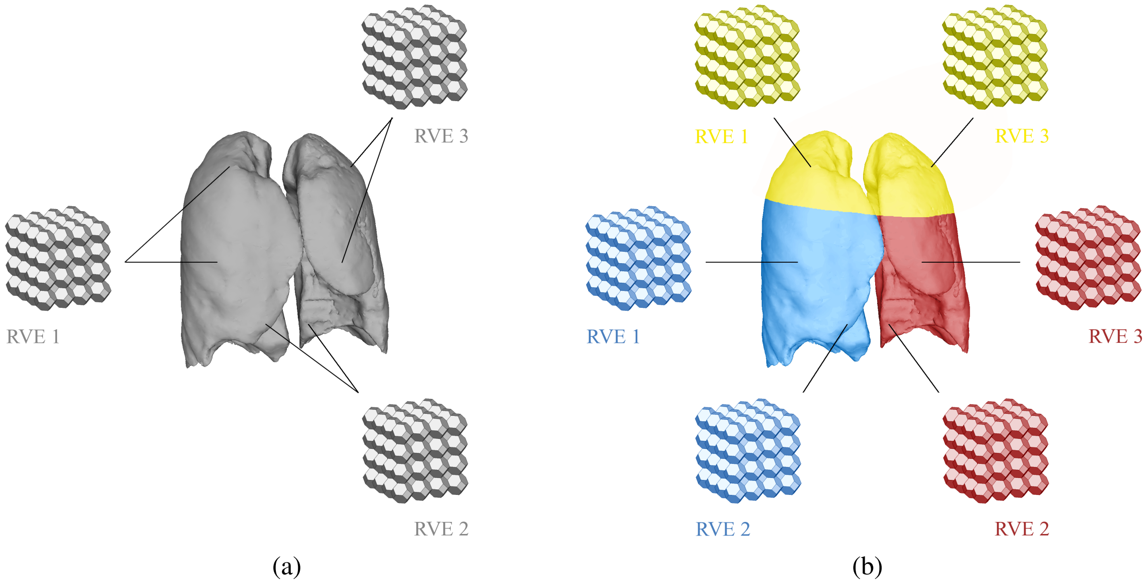

Figure 4.3.2: (a) Serial computation on both levels. Each RVE discretization needs to be defined only once. (b) Parallel simulation on the macro-scale and serial computation on the micro-level. Colors represent individual processors. RVE discretizations have to be accessible on every processor containing macro-elements with the corresponding micro material.

The actual scale transition is performed in every Gauss point of an element implementing a micro material. For organizing local microscopic deformation states and history variables (such as time-dependent surface stresses), a corresponding interface class has to be provided for each Gauss point. In Figure 4.3.1, these structures (indicated by the abbreviation "GP" followed by the ID of the Gauss point) are shown exemplarily for four integration points per element. To avoid redundant information, all Gauss points belonging to elements with an identical micro material resort to the same RVE discretization and corresponding microscopic control routine. Therefore, the GP classes have to provide routines for passing current state vectors to the micro control routine. After having solved the nonlinear BVP in the individual Gauss point, updated microscopic state vectors need to be collected from the control routine again.

The presented implementation essentially allows to hide the complex micro-macro scheme behind a specific material class. Since no modifications of the macroscopic formulation are necessary, the multi-scale approach can be directly applied to coupled scenarios such as FSI problems (see section 5.4.2 for a corresponding numerical example).

A fully coupled multi-scale analysis – especially in case of large three-dimensional problems – is computationally very expensive in practice. Therefore, efficient solvers and parallel computing are of course indispensable and, therefore, utilized in this work (see Wiechert et al. (2007) for details). In each macroscopic iteration step, all RVE simulations can be performed simultaneously without necessitating any data exchange. Therefore, parallelization of the macroscopic problem is straightforward. The individual RVE computations, however, are currently performed serially on each processor. The resulting distribution of macro- and micro-scale discretizations is shown schematically in Figure 4.3.2(b). For comparison, the general set-up of a serial macroscopic simulation is given in Figure 4.3.2(a). In this case, only one RVE discretization per micro material needs to be available. By contrast, RVE discretizations have to be stored redundantly if macro elements referring to the same micro material are distributed over different processors. Depending on the size and complexity of the RVE problem, the chosen serial framework may soon become prohibitive. Therefore, the combination of parallel and serial algorithms implemented within this work can only be regarded as a first step towards nested parallelization (cf. e.g. an Mey et al. (2007) for an implementation using OpenMP).

4.4 Numerical examples

After having discussed in detail the dynamic multi-scale scheme and its implementation, some illustrative numerical examples will now be provided. First, the micro-macro procedure will be validated for homogeneous materials with differently shaped RVEs. Subsequently, simple multi-scale simulations of lung parenchyma will be presented, thereby demonstrating that the developed approach is suitable for coupled, dynamic problems on the micro-level.

4.4.1 Validation

In case of a homogeneous material, the mechanical behavior can be accurately modeled in a single-scale simulation. Corresponding results may, therefore, serve as a reference solution for several multi-scale computations with homogeneous micro-structures of the same material. Exemplarily, a dynamic tension test of a steel cube (edge length $l = 1.0$ cm) modeled by a St. Venant-Kirchhoff material ($E = 210$ GPa, $\nu = 0.3$, $\rho_0 = 7.85$ g/cm^3) and discretized with 27 linear hexahedral elements is presented here. The deformation of the bottom surface was fixed and the cube was sinusoidally loaded by a uniformly distributed tension load on the top surface (cf. equation (3.3.55) with $p_{\mathrm{max}} = 40$ GPa, $T = 4$ s). In the multi-scale simulations, three different scenarios were investigated. Firstly, a cubic micro-structure consisting of 27 linear hexahedral elements was associated with every coarse-scale Gauss point. Secondly, a solid tetrakaidecahedron discretized with 162 linear hexahedral elements was employed as RVE throughout the macro-scale domain. Thirdly, multi-scale models based on both previously mentioned micro-structures were utilized in four coarse-scale elements only whereas a standard constitutive law was applied in the remaining macro-level elements.

Exemplary deformation states are depicted in Figure 4.4.1. The reference solutions of the single-scale simulation were reproduced for all configurations at any time. Owing to the consistent constitutive tensor derived in the micro-macro transition, quadratic convergence behavior was achieved.

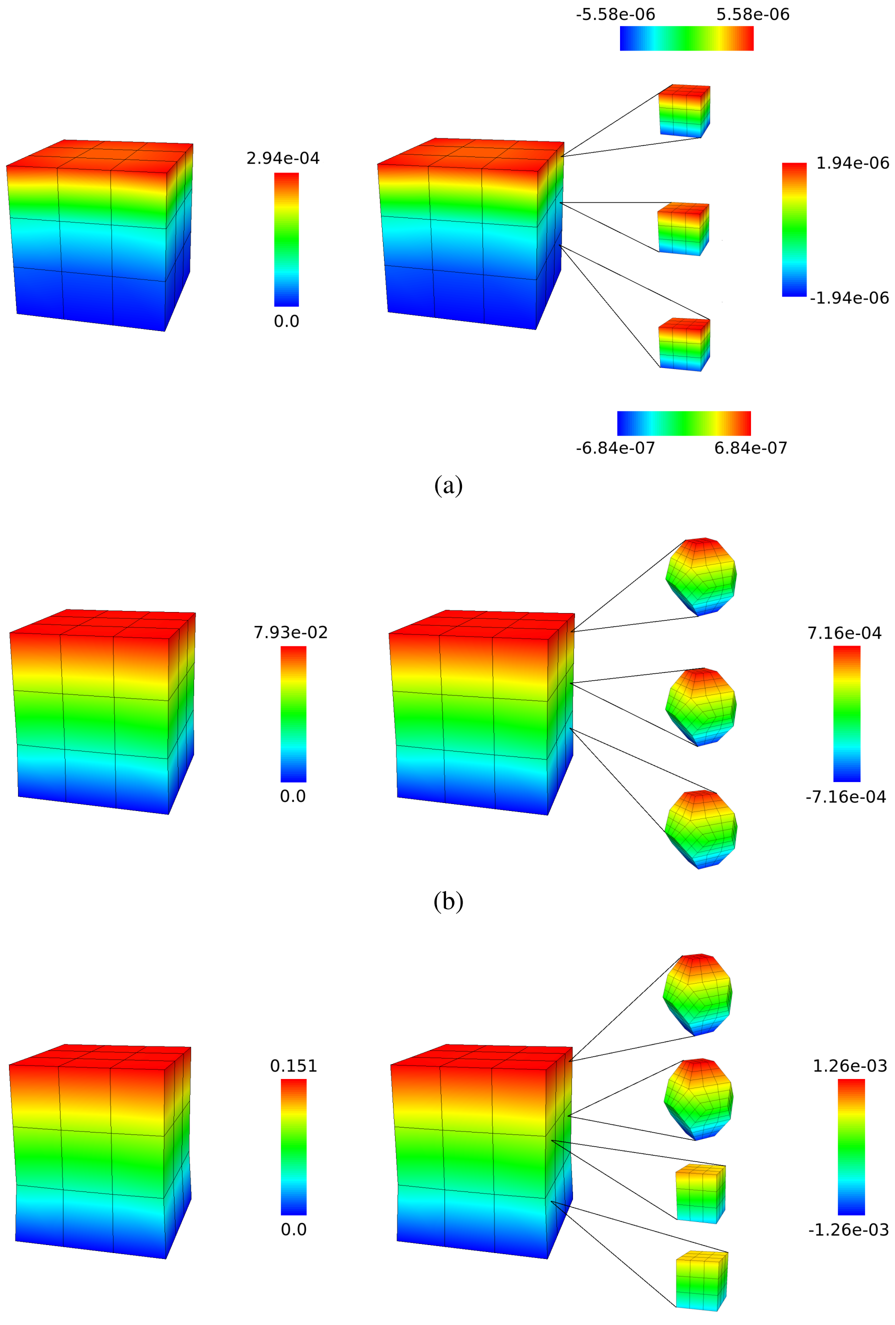

(a)

(b)

(c)

Figure 4.4.1: Deformation states for different fine-scale configurations at different points in time. Colors indicate vertical displacements in cm. Left: Reference solution obtained in single-scale simulation. Right: Multi-scale or combined single- and multi-scale solution with different RVEs. Exemplary micro-structures are enlarged compared to the macro-scale. (a) $t = 0.1$ s, cubic fine-scale. (b) $t = 9.0$ s, solid tetrakaidecahedral fine-scale. (c) $t = 10.0$ s (under maximum load), combined single- and multi-scale solution with different RVEs.

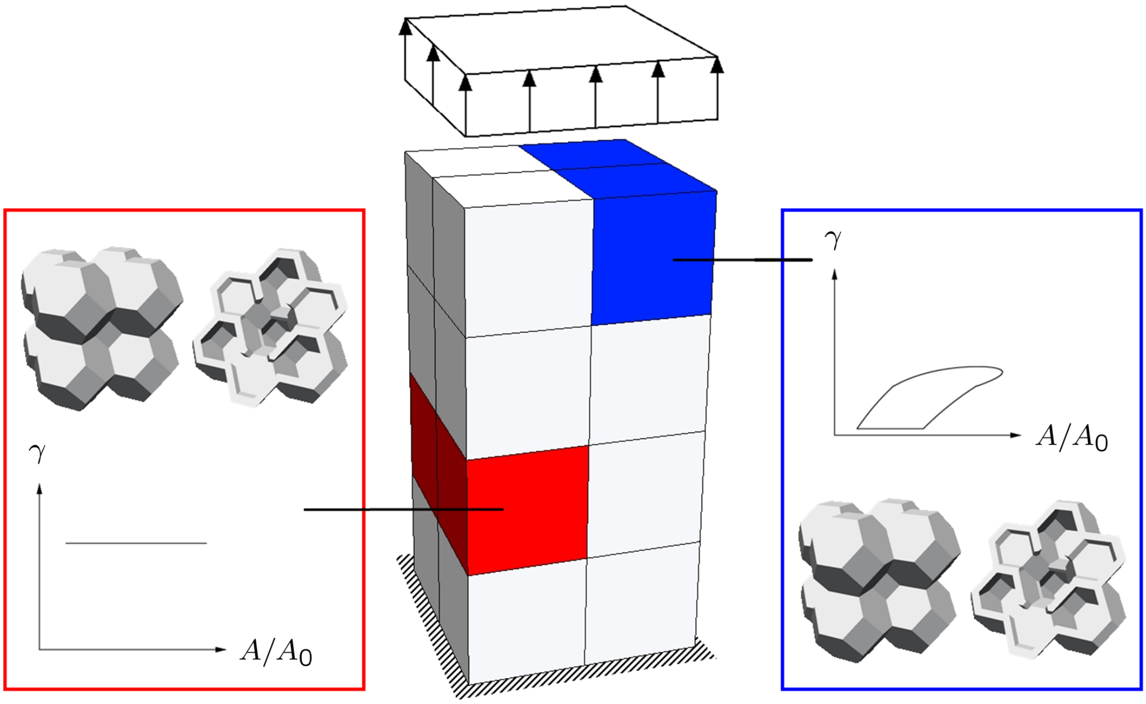

Figure 4.4.2: General set-up of example simulation. In marked coarse-scale elements a multi-scale model was used, whereas a phenomenological constitutive law was employed in the others. The fine-scale was realized by an assemblage of nine hollow tetrakaidecahedra. To show the interior connections between alveoli, a clipped view is provided. Half of the micro-structures were covered with a water film ($\gamma = const.$), the other half was coated with a surfactant lining ($\gamma = \gamma(A)$).

4.4.2 Simple multi-scale model with alveolar micro-structure

Subsequently, the general applicability of the presented approach to lung parenchyma will be demonstrated. In Figure 4.4.2, the set-up of a simple example simulation is illustrated. On the macro-level, a lung tissue strip (5.0 mm×5.0 mm×10.0 mm) was discretized with 16 linear hexahedral elements. The bottom surface was fixed and the top surface was cyclically loaded by a uniformly distributed tension load (cf. equation (3.3.55) with $p_{\mathrm{max}} = 1.0$ kPa, $T = 0.2$ s) in the second part of the simulation. In four macro-scale elements, the developed multi-scale scheme was employed, whereas a classical Neo-Hookean constitutive law ($E_{\mathrm{M}} = 3.0$ kPa, $\nu_{\mathrm{M}} = 0.3$, $\rho_{\mathrm{M;0}} = 2.0\,\mathrm{kg/dm^3}$) was utilized otherwise.

On the micro-scale, an assemblage of nine hollow tetrakaidecahedra (edge length $L = 31.8\,\mu\mathrm{m}$, wall thickness $t = 10.0\,\mu\mathrm{m}$) representing pulmonary alveoli was discretized with 1340 linear hexahedral elements. Connections between alveoli were established based on the labyrinthine algorithm presented in section 3.1. For modeling the microscopic material behavior, a Neo-Hookean material model ($E_{\mathrm{m}} = 6.75$ kPa, $\nu_{\mathrm{m}} = 0.49$, $\rho_{\mathrm{m;0}} = 1.0\,\mathrm{kg/dm^3}$) was utilized in all alveolar samples. In order to introduce regional heterogeneities in the tissue strip, locally different liquid lining compositions were assumed. Half of the micro-structures were coated with a surfactant layer, whereas the other half was covered with a water film. This configuration modeled a domain with surfactant deficiency, a complication often occurring in case of acute lung diseases (see also section 1.2.1). The chosen micro-structure is not expected to be representative for lung parenchyma, i.e. the term RVE actually does not apply here. Furthermore, correct material parameters for alveolar wall tissue are not available at present. However, the resulting inaccuracy seems acceptable since the purpose of this simulation is not to provide quantitatively relevant results, but to illustrate the general suitability of the multi-scale approach for lung parenchyma.

As a start, the influence of the micro-structural heterogeneities on the overall parenchyma behavior was investigated. In the first phase of the simulation, equilibrium surface stresses were gradually applied on alveolar walls. The micro-structures deformed such that the surface energy tending to minimize interfacial area equilibrated the opposing structural energy. Alveolar distortion was more pronounced in ensembles covered with a water film because of the higher surface stresses. Due to the coupling of scales, application of the surface stresses on the micro-level directly induced a heterogeneous macro-scale deformation in the absence of any external loading. Thereby, the coarse-level elements employing the multi-scale approach deformed actively, whereas those elements using the empirical constitutive model were distorted passively. In the second part of the simulation, the uniformly distributed tension load described above was applied on the macro-structure. While surface tension remained constant in the micro-structures covered with a water film, surface stresses in the ensembles coated with a surfactant film varied dynamically according to the time-dependent constitutive model (cf. section 3.3.3). In Figure 4.4.3, selected deformation states of the macro-structure and two representative fine-scale discretizations (one per liquid lining configuration) are shown.

The main motivation for developing a multi-scale model of lung parenchyma is to formulate physiologically reasonable boundary conditions for alveolar simulations. Hence, the impact of the macro-level on the micro-level is also of particular interest here. In order to investigate this effect, a comparative single-scale simulation of the chosen micro-structure with traction-free boundary conditions was conducted. When applying a constant surface tension load on the interior surfaces, the alveolar structure was allowed to deform freely in this case, while it was constrained by the local macro-level deformation state in a multi-scale simulation. In Figure 4.4.4, considerable differences in the resulting alveolar distortions are depicted. Although imposed multi-scale boundary conditions were still simple, alveolar deformation was simulated more realistically than in the comparative simulation neglecting the influence of the surrounding tissue completely.

In summary, the example simulation attested that the devised multi-scale approach enables the mutual coupling of micro- and macro-scale. Furthermore, the algorithm's capability of dealing with coupled, dynamic problems on the fine-scale was demonstrated, thereby proving the general suitability for alveolar micro-structures.

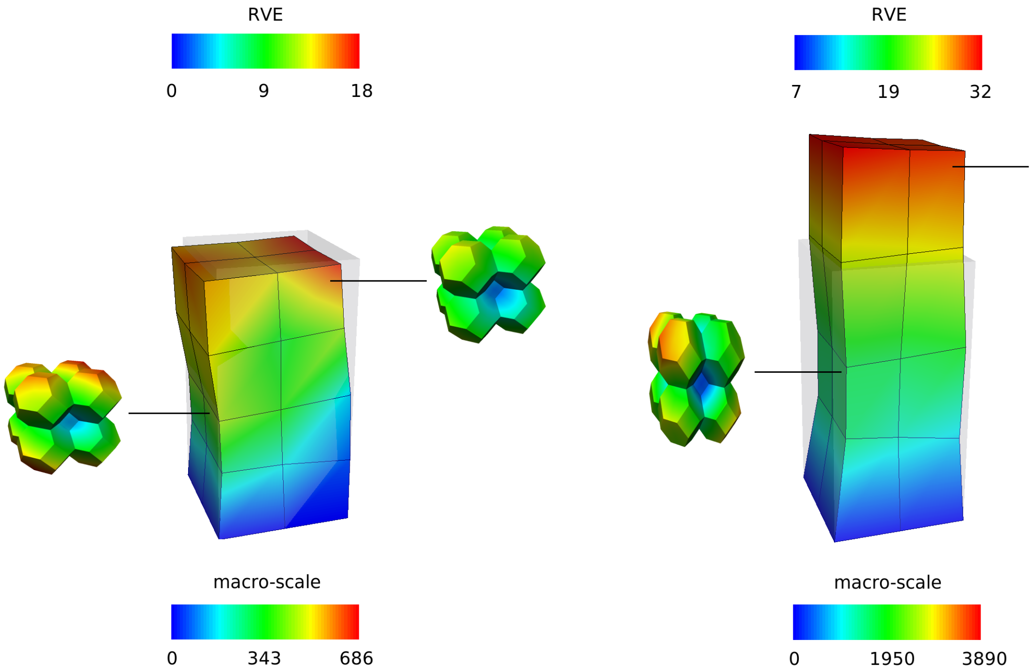

Figure 4.4.3: Deformation states of macro-scale and selected micro-structures (enlarged compared to the macro-scale). Colors indicate displacements in μm. Left: Application of equilibrium surface stresses on fine-scale without any other external loads. Right: Combination of (dynamic) surface stresses on micro-level and maximum external load on macro-level.

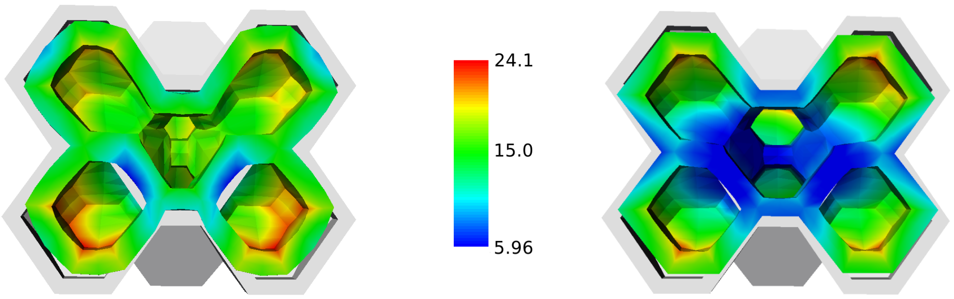

Figure 4.4.4: Deformation state under constant surface tension on the interior surfaces. Undeformed configurations are shown in gray and discretizations are clipped for reasons of visualization. Colors indicate displacements in μm. Left: comparative simulation with traction-free boundary conditions. Right: simulation considering effect of surrounding alveoli through multi-scale boundary conditions (taken from the simulation shown in Figure 4.4.3).

5 Coupling to Airway Model

As discussed in section 1.2, VALI is known to occur primarily in the respiratory zone of the lung. Therefore, novel approaches enabling the simulation of lung parenchyma as a whole while still resolving alveolar scales locally have been derived in the previous chapter. However, for a reasonable investigation of respiratory mechanics during mechanical ventilation, the conducting part of the lung also has to be included in the model. After all, local parenchyma deformations are determined by the distribution of airflow into the peripheral domains. Hence, the development of an overall lung model combining airway and parenchyma models is indispensable.

In the literature, several simplified approaches to characterizing respiratory mechanics at the system level have been reported. Corresponding overall lung models were predominantly based on electrical analogues, see e.g. Lutchen and Gillis (1997), Yuan et al. (1998), Massa et al. (2008), Ganzert et al. (2009), Kent et al. (2009), and the extensive reviews by Bates and Lutchen (2005) and Bates (2009). Main application of these approaches were, for example, the determination of global pressure-volume curves or the calculation of overall properties like the total lung resistance and compliance. However, since the contribution of the peripheral domains to the global lung resistance is small, alveolar structures may develop significant pathology before overall lung function is impaired noticeably. Therefore, although providing valuable general insights, these kinds of global lung models are not suitable for detailed investigations concerning the mechanisms of VALI.

The first step towards a more advanced overall lung model were made by Kowalczyk and Kleiber (1994), who treated parenchyma as a two-dimensional deformable porous medium coupled with a system of branching one-dimensional conduits distributing the air. To the author's knowledge, more elaborate models including both the conducting and the respiratory part of the lung are not yet available. Instead, detailed continuum models were always restricted to isolated domains of the respiratory system, such as individual alveoli (cf. chapter 3), lung parenchyma (cf. chapter 4), or parts of the airway tree.

In Grotberg (2001), Bertram and Gaver (2005), and Kleinstreuer and Zhang (2010), various aspects of flow and transport processes within the conducting zone have been reviewed. Main objectives of previous studies were the investigation of airflow distribution, airway stability, particle deposition, or optimal drug-aerosol targeting. For these purposes, extensive models of idealized airway geometries based on Weibel or Horsfield models (Weibel, 1963; Horsfield et al., 1971) were proposed (cf. e.g. Liu et al. (2002), Green (2004), and Zhang and Kleinstreuer (2004)). However, it was recognized that geometry-specific features have a major influence on local airflow distribution. Therefore, anatomically based airway models were utilized recently, for example in Baoshun and Lutchen (2006), Lin et al. (2007), Luo and Liu (2009), Ma and Lutchen (2009), and Comerford and Wall (2011).

The effects of FSI, though, received relatively little attention so far. Studies concerning closure and reopening of collapsible airways were restricted to idealized models of single airways, see e.g. Heil (1999), Grotberg and Jensen (2004), Hazel and Heil (2005), and Ghadiali and Gaver (2008). The first numerical simulations utilizing CT-based airway models including FSI effects were reported in Wall and Rabczuk (2008) and Küttler et al. (2010). It was demonstrated that airflow patterns, including both axial and secondary velocity profiles, are different when considering the interaction of airflow and wall movement.

Apart from enabling a better reproduction of the in vivo fluid mechanics, FSI simulations also allow for the determination of strains and stresses in the airway wall given that an appropriate constitutive model is chosen. Unfortunately, however, knowledge of wall properties is still quite sparse (Kamm, 1999). In the few published experiments, the behavior of airway tissue was shown to be different in axial and circumferential direction. Values of corresponding Young's moduli, though, varied widely. McKay et al. (2002) investigated the zero-stress state of intra- and extraparenchymal airways experimentally. They found that the level of residual stresses was very different among the studied species. While sheep and rabbit airways exhibited large opening angles when cut open, this was not the case for porcine and human lungs. Therefore, the widespread assumption of negligible residual stresses in computational models of human airways seems to be justified.

When introducing airway flexibility, also the influence of the surrounding lung parenchyma on airway motion and wall stresses needs to be considered. Adler et al. (1998) utilized a rat lung explant system to demonstrate the airway-parenchymal interdependence in bronchoconstriction. To account for this tethering effect in a simplified way, Xia et al. (2010) applied pleural pressure directly to the airway wall. A more realistic approach was proposed by Comerford and Wall (2011) who embedded the airway tree in a block of homogenized compressible tissue loaded by pleural pressure on the enclosing surfaces. Thereby, also the interdependence of neighboring airways not present in the isolated airway tree was taken into account.

An important, even though often disregarded issue for the set-up of computational airway models is the formulation of reasonable flow boundary conditions. Due to limited computational resources and the insufficient resolution of CT imaging techniques (minimum voxel size of 0.5 mm×0.5 mm×0.5 mm), a detailed modeling of all relevant airway structures from the trachea – where the endotracheal tube is situated during mechanical ventilation – down to the terminal bronchioles is not possible. Therefore, airway models are usually restricted to the first generations of the tracheo-bronchial tree. Many existing models simply neglect the influence of the unresolved peripheral structures by imposing zero-traction, i.e. "do-nothing", boundary conditions at the outlets. Consequently, simulated pressure levels in the resolved domain are far from being physiologically reasonable. A different type of boundary conditions was proposed recently by Yin et al. (2010). They prescribed airflow at the outlets according to information on regional ventilation obtained from CT datasets. However, airflow is completely prescribed in this model since the resulting problem is of pure Dirichlet type. Thus, it is unclear what kind of information should actually be provided by corresponding CFD simulations. More reasonable approaches were based on the inclusion of reduced-dimensional models for the non-imageable vessels. For instance, Maury et al. (2005) accounted for the effect of the peripheral airways by means of an equivalent resistance at the outlets. Baffico et al. (2010) complemented this approach by a spring model representing the motion of the thoracic cage. Comerford et al. (2010) proposed to consider the impedance rather than the resistance of the unresolved airways to enable a reasonable investigation of frequency-dependent phenomena.

The formulation of appropriate boundary conditions is particularly difficult if expiratory flow is to be modeled. When prescribing zero-traction boundary conditions on the outlets and Dirichlet conditions on the inlet of the simulation domain, a reversal of the flow direction at the inlet potentially leads to an unstable solution (cf. e.g. Kim et al. (2009)). Therefore, Freitas and Schröder (2008) simply reversed the boundary conditions for the trachea and the single outlets. However, no information about the “inflow” at the outlets during expiration is actually available. More precisely, neither the specific total amount of air flowing into each outlet nor the corresponding variation in time is known. Although many authors claim to simulate expiratory flow in the tracheo-bronchial region, from the author’s point of view, no convincing concepts for prescribing physiologically sensible boundary conditions have been proposed so far.

Above mentioned difficulties come about due to an oversimplified consideration of the unresolved peripheral domain. Thus, if detailed models of the conducting and the respiratory zone were linked, two problems would be solved at once. As already mentioned, local parenchyma deformations could be determined depending on the distribution of air into the peripheral regions. At the same time, airflow in the resolved conducting passages could be simulated more realistically.

In this chapter, a novel approach to combining airway and parenchyma models into one overall continuum lung model will be presented. To compensate for the gap between resolvable airways and the acinar region, general concepts for the homogenization of unresolvable structures will be derived. Based on these preliminary considerations, a coupling of air and parenchyma volumes will be proposed. After setting up the linearized system of equations, corresponding numerical solution procedures will be addressed specifically. The chapter will be completed by first numerical examples illustrating the versatility of the developed volume-coupling approach.

5.1 Preliminary considerations

Since only parts of both the airway tree and the alveolar structures can be resolved, the transport of air down to the respiratory zone cannot be simulated explicitly but has to be modeled. Before the actual coupling approach will be presented in section 5.2, the underlying concepts based on the homogenization of unresolvable structures will be discussed subsequently.

In Figure 5.1.1(a), a CT-based representation of lung parenchyma and the embedded tracheo-bronchial tree is shown. In the last imageable generation, airways end in artificial outlets. In reality, however, branching of the conducting passages continues until the alveolar region is reached. For subsequent considerations, the parenchyma model is conceptually subdivided into different regions. Thereby, each region is assumed to be supplied

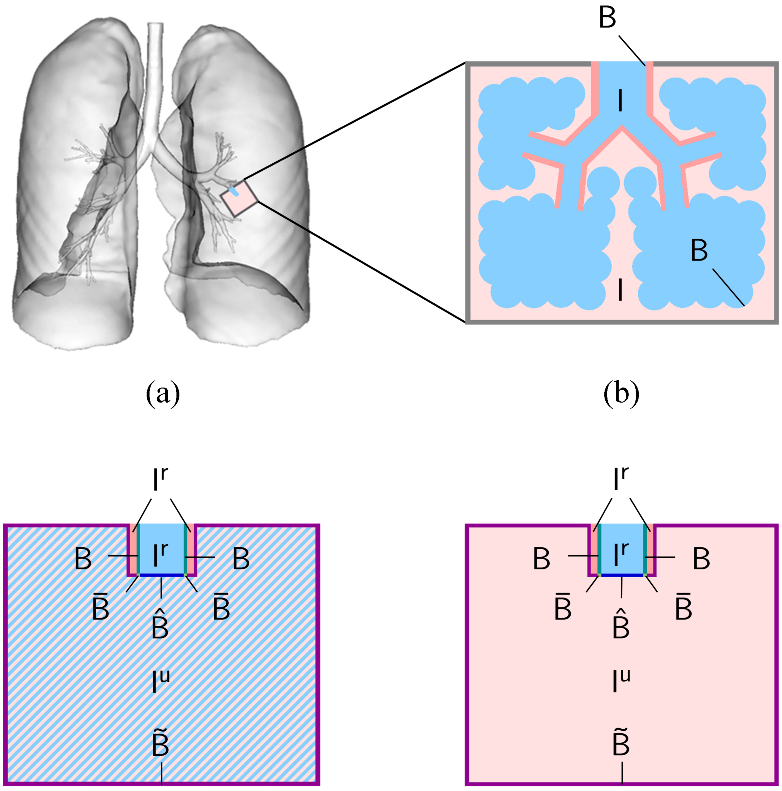

(a) (b)

(c) (d)

Figure 5.1.1: Different modeling approaches for peripheral regions of the lung. (a) CT data illustrating resolved lung lobes and tracheo-bronchial region. The peripheral region considered in the following is marked. (b) Model of peripheral region resolving all airways and individual alveoli. (c) Mixture model with overlapping homogenized fluid and structure domains (indicated by hatching) coupled along the boundary $\tilde{\mathrm{B}} \cup \bar{\mathrm{B}}$. (d) Homogenized solid model.

with air by exactly one terminal branch of the resolvable airway tree. In the following, one of these peripheral domains will be considered exemplarily (see marked region in Figure 5.1.1(a)). First, it will be assumed that all conducting passages and alveoli subsequent to the feeding airway can be resolved (cf. Figure 5.1.1(b) and section 5.1.1). In a next step, the explicit modeling of the peripheral structures will be spared and a homogenized mixture model will be established (cf. Figure 5.1.1(c) and section 5.1.2). Finally, the mixture model will be reformulated such that peripheral airflow is considered only in an implicit way. The resulting purely solid model for the peripheral domain (cf. Figure 5.1.1(d) and section 5.1.3) will be utilized as a basis for a novel approach to coupling continuum models of the airways and lung parenchyma in section 5.2. In the following, the different pre-stages summarized above will be presented in more detail.

5.1.1 Fully resolved model

In reality, the peripheral structures subsequent to the end of the airway tree shown in Figure 5.1.1(a) cannot be modeled explicitly. As a start, however, it is assumed that all conducting passages and alveoli in the region of interest are resolvable. This conceptual model will serve as a starting point for the development of the homogenized models proposed in the following sections.

In Figure 5.1.1(b), a schematic of the fully resolved model is shown. When simulating airflow down to the terminal alveolar sacs, fluid and structure interact at both airway and alveolar walls, which are collectively termed the FSI interface B subsequently. Following the derivations presented in section 2.4, the linear monolithic FSI problem is given by

$$\begin{bmatrix} \mathbf{K}_{\mathsf{II}}^{\mathsf{SS}} & \mathbf{K}_{\mathsf{IB}}^{\mathsf{SS}} & \mathbf{0} & \mathbf{0} \\ \mathbf{K}_{\mathsf{BI}}^{\mathsf{SS}} & \mathbf{K}_{\mathsf{BB}}^{\mathsf{SS}} + \underset{\sim}{\underline{\mathbf{K}}}{}_{\mathsf{BB}}^{\mathsf{FF}} + \underline{\mathbf{K}}_{\mathsf{BB}}^{\mathsf{FA}} & \underline{\mathbf{K}}_{\mathsf{BI}}^{\mathsf{FF}} & \underline{\mathbf{K}}_{\mathsf{BI}}^{\mathsf{FA}} \\ \mathbf{0} & \underset{\sim}{\mathbf{K}}{}_{\mathsf{IB}}^{\mathsf{FF}} + \mathbf{K}_{\mathsf{IB}}^{\mathsf{FA}} & \mathbf{K}_{\mathsf{II}}^{\mathsf{FF}} & \mathbf{K}_{\mathsf{II}}^{\mathsf{FA}} \\ \mathbf{0} & \mathbf{K}_{\mathsf{IB}}^{\mathsf{AS}} & \mathbf{0} & \mathbf{K}_{\mathsf{II}}^{\mathsf{AA}} \end{bmatrix} \begin{bmatrix} \Delta \mathbf{d}_{\mathsf{I}} \\ \Delta \mathbf{d}_{\mathsf{B}} \\ \Delta \mathbf{u}_{\mathsf{I}} \\ \Delta \mathbf{d}_{\mathsf{I}}^{\mathsf{A}} \end{bmatrix} = - \begin{bmatrix} \mathbf{r}_{\mathsf{I}}^{\mathsf{S}} \\ \mathbf{r}_{\mathsf{B}}^{\mathsf{S}} + \underline{\mathbf{r}}_{\mathsf{B}}^{\mathsf{F}} \\ \mathbf{r}_{\mathsf{I}}^{\mathsf{F}} \\ \mathbf{r}_{\mathsf{I}}^{\mathsf{A}} \end{bmatrix} \tag{5.1.1}$$

with underlines and tildes denoting different scalings of the vectors or matrices (cf. equation (2.4.8) for a definition of corresponding abbreviations). For simplicity, information about the current time and nonlinear iteration step as well as dimensions of the zero matrices – which are obvious from the context – is left out here and in the following.

5.1.2 Homogenized mixture model

As a next step, the conducting passages and alveolar sacs peripheral to the last imageable airway are no longer resolved. Instead, tissue and air are "smeared" over the peripheral domain by means of homogenization. Given that the terminal structures are small compared to the overall domain under consideration, it can be assumed that fluid and solid phases in this region are superimposed in time and space. Each macroscopic point in the peripheral domain is, thus, occupied simultaneously by fluid and solid "particles" following their individual motion. In line with the well-known theory of mixtures (Atkin and Craine, 1976), this approach is referred to as the "mixture model" albeit the kinematic assumption is the only congruence. The peripheral region can then be thought of as a balloon inflated by the air transported in the feeding vessel. While the superimposed fluid and solid phases are supposed to be independent of each other in the interior of the homogenized domain, both fields interact along the enclosing boundary. Consequently, airflow into this region directly induces deformation of the homogenized parenchymal structure.

In Figure 5.1.1(c), the outlined scenario is shown schematically. Lumen and wall of the resolved feeding airway (both referred to as I^{r}) are explicitly modeled. At the FSI boundary B, airflow and wall deformation are coupled as usual. The transition section between the resolved airway and the homogenized domain I^{u} is denoted by $\hat{\mathsf{B}}$. It can be thought of as the outflow surface of the feeding vessel into the peripheral region. In the fully resolved model, only conducting passages would meet at this purely artificial boundary. As a consequence of the homogenization process, smeared tissue structures adjoin $\hat{\mathsf{B}}$ in the mixture model. To approximate the physics of the fully resolved model adequately, the overlapping fields have to be completely independent of each other at $\hat{\mathsf{B}}$. Hence, the air transported in the resolved airway enters the homogenized domain without affecting the deformation of the superimposed structure in this section. Along the enclosing boundary of the homogenized domain $\bar{\mathsf{B}} \cup \tilde{\mathsf{B}}$, however, the interaction of overlapping fluid and solid fields has to be considered.

Based on these modeling assumptions, the monolithic FSI problem for the mixture model can be formulated. Since the ALE field is not directly involved in above considerations, corresponding contributions are omitted for the sake of comprehensibility. The resulting linearized system of equations then reads

$$\mathbf{K}^{\mathsf{mix}} \Delta \mathbf{u}^{\mathsf{mix}} = -\mathbf{r}^{\mathsf{mix}} \tag{5.1.2}$$

with

$$\mathbf{K}^{\mathsf{mix}} = \begin{bmatrix}
\mathbf{K}^{\mathsf{SS}}_{\mathsf{I^rI^r}} & \mathbf{K}^{\mathsf{SS}}_{\mathsf{I^rB}} & \mathbf{K}^{\mathsf{SS}}_{\mathsf{I^r}\bar{\mathsf{B}}} & \mathbf{0} & \mathbf{0} & \mathbf{K}^{\mathsf{SS}}_{\mathsf{I^r}\tilde{\mathsf{B}}} & \mathbf{0} & \mathbf{0} & \mathbf{0} \\
\mathbf{K}^{\mathsf{SS}}_{\mathsf{BI^r}} & \mathbf{K}^{\mathsf{SS/FF}}_{\mathsf{BB}} & \mathbf{K}^{\mathsf{SS/FF}}_{\mathsf{B}\bar{\mathsf{B}}} & \mathbf{0} & \mathbf{0} & \mathbf{0} & \underline{\mathbf{K}}^{\mathsf{FF}}_{\mathsf{BI^r}} & \mathbf{0} & \mathbf{0} \\
\mathbf{K}^{\mathsf{SS}}_{\bar{\mathsf{B}}\mathsf{I^r}} & \mathbf{K}^{\mathsf{SS/FF}}_{\bar{\mathsf{B}}\mathsf{B}} & \mathbf{K}^{\mathsf{SS/FF}}_{\bar{\mathsf{B}}\bar{\mathsf{B}}} & \mathbf{K}^{\mathsf{SS}}_{\bar{\mathsf{B}}\hat{\mathsf{B}}} & \mathbf{K}^{\mathsf{SS}}_{\bar{\mathsf{B}}\mathsf{I^u}} & \mathbf{K}^{\mathsf{SS/FF}}_{\bar{\mathsf{B}}\tilde{\mathsf{B}}} & \underline{\mathbf{K}}^{\mathsf{FF}}_{\bar{\mathsf{B}}\mathsf{I^r}} & \underline{\mathbf{K}}^{\mathsf{FF}}_{\bar{\mathsf{B}}\hat{\mathsf{B}}} & \underline{\mathbf{K}}^{\mathsf{FF}}_{\bar{\mathsf{B}}\mathsf{I^u}} \\
\mathbf{0} & \mathbf{0} & \mathbf{K}^{\mathsf{SS}}_{\hat{\mathsf{B}}\bar{\mathsf{B}}} & \mathbf{K}^{\mathsf{SS}}_{\hat{\mathsf{B}}\hat{\mathsf{B}}} & \mathbf{K}^{\mathsf{SS}}_{\hat{\mathsf{B}}\mathsf{I^u}} & \mathbf{0} & \mathbf{0} & \mathbf{0} & \mathbf{0} \\
\mathbf{0} & \mathbf{0} & \mathbf{K}^{\mathsf{SS}}_{\mathsf{I^u}\bar{\mathsf{B}}} & \mathbf{K}^{\mathsf{SS}}_{\mathsf{I^u}\hat{\mathsf{B}}} & \mathbf{K}^{\mathsf{SS}}_{\mathsf{I^uI^u}} & \mathbf{K}^{\mathsf{SS}}_{\mathsf{I^u}\tilde{\mathsf{B}}} & \mathbf{0} & \mathbf{0} & \mathbf{0} \\
\mathbf{K}^{\mathsf{SS}}_{\tilde{\mathsf{B}}\mathsf{I^r}} & \mathbf{0} & \mathbf{K}^{\mathsf{SS/FF}}_{\tilde{\mathsf{B}}\bar{\mathsf{B}}} & \mathbf{0} & \mathbf{K}^{\mathsf{SS}}_{\tilde{\mathsf{B}}\mathsf{I^u}} & \mathbf{K}^{\mathsf{SS/FF}}_{\tilde{\mathsf{B}}\tilde{\mathsf{B}}} & \mathbf{0} & \mathbf{0} & \underline{\mathbf{K}}^{\mathsf{FF}}_{\tilde{\mathsf{B}}\mathsf{I^u}} \\
\mathbf{0} & \utilde{\mathbf{K}}^{\mathsf{FF}}_{\mathsf{I^rB}} & \utilde{\mathbf{K}}^{\mathsf{FF}}_{\mathsf{I^r}\bar{\mathsf{B}}} & \mathbf{0} & \mathbf{0} & \mathbf{0} & \mathbf{K}^{\mathsf{FF}}_{\mathsf{I^rI^r}} & \mathbf{K}^{\mathsf{FF}}_{\mathsf{I^r}\hat{\mathsf{B}}} & \mathbf{0} \\
\mathbf{0} & \mathbf{0} & \utilde{\mathbf{K}}^{\mathsf{FF}}_{\hat{\mathsf{B}}\bar{\mathsf{B}}} & \mathbf{0} & \mathbf{0} & \mathbf{0} & \mathbf{K}^{\mathsf{FF}}_{\hat{\mathsf{B}}\mathsf{I^r}} & \mathbf{K}^{\mathsf{FF}}_{\hat{\mathsf{B}}\hat{\mathsf{B}}} & \mathbf{K}^{\mathsf{FF}}_{\hat{\mathsf{B}}\mathsf{I^u}} \\
\mathbf{0} & \mathbf{0} & \utilde{\mathbf{K}}^{\mathsf{FF}}_{\mathsf{I^u}\bar{\mathsf{B}}} & \mathbf{0} & \mathbf{0} & \utilde{\mathbf{K}}^{\mathsf{FF}}_{\mathsf{I^u}\tilde{\mathsf{B}}} & \mathbf{0} & \mathbf{K}^{\mathsf{FF}}_{\mathsf{I^u}\hat{\mathsf{B}}} & \mathbf{K}^{\mathsf{FF}}_{\mathsf{I^uI^u}}
\end{bmatrix} \tag{5.1.3}$$

and

$$\Delta \mathbf{u}^{\mathsf{mix}} = \begin{bmatrix} \Delta \mathbf{d}_{\mathsf{I^r}} \\ \Delta \mathbf{d}_{\mathsf{B}} \\ \Delta \mathbf{d}_{\bar{\mathsf{B}}} \\ \Delta \mathbf{d}_{\hat{\mathsf{B}}} \\ \Delta \mathbf{d}_{\mathsf{I^u}} \\ \Delta \mathbf{d}_{\tilde{\mathsf{B}}} \\ \Delta \mathbf{u}_{\mathsf{I^r}} \\ \Delta \mathbf{u}_{\hat{\mathsf{B}}} \\ \Delta \mathbf{u}_{\mathsf{I^u}} \end{bmatrix}, \qquad \mathbf{r}^{\mathsf{mix}} = \begin{bmatrix} \mathbf{r}^{\mathsf{S}}_{\mathsf{I^r}} \\ \mathbf{r}^{\mathsf{S}}_{\mathsf{B}} + \underline{\mathbf{r}}^{\mathsf{F}}_{\mathsf{B}} \\ \mathbf{r}^{\mathsf{S}}_{\bar{\mathsf{B}}} + \underline{\mathbf{r}}^{\mathsf{F}}_{\bar{\mathsf{B}}} \\ \mathbf{r}^{\mathsf{S}}_{\hat{\mathsf{B}}} \\ \mathbf{r}^{\mathsf{S}}_{\mathsf{I^u}} \\ \mathbf{r}^{\mathsf{S}}_{\tilde{\mathsf{B}}} + \underline{\mathbf{r}}^{\mathsf{F}}_{\tilde{\mathsf{B}}} \\ \mathbf{r}^{\mathsf{F}}_{\mathsf{I^r}} \\ \mathbf{r}^{\mathsf{F}}_{\hat{\mathsf{B}}} \\ \mathbf{r}^{\mathsf{F}}_{\mathsf{I^u}} \end{bmatrix}. \tag{5.1.4}$$

The entries in the stiffness matrix (5.1.3) connecting different domains and boundaries of the individual fields simply evolve as a consequence of spatial vicinities. $\mathbf{K}^{\mathsf{SS}}_{\tilde{\mathsf{B}}\mathsf{I}^{\mathsf{r}}}$ and $\mathbf{K}^{\mathsf{SS}}_{\mathsf{I}^{\mathsf{r}}\tilde{\mathsf{B}}}$, for example, result from the adjacency of the FSI boundary of the homogenized region and the resolved airway wall. For the FSI contributions in (5.1.3), suitable abbreviations are introduced, e.g.

$$\mathbf{K}^{\mathsf{SS/FF}}_{\mathsf{BB}} = \mathbf{K}^{\mathsf{SS}}_{\mathsf{BB}} + \underset{\eqsim}{\mathbf{K}}{}^{\mathsf{FF}}_{\mathsf{BB}}. \tag{5.1.5}$$

5.1.3 Condensed homogenized model

For the investigation of VALI, the determination of local parenchyma deformations is essential. By contrast, airflow in the peripheral region is only of minor interest. Therefore, in the following, corresponding fluid DOFs $\mathbf{u}_{\mathsf{I}^{\mathsf{u}}}$ are eliminated from the system of equations by means of static condensation. Starting point is the linearized FSI problem of the mixture model (cf. equations (5.1.2)-(5.1.4)). As a first step, all entries associated with $\mathbf{u}_{\mathsf{I}^{\mathsf{u}}}$ are highlighted in color, i.e.

$$\mathbf{K}^{\mathsf{mix}}\Delta\mathbf{u}^{\mathsf{mix}} = -\mathbf{r}^{\mathsf{mix}} \tag{5.1.6}$$

with

$$\mathbf{K}^{\mathsf{mix}} = \begin{bmatrix}
\mathbf{K}^{\mathsf{SS}}_{\mathsf{I}^{\mathsf{r}}\mathsf{I}^{\mathsf{r}}} & \mathbf{K}^{\mathsf{SS}}_{\mathsf{I}^{\mathsf{r}}\mathsf{B}} & \mathbf{K}^{\mathsf{SS}}_{\mathsf{I}^{\mathsf{r}}\bar{\mathsf{B}}} & \mathbf{0} & \mathbf{0} & \mathbf{K}^{\mathsf{SS}}_{\mathsf{I}^{\mathsf{r}}\tilde{\mathsf{B}}} & \mathbf{0} & \mathbf{0} & \mathbf{0} \\
\mathbf{K}^{\mathsf{SS}}_{\mathsf{B}\mathsf{I}^{\mathsf{r}}} & \mathbf{K}^{\mathsf{SS/FF}}_{\mathsf{BB}} & \mathbf{K}^{\mathsf{SS/FF}}_{\mathsf{B}\bar{\mathsf{B}}} & \mathbf{0} & \mathbf{0} & \mathbf{0} & \underline{\mathbf{K}}^{\mathsf{FF}}_{\mathsf{B}\mathsf{I}^{\mathsf{r}}} & \mathbf{0} & \mathbf{0} \\
\mathbf{K}^{\mathsf{SS}}_{\bar{\mathsf{B}}\mathsf{I}^{\mathsf{r}}} & \mathbf{K}^{\mathsf{SS/FF}}_{\bar{\mathsf{B}}\mathsf{B}} & \mathbf{K}^{\mathsf{SS/FF}}_{\bar{\mathsf{B}}\bar{\mathsf{B}}} & \mathbf{K}^{\mathsf{SS}}_{\bar{\mathsf{B}}\hat{\mathsf{B}}} & \mathbf{K}^{\mathsf{SS}}_{\bar{\mathsf{B}}\mathsf{I}^{\mathsf{u}}} & \mathbf{K}^{\mathsf{SS/FF}}_{\bar{\mathsf{B}}\tilde{\mathsf{B}}} & \underline{\mathbf{K}}^{\mathsf{FF}}_{\bar{\mathsf{B}}\mathsf{I}^{\mathsf{r}}} & \underline{\mathbf{K}}^{\mathsf{FF}}_{\bar{\mathsf{B}}\hat{\mathsf{B}}} & \underline{\mathbf{K}}^{\mathsf{FF}}_{\bar{\mathsf{B}}\mathsf{I}^{\mathsf{u}}} \\
\mathbf{0} & \mathbf{0} & \mathbf{K}^{\mathsf{SS}}_{\hat{\mathsf{B}}\bar{\mathsf{B}}} & \mathbf{K}^{\mathsf{SS}}_{\hat{\mathsf{B}}\hat{\mathsf{B}}} & \mathbf{K}^{\mathsf{SS}}_{\hat{\mathsf{B}}\mathsf{I}^{\mathsf{u}}} & \mathbf{0} & \mathbf{0} & \mathbf{0} & \mathbf{0} \\
\mathbf{0} & \mathbf{0} & \mathbf{K}^{\mathsf{SS}}_{\mathsf{I}^{\mathsf{u}}\bar{\mathsf{B}}} & \mathbf{K}^{\mathsf{SS}}_{\mathsf{I}^{\mathsf{u}}\hat{\mathsf{B}}} & \mathbf{K}^{\mathsf{SS}}_{\mathsf{I}^{\mathsf{u}}\mathsf{I}^{\mathsf{u}}} & \mathbf{K}^{\mathsf{SS}}_{\mathsf{I}^{\mathsf{u}}\tilde{\mathsf{B}}} & \mathbf{0} & \mathbf{0} & \mathbf{0} \\
\mathbf{K}^{\mathsf{SS}}_{\tilde{\mathsf{B}}\mathsf{I}^{\mathsf{r}}} & \mathbf{0} & \mathbf{K}^{\mathsf{SS/FF}}_{\tilde{\mathsf{B}}\bar{\mathsf{B}}} & \mathbf{0} & \mathbf{K}^{\mathsf{SS}}_{\tilde{\mathsf{B}}\mathsf{I}^{\mathsf{u}}} & \mathbf{K}^{\mathsf{SS/FF}}_{\tilde{\mathsf{B}}\tilde{\mathsf{B}}} & \mathbf{0} & \mathbf{0} & \underline{\mathbf{K}}^{\mathsf{FF}}_{\tilde{\mathsf{B}}\mathsf{I}^{\mathsf{u}}} \\
\mathbf{0} & \underset{\sim}{\mathbf{K}}{}^{\mathsf{FF}}_{\mathsf{I}^{\mathsf{r}}\mathsf{B}} & \underset{\sim}{\mathbf{K}}{}^{\mathsf{FF}}_{\mathsf{I}^{\mathsf{r}}\bar{\mathsf{B}}} & \mathbf{0} & \mathbf{0} & \mathbf{0} & \mathbf{K}^{\mathsf{FF}}_{\mathsf{I}^{\mathsf{r}}\mathsf{I}^{\mathsf{r}}} & \mathbf{K}^{\mathsf{FF}}_{\mathsf{I}^{\mathsf{r}}\hat{\mathsf{B}}} & \mathbf{0} \\
\mathbf{0} & \mathbf{0} & \underset{\sim}{\mathbf{K}}{}^{\mathsf{FF}}_{\hat{\mathsf{B}}\bar{\mathsf{B}}} & \mathbf{0} & \mathbf{0} & \mathbf{0} & \mathbf{K}^{\mathsf{FF}}_{\hat{\mathsf{B}}\mathsf{I}^{\mathsf{r}}} & \mathbf{K}^{\mathsf{FF}}_{\hat{\mathsf{B}}\hat{\mathsf{B}}} & \mathbf{K}^{\mathsf{FF}}_{\hat{\mathsf{B}}\mathsf{I}^{\mathsf{u}}} \\
\mathbf{0} & \mathbf{0} & \underset{\sim}{\mathbf{K}}{}^{\mathsf{FF}}_{\mathsf{I}^{\mathsf{u}}\bar{\mathsf{B}}} & \mathbf{0} & \mathbf{0} & \underset{\sim}{\mathbf{K}}{}^{\mathsf{FF}}_{\mathsf{I}^{\mathsf{u}}\tilde{\mathsf{B}}} & \mathbf{0} & \mathbf{K}^{\mathsf{FF}}_{\mathsf{I}^{\mathsf{u}}\hat{\mathsf{B}}} & \mathbf{K}^{\mathsf{FF}}_{\mathsf{I}^{\mathsf{u}}\mathsf{I}^{\mathsf{u}}}
\end{bmatrix} \tag{5.1.7}$$

and

$$\Delta\mathbf{u}^{\mathsf{mix}} = \begin{bmatrix} \Delta\mathbf{d}_{\mathsf{I}^{\mathsf{r}}} \\ \Delta\mathbf{d}_{\mathsf{B}} \\ \Delta\mathbf{d}_{\bar{\mathsf{B}}} \\ \Delta\mathbf{d}_{\hat{\mathsf{B}}} \\ \Delta\mathbf{d}_{\mathsf{I}^{\mathsf{u}}} \\ \Delta\mathbf{d}_{\tilde{\mathsf{B}}} \\ \Delta\mathbf{u}_{\mathsf{I}^{\mathsf{r}}} \\ \Delta\mathbf{u}_{\hat{\mathsf{B}}} \\ \Delta\mathbf{u}_{\mathsf{I}^{\mathsf{u}}} \end{bmatrix}, \qquad \mathbf{r}^{\mathsf{mix}} = \begin{bmatrix} \mathbf{r}^{\mathsf{S}}_{\mathsf{I}^{\mathsf{r}}} \\ \mathbf{r}^{\mathsf{S}}_{\mathsf{B}} + \underline{\mathbf{r}}^{\mathsf{F}}_{\mathsf{B}} \\ \mathbf{r}^{\mathsf{S}}_{\bar{\mathsf{B}}} + \underline{\mathbf{r}}^{\mathsf{F}}_{\bar{\mathsf{B}}} \\ \mathbf{r}^{\mathsf{S}}_{\hat{\mathsf{B}}} \\ \mathbf{r}^{\mathsf{S}}_{\mathsf{I}^{\mathsf{u}}} \\ \mathbf{r}^{\mathsf{S}}_{\tilde{\mathsf{B}}} + \underline{\mathbf{r}}^{\mathsf{F}}_{\tilde{\mathsf{B}}} \\ \mathbf{r}^{\mathsf{F}}_{\mathsf{I}^{\mathsf{r}}} \\ \mathbf{r}^{\mathsf{F}}_{\hat{\mathsf{B}}} \\ \mathbf{r}^{\mathsf{F}}_{\mathsf{I}^{\mathsf{u}}} \end{bmatrix}. \tag{5.1.8}$$

From the last equation of the system, the increment of the peripheral airflow velocities is determined by

$$\Delta\mathbf{u}_{\mathsf{I}^\mathsf{u}} = \left(\mathbf{K}^{\mathsf{FF}}_{\mathsf{I}^\mathsf{u}\mathsf{I}^\mathsf{u}}\right)^{-1}\left[\mathbf{r}^{\mathsf{F}}_{\mathsf{I}^\mathsf{u}} - \underset{\sim}{\underline{\mathbf{K}}}^{\mathsf{FF}}_{\mathsf{I}^\mathsf{u}\bar{\mathsf{B}}}\Delta\mathbf{d}_{\bar{\mathsf{B}}} - \underset{\sim}{\underline{\mathbf{K}}}^{\mathsf{FF}}_{\mathsf{I}^\mathsf{u}\tilde{\mathsf{B}}}\Delta\mathbf{d}_{\tilde{\mathsf{B}}} - \mathbf{K}^{\mathsf{FF}}_{\mathsf{I}^\mathsf{u}\hat{\mathsf{B}}}\Delta\mathbf{u}_{\hat{\mathsf{B}}}\right]. \tag{5.1.9}$$

Introduction of equation (5.1.9) into the linear system (5.1.6) yields the following condensed monolithic problem

$$\mathbf{K}^{\mathsf{cond}}\Delta\mathbf{u}^{\mathsf{cond}} = -\mathbf{r}^{\mathsf{cond}} \tag{5.1.10}$$

with

$$\mathbf{K}^{\mathsf{cond}} = \begin{bmatrix}
\mathbf{K}^{\mathsf{SS}}_{\mathsf{I}^\mathsf{r}\mathsf{I}^\mathsf{r}} & \mathbf{K}^{\mathsf{SS}}_{\mathsf{I}^\mathsf{r}\mathsf{B}} & \mathbf{K}^{\mathsf{SS}}_{\mathsf{I}^\mathsf{r}\bar{\mathsf{B}}} & \mathbf{0} & \mathbf{0} & \mathbf{K}^{\mathsf{SS}}_{\mathsf{I}^\mathsf{r}\tilde{\mathsf{B}}} & \mathbf{0} & \mathbf{0} \\
\mathbf{K}^{\mathsf{SS}}_{\mathsf{B}\mathsf{I}^\mathsf{r}} & \mathbf{K}^{\mathsf{SS/FF}}_{\mathsf{B}\mathsf{B}} & \mathbf{K}^{\mathsf{SS/FF}}_{\mathsf{B}\bar{\mathsf{B}}} & \mathbf{0} & \mathbf{0} & \mathbf{0} & \underline{\mathbf{K}}^{\mathsf{FF}}_{\mathsf{B}\mathsf{I}^\mathsf{r}} & \mathbf{0} \\
\mathbf{K}^{\mathsf{SS}}_{\bar{\mathsf{B}}\mathsf{I}^\mathsf{r}} & \mathbf{K}^{\mathsf{SS}}_{\bar{\mathsf{B}}\mathsf{B}} & \check{\mathbf{K}}^{\mathsf{SS/FF}}_{\bar{\mathsf{B}}\bar{\mathsf{B}}} & \mathbf{K}^{\mathsf{SS}}_{\bar{\mathsf{B}}\hat{\mathsf{B}}} & \mathbf{K}^{\mathsf{SS}}_{\bar{\mathsf{B}}\mathsf{I}^\mathsf{u}} & \check{\mathbf{K}}^{\mathsf{SS/FF}}_{\bar{\mathsf{B}}\tilde{\mathsf{B}}} & \mathbf{K}^{\mathsf{FF}}_{\bar{\mathsf{B}}\mathsf{I}^\mathsf{r}} & \check{\mathbf{K}}^{\mathsf{FF}}_{\bar{\mathsf{B}}\hat{\mathsf{B}}} \\
\mathbf{0} & \mathbf{0} & \mathbf{K}^{\mathsf{SS}}_{\hat{\mathsf{B}}\bar{\mathsf{B}}^\mathsf{r}} & \mathbf{K}^{\mathsf{SS}}_{\hat{\mathsf{B}}\hat{\mathsf{B}}} & \mathbf{K}^{\mathsf{SS}}_{\hat{\mathsf{B}}\mathsf{I}^\mathsf{u}} & \mathbf{0} & \mathbf{0} & \mathbf{0} \\
\mathbf{0} & \mathbf{0} & \mathbf{K}^{\mathsf{SS}}_{\mathsf{I}^\mathsf{u}\bar{\mathsf{B}}} & \mathbf{K}^{\mathsf{SS}}_{\mathsf{I}^\mathsf{u}\hat{\mathsf{B}}} & \mathbf{K}^{\mathsf{SS}}_{\mathsf{I}^\mathsf{u}\mathsf{I}^\mathsf{u}} & \mathbf{K}^{\mathsf{SS}}_{\mathsf{I}^\mathsf{u}\tilde{\mathsf{B}}} & \mathbf{0} & \mathbf{0} \\
\mathbf{K}^{\mathsf{SS}}_{\tilde{\mathsf{B}}\mathsf{I}^\mathsf{r}} & \mathbf{0} & \check{\mathbf{K}}^{\mathsf{SS/FF}}_{\tilde{\mathsf{B}}\bar{\mathsf{B}}} & \mathbf{0} & \mathbf{K}^{\mathsf{SS}}_{\tilde{\mathsf{B}}\mathsf{I}^\mathsf{u}} & \check{\mathbf{K}}^{\mathsf{SS/FF}}_{\tilde{\mathsf{B}}\tilde{\mathsf{B}}} & \mathbf{0} & \check{\mathbf{K}}^{\mathsf{SF}}_{\tilde{\mathsf{B}}\hat{\mathsf{B}}} \\
\mathbf{0} & \underset{\sim}{\underline{\mathbf{K}}}^{\mathsf{FF}}_{\mathsf{I}^\mathsf{r}\mathsf{B}} & \underset{\sim}{\underline{\mathbf{K}}}^{\mathsf{FF}}_{\mathsf{I}^\mathsf{r}\bar{\mathsf{B}}} & \mathbf{0} & \mathbf{0} & \mathbf{0} & \mathbf{K}^{\mathsf{FF}}_{\mathsf{I}^\mathsf{r}\mathsf{I}^\mathsf{r}} & \mathbf{K}^{\mathsf{FF}}_{\mathsf{I}^\mathsf{r}\hat{\mathsf{B}}} \\
\mathbf{0} & \mathbf{0} & \underset{\sim}{\underline{\check{\mathbf{K}}}}^{\mathsf{FF}}_{\hat{\mathsf{B}}\bar{\mathsf{B}}} & \mathbf{0} & \mathbf{0} & \underset{\sim}{\underline{\check{\mathbf{K}}}}^{\mathsf{FF}}_{\hat{\mathsf{B}}\tilde{\mathsf{B}}} & \mathbf{0} & \check{\mathbf{K}}^{\mathsf{FF}}_{\hat{\mathsf{B}}\hat{\mathsf{B}}}
\end{bmatrix} \tag{5.1.11}$$

and

$$\Delta\mathbf{u}^{\mathsf{cond}} = \begin{bmatrix}
\Delta\mathbf{d}_{\mathsf{I}^\mathsf{r}} \\
\Delta\mathbf{d}_{\mathsf{B}} \\
\Delta\mathbf{d}_{\bar{\mathsf{B}}} \\
\Delta\mathbf{d}_{\hat{\mathsf{B}}} \\
\Delta\mathbf{d}_{\mathsf{I}^\mathsf{u}} \\
\Delta\mathbf{d}_{\tilde{\mathsf{B}}} \\
\Delta\mathbf{u}_{\mathsf{I}^\mathsf{r}} \\
\Delta\mathbf{u}_{\hat{\mathsf{B}}}
\end{bmatrix}, \qquad
\mathbf{r}^{\mathsf{cond}} = \begin{bmatrix}
\mathbf{r}^{\mathsf{S}}_{\mathsf{I}^\mathsf{r}} \\
\mathbf{r}^{\mathsf{S}}_{\mathsf{B}} + \underline{\mathbf{r}}^{\mathsf{F}}_{\mathsf{B}} \\
\check{\mathbf{r}}^{\mathsf{S}}_{\bar{\mathsf{B}}} + \underline{\check{\mathbf{r}}}^{\mathsf{F}}_{\bar{\mathsf{B}}} \\
\mathbf{r}^{\mathsf{S}}_{\hat{\mathsf{B}}} \\
\mathbf{r}^{\mathsf{S}}_{\mathsf{I}^\mathsf{u}} \\
\check{\mathbf{r}}^{\mathsf{S}}_{\tilde{\mathsf{B}}} \\
\mathbf{r}^{\mathsf{F}}_{\mathsf{I}^\mathsf{r}} \\
\check{\mathbf{r}}^{\mathsf{F}}_{\hat{\mathsf{B}}}
\end{bmatrix}. \tag{5.1.12}$$

In this context, the superimposed accent denotes that corresponding submatrices or -vectors are changed compared to their counterparts in equation (5.1.7) or (5.1.8). For clarification, the modified equations are additionally highlighted in gray. Accordingly, peripheral airflow affects parenchyma deformation along $\bar{\mathsf{B}} \cup \tilde{\mathsf{B}}$ and flow in the resolved domain at $\bar{\mathsf{B}} \cup \hat{\mathsf{B}}$.

The linear problem (5.1.10)-(5.1.12) is absolutely equivalent to the original mixture model (5.1.6)-(5.1.8). However, this reformulation will prove useful for the derivation of the novel coupling approach presented in the following section.

5.2 Volume-coupled fluid-structure interaction

To simplify the condensed homogenized model presented in section 5.1.3 further, it is now additionally assumed that airflow velocities in the peripheral parts are negligible and the problem is mainly pressure-dominated. This hypothesis is deemed suitable since the overall airway cross section increases exponentially as branching progresses by generations (Sapoval et al., 2002). Convective flow velocities decrease as the air moves deeper into peripheral regions until, finally, gas transport is governed by diffusion only. Hence, simulating in detail the fluid field in the homogenized domain is unnecessary. Therefore, the static condensation performed in the previous section is now replaced by an approximate model for the effect of peripheral airflow. This model is based on the insight that the air transported in the feeding vessel causes an inflation of the downstream peripheral region. Assuming that both airflow and (resolved) tissue structures are incompressible, the change in volume of the homogenized parenchyma model, thus, needs to equal the volume of air flowing into it.

Subsequently, a general procedure to determine both airflow and parenchyma volumes will be presented. Furthermore, the coupling of volume changes within the framework of FSI problems will be addressed in detail. Thereby, an efficient approach to combining continuum models of lung parenchyma and the resolved airway tree into one overall lung model will be derived.

5.2.1 Determination of field volume changes

In line with the derivations in the previous section, the following considerations refer to a single feeding airway and its associated peripheral domain (cf. 5.1.1(d)). However, all relationships naturally apply also for the case of multiple outlets and parenchyma regions as will be illustrated by several numerical examples in section 5.4.

5.2.1.1 Outflowing air volume

The volume of air flowing through the artificial outlet $\hat{\mathsf{B}}$ in the time interval $[t_1; t_2]$ can be determined by integrating the flow rate q in time

$$\Delta V^{\mathsf{F}} = \int_{t_1}^{t_2} q \, \mathrm{d}t. \qquad (5.2.1)$$

Thereby, q is defined as the scalar product of the convective fluid velocity at the outlet and the corresponding area vector in the current (i.e. deformed) configuration, viz.

$$q = \int_{\hat{\mathsf{B}}} \left(\boldsymbol{u} - \boldsymbol{u}^{\mathsf{A}} \right) \cdot \mathrm{d}\boldsymbol{A}. \qquad (5.2.2)$$

Introducing the convective velocity (2.2.4) and $\mathrm{d}\boldsymbol{A} = \boldsymbol{n}\,\mathrm{d}A$, the discrete version of the flow rate through an element situated at the outlet reads

$$q^{(e)} = \int_{\hat{\mathsf{B}}^{(e)}} \boldsymbol{c} \cdot \boldsymbol{n}\,\mathsf{d}A. \tag{5.2.3}$$

From equation (2.1.19), the unit normal vector of the outlet surface $\boldsymbol{n}$ is obtained as

$$\boldsymbol{n} = \frac{\tilde{\boldsymbol{n}}}{|\tilde{\boldsymbol{n}}|}. \tag{5.2.4}$$

Using relations (5.2.4) and (2.1.21), the element flow rate (5.2.3) can be reformulated as

$$q^{(e)} = \int_{-1}^{1}\int_{-1}^{1} (c_1 \cdot \tilde{n}_1 + c_2 \cdot \tilde{n}_2 + c_3 \cdot \tilde{n}_3)\, \mathsf{d}\xi_1 \mathsf{d}\xi_2. \tag{5.2.5}$$

Application of Gaussian quadrature then yields

$$\begin{aligned} q^{(e)} &= \sum_{\mathsf{gp}=1}^{\mathsf{ngp}} \left\{ w_{\mathsf{gp}} \sum_{r=1}^{\mathsf{ndim}} \left[\sum_{I=1}^{\mathsf{nnod}} \left(N_I\left(\boldsymbol{\xi}_{\mathsf{gp}}\right)\left(\mathsf{u}_{I;r} - \mathsf{u}^{\mathsf{A}}_{I;r}\right)\right) \tilde{n}_r\left(\boldsymbol{\xi}_{\mathsf{gp}}\right) \right] \right\} = \\ &= \sum_{\mathsf{gp}=1}^{\mathsf{ngp}} \left\{ w_{\mathsf{gp}} \sum_{r=1}^{\mathsf{ndim}} \sum_{s=1}^{\mathsf{ndim}} \sum_{t=1}^{\mathsf{ndim}} \left[\frac{1}{2} \mathscr{E}_{rst} \sum_{I=1}^{\mathsf{nnod}} \left(N_I\left(\boldsymbol{\xi}_{\mathsf{gp}}\right)\left(\mathsf{u}_{I;r} - \mathsf{u}^{\mathsf{A}}_{I;r}\right)\right) \cdot \left(\sum_{J=1}^{\mathsf{nnod}} \left(\frac{\partial N_J}{\partial \xi_1}\left(\boldsymbol{\xi}_{\mathsf{gp}}\right) \mathsf{x}_{J;s} \right) \cdot \right. \right. \right. \\ &\quad \left. \left. \left. \cdot \sum_{K=1}^{\mathsf{nnod}} \left(\frac{\partial N_K}{\partial \xi_2}\left(\boldsymbol{\xi}_{\mathsf{gp}}\right) \mathsf{x}_{K;t} \right) - \sum_{J=1}^{\mathsf{nnod}} \left(\frac{\partial N_J}{\partial \xi_2}\left(\boldsymbol{\xi}_{\mathsf{gp}}\right) \mathsf{x}_{J;s} \right) \sum_{K=1}^{\mathsf{nnod}} \left(\frac{\partial N_K}{\partial \xi_1}\left(\boldsymbol{\xi}_{\mathsf{gp}}\right) \mathsf{x}_{K;t} \right) \right) \right] \right\} \end{aligned} \tag{5.2.6}$$

with $N_I\left(\boldsymbol{\xi}_{\mathsf{gp}}\right)$ being the value of the I-th shape function at the Gauss integration point and w_{gp} referring to the corresponding Gaussian weight. ngp, nnod, and ndim denote the number of element Gauss points, nodes, and dimensions (i.e. $\mathsf{ndim} = 3$ in the three-dimensional case). $\mathscr{E}_{rst}$ corresponds to the Levi-Civita symbol (3.3.26). The factor $\frac{1}{2}$ in equation (5.2.6) comes about due to the nested sum of the dimensional identifiers r, s, and t.

For time integration of the air volume change (5.2.1), a one-step theta scheme is employed, i.e.

$$\Delta V^{\mathsf{F}}_{n+1} = \Delta t\,(\theta q_{n+1} + (1-\theta)\,q_n)\,. \tag{5.2.7}$$

Since the fluid acceleration is assumed to be constant over the time step Δt, fluid velocities vary linearly in time. If the outflow surface was invariant, the flow rate q would, hence, also be a linear function of t. In this case, equation (5.2.7) would be exact given that θ is chosen to be 0.5. In general, however, the outflow surface is changing in time and, thus, $\Delta V^{\mathsf{F}}_{n+1}$ also depends nonlinearly on the time-dependent grid displacements $\mathbf{d}^{\mathsf{A}}_{n+1}$. Although the accuracy and stability of the time integration scheme (5.2.7) has not yet been investigated in detail for this case, it is utilized exclusively in the following.

In section 5.2.2, the proposed volume constraint will be linearized to enable the application of Newton's method. For this purpose, derivatives of ΔV^{F} with respect to airflow velocities and grid displacements have to be calculated. From equation (5.2.7), the following relationship is obtained

$$\frac{\partial \Delta V^{\mathsf{F}}_{n+1}}{\partial \mathbf{z}_{n+1}} = \Delta t\,\theta \frac{\partial q_{n+1}}{\partial \mathbf{z}_{n+1}} \tag{5.2.8}$$

where $\mathbf{z}_{n+1}$ denotes an arbitrary discrete vector. The derivatives of the element flow rate with respect to the airflow velocities in general read

$$\frac{\partial q^{(e)}}{\partial \mathsf{u}_{I;s}} = \sum_{\mathsf{gp}=1}^{\mathsf{ngp}} \left[w_{\mathsf{gp}} N_I\left(\boldsymbol{\xi}_{\mathsf{gp}}\right) \tilde{n}_s\left(\boldsymbol{\xi}_{\mathsf{gp}}\right)\right] \tag{5.2.9}$$

$$\frac{\partial^2 q^{(e)}}{\partial \mathsf{u}_{I;s} \partial \mathsf{u}_{J;t}} = 0 \tag{5.2.10}$$

with $s,t \in \{1,2,3\}$. The first derivative of $q^{(e)}$ with respect to the grid displacement is given by

$$\begin{aligned} \frac{\partial q^{(e)}}{\partial \mathsf{d}^{\mathsf{A}}_{I;s}} = \sum_{\mathsf{gp}=1}^{\mathsf{ngp}} \Bigg\{ w_{\mathsf{gp}} \Bigg\{ \sum_{r=1}^{\mathsf{ndim}} \Bigg[\sum_{K=1}^{\mathsf{nnod}} \left(N_K\left(\boldsymbol{\xi}_{\mathsf{gp}}\right) \left(\mathsf{u}_{K;r} - \mathsf{u}^{\mathsf{A}}_{K;r}\right)\right) \frac{\partial \tilde{n}_r}{\partial \mathsf{d}^{\mathsf{A}}_{I;s}} \left(\boldsymbol{\xi}_{\mathsf{gp}}\right)\Bigg] - \\ - N_I\left(\boldsymbol{\xi}_{\mathsf{gp}}\right) \frac{\partial \mathsf{u}^{\mathsf{A}}_{I;s}}{\partial \mathsf{d}^{\mathsf{A}}_{I;s}} \tilde{n}_s\left(\boldsymbol{\xi}_{\mathsf{gp}}\right)\Bigg\}\Bigg\}. \end{aligned} \tag{5.2.11}$$

The derivatives of the grid velocities and the surface normals with respect to the grid displacements can be determined based on equations (2.3.2) and (3.3.28), respectively. Eventually, the following expression is obtained for the “mixed” derivative

$$\frac{\partial^2 q^{(e)}}{\partial \mathsf{u}_{I;s} \partial \mathsf{d}^{\mathsf{A}}_{J;t}} = \sum_{\mathsf{gp}=1}^{\mathsf{ngp}} \left[w_{\mathsf{gp}} N_I\left(\boldsymbol{\xi}_{\mathsf{gp}}\right) \frac{\partial \tilde{n}_s}{\partial \mathsf{d}^{\mathsf{A}}_{J;t}} \left(\boldsymbol{\xi}_{\mathsf{gp}}\right)\right]. \tag{5.2.12}$$

5.2.1.2 Change in parenchymal volume

In the following, the change in volume of the parenchyma region associated with the feeding airway will be determined. Introducing V^{S}_n and V^{S}_{n+1} as the volume of the domain at the beginning and the end of the time step, the volume change simply reads

$$\Delta V^{\mathsf{S}}_{n+1} = V^{\mathsf{S}}_{n+1} - V^{\mathsf{S}}_n. \tag{5.2.13}$$

In this context, the parenchyma volume is in general given by

$$\begin{aligned} V^{\mathsf{S}} &= \int_{\Omega^{\mathsf{S}}} \mathsf{d}V = \frac{1}{3} \int_{\Omega^{\mathsf{S}}} \left(\frac{\partial x_1}{\partial x_1} + \frac{\partial x_2}{\partial x_2} + \frac{\partial x_3}{\partial x_3}\right) \mathsf{d}V \\ &= \frac{1}{3} \int_{\Omega^{\mathsf{S}}} \nabla \cdot \boldsymbol{x}\, \mathsf{d}V. \end{aligned} \tag{5.2.14}$$

Application of the divergence theorem then yields

$$V^{\mathsf{S}} = \frac{1}{3}\int_{\partial\Omega^{\mathsf{S}}} \boldsymbol{x}\cdot\boldsymbol{n}\,\mathrm{d}A \tag{5.2.15}$$

with $\partial\Omega^{\mathsf{S}} = \bar{\mathsf{B}} \cup \hat{\mathsf{B}} \cup \tilde{\mathsf{B}}$ denoting the enclosing surface and $\boldsymbol{n}$ referring to the local unit normal vector. After introduction of equations (5.2.4) and (2.1.21), the contribution of an element (e) situated at the boundary $\partial\Omega^{\mathsf{S}}$ can be determined by

$$V^{\mathsf{S}(e)} = \frac{1}{3}\int_{-1}^{1}\int_{-1}^{1} (x_1\cdot\tilde{n}_1 + x_2\cdot\tilde{n}_2 + x_3\cdot\tilde{n}_3)\,\mathsf{d}\xi_l\mathsf{d}\xi_m. \tag{5.2.16}$$

To evaluate the integrals, Gaussian quadrature is again utilized, i.e.

$$\begin{aligned}
V^{\mathsf{S}(e)} =& \frac{1}{3}\sum_{\mathsf{gp}}\left[w_{\mathsf{gp}}\sum_{r=1}^{\mathsf{ndim}}(x_r\tilde{n}_r)\right] = \\
=& \frac{1}{3}\sum_{\mathsf{gp}}\left\{w_{\mathsf{gp}}\left\{\sum_{r=1}^{\mathsf{ndim}}\sum_{s=1}^{\mathsf{ndim}}\sum_{t=1}^{\mathsf{ndim}}\frac{1}{2}\mathscr{E}_{rst}\left[\sum_{I=1}^{\mathsf{nnod}}\left(N_I\left(\boldsymbol{\xi}_{\mathsf{gp}}\right)\mathsf{x}_{I;r}\right)\left[\sum_{J=1}^{\mathsf{nnod}}\left(\frac{\partial N_J}{\partial\xi_1}\left(\boldsymbol{\xi}_{\mathsf{gp}}\right)\mathsf{x}_{J;s}\right)\cdot\right.\right.\right.\right. \\
&\left.\left.\left.\left.\cdot\sum_{K=1}^{\mathsf{nnod}}\left(\frac{\partial N_K}{\partial\xi_2}\left(\boldsymbol{\xi}_{\mathsf{gp}}\right)\mathsf{x}_{K;t}\right) - \sum_{J=1}^{\mathsf{nnod}}\left(\frac{\partial N_J}{\partial\xi_2}\left(\boldsymbol{\xi}_{\mathsf{gp}}\right)\mathsf{x}_{J;s}\right)\sum_{K=1}^{\mathsf{nnod}}\left(\frac{\partial N_K}{\partial\xi_1}\left(\boldsymbol{\xi}_{\mathsf{gp}}\right)\mathsf{x}_{K;t}\right)\right]\right]\right\}\right\}.
\end{aligned} \tag{5.2.17}$$

The considerations presented in the previous section regarding the nested sum of dimensional identifiers r, s, and t also hold in this case.

The linearization of the volume constraint introduced in section 5.2.2 involves derivatives of $\Delta V^{\mathsf{S}}_{n+1}$ with respect to the boundary displacements. From equation (5.2.13), the following expressions are obtained

$$\frac{\partial\Delta V^{\mathsf{S}}_{n+1}}{\partial\mathbf{d}_{n+1}} = \frac{\partial V^{\mathsf{S}}_{n+1}}{\partial\mathbf{d}_{n+1}}, \qquad \frac{\partial^2\Delta V^{\mathsf{S}}_{n+1}}{\partial\mathbf{d}_{n+1}\partial\mathbf{d}_{n+1}} = \frac{\partial^2 V^{\mathsf{S}}_{n+1}}{\partial\mathbf{d}_{n+1}\partial\mathbf{d}_{n+1}}. \tag{5.2.18}$$

Corresponding derivatives of the element contributions to the absolute parenchymal volume read

$$\frac{\partial V^{\mathsf{S}(e)}}{\partial\mathsf{d}_{I;s}} = \frac{1}{3}\sum_{\mathsf{gp}}\left\{w_{\mathsf{gp}}\left[N_I\left(\boldsymbol{\xi}_{\mathsf{gp}}\right)\tilde{n}_s\left(\boldsymbol{\xi}_{\mathsf{gp}}\right) + \sum_{r=1}^{\mathsf{ndim}}\left(\left(\sum_{K=1}^{\mathsf{nnod}}N_K\left(\boldsymbol{\xi}_{\mathsf{gp}}\right)\mathsf{x}_{K;r}\right)\frac{\partial\tilde{n}_r}{\partial\mathsf{d}_{I;s}}\left(\boldsymbol{\xi}_{\mathsf{gp}}\right)\right)\right]\right\}, \tag{5.2.19}$$

$$\begin{aligned}
\frac{\partial^2 V^{\mathsf{S}(e)}}{\partial\mathsf{d}_{I;s}\partial\mathsf{d}_{J;t}} =& \frac{1}{3}\sum_{\mathsf{gp}}\left\{w_{\mathsf{gp}}\left[N_I\left(\boldsymbol{\xi}_{\mathsf{gp}}\right)\frac{\partial\tilde{n}_s}{\partial\mathsf{d}_{J;t}}\left(\boldsymbol{\xi}_{\mathsf{gp}}\right) + N_J\left(\boldsymbol{\xi}_{\mathsf{gp}}\right)\frac{\partial\tilde{n}_t}{\partial\mathsf{d}_{I;s}}\left(\boldsymbol{\xi}_{\mathsf{gp}}\right) +\right.\right. \\
&\left.\left. + \sum_{r=1}^{\mathsf{ndim}}\left(\sum_{K=1}^{\mathsf{nnod}}\left(N_K\left(\boldsymbol{\xi}_{\mathsf{gp}}\right)\mathsf{x}_{K;r}\right)\frac{\partial\tilde{n}_r^2}{\partial\mathsf{d}_{I;s}\partial\mathsf{d}_{J;t}}\left(\boldsymbol{\xi}_{\mathsf{gp}}\right)\right)\right]\right\}
\end{aligned} \tag{5.2.20}$$

where the derivatives of the surface normal vectors can be found in equations (3.3.28) and (3.3.31).

5.2.2 Coupling of volume changes

In the previous sections, general expressions for changes in air and parenchyma volumes as functions of boundary displacements and/or velocities have been derived. For a reasonable combination of airway and parenchyma models, corresponding volume changes have to be coupled. Hence, the volume of air flowing through the artificial outlet $\hat{\mathsf{B}}$ has to equal the change in volume of the surrounding parenchyma domain enclosed by $\bar{\mathsf{B}} \cup \hat{\mathsf{B}} \cup \tilde{\mathsf{B}}$. Furthermore, ALE and solid meshes need to be tied along $\hat{\mathsf{B}}$ in order to preclude any gaps between the resolved airway and homogenized peripheral domain.

For the enforcement of the volume constraint, the Lagrange multiplier method as introduced in section 2.5.1 is employed. The corresponding constraint potential is given by

$$\mathcal{W}^{\mathsf{C}} = \lambda\left(\Delta V^{\mathsf{S}} - \Delta V^{\mathsf{F}}\right) \tag{5.2.21}$$

where λ denotes the Lagrange multiplier associated with the volume constraint. ΔV^{S} and ΔV^{F} refer to the parenchymal volume change and the outflowing air volume as introduced in equations (5.2.13) and (5.2.7), respectively. The total variation of the constraint potential (5.2.21) is obtained as

$$\delta\mathcal{W}^{\mathsf{C}} = \delta\lambda\left(\Delta V^{\mathsf{S}} - \Delta V^{\mathsf{F}}\right) + \lambda\delta\left(\Delta V^{\mathsf{S}} - \Delta V^{\mathsf{F}}\right). \tag{5.2.22}$$

In order to determine $\delta\left(\Delta V^{\mathsf{S}} - \Delta V^{\mathsf{F}}\right)$, corresponding primary variables critical for the volume changes need to be identified. In this context, airflow velocities as well as boundary displacements play a role. As already discussed in section 5.1.2, $\hat{\mathsf{B}}$ is a purely artificial boundary introduced in the homogenization process as the transition between resolved and unresolved domains. Consequently, $\hat{\mathsf{B}}$ should deform solely in a passive manner following the motion of the remaining parenchymal boundary. For the volume constraint, $\hat{\mathsf{B}}$ can thus be interpreted as a Dirichlet boundary for parenchymal displacements and coupled fluid grid velocities. Therefore, no variations of the volume changes with respect to these quantities occur.

It is also easy to see that ΔV^{F} is not influenced by the fluid velocities and displacements along $\bar{\mathsf{B}}$. This enclosing boundary of the artificial outlet is part of the FSI interface and, hence,

$$\boldsymbol{c}_{\bar{\mathsf{B}}} = \boldsymbol{0} \tag{5.2.23}$$

holds at any time. Therefore, the flow rate does not depend on $\boldsymbol{u}_{\bar{\mathsf{B}}}$ as well as $\boldsymbol{d}^{\mathsf{A}}_{\bar{\mathsf{B}}}$ and corresponding variations vanish.

Consequently, equation (5.2.22) can be restated as follows

$$\begin{aligned}\delta\mathcal{W}^{\mathsf{C}} &= \delta\lambda\Big(\Delta V^{\mathsf{S}}\big(\boldsymbol{d}_{\tilde{\mathsf{B}}},\boldsymbol{d}_{\bar{\mathsf{B}}},\boldsymbol{d}_{\hat{\mathsf{B}}}\big)-\Delta V^{\mathsf{F}}\big(\boldsymbol{u}_{\hat{\mathsf{B}}},\boldsymbol{d}_{\hat{\mathsf{B}}}\big)\Big)+\lambda\frac{\partial\Delta V^{\mathsf{S}}\big(\boldsymbol{d}_{\tilde{\mathsf{B}}},\boldsymbol{d}_{\bar{\mathsf{B}}},\boldsymbol{d}_{\hat{\mathsf{B}}}\big)}{\partial\boldsymbol{d}_{\tilde{\mathsf{B}}}}\delta\boldsymbol{d}_{\tilde{\mathsf{B}}}+\\ &+\lambda\frac{\partial\Delta V^{\mathsf{S}}\big(\boldsymbol{d}_{\tilde{\mathsf{B}}},\boldsymbol{d}_{\bar{\mathsf{B}}},\boldsymbol{d}_{\hat{\mathsf{B}}}\big)}{\partial\boldsymbol{d}_{\bar{\mathsf{B}}}}\delta\boldsymbol{d}_{\bar{\mathsf{B}}}-\lambda\frac{\partial\Delta V^{\mathsf{F}}\big(\boldsymbol{u}_{\hat{\mathsf{B}}},\boldsymbol{d}_{\hat{\mathsf{B}}}\big)}{\partial\boldsymbol{u}_{\hat{\mathsf{B}}}}\delta\boldsymbol{u}_{\hat{\mathsf{B}}}.\end{aligned}\tag{5.2.24}$$

The above variational form implies that the volume constraint is enforced at any time. For a combination with the models developed so far, however, equation (5.2.24) needs to be discretized in time. In this context, several alternatives are in general conceivable. One possibility would be to satisfy the constraint on average over the time step. Another approach – employed subsequently – is based on the enforcement of the constraint at a discrete point in time, e.g. at the end of the time step $[t_n, t_{n+1}]$. Hence, the continuous Lagrange multiplier λ is replaced with its discrete counterpart λ_{n+1} in the following.

The Lagrange multiplier enforces the volume constraint globally and is, thus, not distributed in space. Therefore, spatial discretization of the variational form (5.2.24) basically reduces to discretizing boundary displacements and velocities. Hence, the discrete weak form of the volume coupling constraint evaluated at t_{n+1} reads

$$\begin{aligned}\delta\mathcal{W}^{\mathsf{C}}_{n+1} &= \delta\lambda\Big(\Delta V^{\mathsf{S}}\big(\mathbf{d}_{\tilde{\mathsf{B}}},\mathbf{d}_{\bar{\mathsf{B}}},\mathbf{d}_{\hat{\mathsf{B}}}\big)-\Delta V^{\mathsf{F}}\big(\mathbf{u}_{\hat{\mathsf{B}}},\mathbf{d}_{\hat{\mathsf{B}}}\big)\Big)_{n+1}+\lambda_{n+1}\left(\frac{\partial\Delta V^{\mathsf{S}}\big(\mathbf{d}_{\tilde{\mathsf{B}}},\mathbf{d}_{\bar{\mathsf{B}}},\mathbf{d}_{\hat{\mathsf{B}}}\big)}{\partial\mathbf{d}_{\tilde{\mathsf{B}}}}\right)_{n+1}\delta\mathbf{d}_{\tilde{\mathsf{B}}}+\\ &+\lambda_{n+1}\left(\frac{\partial\Delta V^{\mathsf{S}}\big(\mathbf{d}_{\tilde{\mathsf{B}}},\mathbf{d}_{\bar{\mathsf{B}}},\mathbf{d}_{\hat{\mathsf{B}}}\big)}{\partial\mathbf{d}_{\bar{\mathsf{B}}}}\right)_{n+1}\delta\mathbf{d}_{\bar{\mathsf{B}}}-\lambda_{n+1}\left(\frac{\partial\Delta V^{\mathsf{F}}\big(\mathbf{u}_{\hat{\mathsf{B}}},\mathbf{d}_{\hat{\mathsf{B}}}\big)}{\partial\mathbf{u}_{\hat{\mathsf{B}}}}\right)_{n+1}\delta\mathbf{u}_{\hat{\mathsf{B}}}.\end{aligned}\tag{5.2.25}$$

For the sake of clarity, the following abbreviations are introduced

$$\mathrm{r}^{\mathsf{C;C}}_{\mathsf{l};n+1}=\Big(\Delta V^{\mathsf{S}}\big(\mathbf{d}_{\tilde{\mathsf{B}}},\mathbf{d}_{\bar{\mathsf{B}}},\mathbf{d}_{\hat{\mathsf{B}}}\big)-\Delta V^{\mathsf{F}}\big(\mathbf{u}_{\hat{\mathsf{B}}},\mathbf{d}_{\hat{\mathsf{B}}}\big)\Big)_{n+1}=\Delta V^{\mathsf{S}}_{n+1}-\Delta V^{\mathsf{F}}_{n+1},\tag{5.2.26}$$

$$\mathbf{f}^{\mathsf{C;S}}_{\#;n+1}=\lambda_{n+1}\frac{\partial\Delta V^{\mathsf{S}}_{n+1}}{\partial\mathbf{d}_{\#;n+1}},\tag{5.2.27}$$

$$\mathbf{h}^{\mathsf{C;F}}_{\hat{\mathsf{B}};n+1}=\lambda_{n+1}\frac{\partial\Delta V^{\mathsf{F}}_{n+1}}{\partial\mathbf{u}_{\hat{\mathsf{B}};n+1}}\tag{5.2.28}$$

with # denoting a particular solid boundary. Hence, the discrete variation of the constraint potential simplifies to

$$\delta\mathcal{W}^{\mathsf{C}}_{n+1}=\mathrm{r}^{\mathsf{C;C}}_{\mathsf{l};n+1}\delta\lambda+\mathbf{f}^{\mathsf{C;S}}_{\tilde{\mathsf{B}};n+1}\delta\mathbf{d}_{\tilde{\mathsf{B}}}+\mathbf{f}^{\mathsf{C;S}}_{\bar{\mathsf{B}};n+1}\delta\mathbf{d}_{\bar{\mathsf{B}}}-\mathbf{h}^{\mathsf{C;F}}_{\hat{\mathsf{B}};n+1}\delta\mathbf{u}_{\hat{\mathsf{B}}}.\tag{5.2.29}$$

Equation (5.2.29) can also be interpreted as the additional virtual work due to the volume coupling. Depending on the involved virtual quantity, the summands can be attributed to either the constraint or the solid and fluid parts, i.e.

$$\delta\mathcal{W}^{\mathsf{C}}_{n+1}=\delta\mathcal{W}^{\mathsf{C;C}}_{n+1}+\delta\mathcal{W}^{\mathsf{C;S}}_{n+1}+\delta\mathcal{W}^{\mathsf{C;F}}_{n+1}\tag{5.2.30}$$

with

$$\delta\mathcal{W}^{\mathsf{C;C}}_{n+1} = \mathsf{r}^{\mathsf{C;C}}_{\mathsf{I};n+1}\delta\lambda, \tag{5.2.31}$$

$$\delta\mathcal{W}^{\mathsf{C;S}}_{n+1} = \mathbf{f}^{\mathsf{C;S}}_{\tilde{\mathsf{B}};n+1}\delta\mathbf{d}_{\tilde{\mathsf{B}}} + \mathbf{f}^{\mathsf{C;S}}_{\bar{\mathsf{B}};n+1}\delta\mathbf{d}_{\bar{\mathsf{B}}}, \tag{5.2.32}$$

$$\delta\mathcal{W}^{\mathsf{C;F}}_{n+1} = -\mathbf{h}^{\mathsf{C;F}}_{\hat{\mathsf{B}};n+1}\delta\mathbf{u}_{\hat{\mathsf{B}}}. \tag{5.2.33}$$

As already discussed in section 2.2, the weak form of the Navier-Stokes equations corresponds to a virtual power expression. Hence, for combining equations (2.2.21) and (5.2.33), the time derivative of the latter needs to be evaluated. In the continuous case, this is equivalent to

$$\delta\mathcal{P}^{\mathsf{C;F}} = \frac{\partial\left(\delta\mathcal{W}^{\mathsf{C;F}}\right)}{\partial t}. \tag{5.2.34}$$

Since the following relations hold

$$\frac{\partial\Delta V^{\mathsf{F}}}{\partial t} = \frac{\partial\left(\int q\,\mathrm{d}t\right)}{\partial t} = q, \qquad \frac{\partial\left(\delta\mathbf{u}_{\hat{\mathsf{B}}}\right)}{\partial t} = \mathbf{0}, \tag{5.2.35}$$

the discrete form of the virtual power (5.2.34) is determined by

$$\delta\mathcal{P}^{\mathsf{C;F}}_{n+1} = -\lambda_{n+1}\frac{\partial q_{n+1}}{\partial\mathbf{u}_{\hat{\mathsf{B}};n+1}}\delta\mathbf{u}_{\hat{\mathsf{B}}} = -\mathbf{f}^{\mathsf{C;F}}_{\hat{\mathsf{B}};n+1}\delta\mathbf{u}_{\hat{\mathsf{B}}} \tag{5.2.36}$$

with

$$\mathbf{f}^{\mathsf{C;F}}_{\hat{\mathsf{B}};n+1} = \lambda_{n+1}\frac{\partial q_{n+1}}{\partial\mathbf{u}_{\hat{\mathsf{B}};n+1}} \tag{5.2.37}$$

being a physical force along boundary $\hat{\mathsf{B}}$. Although the Lagrange multiplier also varies with time, it enforces the constraint instantaneously at a discrete point in time independently of its history. Therefore, no time derivative of λ appears in equation (5.2.36).

Based on the derivations presented so far, the overall residual of the volume-coupled FSI system can be set up and linearized consistently. However, since the FSI part has already been presented before, the focus remains on the additional contributions due to the volume constraint to simplify matters for the time being. Recalling that ALE and solid meshes are tied along the artificial outlet, i.e. $\mathbf{d}_{\hat{\mathsf{B}}} = \mathbf{d}^{\mathsf{A}}_{\hat{\mathsf{B}}}$ and $\mathbf{d}_{\bar{\mathsf{B}}} = \mathbf{d}^{\mathsf{A}}_{\bar{\mathsf{B}}}$, the following linearized problem is obtained

$$\underbrace{\begin{bmatrix} \overset{\mathsf{C}}{\mathbf{K}}{}^{\mathsf{SS}}_{\tilde{\mathsf{B}}\tilde{\mathsf{B}}} & \overset{\mathsf{C}}{\mathbf{K}}{}^{\mathsf{SS}}_{\tilde{\mathsf{B}}\bar{\mathsf{B}}} & \overset{\mathsf{C}}{\mathbf{K}}{}^{\mathsf{SS}}_{\tilde{\mathsf{B}}\hat{\mathsf{B}}} & \overset{\mathsf{C}}{\mathbf{K}}{}^{\mathsf{SF}}_{\tilde{\mathsf{B}}\hat{\mathsf{B}}} & \overset{\mathsf{C}}{\mathbf{K}}{}^{\mathsf{SC}}_{\tilde{\mathsf{B}}\mathsf{I}} \\ \overset{\mathsf{C}}{\mathbf{K}}{}^{\mathsf{SS}}_{\bar{\mathsf{B}}\tilde{\mathsf{B}}} & \overset{\mathsf{C}}{\mathbf{K}}{}^{\mathsf{SS}}_{\bar{\mathsf{B}}\bar{\mathsf{B}}} & \overset{\mathsf{C}}{\mathbf{K}}{}^{\mathsf{SS}}_{\bar{\mathsf{B}}\hat{\mathsf{B}}} & \overset{\mathsf{C}}{\mathbf{K}}{}^{\mathsf{SF}}_{\bar{\mathsf{B}}\hat{\mathsf{B}}} & \overset{\mathsf{C}}{\mathbf{K}}{}^{\mathsf{SC}}_{\bar{\mathsf{B}}\mathsf{I}} \\ \overset{\mathsf{C}}{\mathbf{K}}{}^{\mathsf{FS}}_{\hat{\mathsf{B}}\tilde{\mathsf{B}}} & \overset{\mathsf{C}}{\mathbf{K}}{}^{\mathsf{FA}}_{\hat{\mathsf{B}}\bar{\mathsf{B}}} & \overset{\mathsf{C}}{\mathbf{K}}{}^{\mathsf{FA}}_{\hat{\mathsf{B}}\hat{\mathsf{B}}} & \overset{\mathsf{C}}{\mathbf{K}}{}^{\mathsf{FF}}_{\hat{\mathsf{B}}\hat{\mathsf{B}}} & \overset{\mathsf{C}}{\mathbf{K}}{}^{\mathsf{FC}}_{\hat{\mathsf{B}}\mathsf{I}} \\ \overset{\mathsf{C}}{\mathbf{K}}{}^{\mathsf{CS}}_{\mathsf{I}\tilde{\mathsf{B}}} & \overset{\mathsf{C}}{\mathbf{K}}{}^{\mathsf{CS}}_{\mathsf{I}\bar{\mathsf{B}}} & \overset{\mathsf{C}}{\mathbf{K}}{}^{\mathsf{CS/CA}}_{\mathsf{I}\hat{\mathsf{B}}} & \overset{\mathsf{C}}{\mathbf{K}}{}^{\mathsf{CF}}_{\mathsf{I}\hat{\mathsf{B}}} & \overset{\mathsf{C}}{\mathsf{K}}{}^{\mathsf{CC}}_{\mathsf{II}} \end{bmatrix}^{i}_{n+1}}_{\overset{\mathsf{C}}{\mathbf{K}}{}^{i}_{n+1}} \begin{pmatrix} \Delta\mathbf{d}_{\tilde{\mathsf{B}}} \\ \Delta\mathbf{d}_{\bar{\mathsf{B}}} \\ \Delta\mathbf{d}_{\hat{\mathsf{B}}} \\ \Delta\mathbf{u}_{\hat{\mathsf{B}}} \\ \Delta\lambda \end{pmatrix}^{i+1}_{n+1} = -\begin{pmatrix} \mathbf{r}^{\mathsf{C;S}}_{\tilde{\mathsf{B}}} \\ \mathbf{r}^{\mathsf{C;S}}_{\bar{\mathsf{B}}} \\ \mathbf{r}^{\mathsf{C;F}}_{\hat{\mathsf{B}}} \\ \mathsf{r}^{\mathsf{C;C}}_{\mathsf{I}} \end{pmatrix}^{i}_{n+1} \tag{5.2.38}$$

with

$$\begin{pmatrix} \mathbf{r}^{\mathsf{C;S}}_{\tilde{\mathsf{B}}} \\ \mathbf{r}^{\mathsf{C;S}}_{\bar{\mathsf{B}}} \\ \mathbf{r}^{\mathsf{C;F}}_{\hat{\mathsf{B}}} \\ \mathsf{r}^{\mathsf{C;C}}_{\mathsf{I}} \end{pmatrix}^{i}_{n+1} = \begin{pmatrix} \mathbf{f}^{\mathsf{C;S}}_{\tilde{\mathsf{B}}} \\ \mathbf{f}^{\mathsf{C;S}}_{\bar{\mathsf{B}}} \\ -\,\mathbf{f}^{\mathsf{C;F}}_{\hat{\mathsf{B}}} \\ \mathsf{r}^{\mathsf{C;C}}_{\mathsf{I}} \end{pmatrix}^{i}_{n+1} \tag{5.2.39}$$

and

$$\overset{\mathsf{C}}{\mathbf{K}}{}^{i}_{n+1} = \begin{bmatrix} \dfrac{\partial \mathbf{f}^{\mathsf{C;S}}_{\tilde{\mathsf{B}}}}{\partial \mathbf{d}_{\tilde{\mathsf{B}}}} & \dfrac{\partial \mathbf{f}^{\mathsf{C;S}}_{\tilde{\mathsf{B}}}}{\partial \mathbf{d}_{\bar{\mathsf{B}}}} & \dfrac{\partial \mathbf{f}^{\mathsf{C;S}}_{\tilde{\mathsf{B}}}}{\partial \mathbf{d}_{\hat{\mathsf{B}}}} & \dfrac{\partial \mathbf{f}^{\mathsf{C;S}}_{\tilde{\mathsf{B}}}}{\partial \mathbf{u}_{\hat{\mathsf{B}}}} & \dfrac{\partial \mathbf{f}^{\mathsf{C;S}}_{\tilde{\mathsf{B}}}}{\partial \lambda} \\ \dfrac{\partial \mathbf{f}^{\mathsf{C;S}}_{\bar{\mathsf{B}}}}{\partial \mathbf{d}_{\tilde{\mathsf{B}}}} & \dfrac{\partial \mathbf{f}^{\mathsf{C;S}}_{\bar{\mathsf{B}}}}{\partial \mathbf{d}_{\bar{\mathsf{B}}}} & \dfrac{\partial \mathbf{f}^{\mathsf{C;S}}_{\bar{\mathsf{B}}}}{\partial \mathbf{d}_{\hat{\mathsf{B}}}} & \dfrac{\partial \mathbf{f}^{\mathsf{C;S}}_{\bar{\mathsf{B}}}}{\partial \mathbf{u}_{\hat{\mathsf{B}}}} & \dfrac{\partial \mathbf{f}^{\mathsf{C;S}}_{\bar{\mathsf{B}}}}{\partial \lambda} \\ -\dfrac{\partial \mathbf{f}^{\mathsf{C;F}}_{\hat{\mathsf{B}}}}{\partial \mathbf{d}_{\tilde{\mathsf{B}}}} & -\dfrac{\partial \mathbf{f}^{\mathsf{C;F}}_{\hat{\mathsf{B}}}}{\partial \mathbf{d}_{\bar{\mathsf{B}}}} & -\dfrac{\partial \mathbf{f}^{\mathsf{C;F}}_{\hat{\mathsf{B}}}}{\partial \mathbf{d}_{\hat{\mathsf{B}}}} & -\dfrac{\partial \mathbf{f}^{\mathsf{C;F}}_{\hat{\mathsf{B}}}}{\partial \mathbf{u}_{\hat{\mathsf{B}}}} & -\dfrac{\partial \mathbf{f}^{\mathsf{C;F}}_{\hat{\mathsf{B}}}}{\partial \lambda} \\ \dfrac{\partial \mathsf{r}^{\mathsf{C;C}}_{\mathsf{I};n+1}}{\partial \mathbf{d}_{\tilde{\mathsf{B}}}} & \dfrac{\partial \mathsf{r}^{\mathsf{C;C}}_{\mathsf{I};n+1}}{\partial \mathbf{d}_{\bar{\mathsf{B}}}} & \dfrac{\partial \mathsf{r}^{\mathsf{C;C}}_{\mathsf{I};n+1}}{\partial \mathbf{d}_{\hat{\mathsf{B}}}} & \dfrac{\partial \mathsf{r}^{\mathsf{C;C}}_{\mathsf{I};n+1}}{\partial \mathbf{u}_{\hat{\mathsf{B}}}} & \dfrac{\partial \mathsf{r}^{\mathsf{C;C}}_{\mathsf{I};n+1}}{\partial \lambda} \end{bmatrix}^{i}_{n+1} . \tag{5.2.40}$$

Advantage is taken of the fact that the change in fluid volume does not depend on the velocities and coupled displacements at the FSI boundary as discussed above. Consequently, corresponding linearizations are omitted here. Introducing equations (5.2.8), (5.2.10), (5.2.26), (5.2.27), and (5.2.37) into the constraint system matrix (5.2.40) then yields

$$\overset{\mathsf{C}}{\mathbf{K}}{}^{i}_{n+1} = \begin{bmatrix} \lambda \frac{\partial}{\partial \mathbf{d}_{\tilde{\mathsf{B}}}} \left(\frac{\partial \Delta V^{\mathsf{S}}}{\partial \mathbf{d}_{\tilde{\mathsf{B}}}} \right) & \lambda \frac{\partial}{\partial \mathbf{d}_{\bar{\mathsf{B}}}} \left(\frac{\partial \Delta V^{\mathsf{S}}}{\partial \mathbf{d}_{\tilde{\mathsf{B}}}} \right) & \mathbf{0} & \mathbf{0} & \frac{\partial \Delta V^{\mathsf{S}}}{\partial \mathbf{d}_{\tilde{\mathsf{B}}}} \\ \lambda \frac{\partial}{\partial \mathbf{d}_{\tilde{\mathsf{B}}}} \left(\frac{\partial \Delta V^{\mathsf{S}}}{\partial \mathbf{d}_{\bar{\mathsf{B}}}} \right) & \lambda \frac{\partial}{\partial \mathbf{d}_{\bar{\mathsf{B}}}} \left(\frac{\partial \Delta V^{\mathsf{S}}}{\partial \mathbf{d}_{\bar{\mathsf{B}}}} \right) & \lambda \frac{\partial}{\partial \mathbf{d}_{\hat{\mathsf{B}}}} \left(\frac{\partial \Delta V^{\mathsf{S}}}{\partial \mathbf{d}_{\bar{\mathsf{B}}}} \right) & \mathbf{0} & \frac{\partial \Delta V^{\mathsf{S}}}{\partial \mathbf{d}_{\bar{\mathsf{B}}}} \\ \mathbf{0} & -\lambda \frac{\partial}{\partial \mathbf{d}^{\mathsf{A}}_{\bar{\mathsf{B}}}} \left(\frac{\partial q}{\partial \mathbf{u}_{\hat{\mathsf{B}}}} \right) & -\lambda \frac{\partial}{\partial \mathbf{d}^{\mathsf{A}}_{\hat{\mathsf{B}}}} \left(\frac{\partial q}{\partial \mathbf{u}_{\hat{\mathsf{B}}}} \right) & \mathbf{0} & -\frac{\partial q}{\partial \mathbf{u}_{\hat{\mathsf{B}}}} \\ \frac{\partial \Delta V^{\mathsf{S}}}{\partial \mathbf{d}_{\tilde{\mathsf{B}}}} & \frac{\partial \Delta V^{\mathsf{S}}}{\partial \mathbf{d}_{\bar{\mathsf{B}}}} & \frac{\partial \Delta V^{\mathsf{S}}}{\partial \mathbf{d}_{\hat{\mathsf{B}}}} - \Delta t \theta \frac{\partial q}{\partial \mathbf{d}^{\mathsf{A}}_{\hat{\mathsf{B}}}} & -\Delta t \theta \frac{\partial q}{\partial \mathbf{u}_{\hat{\mathsf{B}}}} & 0 \end{bmatrix}^{i}_{n+1} . \tag{5.2.41}$$

Corresponding derivatives of the field volume changes were already determined in sections 5.2.1.1 and 5.2.1.2. The resulting constraint stiffness matrix $\overset{\mathsf{C}}{\mathbf{K}}{}^{i}_{n+1}$ is rectangular and unsymmetric. This is partly due to the power formulation of the fluid field as pointed out above. Besides, the weak form of the volume constraint does not contain any variations with respect to displacements at $\hat{\mathsf{B}}$ as discussed previously. For a consistent linearization of r^{λ}, however, corresponding derivatives need to be included.

Finally, the overall system of equations for the volume-constrained FSI problem is given by

$$\mathbf{K}^{\mathsf{CFSI};i}_{n+1} \Delta \mathbf{y}^{\mathsf{CFSI};i+1}_{n+1} = -\mathbf{r}^{\mathsf{CFSI};i}_{n+1} \tag{5.2.42}$$

or, in more detail,

$$
\left[\begin{array}{ccccccccc}
\mathbf{K}^{\mathrm{SS}}_{\mathrm{II}} & \mathbf{K}^{\mathrm{SS}}_{\mathrm{IB}} & \mathbf{K}^{\mathrm{SS}}_{\mathrm{I}\bar{\mathrm{B}}} & \mathbf{K}^{\mathrm{SS}}_{\mathrm{I}\hat{\mathrm{B}}} & \mathbf{K}^{\mathrm{SS}}_{\mathrm{I}\tilde{\mathrm{B}}} & \mathbf{0} & \mathbf{0} & \mathbf{0} & \mathbf{0} \\
\mathbf{K}^{\mathrm{SS}}_{\mathrm{BI}} & \mathbf{K}^{\mathrm{SFA}}_{\mathrm{BB}} & \mathbf{K}^{\mathrm{SFA}}_{\mathrm{B}\bar{\mathrm{B}}} & \mathbf{0} & \mathbf{0} & \underline{\mathbf{K}}^{\mathrm{FF}}_{\mathrm{BI}} & \mathbf{0} & \underline{\mathbf{K}}^{\mathrm{FA}}_{\mathrm{BI}} & \mathbf{0} \\
\mathbf{K}^{\mathrm{SS}}_{\bar{\mathrm{B}}\mathrm{I}} & \mathbf{K}^{\mathrm{SFA}}_{\bar{\mathrm{B}}\mathrm{B}} & \mathbf{K}^{\mathrm{SFA}}_{\bar{\mathrm{B}}\bar{\mathrm{B}}} + \overset{\mathrm{C}}{\mathbf{K}}{}^{\mathrm{SS}}_{\bar{\mathrm{B}}\bar{\mathrm{B}}} & \mathbf{K}^{\mathrm{SS}}_{\bar{\mathrm{B}}\hat{\mathrm{B}}} + \overset{\mathrm{C}}{\mathbf{K}}{}^{\mathrm{SS}}_{\bar{\mathrm{B}}\hat{\mathrm{B}}} + \underline{\mathbf{K}}^{\mathrm{FA}}_{\bar{\mathrm{B}}\hat{\mathrm{B}}} & \mathbf{K}^{\mathrm{SS}}_{\bar{\mathrm{B}}\tilde{\mathrm{B}}} + \overset{\mathrm{C}}{\mathbf{K}}{}^{\mathrm{SS}}_{\bar{\mathrm{B}}\tilde{\mathrm{B}}} & \underline{\mathbf{K}}^{\mathrm{FF}}_{\bar{\mathrm{B}}\mathrm{I}} & \underline{\mathbf{K}}^{\mathrm{FF}}_{\bar{\mathrm{B}}\hat{\mathrm{B}}} & \underline{\mathbf{K}}^{\mathrm{FA}}_{\bar{\mathrm{B}}\mathrm{I}} & \overset{\mathrm{C}}{\mathbf{K}}{}^{\mathrm{SC}}_{\bar{\mathrm{B}}\mathrm{I}} \\
\mathbf{K}^{\mathrm{SS}}_{\hat{\mathrm{B}}\mathrm{I}} & \mathbf{0} & \mathbf{K}^{\mathrm{SS}}_{\hat{\mathrm{B}}\bar{\mathrm{B}}} & \mathbf{K}^{\mathrm{SS}}_{\hat{\mathrm{B}}\hat{\mathrm{B}}} & \mathbf{0} & \mathbf{0} & \mathbf{0} & \mathbf{0} & \mathbf{0} \\
\mathbf{K}^{\mathrm{SS}}_{\tilde{\mathrm{B}}\mathrm{I}} & \mathbf{0} & \mathbf{K}^{\mathrm{SS}}_{\tilde{\mathrm{B}}\bar{\mathrm{B}}} + \overset{\mathrm{C}}{\mathbf{K}}{}^{\mathrm{SS}}_{\tilde{\mathrm{B}}\bar{\mathrm{B}}} & \mathbf{0} & \mathbf{K}^{\mathrm{SS}}_{\tilde{\mathrm{B}}\tilde{\mathrm{B}}} + \overset{\mathrm{C}}{\mathbf{K}}{}^{\mathrm{SS}}_{\tilde{\mathrm{B}}\tilde{\mathrm{B}}} & \mathbf{0} & \mathbf{0} & \mathbf{0} & \overset{\mathrm{C}}{\mathbf{K}}{}^{\mathrm{SC}}_{\tilde{\mathrm{B}}\mathrm{I}} \\
\mathbf{0} & \mathbf{K}^{\mathrm{FF/FA}}_{\mathrm{IB}} & \mathbf{K}^{\mathrm{FF/FA}}_{\mathrm{I}\bar{\mathrm{B}}} & \mathbf{K}^{\mathrm{FA}}_{\mathrm{I}\hat{\mathrm{B}}} & \mathbf{0} & \mathbf{K}^{\mathrm{FF}}_{\mathrm{II}} & \mathbf{K}^{\mathrm{FF}}_{\mathrm{I}\hat{\mathrm{B}}} & \mathbf{K}^{\mathrm{FA}}_{\mathrm{II}} & \mathbf{0} \\
\mathbf{0} & \mathbf{0} & \mathbf{K}^{\mathrm{FF/FA}}_{\hat{\mathrm{B}}\bar{\mathrm{B}}} + \overline{\overset{\mathrm{C}}{\mathbf{K}}}{}^{\mathrm{FA}}_{\hat{\mathrm{B}}\bar{\mathrm{B}}} & \overline{\overset{\mathrm{C}}{\mathbf{K}}}{}^{\mathrm{FA}}_{\hat{\mathrm{B}}\hat{\mathrm{B}}} + \mathbf{K}^{\mathrm{FA}}_{\hat{\mathrm{B}}\hat{\mathrm{B}}} & \mathbf{0} & \mathbf{K}^{\mathrm{FF}}_{\hat{\mathrm{B}}\mathrm{I}} & \mathbf{K}^{\mathrm{FF}}_{\hat{\mathrm{B}}\hat{\mathrm{B}}} & \mathbf{K}^{\mathrm{FA}}_{\hat{\mathrm{B}}\mathrm{I}} & \overline{\overset{\mathrm{C}}{\mathbf{K}}}{}^{\mathrm{FC}}_{\hat{\mathrm{B}}\mathrm{I}} \\
\mathbf{0} & \mathbf{K}^{\mathrm{AA}}_{\mathrm{IB}} & \mathbf{K}^{\mathrm{AA}}_{\mathrm{I}\bar{\mathrm{B}}} & \mathbf{K}^{\mathrm{AA}}_{\mathrm{I}\hat{\mathrm{B}}} & \mathbf{0} & \mathbf{0} & \mathbf{0} & \mathbf{K}^{\mathrm{AA}}_{\mathrm{II}} & \mathbf{0} \\
\mathbf{0} & \mathbf{0} & \overset{\mathrm{C}}{\mathbf{K}}{}^{\mathrm{CS}}_{\mathrm{I}\bar{\mathrm{B}}} & \overset{\mathrm{C}}{\mathbf{K}}{}^{\mathrm{CS/CA}}_{\mathrm{I}\hat{\mathrm{B}}} & \overset{\mathrm{C}}{\mathbf{K}}{}^{\mathrm{CS}}_{\mathrm{I}\tilde{\mathrm{B}}} & \mathbf{0} & \overset{\mathrm{C}}{\mathbf{K}}{}^{\mathrm{CF}}_{\mathrm{I}\hat{\mathrm{B}}} & \mathbf{0} & 0
\end{array}\right]^{i}_{n+1}
\left[\begin{array}{c}
\Delta\mathbf{d}_{\mathrm{I}} \\
\Delta\mathbf{d}_{\mathrm{B}} \\
\Delta\mathbf{d}_{\bar{\mathrm{B}}} \\
\Delta\mathbf{d}_{\hat{\mathrm{B}}} \\
\Delta\mathbf{d}_{\tilde{\mathrm{B}}} \\
\Delta\mathbf{u}_{\mathrm{I}} \\
\Delta\mathbf{u}_{\hat{\mathrm{B}}} \\
\Delta\mathbf{d}^{\mathrm{A}}_{\mathrm{I}} \\
\Delta\lambda
\end{array}\right]^{i+1}_{n+1}
= -
\left[\begin{array}{c}
\mathbf{r}^{\mathrm{S}}_{\mathrm{I}} \\
\mathbf{r}^{\mathrm{S}}_{\mathrm{B}} + \underline{\mathbf{r}}^{\mathrm{F}}_{\mathrm{B}} \\
\mathbf{r}^{\mathrm{S}}_{\bar{\mathrm{B}}} + \underline{\mathbf{r}}^{\mathrm{F}}_{\bar{\mathrm{B}}} + \mathbf{r}^{\mathrm{C;S}}_{\bar{\mathrm{B}}} \\
\mathbf{r}^{\mathrm{S}}_{\hat{\mathrm{B}}} \\
\mathbf{r}^{\mathrm{S}}_{\tilde{\mathrm{B}}} + \mathbf{r}^{\mathrm{A}}_{\tilde{\mathrm{B}}} + \mathbf{r}^{\mathrm{C;S}}_{\tilde{\mathrm{B}}} \\
\mathbf{r}^{\mathrm{F}}_{\mathrm{I}} \\
\mathbf{r}^{\mathrm{F}}_{\hat{\mathrm{B}}} + \bar{\mathbf{r}}^{\mathrm{C;F}}_{\hat{\mathrm{B}}} \\
\mathbf{r}^{\mathrm{A}}_{\mathrm{I}} \\
r^{\mathrm{C;C}}_{\mathrm{I}}
\end{array}\right]^{i}_{n+1}
\qquad (5.2.43)
$$

where an overbar denotes scaling with $\frac{1}{\rho^{\mathsf{F}}}$. In contrast to the definitions given in Figure 5.1.1, all solid DOFs not situated along the boundaries are marked by the identifier I. Hence, the distinction of DOFs associated with the resolved airway wall and those in the homogenized domain is dropped for simplicity. Furthermore, several abbreviations for the FSI contributions are introduced in addition to (2.4.8), e.g.

$$\mathbf{K}_{\mathsf{IB}}^{\mathsf{FF/FA}} = \underset{\sim}{\mathbf{K}}_{\mathsf{IB}}^{\mathsf{FF}} + \mathbf{K}_{\mathsf{IB}}^{\mathsf{FA}} = \tau \mathbf{K}_{\mathsf{BB}}^{\mathsf{FF}} + \mathbf{K}_{\mathsf{BB}}^{\mathsf{FA}} \tag{5.2.44}$$

$$\mathbf{K}_{\mathsf{BB}}^{\mathsf{SFA}} = \mathbf{K}_{\mathsf{BB}}^{\mathsf{SS}} + \underline{\mathbf{K}}_{\mathsf{BB}}^{\mathsf{FF/FA}} = \mathbf{K}_{\mathsf{BB}}^{\mathsf{SS}} + \rho^{\mathsf{F}} \mathbf{K}_{\mathsf{BB}}^{\mathsf{FF/FA}}. \tag{5.2.45}$$

Again, the right-hand side vector has to be modified appropriately in the first iteration to account for the history terms in equation (2.4.4).

The Lagrange multiplier can be interpreted as a uniform pressure acting on corresponding boundaries. The contributions of the volume constraint in the FSI system can then be regarded as the resulting nodal forces on the air at the outlet and on the parenchyma block along the enclosing boundary. It is noteworthy that fluid pressure and Lagrange multiplier are not directly coupled at $\hat{\mathsf{B}}$. Instead, the fluid pressure automatically adjusts itself to equilibrate the additional tractions due to the volume constraint. For instance, if the pressure at the outlet would be equal to a given positive pressure at the inlet, no fluid flow would occur in the unconstrained system. However, a positive pressure in general implies a non-zero traction at the outlet. Since the system has to be in equilibrium, the additional forces due to the volume constraint have to equilibrate these tractions, thereby yielding a non-zero Lagrange multiplier. The resulting volume change of the parenchyma block would then directly induce flow in the resolved airway. As a consequence, the outlet pressure would also be adjusted. The above should illustrate conceptually that the solution to the problem is uniquely defined.

In the linear system (5.2.43), the additional constraint equation as well as all linearizations with respect to the Lagrange multiplier are highlighted in yellow. Modified equations of the initial FSI system, i.e. rows in the stiffness matrix and residual vector, are marked in light gray. A comparison with equations (5.1.11)-(5.1.12) reveals that the effect of the volume constraint is similar to that of the static condensation performed in section 5.1.3. Thus, the developed volume coupling approach is deemed suitable for modeling the interplay between airflow in the resolved bronchial tree and parenchyma deformation in an efficient, simplified way.

5.3 Solution techniques

In the previous section, the linearized system for the volume-coupled FSI problem has been derived. Subsequently, the numerical solution of this system will be addressed. After a short introduction to iterative solution techniques in general, a preconditioner developed specifically for the constrained FSI problem will be presented in detail.

5.3.1 General iterative solution procedure

Direct linear solvers, e.g. based on an LU-decomposition of the matrix, are in general not suitable when the system

$$\mathbf{Ax} = \mathbf{f} \tag{5.3.1}$$

is large and sparse. The inevitable “fill-in”, i.e. the replacement of zero matrix entries with non-zero ones during the elimination or factorization process, causes a significant increase in both memory requirements and computation times. Furthermore, the scalability of these solution methods in case of parallel computations is rather poor.

Therefore, usually iterative methods are employed for determining the solution of large and sparse linear systems. Starting with an initial guess $\mathbf{x}^0$, a sequence of solution vectors $\mathbf{x}^k$ is determined that converges towards the exact solution

$$\mathbf{x} = \mathbf{A}^{-1}\mathbf{f}. \tag{5.3.2}$$

The iterative procedure is aborted if

$$\left|\mathbf{r}^{\mathrm{lin};k}\right| = \left|\mathbf{f} - \mathbf{Ax}^k\right| < \epsilon^{\mathrm{lin}} \tag{5.3.3}$$

holds. In this context, $\mathbf{r}^{\mathrm{lin};k}$ denotes the residual of the linear system at iteration k and ϵ^{lin} refers to a user-defined convergence criterion. Consequently, the linear system is solved only approximately. An in-depth overview of available iterative solvers is provided e.g. in Saad (2003).

For the simulations presented in this thesis, an implementation of the generalized minimal residual algorithm – also known as GMRES (Saad and Schulz, 1986) – provided by the AZTEC package (Tuminaro et al., 1999) is employed. This solution method has the property of minimizing for every k the norm of the residual vector $\left|\mathbf{r}^{\mathrm{lin};k}\right|$ over the Krylov subspace given by

$$\mathcal{K}^k\left(\mathbf{A}, \mathbf{r}^{\mathrm{lin};0}\right) = \mathrm{span}\left\{\mathbf{r}^{\mathrm{lin};0}, \mathbf{Ar}^{\mathrm{lin};0}, \mathbf{A}^2\mathbf{r}^{\mathrm{lin};0}, ..., \mathbf{A}^{k-1}\mathbf{r}^{\mathrm{lin};0}\right\} \tag{5.3.4}$$

where $\mathbf{r}^{\mathrm{lin};0}$ is the initial residual.

The convergence behavior of any iterative solver strongly depends on the spectral properties of the system matrix. In this context, the condition number of $\mathbf{A}$ is defined by

$$\bar{\kappa}(\mathbf{A}) = \frac{\bar{\Lambda}_{\mathrm{max}}(\mathbf{A})}{\bar{\Lambda}_{\mathrm{min}}(\mathbf{A})} \tag{5.3.5}$$

with $\bar{\Lambda}_{\mathrm{max}}(\mathbf{A})$, $\bar{\Lambda}_{\mathrm{min}}(\mathbf{A})$ being the maximum and minimum eigenvalue of $\mathbf{A}$, respectively. A small $\bar{\kappa}$ usually implies fast convergence of the linear solver, whereas a large $\bar{\kappa}$ may render the application of an iterative algorithm nearly impossible. To improve its eigenvalue spectrum, the linear system is usually preconditioned by means of suitable linear transformations. For instance, the system (5.3.1) can also be restated as

$$\mathbf{AM}_{\mathrm{R}}^{-1}\mathbf{M}_{\mathrm{R}}\mathbf{x} = \mathbf{f} \tag{5.3.6}$$

where $\mathbf{M}_{\mathsf{R}}$ is an appropriate preconditioning matrix. In this context, the identifier R indicates that equation (5.3.6) involves right (in contrast to left) preconditioning. Subsequent considerations are restricted to this alternative, since it is employed exclusively throughout this work. For determining $\mathbf{x}$, first the intermediate system

$$\left(\mathbf{A}\mathbf{M}_{\mathsf{R}}^{-1}\right)\acute{\mathbf{x}} = \mathbf{f} \tag{5.3.7}$$

is solved iteratively with the GMRES method based on the modified Krylov space

$$\mathcal{K}^{k}_{\mathsf{prec}}\left(\mathbf{A}\mathbf{M}_{\mathsf{R}}^{-1}, \mathbf{r}^{\mathsf{lin;0}}_{\mathsf{prec}}\right) = \mathsf{span}\left\{\mathbf{r}^{\mathsf{lin;0}}_{\mathsf{prec}}, \mathbf{A}\mathbf{M}_{\mathsf{R}}^{-1}\mathbf{r}^{\mathsf{lin;0}}_{\mathsf{prec}}, ..., \left(\mathbf{A}\mathbf{M}_{\mathsf{R}}^{-1}\right)^{k-1}\mathbf{r}^{\mathsf{lin;0}}_{\mathsf{prec}}\right\} \tag{5.3.8}$$

with

$$\mathbf{r}^{\mathsf{lin;0}}_{\mathsf{prec}} = \mathbf{f} - \mathbf{A}\mathbf{M}_{\mathsf{R}}^{-1}\acute{\mathbf{x}}^{0}. \tag{5.3.9}$$

Finally, the original solution can be obtained as

$$\mathbf{x} = \mathbf{M}_{\mathsf{R}}^{-1}\acute{\mathbf{x}}. \tag{5.3.10}$$

From equations (5.3.8)-(5.3.10), it becomes clear that the solution process involves the application of the inverse preconditioning matrix $\mathbf{M}_{\mathsf{R}}^{-1}$ on different vectors. However, $\mathbf{M}_{\mathsf{R}}^{-1}$ is in general not computed explicitly by inverting $\mathbf{M}_{\mathsf{R}}$. Instead, any matrix vector product

$$\mathbf{z} = \mathbf{M}_{\mathsf{R}}^{-1}\mathbf{y} \tag{5.3.11}$$

with arbitrary vectors $\mathbf{z}$ and $\mathbf{y}$ is computed by approximately solving the corresponding linear system

$$\mathbf{M}_{\mathsf{R}}\mathbf{z} = \mathbf{y} \tag{5.3.12}$$

either directly or iteratively. Therefore, the strict distinction between “solver” and “preconditioner” is usually somewhat blurry. In fact, the preconditioner can be interpreted as the actual solver, whereas the Krylov method serves as an accelerator only. Hence, the approximate application of $\mathbf{M}_{\mathsf{R}}^{-1}$ to a vector is subsequently referred to as the solution of the corresponding linear system for simplicity.

Basically, a preconditioner can be any subsidiary approximate solver combined with an outer iteration technique as indicated above. Apart from reducing the condition number of the system matrix, the inverse preconditioning matrix should be easily applicable to a given vector, i.e. solving the linear system (5.3.12) should be as inexpensive as possible, particularly in the parallel case. The specific choice of $\mathbf{M}_{\mathsf{R}}$ is strongly problem dependent. In the following subsection, a preconditioner specifically suitable for the volume-coupled FSI problem will be introduced.

5.3.2 Preconditioner for volume-coupled FSI

The linear problem (5.2.43) corresponds to an unsymmetric saddle point system (cf. also section 2.5.1). A comprehensive review on possible solution methods for this type of problems can be found e.g. in Benzi et al. (2005). Subsequently, a novel preconditioning algorithm will be introduced based on the combination and modification of existing techniques for generalized saddle point problems and monolithic FSI problems.

5.3.2.1 Block preconditioner for saddle point problem

Due to the different characteristics of the involved equations, block preconditioning, i.e. a decomposition into simplified subproblems, seems to be particularly suitable here. An appropriate splitting of the constrained FSI problem is given by

$$\begin{bmatrix} \mathbf{F} & \mathbf{B}^{\mathsf{T}} \\ \hat{\mathbf{B}} & \mathbf{0} \end{bmatrix} \begin{bmatrix} \Delta\mathbf{u} \\ \Delta\boldsymbol{\lambda} \end{bmatrix} = - \begin{bmatrix} \mathbf{r}^{\mathsf{u}} \\ \mathbf{r}^{\lambda} \end{bmatrix} \tag{5.3.13}$$

with the modified FSI matrix

$$\mathbf{F} = \begin{bmatrix}
\mathbf{K}^{\mathsf{SS}}_{\mathsf{II}} & \mathbf{K}^{\mathsf{SS}}_{\mathsf{IB}} & \mathbf{K}^{\mathsf{SS}}_{\mathsf{I\bar{B}}} & \mathbf{K}^{\mathsf{SS}}_{\mathsf{I\hat{B}}} & \mathbf{K}^{\mathsf{SS}}_{\mathsf{I\tilde{B}}} & \mathbf{0} & \mathbf{0} & \mathbf{0} \\
\mathbf{K}^{\mathsf{SS}}_{\mathsf{BI}} & \mathbf{K}^{\mathsf{SFA}}_{\mathsf{BB}} & \mathbf{K}^{\mathsf{SFA}}_{\mathsf{B\bar{B}}} & \mathbf{0} & \mathbf{0} & \underline{\mathbf{K}}^{\mathsf{FF}}_{\mathsf{BI}} & \mathbf{0} & \underline{\mathbf{K}}^{\mathsf{FA}}_{\mathsf{BI}} \\
\mathbf{K}^{\mathsf{SS}}_{\mathsf{\bar{B}I}} & \mathbf{K}^{\mathsf{SFA}}_{\mathsf{\bar{B}B}} & \mathbf{K}^{\mathsf{SFA}}_{\mathsf{\bar{B}\bar{B}}} + \overset{\mathsf{C}}{\mathbf{K}}{}^{\mathsf{SS}}_{\mathsf{\bar{B}\bar{B}}} & \mathbf{K}^{\mathsf{SS}}_{\mathsf{\bar{B}\hat{B}}} + \overset{\mathsf{C}}{\mathbf{K}}{}^{\mathsf{SS}}_{\mathsf{\bar{B}\hat{B}}} + \underline{\mathbf{K}}^{\mathsf{FA}}_{\mathsf{\bar{B}\hat{B}}} & \mathbf{K}^{\mathsf{SS}}_{\mathsf{\bar{B}\tilde{B}}} + \overset{\mathsf{C}}{\mathbf{K}}{}^{\mathsf{SS}}_{\mathsf{\bar{B}\tilde{B}}} & \underline{\mathbf{K}}^{\mathsf{FF}}_{\mathsf{\bar{B}I}} & \underline{\mathbf{K}}^{\mathsf{FF}}_{\mathsf{\bar{B}\hat{B}}} & \underline{\mathbf{K}}^{\mathsf{FA}}_{\mathsf{\bar{B}I}} \\
\mathbf{K}^{\mathsf{SS}}_{\mathsf{\hat{B}I}} & \mathbf{0} & \mathbf{K}^{\mathsf{SS}}_{\mathsf{\hat{B}\bar{B}}} & \mathbf{K}^{\mathsf{SS}}_{\mathsf{\hat{B}\hat{B}}} & \mathbf{0} & \mathbf{0} & \mathbf{0} & \mathbf{0} \\
\mathbf{K}^{\mathsf{SS}}_{\mathsf{\tilde{B}I}} & \mathbf{0} & \mathbf{K}^{\mathsf{SS}}_{\mathsf{\tilde{B}\bar{B}}} + \overset{\mathsf{C}}{\mathbf{K}}{}^{\mathsf{SS}}_{\mathsf{\tilde{B}\bar{B}}} & \mathbf{0} & \mathbf{K}^{\mathsf{SS}}_{\mathsf{\tilde{B}\tilde{B}}} + \overset{\mathsf{C}}{\mathbf{K}}{}^{\mathsf{SS}}_{\mathsf{\tilde{B}\tilde{B}}} & \mathbf{0} & \mathbf{0} & \mathbf{0} \\
\mathbf{0} & \mathbf{K}^{\mathsf{FF/FA}}_{\mathsf{IB}} & \mathbf{K}^{\mathsf{FF/FA}}_{\mathsf{I\bar{B}}} & \mathbf{K}^{\mathsf{FA}}_{\mathsf{I\hat{B}}} & \mathbf{0} & \mathbf{K}^{\mathsf{FF}}_{\mathsf{II}} & \mathbf{K}^{\mathsf{FF}}_{\mathsf{I\hat{B}}} & \mathbf{K}^{\mathsf{FA}}_{\mathsf{II}} \\
\mathbf{0} & \mathbf{0} & \mathbf{K}^{\mathsf{FF/FA}}_{\mathsf{\hat{B}\bar{B}}} + \overset{\mathsf{C}}{\overline{\mathbf{K}}}{}^{\mathsf{FA}}_{\mathsf{\hat{B}\bar{B}}} & \overset{\mathsf{C}}{\overline{\mathbf{K}}}{}^{\mathsf{FA}}_{\mathsf{\hat{B}\hat{B}}} + \mathbf{K}^{\mathsf{FA}}_{\mathsf{\hat{B}\hat{B}}} & \mathbf{0} & \mathbf{K}^{\mathsf{FF}}_{\mathsf{\hat{B}I}} & \mathbf{K}^{\mathsf{FF}}_{\mathsf{\hat{B}\hat{B}}} & \mathbf{K}^{\mathsf{FA}}_{\mathsf{\hat{B}I}} \\
\mathbf{0} & \mathbf{K}^{\mathsf{AA}}_{\mathsf{IB}} & \mathbf{K}^{\mathsf{AA}}_{\mathsf{I\bar{B}}} & \mathbf{K}^{\mathsf{AA}}_{\mathsf{I\hat{B}}} & \mathbf{0} & \mathbf{0} & \mathbf{0} & \mathbf{K}^{\mathsf{AA}}_{\mathsf{II}}
\end{bmatrix}, \tag{5.3.14}$$

the constraint “coupling” matrices

$$\mathbf{B}^{\mathsf{T}} = \begin{bmatrix} \mathbf{0} \\ \mathbf{0} \\ \overset{\mathsf{C}}{\mathbf{K}}{}^{\mathsf{SC}}_{\mathsf{\bar{B}I}} \\ \mathbf{0} \\ \overset{\mathsf{C}}{\mathbf{K}}{}^{\mathsf{SC}}_{\mathsf{\tilde{B}I}} \\ \mathbf{0} \\ \overset{\mathsf{C}}{\overline{\mathbf{K}}}{}^{\mathsf{FC}}_{\mathsf{\hat{B}I}} \\ \mathbf{0} \end{bmatrix}, \qquad \hat{\mathbf{B}} = \begin{bmatrix} \mathbf{0} & \mathbf{0} & \overset{\mathsf{C}}{\mathbf{K}}{}^{\mathsf{CS}}_{\mathsf{I\bar{B}}} & \overset{\mathsf{C}}{\mathbf{K}}{}^{\mathsf{CS/CA}}_{\mathsf{I\hat{B}}} & \overset{\mathsf{C}}{\mathbf{K}}{}^{\mathsf{CS}}_{\mathsf{I\tilde{B}}} & \mathbf{0} & \overset{\mathsf{C}}{\mathbf{K}}{}^{\mathsf{CF}}_{\mathsf{I\hat{B}}} & \mathbf{0} \end{bmatrix}, \tag{5.3.15}$$

the modified FSI residual and vector of unknowns

$$\mathbf{r}^{\mathrm{u}} = \begin{bmatrix} \mathbf{r}_{\mathrm{I}}^{\mathrm{S}} \\ \mathbf{r}_{\mathrm{B}}^{\mathrm{S}} + \underline{\mathbf{r}}_{\mathrm{B}}^{\mathrm{F}} \\ \mathbf{r}_{\bar{\mathrm{B}}}^{\mathrm{S}} + \underline{\mathbf{r}}_{\bar{\mathrm{B}}}^{\mathrm{F}} + \mathbf{r}_{\bar{\mathrm{B}}}^{\mathrm{C;S}} \\ \mathbf{r}_{\hat{\mathrm{B}}}^{\mathrm{S}} \\ \mathbf{r}_{\tilde{\mathrm{B}}}^{\mathrm{S}} + \mathbf{r}_{\tilde{\mathrm{B}}}^{\mathrm{A}} + \mathbf{r}_{\tilde{\mathrm{B}}}^{\mathrm{C;S}} \\ \mathbf{r}_{\mathrm{I}}^{\mathrm{F}} \\ \mathbf{r}_{\hat{\mathrm{B}}}^{\mathrm{F}} + \bar{\mathbf{r}}_{\hat{\mathrm{B}}}^{\mathrm{C;F}} \\ \mathbf{r}_{\mathrm{I}}^{\mathrm{A}} \end{bmatrix}, \qquad \Delta\mathbf{u} = \begin{bmatrix} \Delta\mathbf{d}_{\mathrm{I}} \\ \Delta\mathbf{d}_{\mathrm{B}} \\ \Delta\mathbf{d}_{\bar{\mathrm{B}}} \\ \Delta\mathbf{d}_{\hat{\mathrm{B}}} \\ \Delta\mathbf{d}_{\tilde{\mathrm{B}}} \\ \Delta\mathbf{u}_{\mathrm{I}} \\ \Delta\mathbf{u}_{\hat{\mathrm{B}}} \\ \Delta\mathbf{d}_{\mathrm{I}}^{\mathrm{A}} \end{bmatrix} \tag{5.3.16}$$

and the constraint residual $\mathbf{r}^{\lambda} = \mathbf{r}_{\mathrm{I}}^{\mathrm{C;C}}$. In contrast to equation (5.2.43), the constrained FSI problem is now set up for the case of multiple outlets and associated parenchyma blocks. In this case, each pair of outlet and tissue block requires the introduction of a volume constraint condition enforced by an additional Lagrange multiplier. Hence, the scalar Lagrange multiplier λ and constraint residual $\mathrm{r}_{\mathrm{I}}^{\mathrm{C;C}}$ in equation (5.2.43) are replaced by their corresponding vectorial counterparts $\boldsymbol{\lambda}$ and $\mathbf{r}_{\mathrm{I}}^{\mathrm{C;C}}$, respectively. For simplicity, identifiers for the current time and nonlinear iteration step are omitted here and in the following.

A well-established block preconditioner for this type of linear system is the semi-implicit method for pressure-linked equations (SIMPLE), which was proposed by Caretto et al. (1972) and Patankar and Spalding (1972) for the Navier-Stokes equations. SIMPLE is based on solving the linear system (5.3.13) approximately by a cyclic series of guess-and-correct operations. The corresponding preconditioning matrix is chosen as the following incomplete factorization of the original Jacobian

$$\begin{aligned} \mathbf{A} = \begin{bmatrix} \mathbf{F} & \mathbf{B}^{\mathrm{T}} \\ \hat{\mathbf{B}} & \mathbf{0} \end{bmatrix} &\approx \begin{bmatrix} \mathbf{I} & \mathbf{0} \\ \hat{\mathbf{B}}\mathbf{F}^{-1} & \mathbf{I} \end{bmatrix} \begin{bmatrix} \mathbf{F} & \mathbf{0} \\ \mathbf{0} & -\hat{\mathbf{S}} \end{bmatrix} \begin{bmatrix} \mathbf{I} & \mathbf{D}^{-1}\mathbf{B}^{\mathrm{T}} \\ \mathbf{0} & \frac{1}{\alpha}\mathbf{I} \end{bmatrix} = \\ &= \underbrace{\begin{bmatrix} \mathbf{F} & \mathbf{0} \\ \hat{\mathbf{B}} & -\hat{\mathbf{S}} \end{bmatrix}}_{\mathbf{M}_{\mathrm{R};1}} \underbrace{\begin{bmatrix} \mathbf{I} & \mathbf{D}^{-1}\mathbf{B}^{\mathrm{T}} \\ \mathbf{0} & \frac{1}{\alpha}\mathbf{I} \end{bmatrix}}_{\mathbf{M}_{\mathrm{R};2}} = \mathbf{M}_{\mathrm{R}}. \end{aligned} \tag{5.3.17}$$

In this context, the matrix $\mathbf{D}$ contains the entries of the modified FSI matrix $\mathbf{F}$ on the main diagonal, i.e.

$$\mathbf{D} = \mathrm{diag}(\mathbf{F}) \tag{5.3.18}$$

and $\hat{\mathbf{S}}$ refers to the approximate Schur complement

$$\hat{\mathbf{S}} = \hat{\mathbf{B}}\mathbf{D}^{-1}\mathbf{B}^{\mathrm{T}}. \tag{5.3.19}$$

$\alpha \in (0,1]$ serves as a damping parameter as will become clear later on.

The preconditioning process now involves application of $\mathbf{M}_{\mathrm{R}}^{-1}$ on different vectors. As already mentioned in the previous section, this basically implies the solution of a linear system. For simplicity, subsequent derivations are made with respect to an abstract vector $\mathbf{y}$ representing either a vector of the hitherto existing Krylov space (5.3.8) or the intermediate solution vector in equation (5.3.10). The corresponding linear system (5.3.12) can then be solved by means of a stationary iteration, i.e.

$$\mathbf{z}^{j+1} = \mathbf{z}^{j} + \mathbf{M}_{\mathrm{R}}^{-1}\left(\mathbf{y} - \mathbf{A}\mathbf{z}^{j}\right). \tag{5.3.20}$$

Although not representing the solution and right-hand side vector of the original system (5.3.13), the vectors $\mathbf{z}$ and $\mathbf{y}$ can also be split into an FSI and a constraint part. Hence, the detailed version of equation (5.3.20) reads

$$\begin{bmatrix} \mathbf{z}^{\mathrm{u};j+1} \\ \mathbf{z}^{\lambda;j+1} \end{bmatrix} = \begin{bmatrix} \mathbf{z}^{\mathrm{u};j} \\ \mathbf{z}^{\lambda;j} \end{bmatrix} + \mathbf{M}_{\mathrm{R}}^{-1}\left(\begin{bmatrix} \mathbf{y}^{\mathrm{u}} \\ \mathbf{y}^{\lambda} \end{bmatrix} - \begin{bmatrix} \mathbf{F} & \mathbf{B}^{\mathrm{T}} \\ \hat{\mathbf{B}} & \mathbf{0} \end{bmatrix}\begin{bmatrix} \mathbf{z}^{\mathrm{u};j} \\ \mathbf{z}^{\lambda;j} \end{bmatrix}\right). \tag{5.3.21}$$

Defining now the increment of the solution vector and the residual of the linear system

$$\Delta\mathbf{z}^{j+1} = \begin{bmatrix} \mathbf{z}^{\mathrm{u};j+1} \\ \mathbf{z}^{\lambda;j+1} \end{bmatrix} - \begin{bmatrix} \mathbf{z}^{\mathrm{u};j} \\ \mathbf{z}^{\lambda;j} \end{bmatrix} = \begin{bmatrix} \Delta\mathbf{z}^{\mathrm{u};j+1} \\ \Delta\mathbf{z}^{\lambda;j+1} \end{bmatrix}, \tag{5.3.22}$$

$$\mathbf{r}^{\mathrm{lin}} = \begin{bmatrix} \mathbf{y}^{\mathrm{u}} \\ \mathbf{y}^{\lambda} \end{bmatrix} - \begin{bmatrix} \mathbf{F} & \mathbf{B}^{\mathrm{T}} \\ \hat{\mathbf{B}} & \mathbf{0} \end{bmatrix}\begin{bmatrix} \mathbf{z}^{\mathrm{u};j} \\ \mathbf{z}^{\lambda;j} \end{bmatrix} \tag{5.3.23}$$

allows to restate the stationary iteration (5.3.21) in terms of the following linear problem

$$\mathbf{M}_{\mathrm{R};1}\mathbf{M}_{\mathrm{R};2}\Delta\mathbf{z}^{j+1} = \mathbf{r}^{\mathrm{lin}}. \tag{5.3.24}$$

Here, the decomposition of the preconditioning matrix given in equation (5.3.17) is utilized. The solution of the linear system (5.3.24) can be obtained in two consecutive steps. First, the simplified system

$$\mathbf{M}_{\mathrm{R};1}\Delta\tilde{\mathbf{z}}^{j+1} = \mathbf{r}^{\mathrm{lin}} \tag{5.3.25}$$

is solved for the intermediate increment

$$\Delta\tilde{\mathbf{z}}^{j+1} = \mathbf{M}_{\mathrm{R};2}\Delta\mathbf{z}^{j+1}. \tag{5.3.26}$$

Inserting equations (5.3.17) and (5.3.23) into the simplified system (5.3.25) then yields

$$\begin{bmatrix} \mathbf{F} & \mathbf{0} \\ \hat{\mathbf{B}} & -\hat{\mathbf{S}} \end{bmatrix}\begin{bmatrix} \Delta\tilde{\mathbf{z}}^{\mathrm{u};j+1} \\ \Delta\tilde{\mathbf{z}}^{\lambda;j+1} \end{bmatrix} = \begin{bmatrix} \mathbf{y}^{\mathrm{u}} - \mathbf{F}\mathbf{z}^{\mathrm{u};j} - \mathbf{B}^{\mathrm{T}}\mathbf{z}^{\lambda;j} \\ \mathbf{y}^{\lambda} - \hat{\mathbf{B}}\mathbf{z}^{\mathrm{u};j} \end{bmatrix}. \tag{5.3.27}$$

Due to the chosen decomposition of the preconditioner, FSI and constraint DOFs are decoupled in the first block of equations. Therefore, the FSI part of the problem given by

$$\mathbf{F}\mathbf{z}^{\mathrm{u};j+\frac{1}{2}} = \mathbf{y}^{\mathrm{u}} - \mathbf{B}^{\mathrm{T}}\mathbf{z}^{\lambda;j} \tag{5.3.28}$$

can be treated separately. In this context, the intermediate FSI solution vector $\mathbf{z}^{\mathrm{u};j+\frac{1}{2}}$ satisfies the first block of equations for a given vector $\mathbf{z}^{\lambda;j}$ and is defined by

$$\mathbf{z}^{\mathrm{u};j+\frac{1}{2}} = \mathbf{z}^{\mathrm{u};j} + \Delta\tilde{\mathbf{z}}^{\mathrm{u};j+1}. \tag{5.3.29}$$

The actual solution of equation (5.3.28) will be discussed in more detail in section 5.3.2.2. Thus, for the time being, the focus remains on the SIMPLE procedure.

As a next step, the intermediate constraint increment is calculated from the second block of equations representing the imposed constraint conditions. Moving the summand involving the known intermediate FSI increment vector $\Delta\tilde{\mathbf{z}}^{\mathrm{u};j+1}$ to the right-hand side, the second part of equation (5.3.27) reads

$$-\hat{\mathbf{S}}\Delta\tilde{\mathbf{z}}^{\lambda;j+1} = \mathbf{y}^{\lambda} - \hat{\mathbf{B}}\left(\mathbf{z}^{\mathrm{u};j} + \Delta\tilde{\mathbf{z}}^{\mathrm{u};j+1}\right). \tag{5.3.30}$$

After introduction of the intermediate FSI solution vector (5.3.29), the following linear problem is obtained

$$\hat{\mathbf{S}}\Delta\tilde{\mathbf{z}}^{\lambda;j+1} = -\mathbf{y}^{\lambda} + \hat{\mathbf{B}}\mathbf{z}^{\mathrm{u};j+\frac{1}{2}}. \tag{5.3.31}$$

The size of the above linear system depends on the number of airway outlets and associated parenchyma regions in the simulation model. In general, the number of constraints involved is rather small so that the application of a direct solver like UMFPACK (see Davis and Duff (1997) for details) is acceptable.

Since both blocks of $\Delta\tilde{\mathbf{z}}^{j+1}$ are known now, the actual increment vector $\Delta\mathbf{z}^{j+1}$ can be determined from equation (5.3.26), i.e.

$$\begin{bmatrix} \mathbf{I} & \mathbf{D}^{-1}\mathbf{B}^{\mathrm{T}} \\ \mathbf{0} & \frac{1}{\alpha}\mathbf{I} \end{bmatrix} \begin{bmatrix} \Delta\mathbf{z}^{\mathrm{u};j+1} \\ \Delta\mathbf{z}^{\lambda;j+1} \end{bmatrix} = \begin{bmatrix} \Delta\tilde{\mathbf{z}}^{\mathrm{u};j+1} \\ \Delta\tilde{\mathbf{z}}^{\lambda;j+1} \end{bmatrix}. \tag{5.3.32}$$

Hence, the constraint increment vector simply equates to

$$\Delta\mathbf{z}^{\lambda;j+1} = \alpha\Delta\tilde{\mathbf{z}}^{\lambda;j+1}. \tag{5.3.33}$$

Accordingly, the corresponding solution vector reads

$$\mathbf{z}^{\lambda;j+1} = \mathbf{z}^{\lambda;j} + \Delta\mathbf{z}^{\lambda;j+1} = \mathbf{z}^{\lambda;j} + \alpha\Delta\tilde{\mathbf{z}}^{\lambda;j+1} \tag{5.3.34}$$

where $\alpha \in (0,1]$ can now be easily interpreted as a relaxation parameter in the update of the constraint part of $\mathbf{z}^{j+1}$. Unfortunately, an appropriate α can only be found by trial and error. According to Rehman et al. (2009), however, a good choice for this parameter is more important when SIMPLE is employed as a stand-alone iterative solver than when it is used as a preconditioner.

The constraint increment vector (5.3.33) can be introduced into the first block of equation (5.3.32), i.e.

$$\begin{aligned} \Delta\mathbf{z}^{\mathrm{u};j+1} &= \Delta\tilde{\mathbf{z}}^{\mathrm{u};j+1} - \mathbf{D}^{-1}\mathbf{B}^{\mathrm{T}}\Delta\mathbf{z}^{\lambda;j+1} = \\ &= \Delta\tilde{\mathbf{z}}^{\mathrm{u};j+1} - \alpha\mathbf{D}^{-1}\mathbf{B}^{\mathrm{T}}\Delta\tilde{\mathbf{z}}^{\lambda;j+1}. \end{aligned} \tag{5.3.35}$$

Algorithm 5.1 SIMPLE procedure employed as preconditioner for the volume-coupled FSI problem.

```
for each iteration $j$:
    FSI part:
        Solve (5.3.28) for the intermediate FSI solution vector $\mathbf{z}^{\mathrm{u};j+\frac{1}{2}}$ (cf. Algorithm 5.2)
    Constraint part:
        Solve (5.3.31) for the intermediate constraint increment vector $\Delta\tilde{\mathbf{z}}^{\lambda;j+1}$
        Calculate the new constraint solution vector $\mathbf{z}^{\lambda;j+1}$ (5.3.34)
        Compute the new FSI solution vector $\mathbf{z}^{\mathrm{u};j+1}$ (5.3.37)
```

The FSI solution vector is then given by

$$\mathbf{z}^{\mathrm{u};j+1} = \mathbf{z}^{\mathrm{u};j} + \Delta\mathbf{z}^{\mathrm{u};j+1} \tag{5.3.36}$$

or, using the intermediate FSI solution vector (5.3.29),

$$\mathbf{z}^{\mathrm{u};j+1} = \mathbf{z}^{\mathrm{u};j+\frac{1}{2}} - \alpha\mathbf{D}^{-1}\mathbf{B}^{\mathrm{T}}\Delta\tilde{\mathbf{z}}^{\lambda;j+1}. \tag{5.3.37}$$

At this point, the current overall solution vector $\mathbf{z}^{j+1}$ is completely known and can be used as a starting point for the next iteration.

In summary, one SIMPLE iteration consists of two basic steps (cf. also Algorithm 5.1). Initially, a new intermediate FSI solution vector $\mathbf{z}^{\mathrm{u};j+\frac{1}{2}}$ is determined from the first block of equations using the old constraint solution vector $\mathbf{z}^{\lambda;j}$. Since $\mathbf{z}^{\mathrm{u};j+\frac{1}{2}}$ does not satisfy the imposed constraint conditions, the second block of equations is then utilized to adjust the constraint solution vector $\mathbf{z}^{\lambda;j+1}$. Based on that, the new FSI solution vector $\mathbf{z}^{\mathrm{u};j+1}$ can be calculated in a straightforward manner.

The SIMPLEC preconditioner is an alternative to the classical SIMPLE procedure that can be easily implemented once the general framework is set up. In this case, the diagonal approximation $\mathbf{D}$ of the modified FSI matrix $\mathbf{F}$ is replaced with a diagonal matrix $\tilde{\mathbf{D}}$ whose entries contain the absolute values of the row sums of $\mathbf{F}$. According to Elman et al. (2008), this choice is more effective than the classical one since $\tilde{\mathbf{D}}$ provides a better approximation to $\mathbf{F}$.

Because the different blocks of $\mathbf{z}$ are calculated successively, the SIMPLE(C) algorithm is characterized by a high flexibility with regard to the underlying solution methods. As already mentioned, for the constraint part (5.3.31), a direct solution method is utilized. The solver employed for the FSI part will now be presented in more detail.

5.3.2.2 Block preconditioner for FSI problem

The determination of the intermediate FSI vector involves the solution of the following linear system (cf. equation (5.3.28))

$$\mathbf{F}\mathbf{z}^{\mathrm{u};j+\frac{1}{2}} = \mathbf{y}^{\mathrm{u}} - \mathbf{B}^{\mathrm{T}}\mathbf{z}^{\lambda;j}. \tag{5.3.38}$$

In this context, the modified FSI matrix $\mathbf{F}$ reads

$$
\mathbf{F} = \left[\begin{array}{ccccc|c|cc}
\mathbf{K}^{\mathsf{SS}}_{\mathsf{II}} & \mathbf{K}^{\mathsf{SS}}_{\mathsf{IB}} & \mathbf{K}^{\mathsf{SS}}_{\mathsf{I\bar{B}}} & \mathbf{K}^{\mathsf{SS}}_{\mathsf{I\hat{B}}} & \mathbf{K}^{\mathsf{SS}}_{\mathsf{I\tilde{B}}} & \mathbf{0} & \mathbf{0} & \mathbf{0} \\
\mathbf{K}^{\mathsf{SS}}_{\mathsf{BI}} & \mathbf{K}^{\mathsf{SFA}}_{\mathsf{BB}} & \mathbf{K}^{\mathsf{SFA}}_{\mathsf{B\bar{B}}} & \mathbf{0} & \mathbf{0} & \underline{\mathbf{K}}^{\mathsf{FA}}_{\mathsf{BI}} & \underline{\mathbf{K}}^{\mathsf{FF}}_{\mathsf{BI}} & \mathbf{0} \\
\mathbf{K}^{\mathsf{SS}}_{\mathsf{\bar{B}I}} & \mathbf{K}^{\mathsf{SFA}}_{\mathsf{\bar{B}B}} & \mathbf{K}^{\mathsf{SFA}}_{\mathsf{\bar{B}\bar{B}}} + \overset{\mathsf{C}}{\mathbf{K}}{}^{\mathsf{SS}}_{\mathsf{\bar{B}\bar{B}}} & \mathbf{K}^{\mathsf{SS}}_{\mathsf{\bar{B}\hat{B}}} + \overset{\mathsf{C}}{\mathbf{K}}{}^{\mathsf{SS}}_{\mathsf{\bar{B}\hat{B}}} + \underline{\mathbf{K}}^{\mathsf{FA}}_{\mathsf{\bar{B}\hat{B}}} & \mathbf{K}^{\mathsf{SS}}_{\mathsf{\bar{B}\tilde{B}}} + \overset{\mathsf{C}}{\mathbf{K}}{}^{\mathsf{SS}}_{\mathsf{\bar{B}\tilde{B}}} & \underline{\mathbf{K}}^{\mathsf{FA}}_{\mathsf{\bar{B}I}} & \underline{\mathbf{K}}^{\mathsf{FF}}_{\mathsf{\bar{B}I}} & \underline{\mathbf{K}}^{\mathsf{FF}}_{\mathsf{\bar{B}\hat{B}}} \\
\mathbf{K}^{\mathsf{SS}}_{\mathsf{\hat{B}I}} & \mathbf{0} & \mathbf{K}^{\mathsf{SS}}_{\mathsf{\hat{B}\bar{B}}} & \mathbf{K}^{\mathsf{SS}}_{\mathsf{\hat{B}\hat{B}}} & \mathbf{0} & \mathbf{0} & \mathbf{0} & \mathbf{0} \\
\mathbf{K}^{\mathsf{SS}}_{\mathsf{\tilde{B}I}} & \mathbf{0} & \mathbf{K}^{\mathsf{SS}}_{\mathsf{\tilde{B}\bar{B}}} + \overset{\mathsf{C}}{\mathbf{K}}{}^{\mathsf{SS}}_{\mathsf{\tilde{B}\bar{B}}} & \mathbf{0} & \mathbf{K}^{\mathsf{SS}}_{\mathsf{\tilde{B}\tilde{B}}} + \overset{\mathsf{C}}{\mathbf{K}}{}^{\mathsf{SS}}_{\mathsf{\tilde{B}\tilde{B}}} & \mathbf{0} & \mathbf{0} & \mathbf{0} \\
\hline
\mathbf{0} & \mathbf{K}^{\mathsf{AA}}_{\mathsf{IB}} & \mathbf{K}^{\mathsf{AA}}_{\mathsf{I\bar{B}}} & \mathbf{K}^{\mathsf{AA}}_{\mathsf{I\hat{B}}} & \mathbf{0} & \mathbf{K}^{\mathsf{AA}}_{\mathsf{II}} & \mathbf{0} & \mathbf{0} \\
\hline
\mathbf{0} & \mathbf{K}^{\mathsf{FF/FA}}_{\mathsf{IB}} & \mathbf{K}^{\mathsf{FA/FF}}_{\mathsf{I\bar{B}}} & \mathbf{K}^{\mathsf{FA}}_{\mathsf{I\hat{B}}} & \mathbf{0} & \mathbf{K}^{\mathsf{FA}}_{\mathsf{II}} & \mathbf{K}^{\mathsf{FF}}_{\mathsf{II}} & \mathbf{K}^{\mathsf{FF}}_{\mathsf{I\hat{B}}} \\
\mathbf{0} & \mathbf{0} & \mathbf{K}^{\mathsf{FF/FA}}_{\mathsf{\hat{B}\bar{B}}} + \overset{\mathsf{C}}{\overline{\mathbf{K}}}{}^{\mathsf{FA}}_{\mathsf{\hat{B}\bar{B}}} & \overset{\mathsf{C}}{\overline{\mathbf{K}}}{}^{\mathsf{FA}}_{\mathsf{\hat{B}\hat{B}}} + \mathbf{K}^{\mathsf{FA}}_{\mathsf{\hat{B}\hat{B}}} & \mathbf{0} & \mathbf{K}^{\mathsf{FA}}_{\mathsf{\hat{B}I}} & \mathbf{K}^{\mathsf{FF}}_{\mathsf{\hat{B}I}} & \mathbf{K}^{\mathsf{FF}}_{\mathsf{\hat{B}\hat{B}}}
\end{array} \right]
\tag{5.3.39}
$$

where the dashed lines indicate the partitioning of the matrix into blocks representing the solid, ALE, and fluid fields. Hence, after introduction of some appropriate abbreviations, $\mathbf{F}$ can be simply restated as

$$
\mathbf{F} = \begin{bmatrix} \mathbf{F}^{\mathsf{SS}} & \mathbf{F}^{\mathsf{SA}} & \mathbf{F}^{\mathsf{SF}} \\ \mathbf{F}^{\mathsf{AS}} & \mathbf{F}^{\mathsf{AA}} & \mathbf{0} \\ \mathbf{F}^{\mathsf{FS}} & \mathbf{F}^{\mathsf{FA}} & \mathbf{F}^{\mathsf{FF}} \end{bmatrix}. \tag{5.3.40}
$$

It is noteworthy that the order of equation blocks has been changed here in preparation for the solution process. Accordingly, the constraint coupling matrix as well as the FSI solution and right-hand side vectors can be split into field-specific components, i.e.

$$
\mathbf{B}^{\mathsf{T}} = \left[\begin{array}{ccccc|c|cc} \mathbf{0} & \mathbf{0} & \overset{\mathsf{C}}{\mathbf{K}}{}^{\mathsf{SC}}_{\mathsf{\bar{B}I}} & \mathbf{0} & \overset{\mathsf{C}}{\mathbf{K}}{}^{\mathsf{SC}}_{\mathsf{\tilde{B}I}} & \mathbf{0} & \mathbf{0} & \overset{\mathsf{C}}{\overline{\mathbf{K}}}{}^{\mathsf{FC}}_{\mathsf{\hat{B}I}} \end{array} \right]^{\mathsf{T}} = \begin{bmatrix} \mathbf{B}^{\mathsf{T;S}} \\ \mathbf{0} \\ \mathbf{B}^{\mathsf{T;F}} \end{bmatrix}, \tag{5.3.41}
$$

and

$$
\mathbf{z}^{\mathsf{u};j+\frac{1}{2}} = \left[\begin{array}{c} \mathbf{z}^{\mathsf{u;S}}_{\mathsf{I}} \\ \mathbf{z}^{\mathsf{u;S}}_{\mathsf{B}} \\ \mathbf{z}^{\mathsf{u;S}}_{\mathsf{\bar{B}}} \\ \mathbf{z}^{\mathsf{u;S}}_{\mathsf{\hat{B}}} \\ \mathbf{z}^{\mathsf{u;S}}_{\mathsf{\tilde{B}}} \\ \hline \mathbf{z}^{\mathsf{u;A}}_{\mathsf{I}} \\ \hline \mathbf{z}^{\mathsf{u;F}}_{\mathsf{I}} \\ \mathbf{z}^{\mathsf{u;F}}_{\mathsf{\hat{B}}} \end{array} \right]^{j+\frac{1}{2}} = \begin{bmatrix} \mathbf{z}^{\mathsf{u;S}} \\ \mathbf{z}^{\mathsf{u;A}} \\ \mathbf{z}^{\mathsf{u;F}} \end{bmatrix}^{j+\frac{1}{2}}, \qquad \mathbf{y}^{\mathsf{u}} = \left[\begin{array}{c} \mathbf{y}^{\mathsf{u;S}}_{\mathsf{I}} \\ \mathbf{y}^{\mathsf{u;S}}_{\mathsf{B}} \\ \mathbf{y}^{\mathsf{u;S}}_{\mathsf{\bar{B}}} \\ \mathbf{y}^{\mathsf{u;S}}_{\mathsf{\hat{B}}} \\ \mathbf{y}^{\mathsf{u;S}}_{\mathsf{\tilde{B}}} \\ \hline \mathbf{y}^{\mathsf{u;A}}_{\mathsf{I}} \\ \hline \mathbf{y}^{\mathsf{u;F}}_{\mathsf{I}} \\ \mathbf{y}^{\mathsf{u;F}}_{\mathsf{\hat{B}}} \end{array} \right] = \begin{bmatrix} \mathbf{y}^{\mathsf{u;S}} \\ \mathbf{y}^{\mathsf{u;A}} \\ \mathbf{y}^{\mathsf{u;F}} \end{bmatrix}. \tag{5.3.42}
$$

Since the determination of $\mathbf{z}^{\mathsf{u};j+\frac{1}{2}}$ is part of the preconditioning process, the linear problem

(5.3.38) is solved only approximately. Therefore, a block preconditioning technique as proposed by Küttler (2009) and Küttler et al. (2010) can be adopted here. This approach has proven to be very convenient for complex monolithic FSI problems. Starting point is the following decomposition of the block system matrix

$$\mathbf{F} = \mathbf{L} + \mathbf{D} + \mathbf{U} \tag{5.3.43}$$

with

$$\mathbf{L} = \begin{bmatrix} \mathbf{0} & \mathbf{0} & \mathbf{0} \\ \mathbf{F}^{\mathsf{AS}} & \mathbf{0} & \mathbf{0} \\ \mathbf{F}^{\mathsf{FS}} & \mathbf{F}^{\mathsf{FA}} & \mathbf{0} \end{bmatrix}, \qquad \mathbf{D} = \begin{bmatrix} \mathbf{F}^{\mathsf{SS}} & \mathbf{0} & \mathbf{0} \\ \mathbf{0} & \mathbf{F}^{\mathsf{AA}} & \mathbf{0} \\ \mathbf{0} & \mathbf{0} & \mathbf{F}^{\mathsf{FF}} \end{bmatrix}, \qquad \mathbf{U} = \begin{bmatrix} \mathbf{0} & \mathbf{F}^{\mathsf{SA}} & \mathbf{F}^{\mathsf{SF}} \\ \mathbf{0} & \mathbf{0} & \mathbf{0} \\ \mathbf{0} & \mathbf{0} & \mathbf{0} \end{bmatrix}. \tag{5.3.44}$$

being the lower, diagonal, and upper matrix, respectively. The intermediate FSI solution vector is computed using a relaxed Gauss-Seidel method as e.g. described in Saad (2003). The application of this procedure – which is also known as successive overrelaxation (SOR) – to the linear system (5.3.38) yields

$$(\mathbf{D} + \omega\mathbf{L})\,\mathbf{z}^{\mathsf{u};j+\frac{1}{2};l+1} + (\omega\mathbf{U} - (1-\omega)\,\mathbf{D})\,\mathbf{z}^{\mathsf{u};j+\frac{1}{2};l} = \omega\Big(\mathbf{y}^{\mathsf{u}} - \mathbf{B}^{\mathsf{T}}\mathbf{z}^{\lambda;j}\Big) \tag{5.3.45}$$

where l denotes the Gauss-Seidel iteration counter and $\omega \in (0,2)$ refers to a constant relaxation parameter. After some restructuring, equation (5.3.45) reads

$$\begin{aligned} \mathbf{z}^{\mathsf{u};j+\frac{1}{2};l+1} &= (\mathbf{D} + \omega\mathbf{L})^{-1}\Big(\omega\Big(\mathbf{y}^{\mathsf{u}} - \mathbf{B}^{\mathsf{T}}\mathbf{z}^{\lambda;j}\Big) + ((1-\omega)\,\mathbf{D} - \omega\mathbf{U})\,\mathbf{z}^{\mathsf{u};j+\frac{1}{2};l}\Big) = \\ &= (\mathbf{D} + \omega\mathbf{L})^{-1}\Big(\omega\Big(\mathbf{y}^{\mathsf{u}} - \mathbf{B}^{\mathsf{T}}\mathbf{z}^{\lambda;j}\Big) - \omega(\mathbf{L} + \mathbf{D} + \mathbf{U})\,\mathbf{z}^{\mathsf{u};j+\frac{1}{2};l} + (\mathbf{D} + \omega\mathbf{L})\,\mathbf{z}^{\mathsf{u};j+\frac{1}{2};l}\Big) = \\ &= \mathbf{z}^{\mathsf{u};j+\frac{1}{2};l} + \omega(\mathbf{D} + \omega\mathbf{L})^{-1}\Big(\mathbf{y}^{\mathsf{u}} - \mathbf{B}^{\mathsf{T}}\mathbf{z}^{\lambda;j} - \mathbf{F}\mathbf{z}^{\mathsf{u};j+\frac{1}{2};l}\Big). \end{aligned} \tag{5.3.46}$$

Introduction of the iteration residual

$$\begin{aligned} &\bar{\mathbf{r}}^{\mathsf{u};j+\frac{1}{2};l} = \begin{bmatrix} \bar{\mathbf{r}}^{\mathsf{u;S}} \\ \bar{\mathbf{r}}^{\mathsf{u;A}} \\ \bar{\mathbf{r}}^{\mathsf{u;F}} \end{bmatrix}^{j+\frac{1}{2};l} = \\ &= \begin{bmatrix} \mathbf{y}^{\mathsf{u;S}} - \mathbf{B}^{\mathsf{T;S}}\mathbf{z}^{\lambda;j+\frac{1}{2}} - \mathbf{F}^{\mathsf{SS}}\mathbf{z}^{\mathsf{u;S};j+\frac{1}{2};l} - \mathbf{F}^{\mathsf{SA}}\mathbf{z}^{\mathsf{u;A};j+\frac{1}{2};l} - \mathbf{F}^{\mathsf{SF}}\mathbf{z}^{\mathsf{u;F};j+\frac{1}{2};l} \\ \mathbf{y}^{\mathsf{u;A}} - \mathbf{F}^{\mathsf{AS}}\mathbf{z}^{\mathsf{u;S};j+\frac{1}{2};l} - \mathbf{F}^{\mathsf{AA}}\mathbf{z}^{\mathsf{u;A};j+\frac{1}{2};l} \\ \mathbf{y}^{\mathsf{u;F}} - \mathbf{B}^{\mathsf{T;F}}\mathbf{z}^{\lambda;j+\frac{1}{2}} - \mathbf{F}^{\mathsf{FS}}\mathbf{z}^{\mathsf{u;S};j+\frac{1}{2};l} - \mathbf{F}^{\mathsf{FA}}\mathbf{z}^{\mathsf{u;A};j+\frac{1}{2};l} - \mathbf{F}^{\mathsf{FF}}\mathbf{z}^{\mathsf{u;F};j+\frac{1}{2};l} \end{bmatrix} \end{aligned} \tag{5.3.47}$$

and the inverse "preconditioning" matrix

$$\Big(\bar{\mathbf{M}}^{\mathsf{u}}\Big)^{-1} = (\mathbf{D} + \omega\mathbf{L})^{-1} = \begin{bmatrix} \mathbf{F}^{\mathsf{SS}} & \mathbf{0} & \mathbf{0} \\ \omega\mathbf{F}^{\mathsf{AS}} & \mathbf{F}^{\mathsf{AA}} & \mathbf{0} \\ \omega\mathbf{F}^{\mathsf{FS}} & \omega\mathbf{F}^{\mathsf{FA}} & \mathbf{F}^{\mathsf{FF}} \end{bmatrix}^{-1} \tag{5.3.48}$$

Algorithm 5.2 Relaxed Block-Gauss-Seidel (SOR) procedure employed as approximate solver for the modified FSI problem (5.3.38).

```
for each iteration $l$:
    Compute solid solution increment $\Delta\mathbf{z}^{\mathrm{u;S};j+\frac{1}{2};l+1}$ from (5.3.51) ⇝ field-specific solver
    Update structure solution $\mathbf{z}^{\mathrm{u;S};j+\frac{1}{2};l+1}$ (5.3.52)
    Compute ALE solution increment $\Delta\mathbf{z}^{\mathrm{u;A};j+\frac{1}{2};l+1}$ from (5.3.55) ⇝ field-specific solver
    Update ALE solution $\mathbf{z}^{\mathrm{u;A};j+\frac{1}{2};l+1}$ (5.3.56)
    Compute fluid solution increment $\Delta\mathbf{z}^{\mathrm{u;F};j+\frac{1}{2};l+1}$ from (5.3.58) ⇝ field-specific solver
    Update fluid solution $\mathbf{z}^{\mathrm{u;F};j+\frac{1}{2};l+1}$ (5.3.59)
```

allows for the following short notation of equation (5.3.46)

$$\mathbf{z}^{\mathrm{u};j+\frac{1}{2};l+1} = \mathbf{z}^{\mathrm{u};j+\frac{1}{2};l} + \omega\left(\bar{\mathbf{M}}^{\mathrm{u}}\right)^{-1}\bar{\mathbf{r}}^{\mathrm{u};j+\frac{1}{2};l} \tag{5.3.49}$$

which can now be identified as a stationary Richardson iteration.

The determination of the updated intermediate FSI vector, thus, requires the solution of the following linear problem

$$\bar{\mathbf{M}}^{\mathrm{u}}\Delta\mathbf{z}^{\mathrm{u};j+\frac{1}{2};l+1} = \bar{\mathbf{r}}^{\mathrm{u};j+\frac{1}{2};l}. \tag{5.3.50}$$

In this context, the different equation blocks are solved successively taking into account the modified order introduced above. Thereby, field-specific parallel solvers like multi-grid methods can be utilized. First, the solution of the solid field is determined from

$$\begin{aligned}\mathbf{F}^{\mathrm{SS}}\Delta\mathbf{z}^{\mathrm{u;S};j+\frac{1}{2};l+1} &= \bar{\mathbf{r}}^{\mathrm{u;S};j+\frac{1}{2};l} = \\ &= \mathbf{y}^{\mathrm{u;S}} - \mathbf{B}^{\mathrm{T;S}}\mathbf{z}^{\lambda;j+\frac{1}{2}} - \mathbf{F}^{\mathrm{SS}}\mathbf{z}^{\mathrm{u;S};j+\frac{1}{2};l} - \mathbf{F}^{\mathrm{SA}}\mathbf{z}^{\mathrm{u;A};j+\frac{1}{2};l} - \mathbf{F}^{\mathrm{SF}}\mathbf{z}^{\mathrm{u;F};j+\frac{1}{2};l}\end{aligned} \tag{5.3.51}$$

and

$$\mathbf{z}^{\mathrm{u;S};j+\frac{1}{2};l+1} = \mathbf{z}^{\mathrm{u;S};j+\frac{1}{2};l} + \omega\Delta\mathbf{z}^{\mathrm{u;S};j+\frac{1}{2};l+1}. \tag{5.3.52}$$

In a next step, the update of the ALE solution is calculated from

$$\mathbf{F}^{\mathrm{AA}}\Delta\mathbf{z}^{\mathrm{u;A};j+\frac{1}{2};l+1} = \bar{\mathbf{r}}^{\mathrm{u;A};j+\frac{1}{2};l} - \omega\mathbf{F}^{\mathrm{AS}}\Delta\mathbf{z}^{\mathrm{u;S};j+\frac{1}{2};l+1}. \tag{5.3.53}$$

Introducing the expression for the ALE iteration residual into above equation yields

$$\mathbf{F}^{\mathrm{AA}}\Delta\mathbf{z}^{\mathrm{u;A};j+\frac{1}{2};l+1} = \mathbf{y}^{\mathrm{u;A}} - \mathbf{F}^{\mathrm{AS}}\mathbf{z}^{\mathrm{u;S};j+\frac{1}{2};l} - \mathbf{F}^{\mathrm{AA}}\mathbf{z}^{\mathrm{u;A};j+\frac{1}{2};l} - \omega\mathbf{F}^{\mathrm{AS}}\Delta\mathbf{z}^{\mathrm{u;S};j+\frac{1}{2};l+1}, \tag{5.3.54}$$

which can be simplified using relation (5.3.52), i.e.

$$\mathbf{F}^{\mathrm{AA}}\Delta\mathbf{z}^{\mathrm{u;A};j+\frac{1}{2};l+1} = \mathbf{y}^{\mathrm{u;A}} - \mathbf{F}^{\mathrm{AS}}\mathbf{z}^{\mathrm{u;S};j+\frac{1}{2};l+1} - \mathbf{F}^{\mathrm{AA}}\mathbf{z}^{\mathrm{u;A};j+\frac{1}{2};l}. \tag{5.3.55}$$

The new ALE solution vector then reads

$$\mathbf{z}^{\mathrm{u;A};j+\frac{1}{2};l+1} = \mathbf{z}^{\mathrm{u;A};j+\frac{1}{2};l} + \omega\Delta\mathbf{z}^{\mathrm{u;A};j+\frac{1}{2};l+1}. \tag{5.3.56}$$

Finally, the increment of the fluid solution vector is computed by solving the linear system given by

$$\mathbf{F}^{\mathrm{FF}} \Delta \mathbf{z}^{\mathrm{u;F};j+\frac{1}{2};l+1} = \bar{\mathbf{r}}^{\mathrm{u;F};j+\frac{1}{2};l} - \omega \mathbf{F}^{\mathrm{FS}} \Delta \mathbf{z}^{\mathrm{u;S};j+\frac{1}{2};l+1} - \omega \mathbf{F}^{\mathrm{FA}} \Delta \mathbf{z}^{\mathrm{u;A};j+\frac{1}{2};l+1}. \tag{5.3.57}$$

Insertion of the fluid iteration residual as well as the increments of the solid and ALE solution vectors allows to rewrite equation (5.3.57) as

$$\begin{aligned} \mathbf{F}^{\mathrm{FF}} \Delta \mathbf{z}^{\mathrm{u;F};j+\frac{1}{2};l+1} = \mathbf{y}^{\mathrm{u;F}} - \mathbf{B}^{\mathrm{T;F}} \mathbf{z}^{\lambda;j+\frac{1}{2}} - \mathbf{F}^{\mathrm{FS}} \mathbf{z}^{\mathrm{u;S};j+\frac{1}{2};l+1} - \mathbf{F}^{\mathrm{FA}} \mathbf{z}^{\mathrm{u;A};j+\frac{1}{2};l+1} - \\ - \mathbf{F}^{\mathrm{FF}} \mathbf{z}^{\mathrm{u;F};j+\frac{1}{2};l}. \end{aligned} \tag{5.3.58}$$

The old fluid solution vector is then updated according to

$$\mathbf{z}^{\mathrm{u;F};j+\frac{1}{2};l+1} = \mathbf{z}^{\mathrm{u;F};j+\frac{1}{2};l} + \omega \Delta \mathbf{z}^{\mathrm{u;F};j+\frac{1}{2};l+1}. \tag{5.3.59}$$

The order of the equation blocks is defined such that solid and ALE fields directly influence the fluid solution, whereas the fluid field does not feed back until the next Gauss-Seidel step, see equation (5.3.51). According to Küttler (2009), this choice is beneficial since the effect of the structure field on the fluid is commonly stronger than vice versa. For the same reason, in general no symmetric Gauss-Seidel method is employed for this type of problems.

A summary of the presented relaxed Block-Gauss-Seidel procedure for the modified FSI problem is given in Algorithm 5.2.

5.4 Numerical Examples

5.4.1 Validation

The set-up of a simple numerical simulation suitable for validating the presented volume-coupling approach is shown in Figure 5.4.1. Basically, a cubic parenchyma block (edge length 10 mm) was inflated with air transported through the associated cuboid conducting airway (2.5 mm×2.5 mm×6 mm). Both domains were bordered by a layer of elements (thickness 0.5 mm) representing the block and airway walls, respectively.

For reference purposes, a simulation based on the homogenized mixture model was performed. In this case, fluid and solid domains were superimposed in the peripheral region and coupled at the interior surface of the enclosing block wall denoted by $\tilde{\mathrm{B}}$, see Figure 5.4.1(b). In the volume coupling simulation, the fluid field was not resolved in the peripheral domain. Instead, the volume coupling constraint was introduced to capture the influence of peripheral airflow on parenchyma deformation and flow in the resolved vessel in a simplified way. More precisely, the volume of air flowing through the artificial boundary $\hat{\mathrm{B}}$ in a time step Δt was constrained to be equal to the change in volume of the parenchyma block enclosed by $\tilde{\mathrm{B}} \cup \bar{\mathrm{B}} \cup \hat{\mathrm{B}}$ as defined in 5.4.1(c). In both simulations, FSI

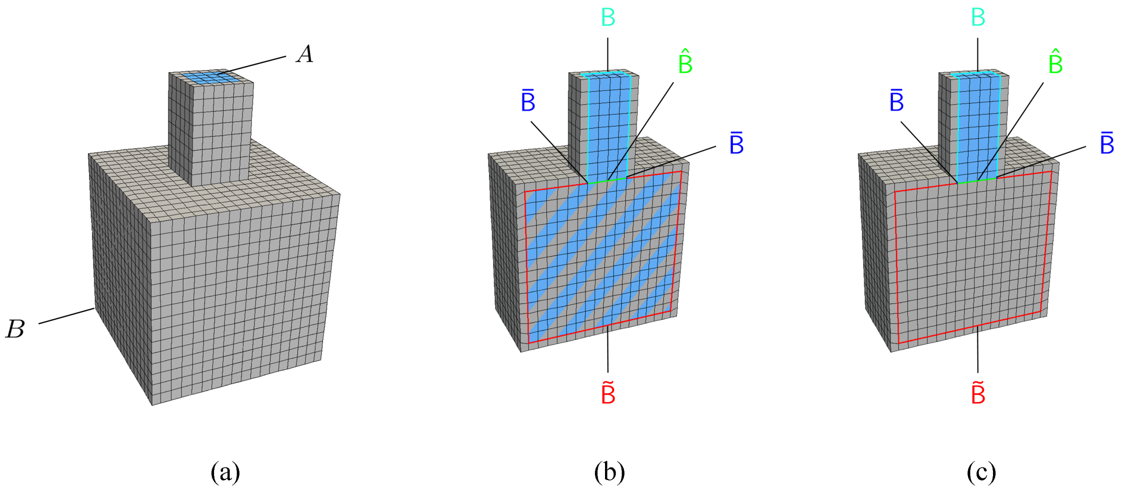

Figure 5.4.1: General set-up of validation example. (a) Definition of points for comparing the fluid pressure (A) and the overall solid displacements (B) in the reference and model simulation. (b) Configuration of reference simulation. (c) Configuration of volume-coupled simulation.

was considered along the resolved airway wall $\mathsf{B} \cup \bar{\mathsf{B}}$. Subsequently, simulation results of the volume-coupled model are referred to as the "model solution" in contrast to the "reference solution" provided by the homogenized mixture model.

A Neo-Hookean constitutive law was chosen for airway and block walls (with Young's modulus $E^{\mathsf{S}}_{\mathsf{wall}} = 50\,\mathrm{kPa}$, Poisson's ratio $\nu^{\mathsf{S}}_{\mathsf{wall}} = 0.3$, and density $\rho^{\mathsf{S}}_{\mathsf{wall}} = 1000\,\mathrm{kg/m^3}$) as well as for the parenchyma block itself (with Young's modulus $E^{\mathsf{S}}_{\mathsf{block}} = 0.675\,\mathrm{kPa}$, Poisson's ratio $\nu^{\mathsf{S}}_{\mathsf{block}} = 0.3$, and density $\rho^{\mathsf{S}}_{\mathsf{block}} = 1000\,\mathrm{kg/m^3}$). For the air in the resolved feeding vessel, the kinematic viscosity was given by $\nu^{\mathsf{F}} = 15\,\mathrm{mm^2/s}$ and the density was chosen as $\rho^{\mathsf{F}} = 1\,\mathrm{kg/m^3}$. On the inlet of the resolved airway, a parabolic inflow profile in vertical direction was prescribed. The maximum velocity was given by

$$u_{\mathsf{max}} = u_0 \sin\left(\frac{2\pi t}{T}\right) \tag{5.4.1}$$

with $u_0 = 2$ m/s and $T = 100\,ms$. The total simulation time was 50 ms in both cases.

The development of the fluid pressures and the overall parenchyma displacements in points A and B defined in Figure 5.4.1(a) is shown in Figure 5.4.2. Reference and model results were in remarkable agreement at all simulated time steps.

In Figure 5.4.3, the distribution of the overall displacements at $t = t_{\mathrm{end}}$ is given for both cases. The overall fluid velocities under maximum inflow – i.e. at $t = t_{\mathrm{mid}}$ – are shown throughout the respective simulation domains in Figure 5.4.4. Flow patterns in the resolved airway were nearly the same. In Figure 5.4.5, corresponding fluid pressures at $t = t_{\mathrm{mid}}$ are depicted. Although the pressure at the inlet (cf. Figure 5.4.2(b)) was almost identical in

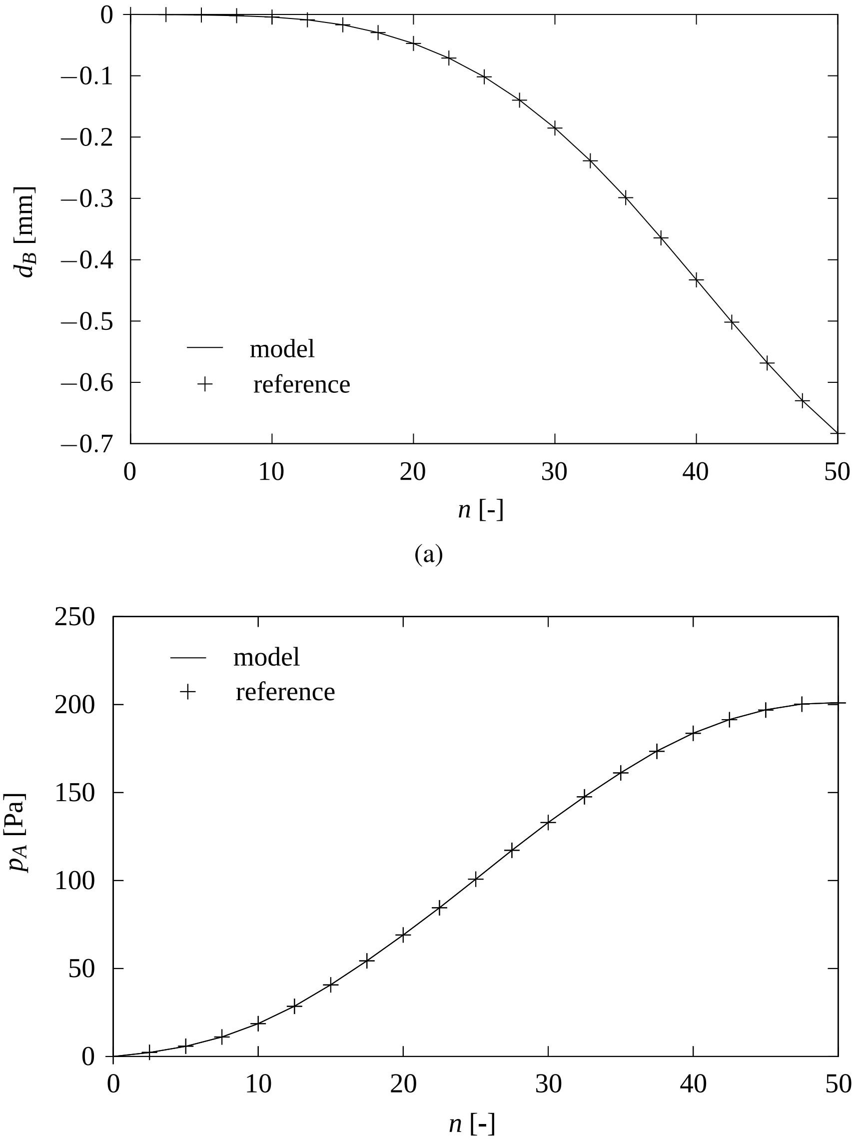

(a)

(b)

Figure 5.4.2: Development of (a) displacements at node B and (b) pressures at node A (confer Figure 5.4.1(a) for positions) over simulated time steps in reference and model simulation.

both cases, its distribution over the length of the resolved airway was slightly different. This comes about due to the flow in the peripheral region (see also Figure 5.4.4) which was assumed to be negligible in the derivation of the volume coupling. Accordingly, the outlet pressure provided by the novel model corresponded to the average of the pressure along $\tilde{\mathsf{B}}$ in the reference simulation. It should be noted that, in reality, airflow within the peripheral domain is impeded by the narrow ramifications. Therefore, the results obtained

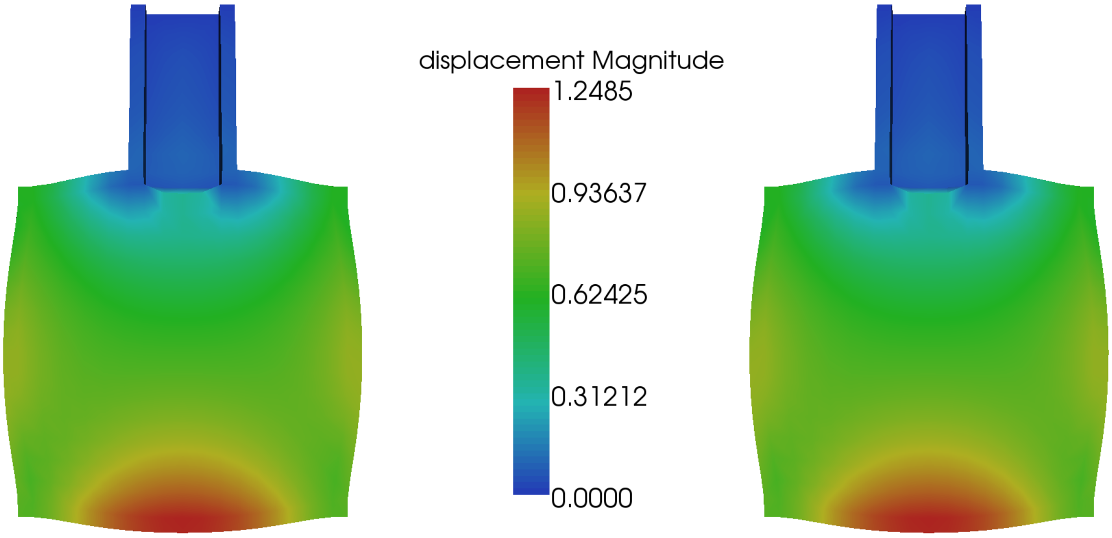

Figure 5.4.3: Clipped view of reference (left) and model (right) solution for overall displacements in mm at $t = t_{\text{end}}$ (i.e. under maximum deformation).

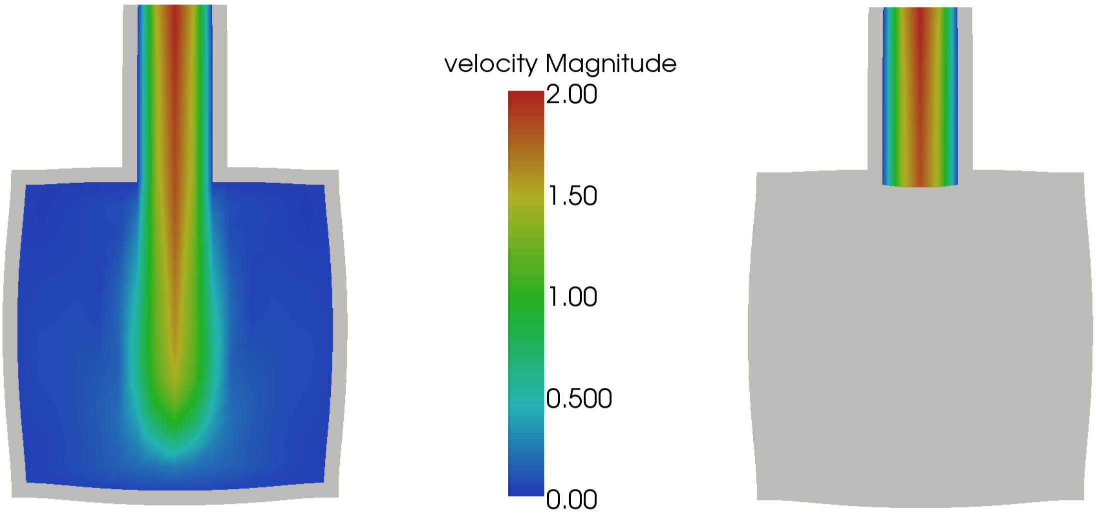

Figure 5.4.4: Clipped view of reference (left) and model (right) solution for overall fluid velocities in m/s at $t = t_{\text{mid}}$ (i.e. under maximum inflow).

by means of the volume-coupled model may be deemed even more physiological than the actual reference solution.

For illustrative purposes, the additional forces due to the volume coupling constraint are

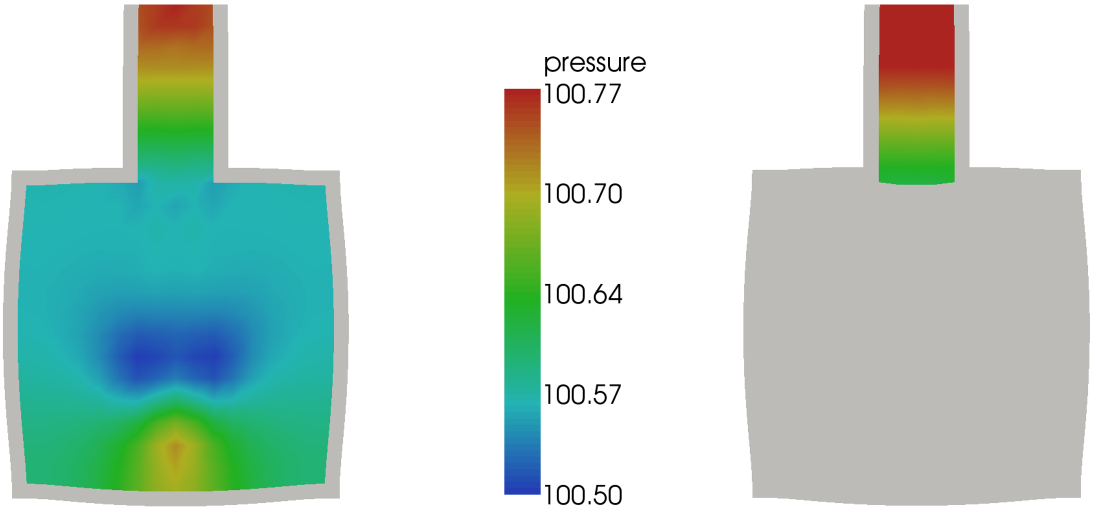

Figure 5.4.5: Clipped view of reference (left) and model (right) pressure solution in Pa at $t = t_{\text{mid}}$ (i.e. under maximum inflow).

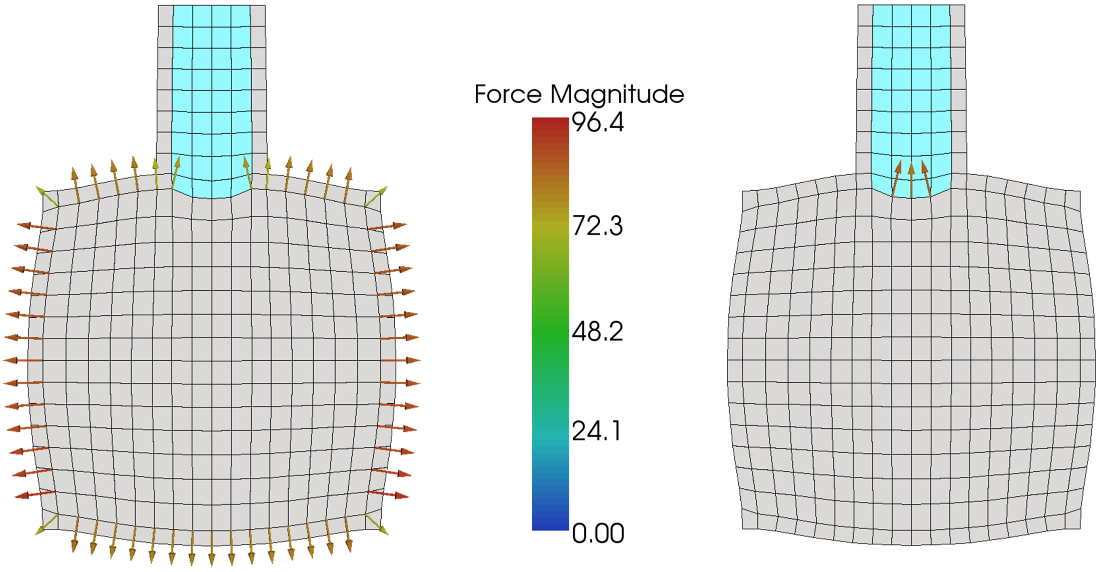

Figure 5.4.6: Forces in µN on parenchyma (left) and air (right) due to the coupling of volume changes.

given in Figure 5.4.6. Consistent with the derivations presented in previous sections, the parenchyma block experienced tractions along $\tilde{\mathsf{B}} \cup \bar{\mathsf{B}}$, whereas the fluid field was loaded along $\hat{\mathsf{B}}$. In this way, the effect of peripheral flow on parenchyma deformation and airflow in the resolved vessel was taken into account properly.

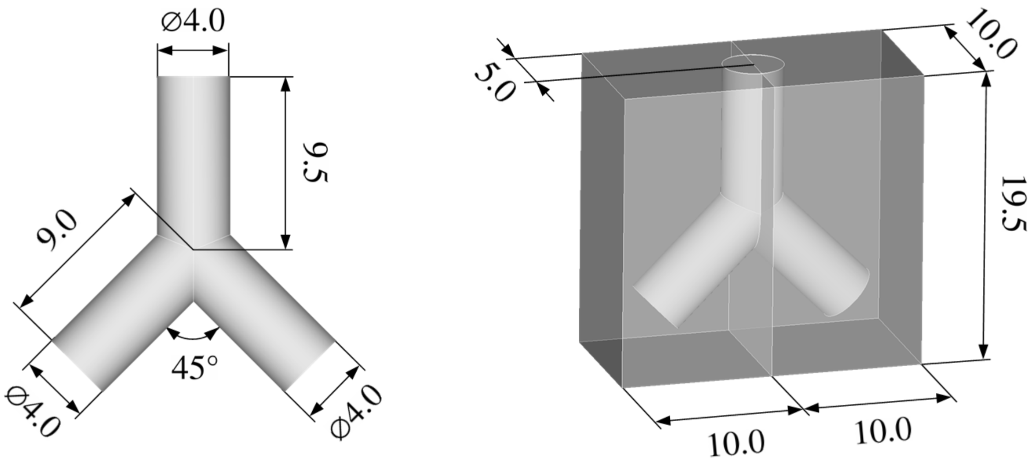

Figure 5.4.7: Dimensions of airways and parenchyma blocks in mm.

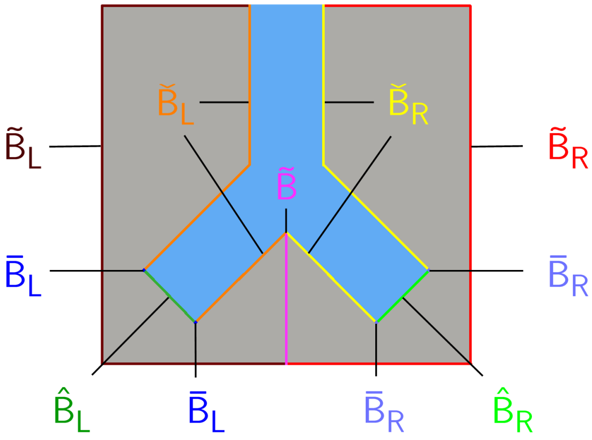

Figure 5.4.8: Definition of boundaries of left (identifier “L”) and right (identifier “R”) blocks and associated airways.

In summary, the model solutions for all simulated fields convincingly matched the corresponding reference solutions. In the following, the applicability of the developed volume coupling approach to cases with multiple airway outlets and associated parenchyma blocks will be demonstrated.

5.4.2 Multiple outlets

In Figure 5.4.7, the geometry of an embedded Y-shaped bifurcation employed subsequently in several numerical simulations is displayed. The cubical parenchyma model was split into two equally big blocks consistent with the two outlets of the immersed cylindrical airways. For simplicity, the wall of the resolved terminal airway was not modeled explicitly. Hence, the homogenized parenchyma directly adjoined the FSI interface that was denoted by $\check{\mathsf{B}}_{\mathsf{L}}$ or $\check{\mathsf{B}}_{\mathsf{R}}$, respectively (see Figure 5.4.8 for a detailed definition of decisive boundaries). However, the modeling approach introduced beforehand was of course applicable also in this case without further modifications.

For each subsystem, a separate volume constraint was introduced. Therefore, the air flowing through the left outlet $\hat{\mathsf{B}}_{\mathsf{L}}$ was coupled to the deformation of the left block enclosed by $\tilde{\mathsf{B}} \cup \tilde{\mathsf{B}}_{\mathsf{L}} \cup \check{\mathsf{B}}_{\mathsf{L}} \cup \bar{\mathsf{B}}_{\mathsf{L}} \cup \hat{\mathsf{B}}_{\mathsf{L}}$. Analogously, the volume of air flowing through the right outlet $\hat{\mathsf{B}}_{\mathsf{R}}$ was constrained to equal the volume change of the right block enclosed by $\tilde{\mathsf{B}} \cup \tilde{\mathsf{B}}_{\mathsf{R}} \cup \check{\mathsf{B}}_{\mathsf{R}} \cup \bar{\mathsf{B}}_{\mathsf{R}} \cup \hat{\mathsf{B}}_{\mathsf{R}}$.

The kinematic viscosity and the density of air were again assumed as $\nu^{\mathsf{F}} = 15\,\mathrm{mm}^2/\mathrm{s}$ and $\rho^{\mathsf{F}} = 1\,\mathrm{kg/m}^3$, respectively. The homogenized parenchyma was modeled using a Neo-Hookean constitutive law with Poisson's ratio $\nu^{\mathsf{S}} = 0.3$ and density $\rho^{\mathsf{S}} = 1000\,\mathrm{kg/m}^3$.

Subsequent simulations were performed on three processors in parallel. For distributing the meshes over the different processors, the open-source MPI-based parallel library ParMETIS was employed. A typical partitioning of the solid and fluid meshes is shown in Figures 5.4.9(a) and 5.4.9(b), respectively. Even though the enclosing boundaries of the parenchyma blocks were distributed over all three processors, evaluation of the surface integrals involved in the computation of the volume changes was straightforward. The accuracy of the results has been verified by comparing with a serial simulation (data not shown).

In the first numerical example, a Young's modulus of $E^{\mathsf{S}}_{\mathsf{L}} = E^{\mathsf{S}}_{\mathsf{R}} = 6.75\,\mathrm{kPa}$ was chosen, i.e. both blocks exhibited the same material properties. On the inlet of the bifurcation, a parabolic inflow profile in vertical direction was prescribed with maximum velocity

$$u_{\mathsf{max}} = \begin{cases} 15\,\frac{\mathrm{m}}{\mathrm{s}^2}\cdot t & \text{for } t \leq 0.1\,\mathrm{s} \\ 1.5\,\frac{\mathrm{m}}{\mathrm{s}} & \text{for } 0.1\,\mathrm{s} < t \leq 0.15\,\mathrm{s} \end{cases} \tag{5.4.2}$$

In Figure 5.4.10(a), the overall deformation of the parenchyma blocks is displayed. To visualize flow patterns in the resolved airways, selected streamlines are shown in Figure 5.4.10(b) where the colors represent the absolute local velocities. The additional forces on parenchyma and air due to the volume constraint are given in Figure 5.4.11. In contrast to the validation example, the FSI interfaces $\check{\mathsf{B}}_{\mathsf{L}}$ and $\check{\mathsf{B}}_{\mathsf{R}}$ were also loaded since they were part of the enclosing boundaries. Due to the locally different element sizes, the absolute value of the forces – which represent the stress resultants of the inflating pressure – varied. On the shared part of the enclosing boundaries $\tilde{\mathsf{B}}$, the forces canceled as expected. The plot in Figure 5.4.12 illustrates the uniform splitting of the outflowing air volume between the two outlets. Hence, the presented example was characterized by a perfectly symmetric distribution of all fields.

In the second example, the Young's modulus of the left parenchyma block was doubled, i.e. $E^{\mathsf{S}}_{\mathsf{L}} = 13.5\,\mathrm{kPa}$. This setting represented a simplified model of heterogeneous lung damage, e.g. resulting from the instability and collapse of peripheral, unresolved airspaces

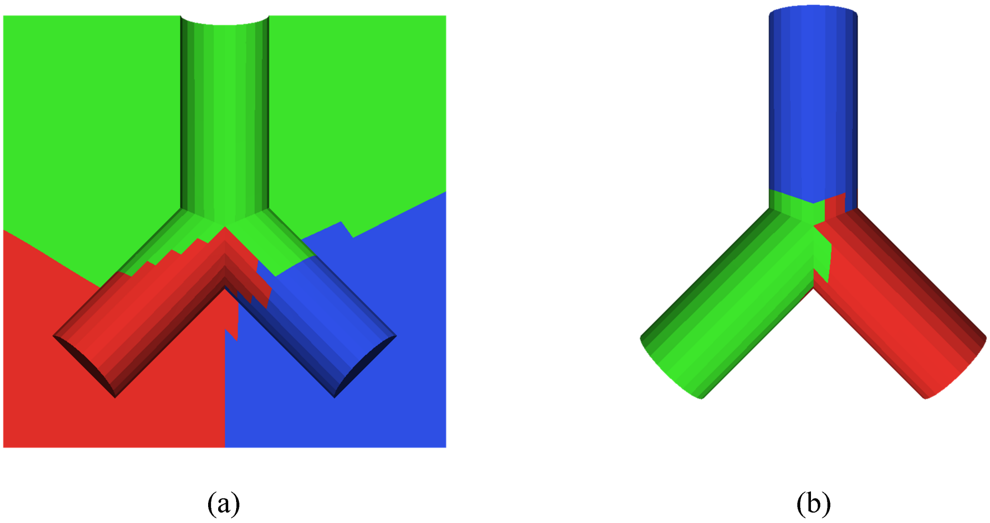

Figure 5.4.9: Distribution of solid (a) and fluid (b) meshes on three processors. For the sake of clarity, a clipped view of the parenchyma blocks is provided.

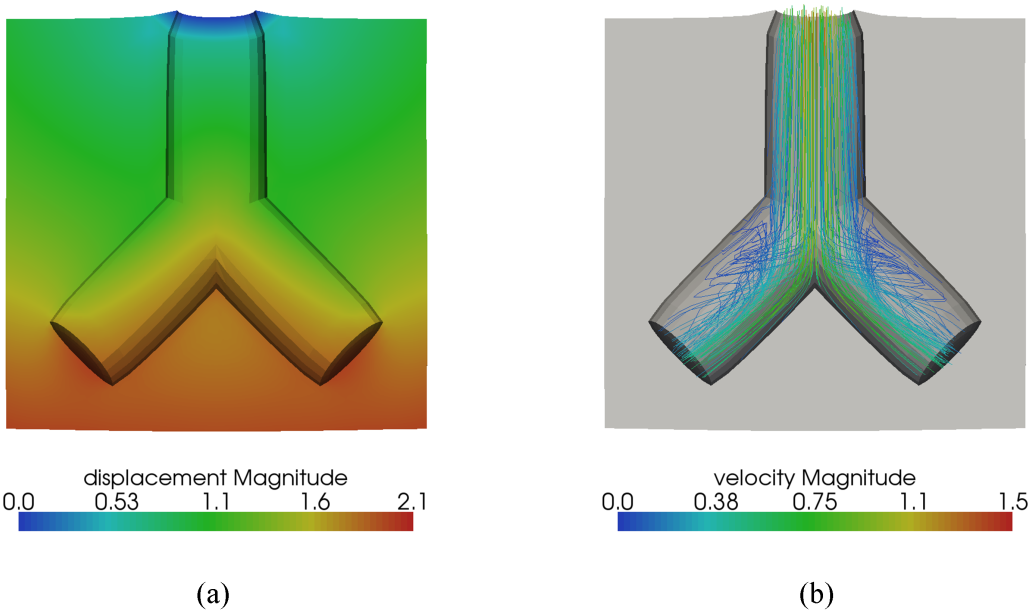

Figure 5.4.10: Symmetric case with prescribed inflow. (a) Overall deformation of parenchyma model in mm. (b) Streamlines of airflow with colors indicating overall velocities in m/s. For the sake of clarity, clipped views are provided.

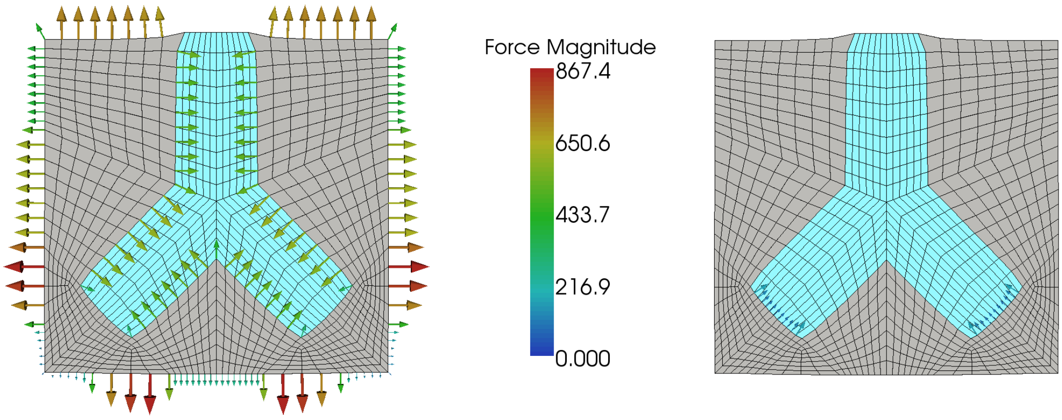

Figure 5.4.11: Forces in μN on parenchyma (left) and air (right) due to the coupling of volume changes in the symmetric case. For the sake of clarity, clipped views are provided.

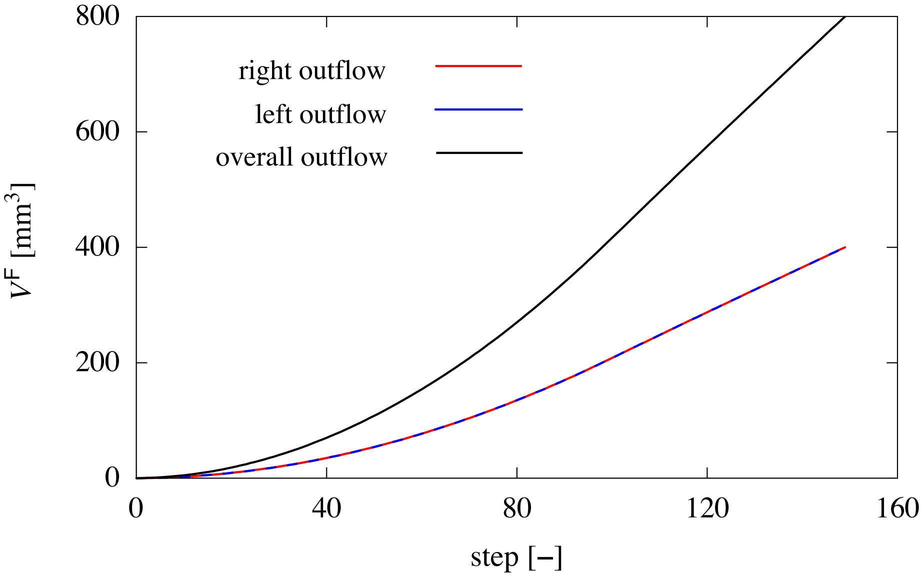

Figure 5.4.12: Splitting of overall outflowing air volumes between the two outlets in the symmetric case.

followed by local atelectasis. Corresponding simulation results for the distribution of overall displacements and air velocities are shown in Figures 5.4.13(a) and 5.4.13(b), respectively. The splitting of air volumes between the two blocks is given in Figure 5.4.14. Most of the incoming air was transported into the softer right parenchyma block resulting in an unsymmetric deformation state.

The next example illustrates that the volume coupling approach can be easily combined with the nested multi-scale method presented in chapter 4. In this way, a simplified overall

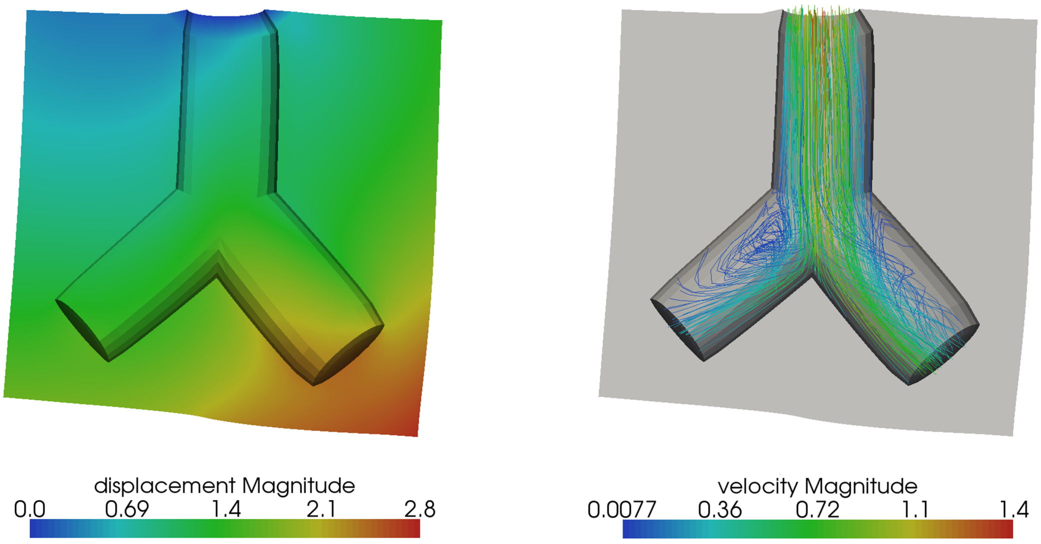

(a)

(b)

Figure 5.4.13: Unsymmetric case (inhomogeneous material parameters) with prescribed inflow. (a) Overall deformation of parenchyma model in mm. (b) Streamlines of airflow with colors indicating overall velocities in m/s. For the sake of clarity, clipped views are provided.

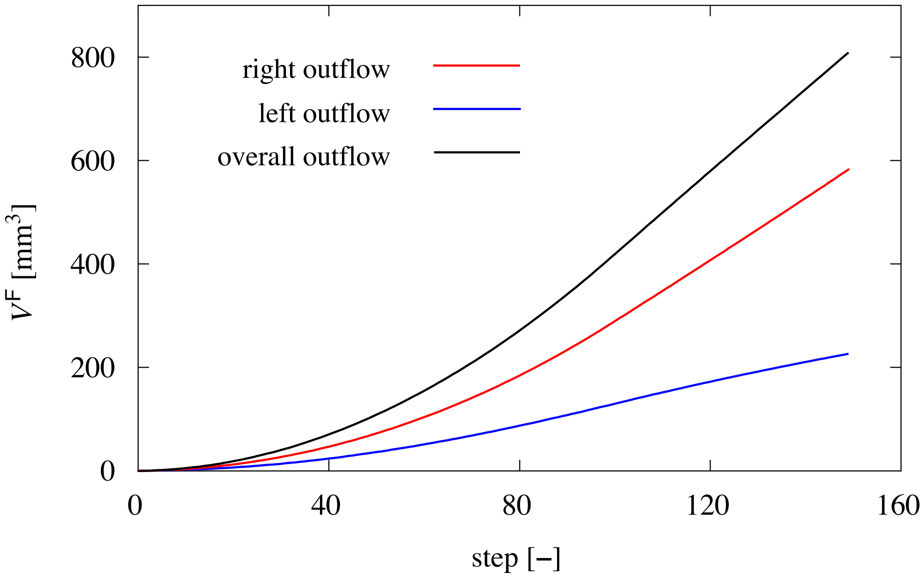

Figure 5.4.14: Splitting of overall outflowing air volumes between the two outlets in the unsymmetric case (inhomogeneous material parameters).

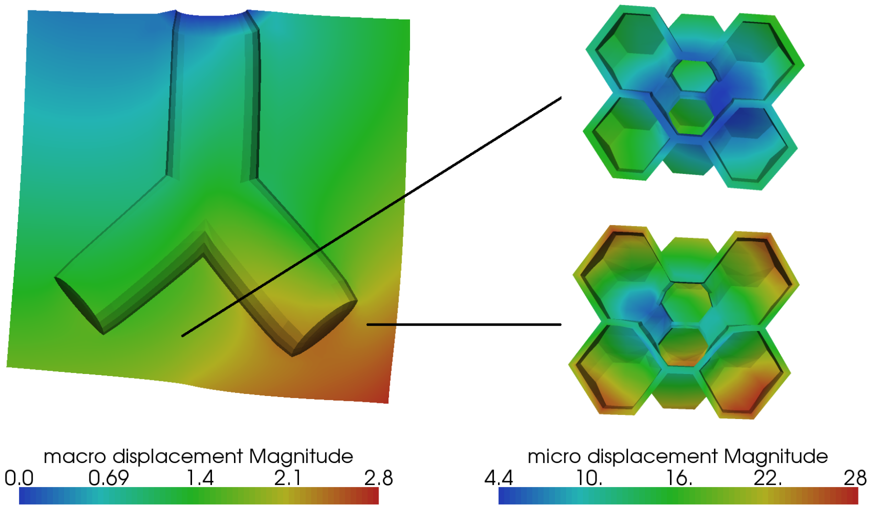

Figure 5.4.15: Combination of volume-coupled FSI and multi-scale approach in the unsymmetric case. Left: overall deformation of parenchyma model in mm. Right: overall deformation of alveolar micro-structures in μm at different locations. For the sake of clarity, clipped views are provided.

lung model comprising the conducting and the respiratory part of the lung down to single alveoli can be established. Throughout the bulk of the parenchyma blocks, the same material model and parameters as in the heterogeneous example discussed beforehand were utilized. At one selected Gauss point in each block, however, the multi-scale approach was employed. In this context, a simple artificial alveolar ensemble was again chosen as a "representative" micro-structure (see also section 4.4.2). For simplicity, no interfacial phenomena were considered in this example. The resulting alveolar displacements were governed by the associated macro-scale deformation state (cf. the right-hand side of Figure 5.4.15). However, since the FE^2 method was applied in two Gauss points only, the specific parameters on the micro-scale hardly affected the overall behavior. Therefore, the deformation state of the parenchyma blocks displayed in Figure 5.4.15 basically coincided with the one given in Figure 5.4.13 for the single-scale simulation.

The previous two examples have shown that a heterogeneous state can be modeled by selecting different material parameters for the parenchyma blocks. However, the overall stiffness also significantly depends on the respective size of the blocks. Therefore, in the following example, the right parenchyma block was enlarged compared to the left one. The other settings were the same as in the symmetric case discussed above. In Figures 5.4.16(a) and 5.4.16(b), the distribution of the overall displacements and airflow velocities is displayed. For a given volume change, the strains in the right parenchyma block were smaller than in the left one due to its larger reference size. Since the stiffness of the material increases with increasing strain, the right block behaved softer than the left one. As a consequence, more air flowed into the right block as is also demonstrated in Figure 5.4.17. Thus, when setting up an overall lung model, the different ventilation units have

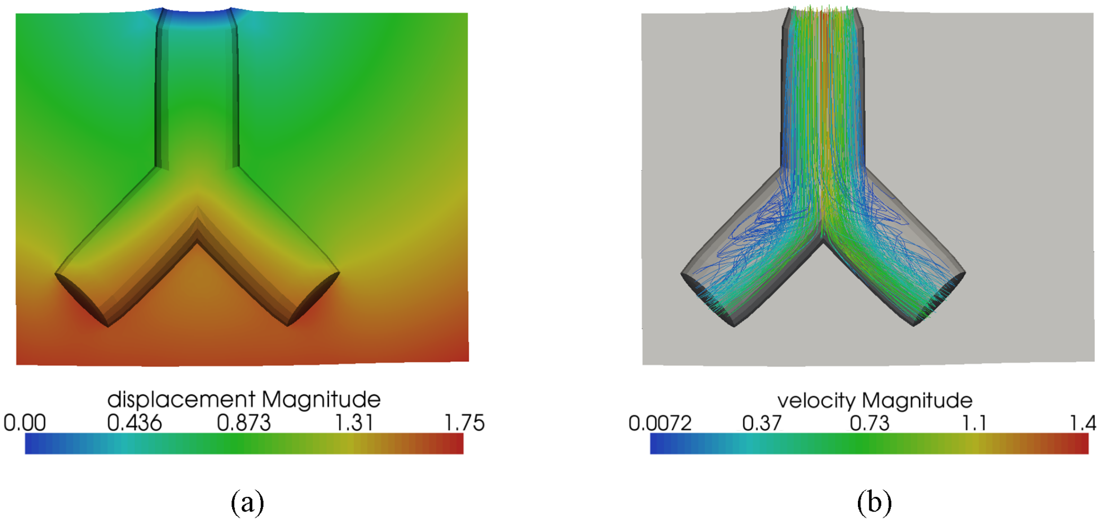

(a)

(b)

Figure 5.4.16: Unsymmetric case (different block sizes) with prescribed inflow. (a) Overall deformation of parenchyma model in mm. (b) Streamlines of airflow with colors indicating overall velocities in m/s. For the sake of clarity, clipped views are provided.

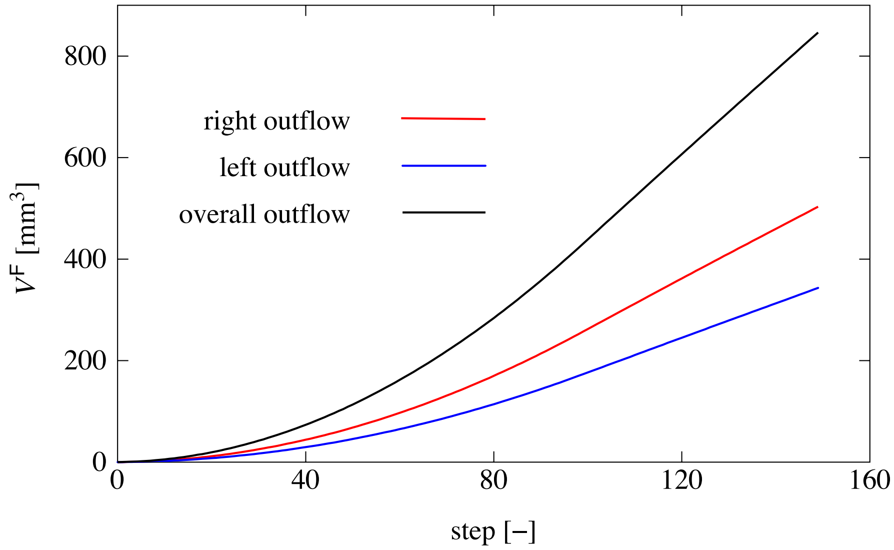

Figure 5.4.17: Splitting of overall outflowing air volumes between the two outlets in the unsymmetric case (different block sizes).

to be carefully defined in order to avoid the accidental introduction of an unphysiological heterogeneity.

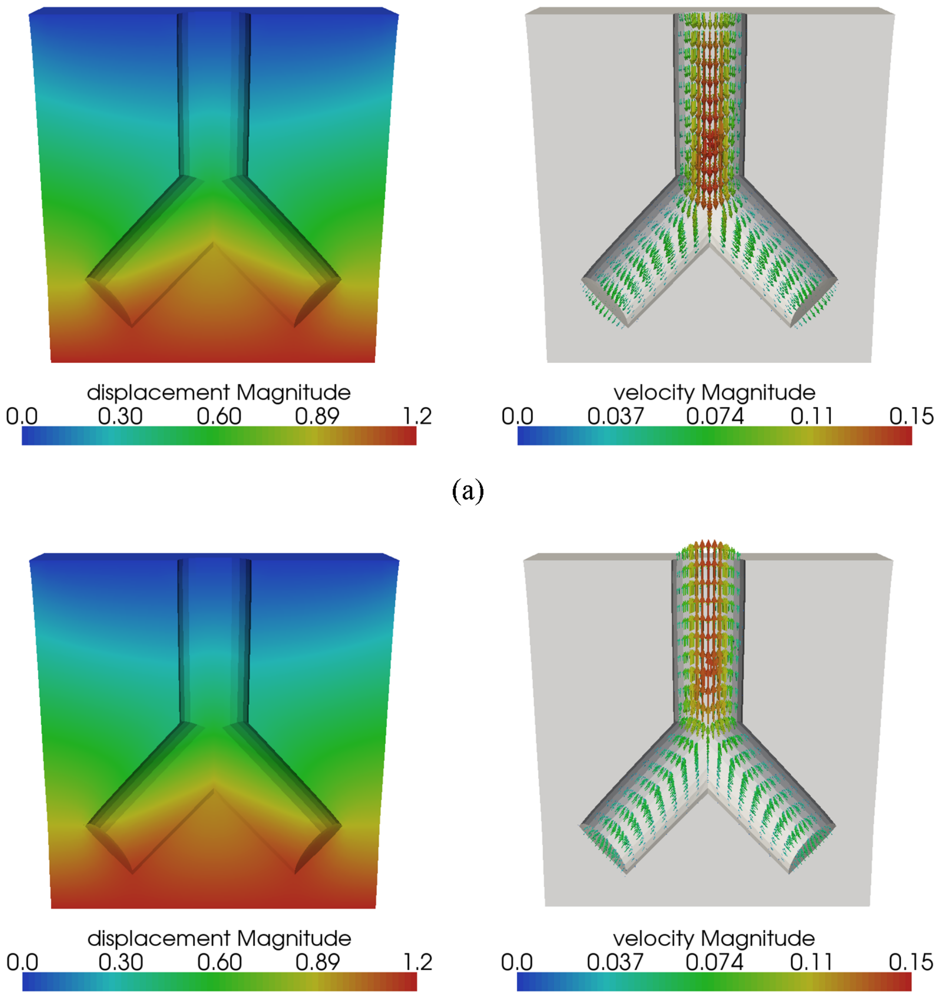

(a)

(b)

Figure 5.4.18: Overall deformations in mm (left) as well as distribution of airflow velocities in m/s (right) at (a) $t_1 = 0.125$ s and (b) at $t_2 = 0.375$ s. For the sake of clarity, clipped views are provided.

So far, the coupling of airflow and parenchyma deformation has been studied for a prescribed inflow at the inlet of the airway model. In case of normal breathing, however, flow is induced by chest wall deformation and diaphragm contraction. The following example demonstrates that the presented volume coupling approach is also suitable for this kind of boundary conditions. At the bottom surface of the blocks, a uniform vertical displacement was prescribed as follows

$$d(t) = d_{\mathsf{max}} \sin\left(\frac{2\pi t}{T}\right) \tag{5.4.3}$$

with $d_{\mathsf{max}} = 2$ mm and $T = 1.0$ s. The simulation ended at $t_{\mathsf{max}} = T/2 = 0.5$ s. A zero-traction boundary condition (also known as “do nothing” condition) was imposed on the air at the inlet. Material models and parameters were adopted from the first example presented in this section, i.e. both parenchyma blocks exhibited the same properties. In Figure 5.4.18, simulation results at $t_1 = 0.125$ s and $t_2 = 0.375$ s are shown. In both cases, the prescribed bottom displacement was exactly the same. Hence, apart from some insignificant dynamic effects, the overall parenchyma displacements were the same at both points in time. However, airflow patterns differed considerably as can be seen on the right-hand side of Figure 5.4.18. At t_1, air had to flow into the blocks to compensate for the increase in parenchymal volume. By contrast, at t_2, the parenchyma volume was decreased again resulting in a reverted flow direction. It is noteworthy that airflow was only induced by the additional forces due to the volume coupling since no other driving forces or Dirichlet boundary conditions were prescribed.

Above example raises hope that the developed overall lung model may enable the simulation of expiration in a reasonable way. During inspiration, the parenchyma blocks serve as air reservoirs that are fed by the associated resolved vessels. Therefore, in the expiration phase, airflow through each outlet is uniquely defined by the strain state and the constitutive model of the associated parenchyma domain. However, detailed investigations to prove the general suitability for expiratory flows still need to be done.

6 Summary and Outlook

In this thesis, the basic building blocks of a continuum lung model have been developed. As a first step, a computational model of pulmonary alveoli has been established. Due to the poor disposability of imaging-based alveolar geometries, a method for generating artificial acinar structures has been derived. A novel labyrinthine algorithm was proposed to generate random pathways through an assemblage of tetrakaidecahedral cells representing individual alveoli. Thereby, specific connection rules were formulated to guarantee the preservation of minimal path lengths within the alveolar ensemble. It has been shown that information provided by the labyrinthine algorithm can be directly used for the generation of three-dimensional geometries suitable for subsequent FE analyses.

For modeling of alveolar tissue behavior, a hyperelastic constitutive law developed originally for arterial tissue has been adapted. The proposed isotropic SEF is composed of two main parts related to the major stress-bearing elements, i.e. the matrix material including elastin fibers and the collagen fiber network. To satisfy the quasi-incompressibility constraint typical of all soft biological tissues, a penalty approach has been implemented. Due to the lack of experimental data for individual alveolar walls, the material model has been fitted to available stress-strain curves of lung tissue sheets.

Since alveolar walls are covered with a thin surfactant layer, the interaction of tissue and liquid lining mechanics has also been included in the computational model. However, instead of explicitly discretizing the fluid film, a novel approach has been proposed based on integrating the interfacial energy in the alveolar wall model. The developed methodology applies to essentially any kind of thin liquid lining and is suitable for arbitrarily curved surfaces. To model the development of local surfactant concentrations and resultant surface stresses, a well-established dynamic transport model considering adsorption, desorption, and squeeze-out processes has been implemented.

As a next step, an overall model of lung parenchyma has been devised. Since modeling all 500 million alveoli in the human respiratory system is not feasible, a combination of two complementary approaches has been suggested. The complex alveolar micro-structure is resolved at certain “hot spots” only, whereas lung parenchyma can be modeled as a homogenized continuum otherwise. To bridge the gap between global parenchymal and local alveolar level, a three-dimensional dynamic nested multi-scale approach has been developed. Assuming a sufficient separation of length scales, a first-order scheme using homogeneous displacement boundary conditions on the fine-scale has been implemented. For the micro-macro transitions, existing homogenization procedures have been adopted. The benefit of the proposed multi-scale approach is twofold; firstly, improved homogenized parenchyma properties are derived based on a detailed modeling of the underlying microstructure. Secondly, the global parenchyma model serves as an “embedding” of locally resolved acinar structures, thereby providing physiologically reasonable boundary conditions on the micro-scale. As a consequence, the quantities of interest on the alveolar level (e.g. stresses and strains in case of VALI) can be simulated more realistically compared to previous models. In first example simulations, the suitability of the developed approach for the intended application has been demonstrated.

Finally, a novel approach to combining the conducting and the respiratory domains in one overall lung model has been derived. Since only parts of both the airway tree and the alveolar structures can be resolved, the transport of air down to the respiratory zone cannot be simulated explicitly but has to be modeled. The developed methodology is based on dividing the parenchyma model into subdomains associated with the outlets of the resolved three-dimensional airway tree. The volume of air passing through each outlet has to be on par with the change in volume of the corresponding tissue subdomain. To enforce this constraint within the framework of FSI problems, the Lagrange multiplier technique has been utilized. For the parallel and iterative solution of the resulting linear systems, a specific preconditioning algorithm has been introduced. The functionality of the developed volume-coupled FSI approach has been proven by first numerical examples illustrating the mutual interaction of airflow and parenchyma deformation.

In summary, it can be stated that continuum models for distinct parts of the lung – i.e. the tracheo-bronchial, the global parenchymal and the local alveolar region – have been developed and successfully combined for the first time. However, although substantial progress towards an overall “virtual lung” model has been made, there is still a lot of work to be done in the future. Subsequently, selected concepts for improving the individual building blocks will be briefly addressed.

The first issue is related to the geometric representation of alveoli. In the long term, utilization of imaging-based alveolar geometries is definitely desirable. So far, however, realistic representations are only available for small animal lungs. Therefore, computational models will continue to rely on artificial acinar morphologies in the near future. A drawback of the geometries proposed in section 3.1, however, is that all alveoli are of the same shape and size. As already mentioned, this limitation may be partly overcome by introducing statistical fluctuations of the vertex positions. The necessary level of irregularity can be specified by comparing available imaging-based and artificial alveolar geometries for smaller species. This information may then be utilized to improve also artificial representations of human alveoli.

With regards to the constitutive model of individual alveolar walls, reliable material parameters still have to be derived. Since corresponding data cannot be obtained experimentally, an alternative approach has to be pursued here. One possibility would be to combine inverse analysis and multi-scale techniques. In this way, the specific micro-geometry of tested lung tissue strips could be resolved locally in the computational model. The tension test could then be simulated repeatedly in silico with varying alveolar material parameters until the computed global load-displacement curves comply with the experimentally derived ones. After having established this procedure for deriving alveolar material parameters, further complexities (e.g. visco-elastic effects) should be included in the constitutive model to allow for a more accurate description of alveolar soft tissue mechanics.

As already indicated in section 3.3, the surfactant model also leaves room for improvement. If ventilation patterns with breath-to-breath variability are to be studied, the description of the steady-state behavior is not sufficient anymore. In this case, a more complicated transport model considering also diffusion processes (cf. section 3.3.3) has to be implemented.

Concerning the developed multi-scale approach, a representative volume element of the alveolar micro-structure still has to be determined. Acinar configurations of arbitrary size needed for corresponding convergence analyses could be easily constructed using the methodology presented in section 3.1. In order to keep the sample size as small as possible, implementation of periodic boundary conditions on the micro-level would be advantageous. In this way, also the quality of the fine-scale solution could be improved. On the macro-level, the phenomenological damping model should be replaced with a micro-mechanically motivated approach in the future. Thereby, no empirical parameters will be left in the dynamic coarse-level problem. Last but not least, the efficiency of the micro-macro approach still has to be improved further to enable large-scale simulations based on actual representative alveolar samples. One promising option would be the employment of model order reduction methods based on pre-computations of micro-level responses (Yvonnet and He, 2007).

To enhance the predictability of the overall lung model, the parenchyma subdomains involved in the volume-coupling of conducting and respiratory zones should be chosen as small as possible. However, the number of imageable airway generations is currently limited. One possible solution to this problem is to complement the resolved airways with reduced-order models of artificially generated space-filling trees (see e.g. Ismail et al. (2011)). Thereby, a partitioning of lung parenchyma into very small compartments would be facilitated.

Apart from improving the existing building blocks, future work will also be concerned with implementing some additional functionalities. For instance, the influence of the pleural membrane or the capillary network on lung tissue mechanics needs to be considered. Besides, gas exchange has to be modeled to allow for a reasonable evaluation of different ventilation strategies. After all, prevention of VALI is only one issue involved in the definition of clinically relevant ventilation protocols. Obviously, the most protective strategy in this regard would imply no intervention at all. However, sufficient oxygenation has to be guaranteed in any case.

Finally, the applicability of all developed computational approaches to realistic scenarios has to be proven in large-scale simulations. After an adequate validation, the overall lung model will be utilized to study the effects of different ventilator settings on local alveolar stresses and strains. As already mentioned in section 1.3, resulting biological responses will then be investigated by simulating these conditions experimentally in a bioreactor (Dassow et al., 2010). Hopefully, this combination of computational and experimental approaches will give deeper insights into the mechanisms of VALI and set the agenda for more protective ventilation protocols. The presented models are, however, by no means restricted to this particular application. Since the introduced approaches are mainly built up from first principles, they could also be utilized for investigating a variety of other interesting problems such as asthma, emphysema, or targeted drug delivery. Hence, the developed models may be valuable for providing a better understanding of respiratory mechanics in general and answering a number of specific questions brought up by the medical and biological community.

A Details concerning artificial morphology

A.1 Conversion between cell IDs and coordinates

During the generation of a labyrinth through a given assemblage of tetrakaidecahedra, it is beneficial to convert between the consecutive cell *ID* numbering and the artificial coordinates of the cell center (cf. Figure 3.1.3) and the other way round. For the following definitions, it is important to recall that the division of two integers produces an integer result by ignoring decimals. The expression **int**(#) is introduced to emphasize this truncation where # denotes the corresponding quotient.

If the cell *ID* is known and the corresponding coordinates have to be derived, different cases have to be distinguished. First, a temporary variable *a* has to be defined as follows

$$a = \mathbf{int}\left(\frac{ID}{mn + (m-1)(n-1)}\right), \tag{A.1.1}$$

where m and n are the number of tetrakaidecahedral cells on the main planes in x_1- and x_2-direction, respectively. After introduction of another temporary variable b

$$b = ID - a\left(mn + (m-1)(n-1)\right), \tag{A.1.2}$$

the x_3-coordinate of the cell is evaluated as follows

$$x_3 = \begin{cases} 2a & \text{if } \mathbf{int}\left(\frac{b}{mn}\right) = 0 \\ 2a+1 & \text{if } \mathbf{int}\left(\frac{b}{mn}\right) \neq 0 \end{cases}. \tag{A.1.3}$$

The subsequent derivation of x_1- and x_2-coordinates of the cell depends on whether the previously calculated x_3-coordinate is an even or an odd integer. In the former case, the missing coordinates are obtained as

$$x_2 = \mathbf{int}\left(\frac{2\left(ID - \mathbf{int}\left(\frac{x_3}{2}\right)(mn + (m-1)(n-1))\right)}{n}\right) \tag{A.1.4}$$

$$x_1 = 2\left(ID - \mathbf{int}\left(\frac{x_3}{2}\right)(mn + (m-1)(n-1)) - \mathbf{int}\left(\frac{x_2}{2}\right)n\right). \tag{A.1.5}$$

For x_3 being odd, x_1 and x_2 can be calculated to

$$x_2 = \mathbf{int}\left(\frac{2\left(ID - \mathbf{int}\left(\frac{x_3}{2}\right)(m-1)(n-1) - \mathbf{int}\left(\frac{x_3+1}{2}\right)mn\right)}{n-1}\right) \tag{A.1.6}$$

$$x_1 = 2\left(ID - \mathbf{int}\left(\frac{x_3}{2}\right)(m-1)(n-1) - \mathbf{int}\left(\frac{x_3+1}{2}\right)mn - \mathbf{int}\left(\frac{x_2}{2}\right)(n-1)\right) + 1. \tag{A.1.7}$$

If, on the contrary, the coordinates of the cell center are known and the corresponding cell ID has to be derived, three temporal variables need to be introduced, namely

$$c = mn, \tag{A.1.8}$$

$$d = (m-1)(n-1), \tag{A.1.9}$$

and

$$e = \begin{cases} n & \text{if } x_1, x_2, x_3 \text{ even} \\ n-1 & \text{if } x_1, x_2, x_3 \text{ odd.} \end{cases} \tag{A.1.10}$$

The cell ID can then be calculated as follows

$$ID = \mathbf{int}\left(\frac{x_3+1}{2}\right)c + \mathbf{int}\left(\frac{x_3}{2}\right)d + \mathbf{int}\left(\frac{x_2}{2}\right)e + \mathbf{int}\left(\frac{x_1}{2}\right). \tag{A.1.11}$$

A.2 Construction of three-dimensional geometries

As already indicated in section 3.1.2, two adjacent cells within an alveolar assemblage can be connected by deleting the common surface. Hence, the output of the labyrinthine algorithm is a list of all deleted surfaces per cell (cf. Figure 3.1.4 for a definition of local surface IDs). Based on this information, three-dimensional alveolar geometries can be constructed following the procedure summarized in Algorithm A.1.

First, the mid planes of the artificial alveoli are constructed. For a given characteristic length L defined in Figure 3.1.1, all permutations of $(0, \pm\frac{\sqrt{2}}{4}L, \pm\frac{\sqrt{2}}{2}L)$ are Cartesian coordinates of the vertices of a tetrakaidecahedron centered at the origin. Depending on its unique ID, the alveolus can then be shifted to its final position within the assemblage. Lines connecting the vertices are created as shown in Figure A.2.1. In this context, all hexagonal faces are divided into quadrilaterals to simplify both the automatic generation of surfaces and the structural meshing later on. However, additional lines are introduced only if the respective surfaces are not empty according to the labyrinthine algorithm.

The resulting three-dimensional geometry should contain alveolar walls with a finite, user-defined thickness t. After determination of the normal vectors, parallel planes at an interval of $\frac{t}{2}$ in the inward direction can be defined for every non-empty surface. By intersecting these planes, a new vertex associated with the given mid plane vertex can be determined. In this context, a simple 3x3 linear system has to be solved. Interior vertices are connected

Algorithm A.1 Generation of three-dimensional acinar geometries based on information provided by the labyrinthine algorithm.

```
Define characteristic length $L$ and wall thickness $t$ of assemblage
Read input from labyrinthine algorithm (surfaces to be deleted)

for all cells on main levels:
    Construct interior volumes (except intersections), see Algorithm A.2
for all cells on ancillary levels:
    Construct interior volumes (except intersections), see Algorithm A.2
for all cells:
    Construct interior intersection volumes, see Algorithm A.3
    Construct outer volumes, see Algorithm A.4

Write all created lines, surfaces, and volumes to batch file
```

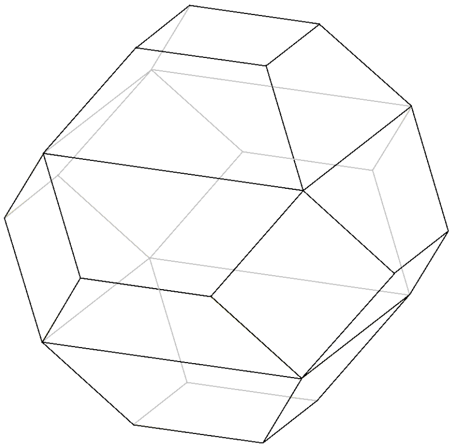

Figure A.2.1: Lines needed for the construction of a single closed artificial alveolus. Black lines are located in the front whereas gray lines are hidden.

by lines with each other as well as with their mid plane counterparts. Hence, for each non-empty mid plane surface, five additional surfaces as well as the corresponding enclosed volume can be created. All constructed geometric entities are entitled as “interior” objects since they are obtained by translating the mid plane in inward direction. The procedure presented so far is subsumed in Algorithm A.2. In Figure A.2.2, selected interior volumes created for two interconnected alveoli are displayed. The highlighted surfaces illustrate the resulting gap at the connecting point. This comes about due to the fact that each mid plane vertex shared by two alveoli is associated with two distinct interior vertices. Consequently, specific so-called “intersection volumes” have to be generated in a next step in order to enable an appropriate transition between the individual alveoli.

For each shared mid plane vertex that is part of an empty surface, an associated intersection vertex has to be determined. Again, parallel planes at an interval of $\frac{t}{2}$ in the inward

Algorithm A.2 Construction of interior volumes of an artificial alveolus.

```
Mid plane surfaces
Construct all vertices $\mathcal{V}_{\text{mid}}$ of mid planes
Define all lines $\mathcal{L}_{\text{mid}}$ connecting mid plane vertices (except those crossing empty surfaces)
Define all non-empty and empty mid plane surfaces $\mathcal{S}_{\text{mid}}$ and $\tilde{\mathcal{S}}_{\text{mid}}$, respectively
Determine normals of all surfaces including empty ones

Interior surfaces
Construct all vertices $\mathcal{V}_{\text{int}}$ of interior surfaces:
    for all $v$ in $\mathcal{V}_{\text{mid}}$:
        Find the 3 distinct normals of adjacent surfaces
        Define parallel planes at intervals of $\frac{t}{2}$
        Determine interior vertex by solving the intersection problem
Construct all lines $\mathcal{L}_{\text{int}}$ connecting interior vertices (except those crossing empty surfaces)
Construct all non-empty interior surfaces $\mathcal{S}_{\text{int}}$

Interior volumes
for all $s$ in $\mathcal{S}_{\text{mid}}$:
    for all $v$ in $\mathcal{V}^s_{\text{mid}}$:
        Create connection line with vertex of associated interior surface
    for all $l$ in $\mathcal{L}^s_{\text{mid}}$:
        Create surface connecting $l$ with its counterpart on interior surface
    Construct interior volume
```

direction can be defined. In contrast to the construction of the interior volumes, however, planes associated with different alveoli are intersected. Two different cases have to be distinguished in general. If the empty surface is square, then the planes parallel to the two adjacent non-empty surfaces owned by one alveolus have to be intersected with the empty surface. If, however, the empty surface is part of a hexagon, the situation becomes more complicated. In order to render the geometric construction as well as later meshing as simple as possible, an approximation to the actual intersection is utilized here. The planes parallel to the two adjacent non-empty surfaces owned by one alveolus and the plane parallel to the neighboring quadratic surface owned by the connected alveolus are intersected. For each line of an empty surface, two intersection nodes are created in this way. After generation of lines connecting the intersection vertices with each other as well as with the associated interior vertices, four additional surfaces and the corresponding enclosed intersection volume can be created. The procedure discussed above is summarized in Algorithm A.3.

As demonstrated in Figures A.2.3(a) and A.2.3(b), the employed approximate intersection in case of a hexagonal connection surface leads to slight kinks in the transition regions. The severity of this inaccuracy depends on the chosen thickness of the alveolar walls. For comparison, the correct intersection of the interior surfaces is given in Figure A.2.3(c). The geometry of the exact transition is far more complicated than in case of the approximate intersection shown in Figure A.3(b). Hence, the introduced error seems acceptable here.

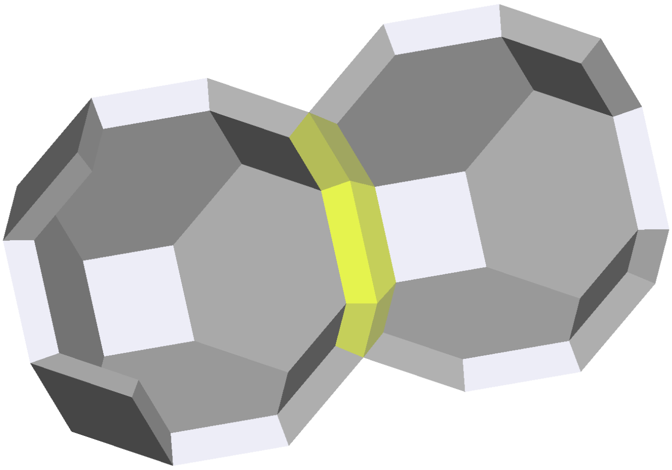

Figure A.2.2: Interior volumes shown exemplarily for two interconnected alveoli. For the sake of lucidity, volumes located in front are omitted.

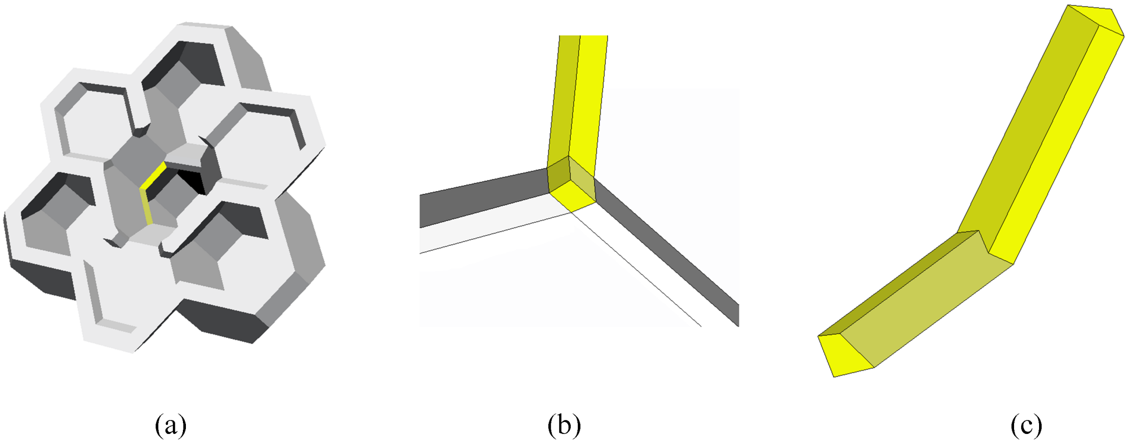

(a)

(b)

(c)

Figure A.2.3: Intersection of walls for connected alveoli. (a) Clipped view of small alveolar assemblage with two highlighted intersection volumes. (b) Detailed view of intersection volumes generated according to Algorithm A.3. (c) Geometrically correct intersection of alveolar walls.

It is noteworthy that the intersection volumes surrounding an empty surface can be interpreted as the alveolar entrance ring. Since this region is, from the geometric point of view, separated from the remaining alveolar wall, one can easily assign specific properties to it, e.g. in terms of different connective tissue fiber distributions.

Finally, the outer volumes of the alveolar walls have to be constructed. In Figure A.2.4, selected interior surfaces for two neighboring, unconnected alveoli are displayed. The shared mid plane is associated with two interior volumes. Therefore, the interior volume

Algorithm A.3 Generation of interior intersecting volumes resulting from the connection of alveoli through surfaces defined by the labyrinthine algorithm.

```
for all $s$ in $\tilde{\mathcal{S}}_{\mathsf{mid}}$ (i.e. empty surfaces):
    for all $v$ in $\mathcal{V}^{s}_{\mathsf{mid}}$:
        if $s$ is part of a hexagonal surface:
            Find 2 distinct normals of adjacent non-empty surfaces owned by cell
            Find normal of adjacent quadratic surface owned by connected cell
            Define 3 parallel planes at intervals of $\frac{t}{2}$
            Determine interior intersection vertex by solving the intersection problem
        else:
            Find 2 distinct normals of adjacent non-empty surfaces owned by cell
            Define 2 parallel planes at intervals of $\frac{t}{2}$
            Determine interior intersection vertex by intersecting the planes with $s$
    for all $l$ in $\mathcal{L}^{s}_{\mathsf{mid}}$:
        for all $v$ in $\mathcal{V}^{l}_{\mathsf{mid}}$:
            Create lines connecting $v$ with its 2 associated interior vertices
            Create lines connecting interior vertices with associated intersection vertex
        Create line connecting interior intersection vertices
        Construct enclosing surfaces based on line definitions
        Create interior intersection volume
```

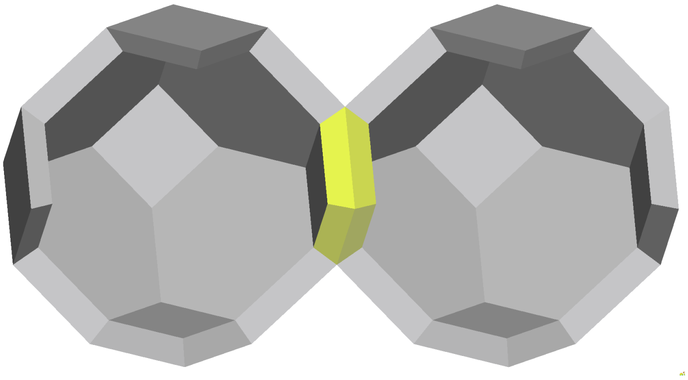

Figure A.2.4: Interior volumes at shared mid planes serve as outer volumes for adjacent, unconnected alveoli.

of one alveolus serves as the outer volume of the other one and vice versa. However, for all mid planes located on the exterior of the assemblage, additional outer volumes need to be created. Essentially, the generation of these volumes follows the procedures described above. Again, planes parallel to the adjacent mid planes are defined and intersected in order to determine the outer vertices. However, the mid planes are now translated by $\frac{t}{2}$ in the outward direction. Detailed instructions for the generation of the outer volumes are given in Algorithm A.4. Eventually, a three-dimensional alveolar assemblage with a uniform wall thickness t is created. Since the geometry is composed of hexahedral shapes

Algorithm A.4 Construction of outer volumes for exterior alveoli.

```
for all $s$ in $\mathcal{S}_{\mathsf{mid}}$:
    if $s$ is located on the outside of the assemblage:
        for all $v$ in $\mathcal{V}^s_{\mathsf{mid}}$:
            if $v$ belongs to one cell only:
                Find 3 normals of adjacent surfaces
            else:
                if $v$ belongs to two cells:
                    Find 2 normals of adjacent outside surfaces owned by cell
                    Find normal of 1 adjacent outside surface owned by connected
                        cell
                else:
                    Find 3 normals of adjacent outside surfaces (one per cell)
            Define parallel planes at intervals of $\frac{t}{2}$
            Determine exterior vertex by solving the intersection problem
        Create lines connecting exterior vertices with corresponding vertices on $\mathcal{S}_{\mathsf{mid}}$
        Create lines connecting exterior vertices with each other
        Construct enclosing surfaces based on line definitions
        Create outer volume
```

only, structured meshing is straightforward. Furthermore, all constructed vertices, lines, surfaces, and volumes can be addressed individually, thus boundary conditions can be easily applied.

Bibliography

Adami, S., Hu, X. Y., and Adams, N. A. (2010). A conservative SPH method for surfactant dynamics. *Journal of Computational Physics*, 229:1909–1926.

Adler, A., Cowley, E. A., Bates, J. H. T., and Eidelman, D. H. (1998). Airway-parenchymal interdependence after airway contraction in rat lung explants. *Journal of Applied Physiology*, 85:231–237.

Al Jamal, R., Roughley, P. J., and Ludwig, M. S. (2001). Effect of glycosaminoglycan degradation on lung tissue viscoelasticity. *American Journal of Physiology – Lung Cellular and Molecular Physiology*, 280:L306–L315.

Amato, M. B. P., Barbas, C. S. V., Medeiros, D. M., Magaldi, R. B., Schettino, G. P. P., Lorenzi-Filho, G., Kairalla, R. A., Deheinzelin, D., Munoz, C., Oliveira, R., Takagaki, T. Y., and Carvalho, C. R. R. (1998). Effect of a protective-ventilation strategy on mortality in the acute respiratory distress syndrome. *The New England Journal of Medicine*, 338:347–354.

an Mey, D., Sarholz, S., and Terboven, C. (2007). Nested parallelization with OpenMP. *International Journal of Parallel Programming*, 35:459–476.

Archie, J. P. (1973). A mathematical model for pulmonary mechanics: Alveolar surface contribution. *International Journal of Engineering Science*, 11:659–671.

Atkin, R. J. and Craine, R. E. (1976). Continuum theory of mixtures: basic theory and historical developement. *The Quarterly Journal of Mechanics and Applied Mathematics*, 29:209–244.

Baffico, L., Grandmont, C., and Maury, B. (2010). Multiscale modelling of the respiratory tract. *Mathematical Models and Methods in Applied Sciences*, 20:59–93.

Ball, J. M. (1977). Convexity conditions and existence theorems in nonlinear elasticity. *Archive for Rational Mechanics and Analysis*, 63:337–403.

Balzani, D., Neff, P., Schröder, J., and Holzapfel, G. A. (2006). A polyconvex framework for soft biological tissues. Adjustment to experimental data. *International Journal of Solids and Structures*, 43:6052–6070.

Baoshun, M. and Lutchen, K. R. (2006). An anatomically based hybrid computational model of the human lung and its application to low frequency oscillatory mechanics. *Annals of Biomedical Engineering*, 14:1691–1704.

Bastacky, J., Lee, C. Y. C., Goerke, J., Koushafar, H., Yager, D., Kenaga, L., Speed, T. P., Chen, Y., and Clements, J. A. (1995). Alveolar lining layer is thin and continuous: low-temperature scanning electron microscopy of rat lung. *Journal of Applied Physiology*, 79:1615–1628.

Bates, J. H. T. (1998). A micromechanical model of lung tissue rheology. *Annals of Biomedical Engineering*, 26:679–687.

Bates, J. H. T. (2009). *Lung Mechanics – An inverse modeling approach*. Cambridge University Press.

Bates, J. H. T. and Lutchen, K. R. (2005). The interface between measurement and modeling of peripheral lung mechanics. *Respiratory Physiology & Neurobiology*, 148:153–164.

Bayreuther, C. (2004). *Mehrskalenmodelle in der Festkörpermechanik und Kopplung von Mehrgittermethoden mit Homogenisierungsmethoden*. PhD thesis, Universität Stuttgart.

Belytschko, T., Liu, W. K., and Moran, B. (2005). *Nonlinear finite elements for continua and structures*. Wiley.

Benzi, M., Golub, G. H., and Liesen, J. (2005). Numerical solution of saddle point problems. *Acta Numerica*, 14:1–137.

Berend, N., Rynell, A. C., and Ward, H. E. (1991). Structure of a human pulmonary acinus. *Thorax*, 46:117–121.

Bernard, G. R. (2005). Acute respiratory distress syndrome. A historical perspective. *American Journal of Respiratory and Critical Care Medicine*, 172:798–806.

Bernard, G. R., Artigas, A., Brigham, K. L., Carlet, J., Falke, K., Hudson, L., Lamy, M., Legall, J. R., Morris, A., and Spragg, R. (1994). The American European consensus conference on ARDS: definition mechanisms, relevant outcomes and clinical trial coordination. *American Journal of Respiratory Critical Care Medicine*, 149:818–824.

Bertram, C. D. and Gaver, D. P. (2005). Biofluid mechanics of the pulmonary system. *Annals of Biomedical Engineering*, 33:1681–1688.

Bonet, J. and Wood, R. D. (2008). *Nonlinear continuum mechanics for finite element analysis*. Cambridge University Press.

Brewer, K. K., Sakai, H., Alencar, A. M., Majumdar, A., Arold, S. P., Lutchen, K. R., Ingenito, E. P., and Suki, B. (2003). Lung and alveolar wall elastic and hysteretic behavior in rats: effects of in vivo elastase treatment. *Journal of Applied Physiology*, 95(5):1926–1936.

Brooks, A. N. and Hughes, T. J. R. (1982). Streamline Upwind/Petrov-Galerkin formulations for convection dominated flows with particular emphasis on the incompressible Navier-Stokes equations. *Computer Methods in Applied Mechanics and Engineering*, 32:199–259.

Brower, R. G., Lanken, P. N., MacIntyre, N., Matthay, M. A., Morris, A., Ancukiewicz, M., Schoenfeld, D., and Thompson, B. T. (2004). ARDS clinical trials network. Higher versus lower positive end expiratory pressures in patients with acute respiratory distress syndrome. *The New England Journal of Medicine*, 351:327–336.

Burrowes, K. S. (2005). *An anatomically-based mathematical model of the human pulmonary circulation*. PhD thesis, University of Auckland.

Butt, H.-J., Graf, K., and Kappl, M. (2003). *Physics and chemistry of interfaces*. Wiley.

Caretto, L. S., Gosman, A. D., Patankar, S. V., and Spalding, D. B. (1972). Two calculation procedures for steady, three-dimensional flows with recirculation. In *Lecture Notes in Physics*, pages 60–68. Springer.

Carney, D. E., DiRocco, J. D., and Nieman, G. F. (2005). Dynamic alveolar mechanics and ventilator-induced lung injury. *Critical Care Medicine*, 33:S122–S128.

Cavalcante, F. S. A., Ito, S., Brewer, K. K., Sakai, H., Alencar, A. M., Almeida, M. P., Andrade, J. S., Majumdar, A., Ingenito, E. P., and Suki, B. (2005). Mechanical interactions between collagen and proteoglycans: implications for the stability of lung tissue. *Journal of Applied Physiology*, 98(2):672–679.

Chandran, P. L. and Barocas, V. H. (2006). Affine versus non-affine fibril kinematics in collagen networks: theoretical studies of network behavior. *Journal of Biomechanical Engineering*, 128:259–270.

Chessa, J. and Belytschko, T. (2003). An enriched finite element method and level sets for axisymmetric two-phase flow with surface tension. *International Journal for Numerical Methods in Engineering*, 58:2041–2064.

Chung, J. and Hulbert, G. M. (1993). A time integration algorithm for structural dynamics with improved numerical dissipation: the generalized-alpha method. *Journal of Applied Mechanics*, 60:371–375.

Comerford, A., Förster, C., and Wall, W. A. (2010). Structured tree impedance outflow boundary conditions for 3D lung simulations. *Journal of Biomechanical Engineering*, 132:081002–1–10.

Comerford, A. and Wall, W. A. (2011). Fluid structure interaction models of the bronchial airways: Understanding the influence of peripheral airways and lung parenchyma. *International Journal for Numerical Methods in Biomedical Engineering*, submitted.

Dale, P. J., Matthews, F. L., and Schroter, R. C. (1980). Finite element analysis of lung alveolus. *Journal of Biomechanics*, 13:865–873.

Dassow, C., Wiechert, L., Martin, C., Schumann, S., Müller-Newen, G., Pack, O., Guttmann, J., Wall, W. A., and Uhlig, S. (2010). Biaxial distension of precision-cut lung slices. *Journal of Applied Physiology*, 108:713–721.

Davis, T. and Duff, I. S. (1997). An unsymmetric-pattern multifrontal method for sparse LU factorization. *SIAM Journal on Matrix Analysis and Applications*, 18:140–158.

De Souza Neto, E. A., Peric, D., Dutko, M., and Owen, D. R. J. (1996). Design of simple low order finite elements for large strain analysis of nearly incompressible solids. *International Journal of Solids and Structures*, 33:3277–3296.

Delfino, A., Stergiopulos, N., Moore Jr., J. E., and Meister, J.-J. (1997). Residual strain effects on the stress field in a thick wall finite element model of the human carotid bifurcation. *Journal of Biomechanics*, 30:777–786.

Denny, E. and Schroter, R. C. (1995). The mechanical behavior of a mammalian lung alveolar duct model. *Journal of Biomechanical Engineering*, 117:254–261.

Denny, E. and Schroter, R. C. (1996). A mathematical model for the morphology of the pulmonary acinus. *Journal of Biomechanical Engineering*, 118:210–215.

Denny, E. and Schroter, R. C. (1997). Relationships between alveolar size and fibre distribution in a mammalian lung alveolar duct model. *Journal of Biomechanical Engineering*, 119:289–297.

Denny, E. and Schroter, R. C. (2000). Viscoelastic behavior of a lung alveolar duct model. *Journal of Biomechanical Engineering*, 122:143–151.

Denny, E. and Schroter, R. C. (2006). A model of non-uniform lung parenchyma distortion. *Journal of Biomechanics*, 39:652–663.

Dettmer, W. and Peric, D. (2005). A computational framework for free surface fluid flows accounting for surface tension. *Computer Methods in Applied Mechanics and Engineering*, 195:3038–3071.

DiRocco, J. D., Carney, D. E., and Nieman, G. F. (2005). The mechanism of ventilator-induced lung injury: role of dynamic alveolar mechanics. In *Yearbook of Intensive Care and Emergency Medicine 2005*, pages 80–92. Springer.

Dirocco, J. D., Pavone, L. A., Carney, D. E., Lutz, C. J., Gatto, L. A., Landas, S. K., and Nieman, G. F. (2006). Dynamic alveolar mechanics in four models of lung injury. *Intensive Care Medicine*, 32:140–148.

Donea, J. and Huerta, A. (2003). *Finite element methods for flow problems*. Wiley.

Drenckhahn, D. and Zenker, W., editors (1985). *Benninghoff Anatomie*. Urban & Schwarzenberg.

Dreyfuss, D. and Saumon, G. (1998). Ventilator-induced lung injury – lessons from experimental studies. *American Journal of Respiratory and Critical Care Medicine*, 157:294–323.

E, W., Engquist, B., Li, X., Ren, W., and Vanden-Eijnden, E. (2007). Heterogeneous multiscale methods: A review. *Communications in Computational Physics*, 2:367–450.

Ehret, A. E. and Itskov, M. (2007). A polyconvex hyperelastic model for fiber-reinforced materials in application to soft tissues. *Journal of Materials Science*, 42:8853–8863.

Elman, H., Howle, V. E., Shadid, J., Shuttleworth, R., and Tuminaro, R. (2008). A taxonomy and comparison of parallel block multi-level preconditioners for the incompressible Navier-Stokes equations. *Journal of Computational Physics*, 227:1790–1808.

Ethier, C. R. and Simmons, C. A. (2007). *Introductory biomechanics: from cells to organisms*. Cambridge University Press.

Faffe, D. S., Rocco, P. R. M., Negri, E. M., and Zin, W. A. (2002). Comparison of rat and mouse pulmonary tissue mechanical properties and histology. *Journal of Applied Physiology*, 92:230–234.

Felici, M., Filoche, M., and Sapoval, B. (2003). Diffusional screening in the human pulmonary acinus. *Journal of Applied Physiology*, 94:2010–2016.

Feyel, F. (2003). A multilevel finite element method (FE^2) to describe the response of highly non-linear structures using generalized continua. *Computer Methods in Applied Mechanics and Engineering*, 192:3233–3244.

Feyel, F. and Chaboche, J.-L. (2000). FE^2 multiscale approach for modelling the elastoviscoplastic behaviour of long fibre SiC/Ti composite materials. *Computer Methods in Applied Mechanics and Engineering*, 183:309–330.

Förster, C. (2007). *Robust methods for fluid-structure interaction with stabilised finite elements*. PhD thesis, Universität Stuttgart.

Franca, L. and Hughes, T. J. R. (1988). Two classes of mixed finite element methods. *Computer Methods in Applied Mechanics and Engineering*, 69:89–129.

Frankus, A. and Lee, G. C. (1974). A theory for distortion studies of lung parenchyma based on alveolar membrane properties. *Journal of Biomechanics*, 7:101–107.

Frantzeskaki, F., Amygdalou, A., Rasmussen, T. R., Vassiliou, M. P., and Behrakis, P. K. (2003). Effects of PEEP on inspiratory and expiratory mechanics in adult respiratory distress syndrome. *Respiratory Medicine*, 97:159–166.

Freitas, R. K. and Schröder, W. (2008). Numerical investigation of the three-dimensional flow in a human lung model. *Journal of Biomechanics*, 41:2446–2457.

Fukaya, H., Martin, C. J., Young, A. C., and Katsura, S. (1968). Mechanial properties of alveolar walls. *Journal of Applied Physiology*, 25:689–695.

Fung, Y. C. (1967). Elasticity of soft biological tissues in simple elongation. *American Journal of Physiology*, 213:1532–1544.

Fung, Y. C. (1975). Does the surface tension make the lung inherently unstable? *Circulation Research*, 37:497–502.

Fung, Y. C. (1981). *Biomechanics: Mechanical properties of living tissues*. Springer.

Fung, Y. C. (1988). A model of the lung structure and its validation. *Journal of Applied Physiology*, 64:2132–2141.

Gamnitzer, P. (2010). *Residual-based variational multiscale methods for turbulent flows and fluid-structure interaction*. PhD thesis, Technische Universität München.

Ganzert, S., Möller, K., Steinmann, D., Schumann, S., and Guttmann, J. (2009). Pressure-dependent stress relaxation in acute respiratory distress syndrome and healthy lungs: an investigation based on a viscoelastic model. *Critical Care*, 13:R199.

Gao, J., Huang, W., and Yen, R. T. (2006). Mechanical properties of human lung parenchyma. *Biomedical Sciences Instrumentation*, 42:172–180.

Gasser, T. C., Ogden, R. W., and Holzapfel, G. A. (2006). Hyperelastic modelling of arterial layers with distributed collagen fibre orientations. *Journal of the Royal Society Interface*, 3:15–35.

Gattinoni, L., Caironi, P., Pelosi, P., and Goodman, L. R. (2001). What has computed tomography taught us about the acute respiratory distress syndrome? *American Journal of Respiratory and Critical Care Medicine*, 164:1701–1711.

Gattinoni, L., D'Andrea, L., Pelosi, P., Vitale, G., Pesenti, A., and Fumagalli, R. (1993). Regional effects and mechanism of positive-end-expiratory pressure in early adult respiratory distress syndrome. *The Journal of the American Medical Association*, 269:2122–2127.

Gatto, L. A. and Fluck, R. R. (2004). Alveolar mechanics in the acutely injured lung: role of alveolar instability in the pathogenesis of ventilator-induced lung injury. *Respiratory Care*, 49:1045–1055.

Gee, M. W., Förster, C., and Wall, W. A. (2010). A computational strategy for prestressing patient–specific biomechanical problems under finite deformation. *International Journal for Numerical Methods in Biomedical Engineering*, 1:52–72.

Geers, M. G. D., Kouznetsova, V., and Brekelmans, W. A. M. (2010). Multi-scale computational homogenization: Trends & challenges. *Journal of Computational and Applied Mathematics*, 234:2175–2182.

Gefen, A., Elad, D., and Shiner, R. J. (1999). Analysis of stress distribution in the alveolar septa of normal and simulated emphysematic lungs. *Journal of Biomechanics*, 32:891–897.

Gefen, A., Halpern, P., Shiner, R. J., Schroter, R. C., and Elad, D. (2001). Analysis of mechanical stresses within the alveolar septa leading to pulmonary edema. *Technology and Health Care*, 9:257–267.

Ghadiali, S. N. and Gaver, D. P. (2008). Biomechanics of liquid-epithelium interactions in pulmonary airways. *Respiratory Physiology & Neurobiology*, 163:232–243.

Ghosh, S., Lee, K., and Raghavan, P. (2001). A multi-level computational model for multi-scale damage analysis in composite and porous materials. *International Journal for Solids and Structures*, 38:2335–2385.

Gil, J., Bachofen, H., Gehr, P., and Weibel, E. R. (1979). Alveolar volume-surface area relation in air- and saline-filled lungs fixed by vascular perfusion. *Journal of Applied Physiology*, 47:990–1001.

Gitman, I. M. (2006). *Representative volumes and multi-scale modeling of quasi-brittle materials*. PhD thesis, Technische Universiteit Delft.

Gravemeier, V., Lenz, S., and Wall, W. A. (2008). Towards a taxonomy for multiscale methods in computational mechanics: building blocks of existing methods. *Computational Mechanics*, 41:279–291.

Gravemeier, V. and Wall, W. A. (2008). A space-time formulation and improved spatial reconstruction for the "divide-and-conquer" multiscale method. *Computer Methods in Applied Mechanics and Engineering*, 197:678–692.

Gray, H. (1918). *Anatomy of the Human Body*. Philadelphia: Lea & Febiger.

Green, A. S. (2004). Modelling of peak-flow wall shear stress in major airways of the lung. *Journal of Biomechanics*, 37(5):661–667.

Gregory, T. J., Longmore, W. J., Moxley, M. A., Whitsett, J. A., Reed, C. R., Fowler, A. A., Hudson, L. D., Maunder, R. J., Crim, C., and Hyers, T. M. (1991). Surfactant chemical composition and biophysical activity in acute respiratory distress syndrome. *The Journal of Clinical Investigation*, 88(6):1976–1981.

Gresho, P. M. and Sani, R. L. (2000). *Incompressible flow and the finite element method – volume two: isothermal flow*. Wiley.

Griese, M. (1999). Pulmonary surfactant in health and human lung diseases: State of the art. *European Respiratory Journal*, 13:1455–1476.

Gross, S. and Reusken, A. (2007). An extended pressure finite element space for two-phase incompressible flows with surface tension. *Journal of Computational Physics*, 224:40–58.

Grotberg, J. B. (2001). Respiratory fluid mechanics and transport processes. *Annual Review of Biomedical Engineering*, 3:421–457.

Grotberg, J. B. and Jensen, O. E. (2004). Biofluid mechanics in flexible tubes. *Annual Review of Fluid Mechanics*, 36:121–147.

Grytz, R. (2008). *Computational modeling and remodeling of human eye tissues as biomechanical structures at multiple scales*. PhD thesis, Ruhr-Universiät Bochum.

Guyton, A. C. and Hall, J. E. (1997). *Human physiology and mechanisms of disease*. Saunders.

Haberthür, C., Guttman, J., Osswald, P. M., and Schweitzer, M. (2001). *Beatmungskurven – Kursbuch und Atlas*. Springer.

Haefeli-Bleuer, B. and Weibel, E. R. (1988). Morphometry of the human pulmonary acinus. *Anatomical Record*, 220:401–414.

Halter, J. M., Steinberg, J. M., Schiller, H. J., DaSilva, M., Gatto, L. A., Landas, S., and Nieman, G. F. (2003). Positive end-expiratory pressure after a recruitment maneuver prevents both alveolar collapse and recruitment/derecruitment. *American Journal of Respiratory and Critical Care Medicine*, 167:1620–1626.

Hansen, J. E. and Ampaya, E. P. (1975). Human air space shapes, sizes, areas, and volumes. *Journal of Applied Physiology*, 38:990–995.

Hawgood, S. and Clements, J. A. (1990). Pulmonary surfactant and its apoproteins. *The Journal of Clinical Investigation*, 86:1–6.

Hazel, A. L. and Heil, M. (2005). Finite-Reynolds-number effects in steady, three-dimensional airway reopening. *Journal of Biomechanical Engineering*, 128:573–578.

Heil, M. (1999). Airway closure: Occluding liquid bridges in strongly buckled elastic tubes. *Journal of Biomechanical Engineering*, 121:487–493.

Heroux, M. A., Bartlett, R. A., Howle, V. E., Hoekstra, R. J., Hu, J. J., Kolda, T. G., Lehoucq, R. B., Long, K. R., Pawlowski, R. P., Phipps, E. T., Salinger, A. G., Thornquist, H. K., Tuminaro, R. S., Willenbring, J. M., Williams, A., and Stanley, K. S. (2005). An overview of the trilinos project. *ACM Transactions on Mathematical Software*, 31:397–423.

Hill, R. (1963). Elastic properties of reinforced solids: some theoretical principles. *Journal of the Mechanics and Physics of Solids*, 11:357–372.

Hill, R. (1972). On constitutive macro-variables for heterogeneous solids at finite strain. *Proceedings of the Royal Society A*, 326:131–147.

Hills, B. A. (1999). An alternative view of the role(s) of surfactant and the alveolar model. *Journal of Applied Physiology*, 87:1567–1583.

Holzapfel, G. (2001). *Nonlinear solid mechanics*. Wiley.

Holzapfel, G. A., Gasser, T. C., and Ogden, R. W. (2000). A new constitutive framework for arterial wall mechanics and a comparative study of material models. *Journal of Elasticity*, 61:1–48.

Holzapfel, G. A., Gasser, T. C., and Ogden, R. W. (2004). Comparison of a multi-layer structural model for arterial walls with a Fung-type model, and issues of material stability. *Journal of Biomechanical Engineering*, 126:264–275.

Hoppin, F. G., Lee, G. C., and Dawson, S. V. (1975). Properties of lung parenchyma in distortion. *Journal of Applied Physiology*, 39:742–751.

Horsfield, K., Dart, G., Olson, D. E., Filley, G. F., and Cumming, G. (1971). Models of the human bronchial tree. *Journal of Applied Physiology*, 31:207–217.

Hubmayr, R. D. (2002). Perspective on lung injury and recruitment – a skeptical look at the opening and collapse story. *American Journal of Respiratory and Critical Care Medicine*, 165:1647–1653.

Hughes, T. J. R. (2000). *The finite element method – linear static and dynamic finite element analysis*. Dover Publications.

Hughes, T. J. R., Franca, L. P., and Balestra, M. (1986). A new finite element formulation for computational fluid dynamics: V. Circumventing the Babuska-Brezzi condition: a stable Petrov-Galerkin formulation of the Stokes problem accommodating equal-order interpolation. *Computer Methods in Applied Mechanics and Engineering*, 59:85–99.

Humphrey, J. D. (2003). Continuum biomechanics of soft biological tissues. *Proceedings of the Royal Society A*, 459:3–46.

Humphrey, J. D. and Yin, F. C. (1987). A new constitutive formulation for characterizing the mechanical behavior of soft tissues. *Biophysical Journal*, 52:563–570.

Hund, A. and Ramm, E. (2007). Locality constraints within multiscale model for non-linear material behaviour. *International Journal for Numerical Methods in Engineering*, 70:1613–1632.

Ibrahimbegovic, A. and Markovic, D. (2003). Strong coupling methods in multi-phase and multi-scale modeling of inelastic behavior of heterogeneous structures. *Computer Methods in Applied Mechanics and Engineering*, 192:3089–3107.

Ingenito, E. P., Mark, L., and Davison, B. (1994). Effects of acute lung injury on dynamic tissue properties. *Journal of Applied Physiology*, 77:2689–2697.

Ingenito, E. P., Mark, L., Morris, J., Espinosa, F. F., Kamm, R. D., and Johnson, M. (1999). Biophysical characterization and modeling of lung surfactant components. *Journal of Applied Physiology*, 86:1702–1714.

International Consensus Conferences in Intensive Care Medicine (1999). Ventilator-associated lung injury in ARDS. *Intensive Care Medicine*, 25:1444–1452.

Ismail, M., Comerford, A., and Wall, W. A. (2011). Coupled and reduced dimensional modelling of respiratory mechanics during spontaneous breathing. *In preparation*.

Kamm, R. D. (1999). Airway wall mechanics. *Annual Review of Biomedical Engineering*, 1:47–72.

Kamm, R. D. and Kaazempur-Mofrad, M. R. (2004). On the molecular basis for mechanotransduction. *Mechanics & Chemistry of Biosystems*, 1:201–209.

Karakaplan, A. D., Bieniek, M. P., and Skalak, R. (1980). A mathematical model of lung parenchyma. *Journal of Biomechanical Engineering*, 102:124–136.

Kent, R. W., Woods, W. A., Salzar, R. S., Damon, A. M., and Bass, C. R. (2009). The transient relationship between pressure and volume in the pediatric pulmonary system. *Journal of Biomechanics*, 42:1656–1663.

Kim, H. J., Figueroa, C. A., Hughes, T. J. R., Jansen, K. E., and Taylor, C. A. (2009). Augmented lagrangian method for constraining the shape of velocity profiles at outlet boundaries for three-dimensional finite element simulations of blood flow. *Computer Methods in Applied Mechanics and Engineering*, 198:3551–3566.

Kimmel, E. and Budiansky, B. (1990). Surface tension and the dodecahedron model for lung elasticity. *Journal of Biomechanical Engineering*, 112:160–167.

Kitaoka, H., Nieman, G. F., Fujino, Y., Carney, D. E., DiRocco, J. D., and Kawase, I. (2007). A 4-dimensional model of the alveolar structure. *The Journal of Physiological Sciences*, 57:175–185.

Kitaoka, H., Tamura, S., and Takaki, R. (2000). A three-dimensional model of the human pulmonary acinus. *Journal of Applied Physiology*, 88:2260–2268.

Kleinstreuer, C. and Zhang, Z. (2010). Airflow and particle transport in the human respiratory system. *Annual Review of Fluid Mechanics*, 42:301–334.

Klöppel, T., Popp, A., Küttler, U., and Wall, W. A. (2011). Fluid-structure interaction for non-conforming interfaces based on a dual mortar formulation. *Computer Methods in Applied Mechanics and Engineering*, accepted.

Knoll, D. A. and Keyes, D. E. (2004). Jacobian-free Newton-Krylov methods: a survey of approaches and applications. *Journal of Computational Physics*, 193:357–397.

Kojic, M., Vlastelica, I., Stojanovic, B., Rankovic, V., and Tsuda, A. (2006). Stress integration procedures for a biaxial isotropic material model of biological membranes and for hysteretic models of muscle fibres and surfactant. *International Journal for Numerical Methods in Engineering*, 68:893–909.

Kouznetsova, V., Brekelmans, W. A. M., and Baaijens, F. P. T. (2001). An approach to micro-macro modeling of heterogeneous materials. *Computational Mechanics*, 27:37–48.

Kouznetsova, V. G. (2002). *Computational homogenization for the multi-scale analysis of multi-phase materials*. PhD thesis, Technische Universiteit Eindhoven.

Kouznetsova, V. G., Geers, M. G. D., and Brekelmans, W. A. M. (2004). Multi-scale second-order computational homogenization of multi-phase materials: a nested finite element solution strategy. *Computer Methods in Applied Mechanics and Engineering*, 193:5525–5550.

Kowalczyk, P. and Kleiber, M. (1994). Modelling and numerical analysis of stresses and strains in the human lung including tissue-gas interaction. *European Journal of Mechanics A/Solids*, 13:367–393.

Kowe, R., Schroter, R. C., Matthews, F. L., and Hitchings, D. (1986). Analysis of elastic and surface tension effects in the lung alveolus using finite element methods. *Journal of Biomechanics*, 19:541–549.

Krueger, M. A. and Gaver, D. P. (2000). A theoretical model of pulmonary surfactant multilayer collapse under oscillating area conditions. *Journal of Colloid and Interface Science*, 229:353–364.

Küttler, U. (2009). *Effiziente Lösungsverfahren für Fluid-Struktur-Interaktions-Probleme*. PhD thesis, Technische Universität München.

Küttler, U., Gee, M. W., Förster, C., Comerford, A., and Wall, W. A. (2010). Coupling strategies for biomedical fluid-structure interaction problems. *International Journal for Numerical Methods in Biomedical Engineering*, 26:305–321.

Lande, B. and Mitzner, W. (2006). Analysis of lung parenchyma as a parametric porous medium. *Journal of Applied Physiology*, 101:926–933.

Lanir, Y. (1983). Constitutive equations for the lung tissue. *Journal of Biomechanical Engineering*, 105:374–380.

Larsen, R. and Ziegenfuß, T. (2004). *Beatmung*. Springer.

Lee, S. and Sundararaghavan, V. (2009). Multi-scale homogenization of moving interface problems with flux jumps: application to solidification. *Computational Mechanics*, 44:297–307.

Lin, C.-L., Tawhai, M. H., McLennan, G., and Hoffman, E. A. (2007). Characteristics of the turbulent laryngeal jet and its effect on airflow in the human intra-thoracic airways. *Respiratory Physiology & Neurobiology*, 157:295–309.

Liu, Y., So, R. M. C., and Zhang, C. H. (2002). Modeling the bifurcating flow in a human lung airway. *Journal of Biomechanics*, 35:465–473.

Luenberger, D. G. (2003). *Linear and nonlinear programming*. Kluwer Academic Publishers.

Lum, H. and Mitzner, W. (1987). A species comparison of alveolar size and surface forces. *Journal of Applied Physiology*, 62:1865–1871.

Luo, H. Y. and Liu, Y. (2009). Particle deposition in a CT-scanned human lung airway. *Journal of Biomechanics*, 42:1869–1876.

Lutchen, K. R. and Gillis, H. (1997). Relationship between heterogeneous changes in airway morphometry and lung resistance and elastance. *Journal of Applied Physiology*, 83:1192–1201.

Ma, B. and Lutchen, K. (2009). CDF simulation of aerosol deposition in an anatomically based human large-medium airway model. *Annals of Biomedical Engineering*, 37:271–285.

MacCallum, N. and Evans, T. (2004). Acute lung injury. *Anaesthesia and Intensive Care Medicine*, 5:389–391.

Maceri, F., Marino, M., and Vairo, G. (2010). A unified multiscale mechanical model for soft collageneous tissues with regular fiber arrangement. *Journal of Biomechanics*, 43:355–363.

Maksym, G. N., Fredberg, J. J., and Bates, J. H. T. (1998). Force heterogeneity in a two-dimensional network model of lung tissue elasticity. *Journal of Applied Physiology*, 85:1223–1229.

Marsden, J. E. and Hughes, T. J. R. (1983). *Mathematical foundations of elasticity*. Dover Publications.

Massa, C. B., Allen, G. B., and Bates, J. H. T. (2008). Modeling the dynamics of recruitment and derecruitment in mice with acute lung injury. *Journal of Applied Physiology*, 105:1813–1821.

Matsuda, M., Fung, Y. C., and Sobin, S. S. (1987). Collagen and elastin fibers in human pulmonary alveolar mouths and ducts. *Journal of Applied Physiology*, 63:1185–1194.

Maury, B., Meunier, N., Soulah, A., and Vial, L. (2005). Outlet dissipative conditions for air flow in the bronchial tree. *ESAIM Proceedings*, 14:201–212.

McKay, K. O., Wiggs, B. R., Pare, P. D., and Kamm, R. D. (2002). Zero-stress state of intra- and extraparenchymal airways from human, pig, rabbit, and sheep lung. *Journal of Applied Physiology*, 92:1261–1266.

Mead, J., Takishima, T., and Leith, D. (1970). Stress distribution in lungs: a model of pulmonary elasticity. *Journal of Applied Physiology*, 28:596–608.

Mercer, R. R. and Crapo, J. D. (1987). Three-dimensional reconstruction of the rat acinus. *Journal of Applied Physiology*, 63:785–794.

Mercer, R. R. and Crapo, J. D. (1990). Spatial distribution of collagen and elastin fibers in the lungs. *Journal of Applied Physiology*, 69:756–765.

Mercer, R. R., Laco, J. M., and Crapo, J. D. (1987). Three-dimensional reconstruction of alveoli in the rat lung for pressure-volume relationships. *Journal of Applied Physiology*, 62:1480–1487.

Mercer, R. R., Russell, M. L., and Crapo, J. D. (1994). Alveolar septal structure in different species. *Journal of Applied Physiology*, 77:1060–1066.

Michel, J. C., Moulinec, H., and Suquet, P. (1999). Effective properties of composite materials with periodic microstructure: a computational approach. *Computer Methods in Applied Mechanics and Engineering*, 172:109–143.

Miehe, C. (1996). Numerical computation of algorithmic (consistent) tangent moduli in large-strain computational inelasticity. *Computer Methods in Applied Mechanics and Engineering*, 134:223–240.

Miehe, C. (2003). Computational micro-to-macro transitions for discretized microstructures of heterogeneous materials at finite strains based on the minimization of averaged incremental energy. *Computer Methods in Applied Mechanics and Engineering*, 192:559–591.

Miehe, C. and Koch, A. (2002). Computational micro-to-macro transitions of discretized microstructures undergoing small strains. *Archive of Applied Mechanics*, 72:300–317.

Moloney, E. D. and Griffiths, M. J. D. (2004). Protective ventilation of patients with acute respiratory distress syndrome. *British Journal of Anaesthesia*, 92:261–270.

Mols, G., Priebe, H.-J., and Guttmann, J. (2006). Alveolar recruitment in acute lung injury. *British Journal of Anaesthesia*, 96:156–166.

Morris, J. (1998). Characterization of the dynamic behavior of lung surfactant and its components. Master's thesis, Massachusetts Institute of Technology.

Morris, J., Ingenito, E. P., Mark, L., Kamm, R. D., and Johnson, M. (2001). Dynamic behavior of lung surfactant. *Journal of Biomechanical Engineering*, 123:106–113.

Nemat-Nasser, S. and Hori, M. (1999). *Micromechanics: overall properties of heterogeneous materials*. North-Holland.

Ochs, M., Nyengaard, J. R., Jung, A., Knudsen, L., Voigt, M., Wahlers, T., Richter, J., and Grundersen, H. J. G. (2004). The number of alveoli in the human lung. *American Journal of Respiratory and Critical Care Medicine*, 169:120–124.

Oeckler, R. A. and Hubmayr, R. D. (2007). Ventilator-associated lung injury: a search for better therapeutic targets. *European Respiratory Journal*, 30:1216–1226.

Oezdemir, I., Brekelmans, W. A. M., and Geers, M. G. D. (2008). FE^2 computational homogenization for the thermo-mechanical analysis of heterogeneous solids. *Computer Methods in Applied Mechanics and Engineering*, 198:602–613.

Ogden, R. W. (1997). *Non-linear elastic deformations*. Dover Publications.

Oldmixon, E. H., Butler, J. P., and Hoppin, F. G. (1989). Lengths and topology of alveolar septal borders. *Journal of Applied Physiology*, 67:1930–1940.

Olson, L. and Kock, E. (1994). A variational approach for modelling surface tension effects in inviscid fluids. *Computational Mechanics*, 14:140–153.

Otis, D. R., Ingenito, E. P., Kamm, R. D., and Johnson, M. (1994). Dynamic surface tension of surfactant TA: experiments and theory. *Journal of Applied Physiology*, 77:2681–2688.

Owen, M. R. and Lewis, M. A. (2001). The mechanics of lung tissue under high-frequency ventilation. *SIAM Journal on Applied Mathematics*, 61:1731–1761.

Patankar, S. V. and Spalding, D. B. (1972). A calculation procedure for heat, mass and momentum transfer in three-dimensional parabolic flows. *International Journal of Heat and Mass Transfer*, 15:1787–1806.

Peric, D., de Souza Neto, E. A., Feijóo, R. A., Partovi, M., and Molina, A. J. C. (2010). On micro-to-macro transitions for multi-scale analysis of non-linear heterogeneous materials: Unified variational basis and finite element implementation. *International Journal for Numerical Methods in Engineering*, 87:149–170.

Perlman, C. E. and Bhattacharya, J. (2007). Alveolar expansion imaged by optical sectioning microscopy. *Journal of Applied Physiology*, 103:1037–1044.

Popp, A., Wendel, M., Knels, L., Koch, T., and Koch, E. (2006). Imaging of the three-dimensional alveolar structure and the alveolar mechanics of a ventilated and perfused isolated rabbit lung with Fourier domain optical coherence tomography. *Journal of Biomedical Optics*, 11:014015–1–9.

Prange, H. D. (2003). Laplace's law and the alveolus: a misconception of anatomy and a misapplication of physics. *Advances in Physiology Education*, 27:34–40.

Ranieri, V. M., Suter, P. M., Tortorella, C., De Tullio, R., Dayer, J. M., Brienza, A., Bruno, F., and Slutsky, A. S. (1999). Effect of mechanical ventilation on inflammatory mediators in patients with acute respiratory distress syndrome: A randomized controlled trial. *Journal of the American Medical Association*, 282:54–61.

Rausch, S., Haberthuer, D., Stampanoni, M., Schittny, J. C., and Wall, W. A. (2011a). Local strain distribution in real three-dimensional alveolar geometries. *Annals of Biomedical Engineering*, DOI: 10.1007/s10439-011-0328-z.

Rausch, S., Martin, C., Bornemann, P. B., Uhlig, S., and Wall, W. A. (2011b). Material model of lung parenchyma based on living precision-cut lung slice testing. *Journal of the Mechanical Behavior of Biomedical Materials*, 4:583–592.

Rehman, M., Vuik, C., and Segal, G. (2009). Preconditioners for the steady incompressible Navier-Stokes problem. *International Journal of Applied Mathematics*, 38:223–232.

Röhrnbauer, B. (2006). A numerical model for lung parenchymal tissue. Master's thesis, Technische Universität München.

Rubenfeld, G. D., Caldwell, E., Peabody, E., Weaver, J., Martin, D. P., Neff, M., Stern, E. J., and Hudson, L. D. (2005). Incidence and outcomes of acute lung injury. *The New England Journal of Medicine*, 353:1685–1693.

Saad, Y. (2003). *Iterative methods for sparse linear systems*. SIAM.

Saad, Y. and Schulz, M. (1986). GMRES: A generalized minimal residual algorithm for solving nonsymmetric linear systems. *SIAM Journal on Scientific and Statistical Computing*, 7:856–869.

Samaey, G., Roose, D., and Kevrekidis, I. G. (2005). The gap-tooth scheme for homogenization problems. *SIAM Multiscale Modeling and Simulation*, 4:278–306.

Sansour, C. (2008). On the physical assumptions underlying the volumetric-isochoric split and the case of anisotropy. *European Journal of Mechanics A/Solids*, 27:28–39.

Sapoval, B., Filoche, M., and Weibel, E. R. (2002). Smaller is better–but not too small: A physical scale for the design of the mammalian pulmonary acinus. *Proceedings of the National Academy of Sciences USA*, 99:10411–10416.

Scarpelli, E. M. (1998). The alveolar surface network: A new anatomy and its physiological significance. *Anatomical Record*, 251:491–527.

Scarpelli, E. M. and Hills, B. A. (2000). Opposing views on the alveolar surface, alveolar models and the role of surfactant. *Journal of Applied Physiology*, 89:408–412.

Schittny, J. C., Mund, S. I., and Stampanoni, M. (2008). Evidence and structural mechanism for late lung alveolarization. *American Journal of Physiology – Lung Cellular and Molecular Physiology*, 294:L246–L254.

Schreider, J. P. and Raabe, O. G. (1981). Structure of the human respiratory acinus. *American Journal of Anatomy*, 162:221–232.

Shan, Z. and Gokhale, A. M. (2002). Representative volume element for non-uniform micro-structure. *Computational Materials Science*, 24:361–379.

Slutsky, A. S. (1999). Lung injury caused by mechanical ventilation. *Chest*, 116:9S–15S.

Smit, R. J. M., Brekelmans, W. A. M., and Meijer, H. E. H. (1998). Prediction of the mechanical behavior of nonlinear heterogeneous systems by multi-level finite element modeling. *Computer Methods in Applied Mechanics and Engineering*, 155:181–192.

Sobin, S. S., Fung, Y. C., and Tremer, H. M. (1988). Collagen and elastin fibers in human pulmonary alveolar walls. *Journal of Applied Physiology*, 64:1659–1675.

Somer, D. D., de Souza Neto, E. A., Dettmer, W., and Peric, D. (2009). A sub-stepping scheme for multi-scale analysis of solids. *Computer Methods in Applied Mechanics and Engineering*, 198:1006–1016.

Spieth, P. M., Carvalho, A. R., Pelosi, P., Hoehn, C., Meissner, C., Kasper, M., Hübler, M., von Neindorff, M., Dassow, C., Barrenschee, M., Uhlig, S., Koch, T., and Gama de Abreu, M. (2009). Variable tidal volumes improve lung protective ventilation strategies in experimental lung injury. *American Journal of Respiratory and Critical Care Medicine*, 179:684–693.

Stahl, C. A., Schumann, S., Knorpp, H., Schneider, M., Möller, K., and Guttmann, J. (2006). Intravital endo-microscopy of alveoli: A new method to visualize alveolar dynamics. *Journal of Biomechanics*, 39:S598.

Stamenovic, D. (1990). Micromechanical foundations of pulmonary elasticity. *Physiological Reviews*, 70:1117–1134.

Stamenovic, D. and Wilson, T. A. (1985). A strain energy function for lung parenchyma. *Journal of Biomechanical Engineering*, 107:81–86.

Strang, G. (1986). *Introduction to applied mathematics*. Wellesley-Cambridge Press.

Sugihara, T., Martin, C. J., and Hildebrandt, J. (1971). Length-tension properties of alveolar wall in man. *Journal of Applied Physiology*, 30:874–878.

Suki, B., Ito, S., Stamenovic, D., Lutchen, K. R., and Ingenito, E. P. (2005). Biomechanics of the lung parenchyma: Critical roles of collagen and mechanical forces. *Journal of Applied Physiology*, 98:1892–1899.

Suquet, P. M. (1985). Local and global aspects in the mathematical theory of plasticity. In *Plasticity today: modelling methods and applications*, pages 279–310. Elsevier.

Sznitman, J. and Heimsch, T. (2009). Respiratory flow phenomena and gravitational deposition in a three-dimensional space-filling model of the pulmonary acinar tree. *Journal of Biomechanical Engineering*, 131:031010–1–16.

Tai, R. C. and Lee, G. C. (1981). Isotropy and homogeneity of lung tissue deformation. *Journal of Biomechanics*, 14:243–252.

Takayama, I., Terada, N., Baba, T., Ueda, H., Fujii, Y., Kato, Y., and Ohno, S. (2000). Dynamic ultrastructure of mouse pulmonary alveoli revealed by an in vivo cryotechnique in combination with freeze-substitution. *Journal of Anatomy*, 197:199–205.

Tang, H., Buehler, M. J., and Moran, B. (2009). A constitutive model of soft tissue: from nanoscale collagen to tissue continuum. *Annals of Biomedical Engineering*, 37:1117–1130.

Temizer, I. and Wriggers, P. (2008). On the computation of the macroscopic tangent for multiscale volumetric homogenization problems. *Computer Methods in Applied Mechanics and Engineering*, 198:495–510.

Temizer, I. and Wriggers, P. (2010). Thermal contact conductance characterization via computational contact homogenization: A finite deformation theory frame. *International Journal for Numerical Methods in Engineering*, 83:27–58.

Temizer, I. and Zohdi, T. I. (2006). A numerical method for homogenization in non-linear elasticity. *Computational Mechanics*, 40:281–298.

Terada, K., Hori, M., Kyoya, T., and Kikuchi, N. (2000). Simulation of the multi-scale convergence in computational homogenization approaches. *International Journal of Solids and Structures*, 37:2285–2311.

Terada, K. and Kikuchi, N. (1995). Nonlinear homogenization method for practical applications. In *Computational methods in micromechanics*, pages 1–16. ASME Press.

Terada, K. and Kikuchi, N. (2001). A class of general algorithms for multi-scale analyses of heterogeneous media. *Computer Methods in Applied Mechanics and Engineering*, 190:5427–5464.

The Acute Respiratory Distress Syndrome Network (2000). Ventilation with lower tidal volumes as compared with traditional tidal volumes for acute lung injury and the acute respiratory distress syndrome. *The New England Journal of Medicine*, 342:1301–1308.

Toshima, M., Ohtani, Y., and Ohtani, O. (2004). Three-dimensional architecture of elastin and collagen fiber networks in the human and rat lung. *Archives of Histology and Cytolology*, 67:31–40.

Tsushima, K., King, L. S., Aggarwal, N. R., De Gorordo, A., D'Alessio, F. R., and Kubo, K. (2009). Acute lung injury review. *Internal Medicine*, 48:621–630.

Tuminaro, R. S., Heroux, M., Hutchinson, S. A., and Shadid, J. N. (1999). Official aztec user's guide: Version 2.1. Technical report, SAND99-8801J, Sandia National Laboratories.

Uhlig, S. (2002). Ventilation-induced lung injury and mechanotransduction: Stretching it too far? *American Journal of Physiology – Lung Cellular and Molecular Physiology*, 282:L892–L896.

Vawter, D. L. (1980). A finite element model for macroscopic deformation of the lung. *Journal of Biomechanical Engineering*, 102:1–7.

Veldhuizen, E. J. and Haagsman, H. P. (2000). Role of pulmonary surfactant components in surface film formation and dynamics. *Biochimica et Biophysica Acta*, 1467:255–270.

Vermaak, J. S., Mays, C. W., and Kuhlmann-Wilsdorf, D. (1968). On surface stress and surface tension. I. Theoretical considerations. *Surface Science*, 12:128–133.

Vlahakis, N. E. and Hubmayr, R. D. (2003). Response of alveolar cells to mechanical stress. *Current Opinion in Critical Care*, 9:2–8.

von Bahr, M. (2003). *Wetting and capillary flow of surfactant solutions and inks*. PhD thesis, Lund University.

von Neergaard, K. (1929). New notions on a fundamental principle of respiratory mechanics: The retractile force of the lung, dependent on the surface tension in the alveoli. *The Journal of Experimental Medicine*, 66:373–94.

Wall, W. A. (1999). *Fluid-Struktur-Interaktion mit stabilisierten Finiten Elementen*. PhD thesis, Universität Stuttgart.

Wall, W. A., Bornemann, B., and Cyron, C. (2010a). *Nichtlineare Kontinuumsmechanik*. Institute for Computational Mechanics, Technische Universität München.

Wall, W. A. and Gee, M. W. (2010). BACI: A parallel multiphysics simulation environment. Technical report, Institute for Computational Mechanics, Technische Universität München.

Wall, W. A. and Rabczuk, T. (2008). Fluid-structure interaction in lower airways of CT-based lung geometries. *International Journal for Numerical Methods in Fluids*, 57:653–675.

Wall, W. A., Wiechert, L., Comerford, A., and Rausch, S. (2010b). Towards a comprehensive computational model for the respiratory system. *International Journal for Numerical Methods in Biomedical Engineering*, 26:807–827.

Ware, L. B. and Matthay, M. A. (2000). The acute respiratory distress syndrome. *The New England Journal of Medicine*, 342:1334–1349.

Watz, H., Breithecker, A., Rau, W. S., and Kriete, A. (2005). Micro-CT of the human lung: imaging of alveoli and virtual endoscopy of an alveolar duct in a normal lung and in a lung with centrilobular emphysema – initial observations. *Radiology*, 236:1053–1058.

Wei, H.-H., Fujioka, H., Hirschl, R. B., and Grotberg, J. B. (2005). A model of flow and surfactant transport in an oscillatory alveolus partially filled with liquid. *Physics of Fluids*, 17:031510–1–16.

Weibel, E. R. (1963). *Morphometry of the human lung*. Springer.

Weibel, E. R. (1984). *The pathway for oxygen*. Harvard University Press.

Weibel, E. R., Sapoval, B., and Filoche, M. (2005). Design of peripheral airways for efficient gas exchange. *Respiratory Physiology & Neurobiology*, 148:3–21.

West, J. B. (2008). *Respiratory physiology – The essentials*. Lippincott Williams & Wilkins.

Wiechert, L., Metzke, R., and Wall, W. A. (2009). Modeling the mechanical behavior of lung tissue at the micro-level. *Journal of Engineering Mechanics*, 135:434–438.

Wiechert, L., Rabczuk, T., Comerford, A., Metzke, R., and Wall, W. A. (2008). Towards stresses and strains in the respiratory system. *ESAIM Proceedings*, 23:98–113.

Wiechert, L., Rabczuk, T., Gee, M. W., Metzke, R., and Wall, W. A. (2007). Coupled problems in computational modeling of the respiratory system. In *High Performance Computing on Vector Systems 2007*, pages 145–166. Springer.

Wiechert, L. and Wall, W. A. (2010). A nested dynamic multi-scale approach for 3D problems accounting for micro-scale multi-physics. *Computer Methods in Applied Mechanics and Engineering*, 199:1342–1351.

Xia, G., Tawhai, M. H., Hoffman, E. A., and Lin, C.-L. (2010). Airway wall stiffening increases peak wall shear stress: a fluid-structure interaction study in rigid and compliant airways. *Annals of Biomedical Engineering*, 38:1836–1853.

Yager, D., Feldman, H., and Fung, Y. C. (1992). Microscopic vs. macroscopic deformation of the pulmonary alveolar duct. *Journal of Applied Physiology*, 72:1348–1354.

Yin, Y., Choi, J., Hoffman, A. H., Tawhai, M. H., and Lin, C.-L. (2010). Simulation of pulmonary airflow with a subject-specific boundary condition. *Journal of Biomechanics*, 43:2159–2163.

Yuan, H., Ingenito, E. P., and Suki, B. (1997). Dynamic properties of lung parenchyma: mechanical contributions of fiber network and interstitial cells. *Journal of Applied Physiology*, 83:1420–1431.

Yuan, H., Kononov, S., Cavalcante, F. S., Lutchen, K. R., Ingenito, E. P., and Suki, B. (2000). Effects of collagenase and elastase on the mechanical properties of lung tissue strips. *Journal of Applied Physiology*, 89:3–14.

Yuan, H., Suki, B., and Lutchen, K. R. (1998). Sensitivity analysis for evaluating nonlinear models of lung mechanics. *Annals of Biomedical Engineering*, 26:230–241.

Yvonnet, J. and He, Q.-C. (2007). The reduced model multiscale method (R3M) for the non-linear homogenization of hyperelastic media at finite strains. *Journal of Computational Physics*, 223:341–368.

Zhang, Z. and Kleinstreuer, C. (2004). Airflow structures and nano-particle deposition in a human upper airway model. *Journal of Computational Physics*, 198:178–210.

Zienkiewicz, O. C. and Taylor, R. L. (2006). *The finite element method for solid and structural mechanics*. Butterworth Heinemann.

Zienkiewicz, O. C., Taylor, R. L., and Zhu, J. Z. (2005). *The finite element method – Its basis & fundamentals*. Butterworth Heinemann.

Zohdi, T. I. and Wriggers, P. (2005). *Introduction to computational micromechancis*. Springer.

Zulliger, M. A., Fridez, P., Hayashi, K., and Stergiopulos, N. (2003). A strain energy function for arteries accounting for wall composition and structure. *Journal of Biomechanics*, 37:989–1000.